Large Fluid-Driven Deformations of Porous Annuli:

Solutions via Chebyshev Spectral Collocation

Lucy C Auton

Oriel College

Department of Engineering Science

A thesis submitted for the degree of

Doctor of Philosophy

Michaelmas Term 2018

Acknowledgements

I'll keep this brief (unlike the thesis itself). I want to say a huge thank you to my supervisor, Chris MacMinn, for his teaching, support, guidance and fascinating discussions during my entire DPhil... oh and his *slight* perfectionism. It has definitely rubbed off on me... to some extent!

I'd also like to say thanks to a few other academic with whom a few discussions have proved invaluable: Andrew Wells for his input on physical interpretations; Patrick Farrell for his numerical analysis input — in particular introducing me to the Bernstein ellipse less than a fortnight before my submission; Peter Howell for his clear cut views on plastic strains; Ian Griffiths for his asymptotical insight and finally Simon Mathias for pointing me in the direction of Chebyshev pseudospectral methods during a numerics course I attended in Durham.

And just a quick thank you to my friends and family (in particular my mum!) especially those who I have roped in to proof-reading for me, and to my parents for graciously putting up with my blaring music while I was working on finalising this thesis throughout Christmas 2018.

Abstract

The radially outward flow of fluid into a porous medium occurs in many practical problems, from transport across vascular walls to the pressurisation of boreholes. As the driving pressure becomes non-negligible relative to the stiffness of the solid structure, the poromechanical coupling between the fluid and the solid has an increasingly strong impact on the flow. For very large pressures or very soft materials, as is the case for hydraulic fracturing and arterial flows, this coupling can lead to large elastic deformations or plastic flow and hence to strong deviations from a classical, linear poroelastic response. In this thesis, we investigate large deformation poroelasticity and poroelasto-plasticity via the use of a simple axisymmetric model problem. We use the relative simplicity of this model problem to conduct the first systematic analysis of the effects of driving method, geometry and numerous facets of nonlinearity on the resulting flow and deformation. We consider two different permeability laws (constant *vs.* Kozeny-Carman), two stress-strain relationships (Hencky *vs.* linear), and two constitutive solid behaviours (elasticity *vs*. elasto-plasticity). We solve these models analytically when possible and using Chebyshev spectral collocation in general. Large deformations are inherently nonlinear, and these nonlinear effects manifest themselves within the kinematics, permeability, and elastic or plastic stress-strain relations. By isolating each of these effects, we assess the impact of different model simplifications for a wide range of parameter values. In addition to the physical insight they provide, our results and numerical codes could prove useful for benchmarking general numerical-simulation tools.

Contents

List of Figures

Chapter 1

Introduction

The radially outward flow of fluid into a porous medium is central to many practical problems in, for example, geomechanics, biophysics, and filtration. In geomechanics, pile driving involves the mechanical expansion of a cylindrical cavity in a fluid-saturated soil, generating large pore pressures in the surrounding medium that gradually relax through consolidation [*e.g.*, 76]. Similarly, fluid injection into boreholes involves the pressurisation of a cylindrical cavity in a soil or rock, driving flow radially outward into the surrounding medium [*e.g*, 32, 79, 83, 84]. Biophysical applications include injection into subcutaneous tissue [96] and blood flow through arteries and vascular networks, which have permeable walls [*e.g.,* 9, 10, 54, 56, 58, 77, 86]. Radially outward flow is also relevant to the design of cylindrical filters [24, 43]. In many of these cases, the driving pressure is sufficiently large relative to the stiffness of the solid structure that the poromechanical coupling between the fluid and the solid has an important impact on the flow. Classically, this coupling is described by the iconic theory of linear poroelasticity [*e.g*, 14, 101], which combines Darcy's law with linear elasticity in a linearised kinematic framework and is valid for infinitesimal deformations of the solid. However, soft materials such as biological tissues, weak materials such as soils, thin structures such as vasculature, and scenarios involving large injection pressures such as hydraulic fracturing may result in substantial deformations that violate

this linear theory. Large deformations are inherently nonlinear from the perspective of kinematics, and typically also result in nonlinear constitutive behaviour such as nonlinear elasticity, deformation-dependent permeability or even plastic flow. Recent work in biomechanics and geomechanics, in particular, has focussed on capturing the complex material- and application-specific behaviours of tissues and soils [*e.g.*, 4, 19, 36, 88, 90, 94, 100].

The goal of this thesis is to provide fundamental physical insight into large deformation poromechanics by focussing on a simple axisymmetric model problem. As such, we restrict our consideration to injecting fluid radially outward into a cylindrical tube of porous material, such that each annular cross-section is in plane strain. We either fix the outer boundary in place or subject it to a constant radial effective stress. We work with relatively generic constitutive laws to avoid obscuring the universal physics of these problems with material-specific behaviour. We look at the competing physical mechanisms and their relative importance for the range of applications discussed above. Each application has a range of relevant geometries; for example, flow through artery walls can be modelled by a thin annulus, while to model a cavity expansion problem the soil surrounding the cavity can be modelled as a very thick annulus. We survey a large range of wall-thicknesses to see how geometry impacts the various mechanisms at play.

Historically, uniaxial deformation has been a key model problem for studying the importance of nonlinearity, both mathematically and experimentally [*e.g.,* 13, 45, 61, 70]. The uniaxial problem is important for a variety of practical applications; for example, many composite manufacturing processes involve the uniaxial injection of a resin gel or metal melt into a deformable porous matrix [74]. Mathematically, the uniaxial problem is inherently simple since the flow and deformation fields are strictly one-dimensional and the exact relationship between displacement and porosity is linear [61]. Radial deformations are more challenging despite the fact that the velocity and displacement fields remain one-dimensional, due to the fact that the stress and strain fields become biaxial and the exact relationship between the porosity and displacement becomes nonlinear.

Radial poroelastic deformations have been studied using linear poroelasticity in the context of both fluid injection or extraction from boreholes [*e.g*, 32, 79, 84] and arterial blood flow [*e.g.*, 54, 56]. Nonlinear effects have attracted interest primarily in the latter case, specifically in the context of fluid flow through artery walls. For example, Klanchar and Tarbell [58] introduced deformation-dependent permeability within a linear poroelastic framework. Barry and Aldis [9] and Barry and Mercer [10] accounted partially for the nonlinear kinematics of large deformations while retaining linear elasticity. In a different context, MacMinn et al. [60] developed a rigorous and fully nonlinear model, but for a strictly volumetric constitutive law and assuming constant permeability. None of these previous works explicitly defined or explored the general parameter space for axisymmetric deformations, nor did they systematically assess the relative importance of nonlinear kinematics, deformation-dependent permeability and nonlinear elasticity.

When the shear stress exceeds the yield strength of the porous material, a poroelasto-plastic model is needed. Large radial plastic deformations have been considered in the context of cavity expansion [23, 28, 47, 99, 111, 112]. Carter et al. [23], Vesic [99] and Yu and Houlsby [112] all model the problem of cavity expansion in a semi-infinite domain, while Yu [111] extends the model to that of a finite domain. Although the kinematics of the material is treated rigorously near the cavity, all these problems are concerned with purely mechanical loading and neglect the effect of fluid flow in the subsurface. Radial poroelasto-plastic deformations have been considered in the context of borehole integrity problems in numerous studies [*e.g*, 81, 102, 104–106], although all these problems linearised the kinematics of the system under the assumption of infinitesimal strains, which is inherently violated by the inclusion of plasticity. None of these works have developed a kinematically rigorous poroelasto-plastic model, nor have they examined the relative importance of inclusion of plasticity and these additional facets of nonlinearity.

Throughout this thesis we use Chebyshev spectral collocation to solve the differential equations that result from our model problem. Spectral methods first gained popularity in

the 1970's and were recognised as one of the key technologies for the solution of partial differential equations (PDEs) [91]. In general, spectral collocation methods ('pseudospectral methods') involve a set of basis functions with the property that each function is zero at all but one of the discrete number of solution (or collocation) points that discretise the domain. A global polynomial interpolant is then constructed via a linear combination of these basis functions and the derivatives of the original function are approximated via derivatives of the interpolant. Classical Fourier spectral collocation uses trigonometric polynomials on an equispaced grid for periodic problems. Chebyshev spectral collocation is the simplest pseudospectral method for finite domains, using Chebyshev points (the maxima of Chebyshev's polynomial) as the collocation points and algebraic polynomials as the basis functions. One advantage of using spectral collocation for solving differential equations is that it couples the behaviour of the interpolant at each collocation point to every other collocation point.

In Chapter 2, we introduce the purely poroelastic model problem, deriving the kinematic relations and discussing the various constitutive laws for both elasticity and permeability. We also present the initial, boundary and driving conditions and construct the full transient poroelastic closed initial boundary value problems (IBVPs) in one variable.

In Chapter 3, we study the steady-state response of a poroelastic cylinder to fluid injection. We present both the analytical solutions for the tractable cases and discuss the Chebyshev pseudospectral numerical scheme for the rest. We discuss classical solution methods for solving boundary value problems (BVPs), their limitations, and our chosen numerical approach — that is using Chebyshev spectral collocation and Newton iterations to solve the BVP. We introduce in more detail the theory behind Chebyshev spectral collocation and define the Chebyshev differentiation matrix. We discuss convergence and 'spectral accuracy' and demonstrate this for classical linear poroelasticity, for which we have an explicit analytical solution. We show that the numerical solution rapidly converges to the analytical solution as the number of grid points increase and discuss the impact of

geometry on the rate of convergence. We consider the qualitative and quantitative impacts of kinematic and constitutive nonlinearity, highlighting the strong impact of deformation-dependent permeability. We show that the wall thickness (thick *vs*. thin) and the outer boundary condition (free *vs*. constrained) play a central role in controlling the mechanics.

In Chapter 4, we study the transient response of a poroelastic cylinder to sudden fluid injection. We present analytical solutions for flow-driven classical linear poroelasticity and discuss the extension of the Chebyshev spectral collocation method, as developed for the steady state problem, to the transient IBVP. We consider the impacts of kinematic and constitutive nonlinearity, both separately and in combination, and we highlight the central role of driving method in the evolution of the response. We show that the various facets of nonlinearity may either accelerate or decelerate the transient response relative to linear poroelasticity, depending on the boundary conditions and the initial geometry, and that an imposed fluid pressure leads to a much faster response than an imposed fluid flux.

In Chapter 5, we approach the problem of fluid-driven deformation of a borehole by developing a large-deformation model for radially outward fluid injection into a partially permeable elastic–perfectly-plastic cohesive granular material from a cylindrical cavity in plane strain, isolating the additional deformation due to fluid injection from the compressive base-state to which the subsurface is subject. We introduce a simple parameter that smoothly transitions the mechanism of loading from an applied mechanical load at the boundary to a pore-pressure gradient throughout the material, transitioning the material from impermeable to fully permeable. This enables coated boreholes and low permeability materials to be modelled as 'partially permeable' which is more representative of their true behaviour. We consider only the steady-state poroelasto-plastic behaviour, once again expressing the governing equations as a coupled free-boundary BVP in terms of one variable. We present analytical solutions when tractable and discuss the extension of the Chebyshev spectral collocation method to the poroelasto-plastic problem now with a coupled free-boundary domain. We focus in particular on the difference between (poro)elastic and

(poro)elasto-plastic deformations, and the transition from impermeable to fully permeable. We find that the inclusion of plasticity leads to larger deformations, particularly in the plastic region, and as such model choice becomes increasingly significant in this region; the elastic region remains insensitive to these changes. Similarly, increasing the permeability at the cavity wall also leads to larger deformations throughout, again making plastic model choice increasingly important. We also include an extensive parameter review of shales, clays and sands in Appendix G.

Finally, in Chapter 6, we summarise the key findings of the thesis. We reflect on the many direct applications of this work such as the use of these models (and codes — see Electronic Supplementary material of Auton and MacMinn [6]) for the benchmarking of general numerical-simulation tools (*e.g.,* finite-element codes). This is particularly useful as relatively few benchmarks are available in the context of large-deformation poromechanics.

Chapter 2

The governing equations of 2D axisymmetric poroelasticity

We consider the radially outward injection of fluid from a line source, which is characterised by either a fixed pressure difference or a fixed flow rate, located at the centre of a porous cylinder of inner radius a and outer radius b. We assume axisymmetry and model the two-dimensional annular cross-section, assuming that the material is constrained in the axial direction and is therefore in plane strain. We assume that the inner boundary is mechanically free so that the inner radius $a = a(t)$ expands in response to injection. We assume that the outer boundary is either subject to a constant radial effective stress σ_b', in which case the outer radius $b = b(t)$ also expands in response to injection (Fig. 2.1, left), or that the outer boundary is constrained such that the outer radius $b \equiv b(0)$ is fixed (Fig. 2.1, right). The latter situation is useful for comparison to numerical simulations and experiments [*e.g.*, 60].

2.1 Summary of theory

Large-deformation poromechanics is a continuum approach to modelling the interactions of two superposed phases, a porous solid skeleton and an interstitial fluid [*e.g.*, 61]. We

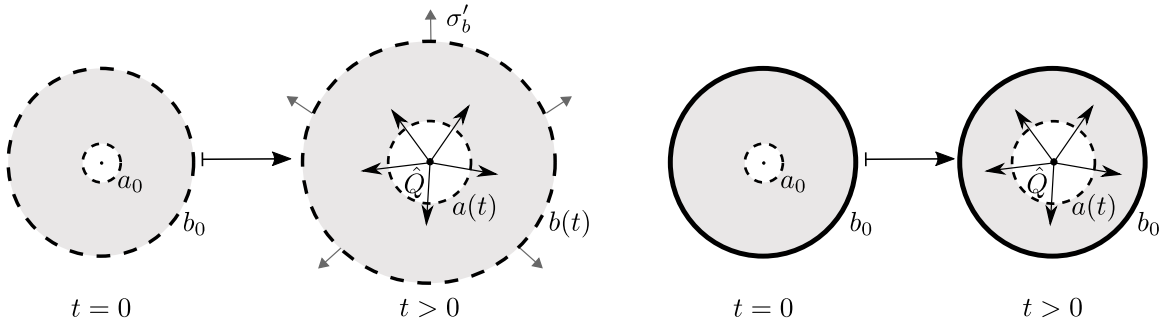

Figure 2.1: We consider both the transient and subsequent steady-state response of a poroelastic cylinder to sudden fluid injection. The fluid flows radially outward through the cylinder which has initial inner radius a_0 and initial outer radius $r = b_0$. The inner boundary is free to move, while the outer boundary is either subject to a fixed radial effective stress σ_b' (left) or fixed in place (right). We initialise the problem from a relaxed state and we study the transient evolution of the problem towards its steady state. Note that we assume plane strain and adopt the convention of tension being positive.

next summarise this theory in the context of axisymmetric flow and deformation.

2.1.1 Kinematics

The fluid velocity $\mathbf{v}_f$, solid displacement $\mathbf{u}_s$, and solid velocity $\mathbf{v}_s$ each have only one component,

$$\mathbf{u}_s = u_s(r,t)\hat{\mathbf{e}}_r,\ \mathbf{v}_s = v_s(r,t)\hat{\mathbf{e}}_r,\ \text{and}\ \mathbf{v}_f = v_f(r,t)\hat{\mathbf{e}}_r, \tag{2.1}$$

where the subscripts s and f denote quantities related to the solid and to the fluid, respectively, r is the Eulerian radial coordinate ($a \leq r \leq b$), t is time, and $\hat{\mathbf{e}}_r$ is the radial unit vector. It is conventional to work in a Lagrangian reference frame when modelling solid deformations, while an Eulerian (spatial) reference frame is the usual choice for fluid deformations. Due to the coupling of fluid flow and deforming solid skeleton, working in either reference frame leads to complications. In a Lagrangian reference frame, the governing equations, which are defined on a fixed domain, are significantly more nonlinear than their Eulerian counterparts. We choose to work in an Eulerian reference frame as, for this problem, the resulting complication of moving boundaries is less problematic than this additional nonlinearity; additionally an Eulerian reference frame is simply more intuitive.

Hence, the displacement is given by

$$u_s(r,t) = r - R(r,t), \tag{2.2}$$

where $R(r,t)$, the Lagrangian radial co-ordinate, denotes the reference position of the material that is located at position r at time t. Without loss of generality, we take the reference state to be relaxed and undeformed. The deformation is fully characterised by the deformation gradient tensor $\mathbf{F} = (\mathbf{I} - \nabla \mathbf{u_s})^{-1}$, where $\mathbf{I}$ denotes the identity tensor and $(\cdot)^{-1}$ the inverse. For an axisymmetric deformation, this can be written

$$\mathbf{F} = \begin{pmatrix} \lambda_r & 0 & 0 \\ 0 & \lambda_\theta & 0 \\ 0 & 0 & \lambda_z \end{pmatrix}, \tag{2.3}$$

where λ_r, λ_θ, and λ_z are the three principal stretch ratios.[1] For plane strain, these are given by

$$\lambda_r = \left(1 - \frac{\partial u_s}{\partial r}\right)^{-1}, \quad \lambda_\theta = \left(1 - \frac{u_s}{r}\right)^{-1}, \quad \text{and} \quad \lambda_z \equiv 1. \tag{2.4}$$

Note that although the displacement field is one dimensional, the state of strain is indeed two dimensional (*i.e.*, both λ_r and λ_θ are distinct and nontrivial).

The Jacobian determinant $J \equiv \det(\mathbf{F})$ measures the local volume change,

$$J = \lambda_r \lambda_\theta \lambda_z = \lambda_r \lambda_\theta. \tag{2.5}$$

We assume that the solid and fluid phases are individually incompressible, such that deformation occurs only through rearrangement of the solid skeleton with corresponding

[1] In general, λ_i^2 are the eigenvalues of $\mathbf{F}\mathbf{F}^{\mathsf{T}}$.

changes in the local porosity or fluid fraction, ϕ_f. This then requires that

$$J(r,t) = \frac{1-\phi_{f,0}}{1-\phi_f}, \tag{2.6}$$

where $\phi_{f,0}$ is the reference (relaxed) porosity, which we take to be uniform. Combining Equations (2.4–2.6), we obtain an explicit nonlinear expression for porosity in terms of displacement,

$$\frac{\phi_f - \phi_{f,0}}{1-\phi_{f,0}} = \frac{1}{r}\frac{\partial}{\partial r}\left(r u_s - \frac{1}{2}u_s^2\right). \tag{2.7}$$

Conservation of mass for the fluid-solid mixture is given by

$$\frac{\partial \phi_f}{\partial t} + \frac{1}{r}\frac{\partial}{\partial r}\left(r\phi_f v_f\right) = 0 \quad \text{and} \quad \frac{\partial \phi_f}{\partial t} - \frac{1}{r}\frac{\partial}{\partial r}\left[r(1-\phi_f)v_s\right] = 0, \tag{2.8}$$

where $1-\phi_f$ is the local solid fraction. Conservation of solid volume requires that

$$\int_a^b 2\pi r\,(1-\phi_f)\,\mathrm{d}r = \pi\left(b_0^2 - a_0^2\right)(1-\phi_{f,0}), \tag{2.9}$$

and it can be shown that Equation (2.9) is identically satisfied by Equation (2.7), subject to the kinematic boundary conditions $u_s(a,t) = a(t) - a_0$ and $u_s(b,t) = b(t) - b_0$, where $a_0 := a(0)$ and $b_0 := b(0)$ denote the initial inner and outer radii, respectively.

2.1.2 Mechanical equilibrium

In the absence of body forces and neglecting inertia, mechanical equilibrium requires that

$$\boldsymbol{\nabla}\cdot\boldsymbol{\sigma} = 0, \tag{2.10}$$

where $\boldsymbol{\sigma}$ is the total stress supported by the fluid-solid mixture. The total stress can be decomposed as

$$\boldsymbol{\sigma} = \boldsymbol{\sigma'} - p\mathbf{I}, \tag{2.11}$$

where Terzaghi's effective stress σ' is the portion of the stress supported through deformation of the solid skeleton, and where we adopt the convention of tension being positive. Equation (2.11) provides mechanical coupling between the fluid and the solid. Combining Equations (2.10) and (2.11) leads, for an axisymmetric deformation, to

$$\frac{\partial \sigma_r'}{\partial r} + \frac{\sigma_r' - \sigma_\theta'}{r} = \frac{\partial p}{\partial r}, \tag{2.12}$$

where σ_r' and σ_θ' are the radial and azimuthal ('hoop') components of the effective stress, respectively.

2.1.3 Darcy's Law

We assume that fluid flows relative to the solid skeleton according to Darcy's law. In the absence of gravity and other body forces, this can be written

$$\phi_f(v_f - v_s) = -\frac{k(\phi_f)}{\mu}\frac{\partial p}{\partial r}, \tag{2.13}$$

where μ is the dynamic viscosity of the fluid, p is the fluid (pore) pressure, and $k(\phi_f)$ is the permeability, which we take to be an isotropic function of porosity (see §2.3).

We model injection as a line source at the origin with flow rate per unit length $\hat{Q}(t)$. Thus, Equations (2.8) can be subtracted and integrated to give

$$2\pi r[\phi_f v_f + (1 - \phi_f)v_s] = \hat{Q}(t). \tag{2.14}$$

Combining Equation (2.14) with Equations (2.8) and (2.13), we eliminate ϕ_s, v_s, and v_f to obtain

$$\frac{\partial \phi_f}{\partial t} + \frac{1}{r}\frac{\partial}{\partial r}\left(\phi_f \frac{\hat{Q}(t)}{2\pi} - r(1-\phi_f)\frac{k(\phi_f)}{\mu}\frac{\partial p}{\partial r}\right) = 0, \tag{2.15a}$$

where along the way we obtain expressions for v_f and v_s,

$$v_f = \frac{\hat{Q}(t)}{2\pi r} - \frac{1-\phi_f}{\phi_f}\frac{k(\phi_f)}{\mu}\frac{\partial p}{\partial r} \quad \text{and} \quad v_s = \frac{\hat{Q}(t)}{2\pi r} + \frac{k(\phi_f)}{\mu}\frac{\partial p}{\partial r}. \tag{2.15b}$$

Via consideration of the kinematics additionally we find that

$$v_s = \frac{\mathrm{D}u_s}{\mathrm{D}t} = \lambda_r \frac{\partial u_s}{\partial t}, \tag{2.16}$$

where $\frac{D}{Dt} := \left(\frac{\partial}{\partial t} + \boldsymbol{v}_s \cdot \nabla\right)$ is the material time derivative. We next link the fluid pressure to the stress in the solid.

2.1.4 Linearisation

We have now considered kinematics, mechanical equilibrium, Terzaghi's effective stress and Darcy's Law. The model thus far is exact for axisymmetric plane strain, assuming only that the fluid and solid constituents are individually incompressible.

The common assumption of infinitesimal deformations, or more accurately of infinitesimal strains, leads to classical linear poroelasticity [61, 101]. This corresponds here to the assumptions that $u_s/r \ll 1$ and $\partial u_s/\partial r \ll 1$. Note that this will clearly be a bad assumption near the inner radius if u_s becomes comparable to a_0. Linearising Equations (2.7), (2.15a) and (2.16) leads to

$$\frac{\phi_f - \phi_{f,0}}{1-\phi_{f,0}} \approx \frac{1}{r}\frac{\partial}{\partial r}\left(r u_s\right), \tag{2.17a}$$

$$\frac{\partial \phi_f}{\partial t} - \frac{1}{r}\frac{\partial}{\partial r}\left(r(1-\phi_{f,0})\frac{k(\phi_{f,0})}{\mu}\frac{\partial p}{\partial r}\right) \approx 0, \tag{2.17b}$$

and

$$v_s \approx \frac{\partial u_s}{\partial t} \tag{2.17c}$$

respectively. Note that Equation (2.9) is not identically satisfied by Equation (2.17a), im-

plying that the linearised model is not rigorously mass conservative. We next consider the constitutive behaviour of the solid.

2.2 Constitutive laws: elasticity

In this chapter we assume that the solid deforms elastically, meaning that the relationships between stress and strain and between strain and displacement are quasi-static (*i.e.*, rate independent) and reversible (*i.e.*, history independent). For elastic deformations, we relate "stress" to strain via

$$\text{“stress”} = \begin{bmatrix} \mathcal{M}\varepsilon_r + \Lambda\varepsilon_\theta & 0 & 0 \\ 0 & \Lambda\varepsilon_r + \mathcal{M}\varepsilon_\theta & 0 \\ 0 & 0 & \Lambda\left(\varepsilon_r + \varepsilon_\theta\right) \end{bmatrix}, \tag{2.18}$$

where the particular measure of stress will depend on the strain measure and where ε_r and ε_θ denote the radial and azimuthal strains, respectively. We investigate the impact of these relationships on the results by considering both linear and nonlinear elasticity laws.

2.2.1 Hencky elasticity

Hencky elasticity is a generic constitutive law that captures the kinematic aspects of large deformations without introducing material-specific complexity. More specifically, Hencky elasticity is a simple, nonlinear, hyperelastic model that is based on a logarithmic strain measure and provides good agreement with experiments for moderate (in the order of tens of percent) deformations [2, 3, 42] across a wide range of materials. To illustrate this, Anand [2] considers data from literature to examine the Hencky strain prediction. Anand [2] examines barium, calcium, tin, silver, aluminium, copper, iron, molybdenum, tanta-

lum, and vulcanised natural rubber in uniaxial compression; vulcanised natural rubber and a polyurethane foam rubber in tension and also vulcanised natural rubber in pure shear. In compression, for the range of stretches available for each of these materials, Hencky showed good agreement; this range of stretches was limited to a few percent for some of the materials and up to around 40% for others. In uniaxial tension, polyurethane foam rubber showed good agreement for all available data, up to around 100% stretch while for vulcanised natural rubber the agreement was good for around a 40% stretch but for stretches in the range 40–170% the Hencky prediction diverged from experimental data. Similarly, for vulcanised natural rubber in pure shear, agreement is good for stretches up to around 30%, after which Hencky predictions diverge from experimental data.

Hencky elasticity has several advantageous properties [11], including that it uses the same elastic parameters as linear elasticity and is asymptotically equivalent to linear elasticity in the limit of infinitesimal strain. Hencky elasticity is therefore a convenient and appropriate model for a wide range of materials under moderate deformations [2, 11, 42, 108]. Note that whereas moderate to large elastic deformations are common in the context of soft filters and tissues, soils and rocks are unlikely to behave elastically beyond small strains. We work here in terms of Lamé's first parameter $\Lambda \equiv \dfrac{E\nu}{(1+\nu)(1-2\nu)}$ and the p-wave or oedometric modulus $\mathcal{M} \equiv \dfrac{E(1-\nu)}{(1+\nu)(1-2\nu)}$, where ν and E are the Poisson ratio and the Young modulus, respectively.

For the displacement field given in Equation (2.2), the Hencky strain tensor is

$$\boldsymbol{\varepsilon} = \begin{bmatrix} \ln\lambda_r & 0 & 0 \\ 0 & \ln\lambda_\theta & 0 \\ 0 & 0 & 0 \end{bmatrix}, \tag{2.19}$$

which again has two nontrivial components since axisymmetric displacement leads to both

radial and azimuthal strains.

For Hencky elasticity, is is appropriate to use the Kirchhoff effective stress tensor, $\boldsymbol{s}'$, in Equation (2.18) to relate stress to strain; we relate $\boldsymbol{s}'$ to the effective Cauchy stress tensor $\boldsymbol{\sigma}'$ via [2, 3, 108]

$$\boldsymbol{s}' \equiv J\boldsymbol{\sigma}'. \tag{2.20}$$

Thus, for Hencky elasticity, effective stress is related to displacement via

$$\boldsymbol{\sigma}' = \begin{bmatrix} \mathcal{M}\dfrac{\ln\lambda_r}{J} + \Lambda\dfrac{\ln\lambda_\theta}{J} & 0 & 0 \\ 0 & \Lambda\dfrac{\ln\lambda_r}{J} + \mathcal{M}\dfrac{\ln\lambda_\theta}{J} & 0 \\ 0 & 0 & \Lambda\left(\dfrac{\ln\lambda_r + \ln\lambda_\theta}{J}\right) \end{bmatrix}. \tag{2.21}$$

On substitution of Equation (2.21) into Equation (2.12), we arrive at

$$\frac{\partial p}{\partial r} = \frac{\partial}{\partial r}\left(\mathcal{M}\,\frac{\ln\lambda_r}{J} + \Lambda\frac{\ln\lambda_\theta}{J}\right) + \frac{\mathcal{M}-\Lambda}{r}\left(\frac{\ln\lambda_r}{J} - \frac{\ln\lambda_\theta}{J}\right). \tag{2.22}$$

Note that the right-hand side of Equation (2.22) is a function of u_s only. In combination with Equations (2.7) and (2.15a), this then provides a nonlinear PDE for u_s.

2.2.2 Linear elasticity

Linear elasticity combines a linear relationship between strain and displacement with a linear relationship between stress and strain. The linear (small or infinitesimal) strain tensor is

$$\boldsymbol{\varepsilon} = \begin{bmatrix} \dfrac{\partial u_s}{\partial r} & 0 & 0 \\ 0 & \dfrac{u_s}{r} & 0 \\ 0 & 0 & 0 \end{bmatrix} \tag{2.23}$$

and where Cauchy effective stress is related to strain via Equation (2.18). Hence, for linear elasticity, stress is related to displacement via

$$\boldsymbol{\sigma}' = \begin{bmatrix} \mathcal{M}\dfrac{\partial u_s}{\partial r} + \Lambda\dfrac{u_s}{r} & 0 & 0 \\ 0 & \Lambda\dfrac{\partial u_s}{\partial r} + \mathcal{M}\dfrac{u_s}{r} & 0 \\ 0 & 0 & \Lambda\left(\dfrac{\partial u_s}{\partial r} + \dfrac{u_s}{r}\right) \end{bmatrix}. \tag{2.24}$$

On substitution of Equation (2.24) into Equation (2.12), we obtain

$$\frac{\partial p}{\partial r} = \frac{\partial}{\partial r}\left[\mathcal{M}\,\frac{\partial u_s}{\partial r} + \Lambda\frac{u_s}{r}\right] + \frac{\mathcal{M}-\Lambda}{r}\left(\frac{\partial u_s}{\partial r} - \frac{u_s}{r}\right) = \mathcal{M}\,\frac{\partial}{\partial r}\left[\frac{1}{r}\frac{\partial}{\partial r}\left(r u_s\right)\right]. \tag{2.25}$$

Linear elasticity is in some sense an idealised constitutive behaviour that most materials will approximately follow for small deformations, and from which most materials will deviate as deformations become finite. As discussed above, Hencky elasticity reduces to linear elasticity for infinitesimal strains; that is, Equations (2.19) and (2.21) reduce to Equation (2.23) and Equation (2.24), respectively, for $u_s/r \ll 1$ and $\partial u_s/\partial r \ll 1$. Alternatively, linear elasticity can instead be viewed as an exact constitutive law for an idealised material, for which it would be valid for arbitrarily large deformations. As for Hencky elasticity, Equation (2.25) can be combined with Equations (2.7) and (2.15a) to provide a PDE for u_s.

2.2.3 Hencky elasticty *vs* linear elasticity

For a simple uniaxial deformation, Hencky elasticity reduces to

$$\frac{\sigma'}{\mathcal{M}} = \frac{\ln\lambda}{\lambda}, \tag{2.26}$$

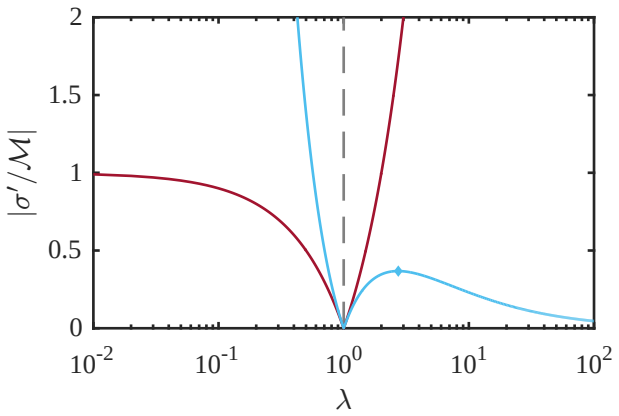

Figure 2.2: The absolute value of the dimensionless effective stress *vs.* the stretch for uniaxial deformation according to linear elasticity (red) and Hencky elasticity (blue). Hencky elasticity provides a stiffer response than linear elasticity in compression ($\lambda < 1$) and a softer response in tension ($\lambda > 1$). In tension, the stress predicted by Hencky elasticity reaches a maximum value of $\sigma'/\mathcal{M} = 1/e$ for a stretch of $\lambda = e$ (blue diamond) before decreasing asymptotically to zero. The two models agree in the limit of small strain, $|\lambda - 1| \ll 1$. Note that for moderate deformations — that is, for strains in the in the order of tens of percent — Hencky elasticity offers good agreement with a variety of materials.

where σ' is the normal effective stress, and $\lambda = 1 + \Delta L/L$ is the stretch, with ΔL the change in overall length and L the original length. Linear elasticity instead predicts

$$\frac{\sigma'}{\mathcal{M}} = \lambda - 1. \tag{2.27}$$

As seen in Figure 2.2, in uniaxial compression, Hencky elasticity provides a stiffer response than linear elasticity, with the stress diverging as the thickness of the material approaches zero; in uniaxial tension, Hencky elasticity provides a softer response than linear elasticity, with the stress reaching a maximum and then decaying asymptotically to zero.

In what follows, we use 'Hencky elasticity' to refer to Equations (2.19–2.22) and 'linear elasticity' to refer to Equations (2.23–2.25).

2.2.4 Linearised poroelasticity

We now combine linearised kinematics (§2.1.4) with linear elasticity (§2.2.2). This then allows us to write Equation (2.25) directly in terms of ϕ_f using Equation (2.17),

$$\frac{\partial p}{\partial r} \approx \mathcal{M} \frac{\partial}{\partial r} \left(\frac{\phi_f - \phi_{f,0}}{1 - \phi_{f,0}} \right). \tag{2.28}$$

Equation (2.17) can then be rewritten as a linear second-order parabolic PDE for ϕ_f.

2.3 Constitutive laws: permeability

The solid skeleton deforms through rearrangement of the pore structure, leading to changes in the porosity. This is then likely to alter the permeability of the material. We consider the impact of this simplification by comparing results for constant permeability with results for deformation-dependent permeability. As in MacMinn et al. [61], we adopt a normalised Kozeny-Carman formula,

$$k(\phi_f) = k_0 \frac{(1 - \phi_{f,0})^2}{\phi_{f,0}^3} \frac{\phi_f^3}{(1 - \phi_f)^2}, \tag{2.29}$$

where $k_0 \equiv k(\phi_{f,0})$ is the reference permeability. Although not quantitatively appropriate for all materials, this relation captures the important qualitative behaviour that $k(\phi_f)$ vanishes as ϕ_f vanishes and $k(\phi_f)$ diverges as ϕ_f tends to one. This nonlinear effect is neglected in classical linear poroelasticity, in which case the permeability function is simply $k(\phi_f) = k(\phi_{f,0}) \equiv k_0$

Note that many materials have a naturally anisotropic permeability. In addition, anisotropic deformations may lead to the emergence of anisotropic permeability. For example, fluid flow through the walls of a porous cylinder leads to compression in the radial direction and stretching in the azimuthal direction, which might be expected to reduce the azimuthal permeability while enhancing the radial permeability. We neglect natural anisotropy here

for simplicity; induced anisotropy is irrelevant under the requirement of axisymmetry.

2.4 Boundary, initial and driving conditions

2.4.1 Boundary conditions

The inner boundary is mechanically free, thus the normal effective stress must vanish,

$$\sigma'_r(a,t) = 0. \tag{2.30}$$

The inner boundary is also a material boundary, subject to the kinematic conditions

$$u_s(a,t) = a(t) - a_0 \tag{2.31a}$$

and

$$v_s(a,t) = \frac{\mathrm{d}a}{\mathrm{d}t}. \tag{2.31b}$$

At the outer boundary, we enforce a vanishing pressure without loss of generality

$$p(b,t) = 0. \tag{2.32}$$

Additionally, we consider the two distinct sets of outer boundary conditions imposing either a fixed position (no displacement) or a fixed radial effective stress,

$$u_s(b,t) = 0 \tag{2.33a}$$

or

$$\sigma'_r(b,t) = \sigma'_b, \tag{2.33b}$$

respectively. We refer to the former as 'constrained' and to the latter, for the limiting case of $\sigma_b' \equiv 0$, as 'unconstrained'. The latter case involves a moving boundary, and is therefore additionally subject to the kinematic conditions

$$u_s(b,t) = b(t) - b_0 \tag{2.34a}$$

and

$$v_s(b,t) = \frac{\mathrm{d}b}{\mathrm{d}t}. \tag{2.34b}$$

Note that for linearised kinematics coupled with linear elasticity, the inner and outer conditions are applied at $a = a_0$ and $b = 1$, respectively, and as such the kinematic conditions, Equations (2.31a) and (2.34a) are not required.

Condition (2.33a) is convenient for comparison with experiments and numerical simulations (*e.g.*, [60]), and is relevant to industrial applications such as filtration. Condition (2.33b) is likely to be more relevant to biomedical and geotechnical applications.

2.4.2 Initial conditions

We initialise the model by specifying $u_s(r,0) = u_{s,0}(r)$ and assuming that the cylinder starts from rest ($v_s(r,0) = v_f(r,0) = 0$). For both the constrained and unconstrained cylinders, we start from a relaxed (undeformed and stress-free) state, such that $u_{s,0} = 0$. This implies that $\phi_f(r,0) = \phi_{f,0}$, so that the initial state is the reference state and this is consistent with the boundary conditions. However, for the general case $\sigma_b' \not\equiv 0$, a stress-free initial condition does not satisfy these boundary conditions. Hence, we solve the corresponding purely elastic ('drained') problem subjected to $B^{a_0}[u_s] = B_2^{b_0}[u_s] = 0$ and then use this solution as a consistent initial condition for the evolution of the fluid-driven problem (see §4.1.2.2). For classical linear poroelasticity, this initial condition corresponds to a uniform porosity that is distinct from the reference porosity $\phi_{f,0}$.

2.4.3 Driving conditions

For $t > 0$, we assume that fluid is injected from the origin either at an imposed constant volume flow rate per unit length $\hat{Q}$ or via an imposed constant pressure drop $\Delta p := p(a,t) - p(b,t)$. It is straightforward to enforce the former condition since $\hat{Q}$ appears explicitly in the PDE. Enforcing the latter condition is less straightforward. To enforce a constant pressure drop Δp, we must derive an associated expression for the evolving flow rate $\hat{Q}(t)$. To do so, we rearrange and integrate the expression for v_s from Equation (2.15b), using Equation (2.32), to obtain

$$\hat{Q}(t) = \frac{\Delta p + \mu \displaystyle\int_a^b \frac{v_s}{k(\phi_f)}\,\mathrm{d}r}{\dfrac{\mu}{2\pi}\displaystyle\int_a^b \frac{1}{rk(\phi_f)}\,\mathrm{d}r} \tag{2.35}$$

where v_s is defined in Equation (2.16) and for linearised kinematics, we replace the latter expression with Equation (2.17c). Equation (2.35) also applies at steady state, for which $v_s \equiv 0$ by definition.

Note that the steady state response of the cylinder to an imposed value of $\hat{Q}$ corresponds to some *a priori* unknown value of Δp. As a result, the same steady state can be achieved by instead imposing this value of Δp. However, the transient evolution to this identical steady state will be very different (*c.f.,* §4.2.1)

2.5 Non-dimensionalisation and parameters

To proceed, we non-dimensionalise via the scaling

$$\tilde{r} = \frac{r}{b_0},\ \tilde{u}_s = \frac{u_s}{b_0},\ \tilde{a} = \frac{a}{b_0},\ \tilde{b} = \frac{b}{b_0},\ \tilde{\sigma}_i' = \frac{\sigma_i'}{\mathcal{M}},\ \tilde{t} = \frac{t}{T_{\mathrm{pe}}},\ \tilde{p} = \frac{p}{\mathcal{M}}, \tag{2.36}$$

where $T_{\mathrm{pe}} := b_0^2\mu/k_0\mathcal{M}$ is the characteristic poroelastic timescale. We can then rewrite Equation (2.15a) in dimensionless form,

$$\frac{\partial\phi_f}{\partial\tilde{t}} + \frac{1}{\tilde{r}}\frac{\partial}{\partial\tilde{r}}\left(\phi_f q(\tilde{t}) - \tilde{r}(1-\phi_f)\tilde{k}(\phi_f)\frac{\partial\tilde{p}}{\partial\tilde{r}}\right) = 0, \tag{2.37}$$

where $\tilde{k}(\phi_f) = k(\phi_f)/k_0$. Injection is characterised either by a fixed dimensionless flow rate q or by a fixed dimensionless pressure drop $\Delta\tilde{p}$,

$$q := \frac{\mu\hat{Q}}{2\pi k_0\mathcal{M}} \quad \text{or} \quad \Delta\tilde{p} := \frac{\Delta p}{\mathcal{M}}, \tag{2.38}$$

where, in the latter case, $q(\tilde{t})$ evolves in time and must be calculated from $\Delta\tilde{p}$ as part of the solution (*c.f.,* §2.4.3). Both of these quantities compare the characteristic pressure due to injection with the characteristic elastic stiffness of the material. The model is additionally characterised by the value of $\phi_{f,0}$ and three other dimensionless parameters:

$$\Gamma := \frac{\Lambda}{\mathcal{M}}\left(\equiv \frac{\nu}{1-\nu}\right), \quad \tilde{a}_0 := \frac{a_0}{b_0}, \quad \text{and} \quad \tilde{\sigma}_b' := \frac{\sigma_b'}{\mathcal{M}}. \tag{2.39}$$

Since $\nu \in [-1, 1/2]$, this implies $\Gamma \in [-1/2, 1]$ such that $\Gamma = 1$ corresponds to an incompressible material. We work in dimensionless quantities going forward, dropping the tildes for convenience.

2.6 Summary of models

Thus far, we have developed several different models for the response of a poroelastic cylinder to radially outward flow by considering two different representations of the kinematics (linearised and rigorous), two different elasticity laws (linear and Hencky), and two different permeability laws (constant and Kozeny-Carman). We categorise these models as linear 'L' (linearised kinematics with linear elasticity), quasi-linear 'Q' (rigorous kinemat-

ics with linear elasticity), and nonlinear 'N' (rigorous kinematics with Hencky elasticity). For each of these, we consider both constant 'k_0' and Kozeny-Carman 'k_{KC}' permeability. We then have six combinations: L-k_0, L-k_{KC}, Q-k_0, Q-k_{KC}, N-k_0, and N-k_{KC}. Note that L-k_0 is classical linear poroelasticity and N-k_{KC} is fully nonlinear poroelasticity; the other four models are intermediate between these two extremes. Note that the L-k_{KC} model has nonlinear strains in the permeability function, yet the kinematics of the model are linearised in strain, and therefore it is asymptotically inconsistent. However, this model allows us to isolate the impact of deformation-dependent permeability from that of the nonlinear kinematics and nonlinear elasticity. Note also that we do not combine linearised kinematics with Hencky elasticity; linearising the kinematics requires that $u_s/r \ll 1$ and $\partial u_s/\partial r \ll 1$, under which assumptions Hencky elasticity reduces to linear elasticity.

2.6.1 Governing equations

The conservation laws for the three classes of models, Equation (2.15a) for the Q and N models and Equation (2.17b) for the L models, are written terms of ϕ_f and p. For the L models, it is straightforward to rewrite this as a partial differential equation (PDE) in ϕ_f using Equations (2.17a) and (2.25). For the Q and N models, however, this process is much less straightforward. Additionally, the boundary conditions for all models are written in terms of u_s and σ_r', the latter being readily expressible in terms of u_s and its derivatives. To rewrite all of these problems as closed IBVPs in terms of a single dependent variable, we therefore use u_s in lieu of ϕ_f.

2.6.2 L models

Equations (2.25) and (2.17) yield

$$\frac{\partial u_s}{\partial t} = v_s = \frac{q}{r} + k[u_s]\frac{\partial}{\partial r}\left[\frac{1}{r}\frac{\partial}{\partial r}(r u_s)\right], \tag{2.40a}$$

where

$$k[u_s] \equiv 1 \quad \text{or} \quad k[u_s] = \frac{\left[(1-\phi_{f,0})\left(\frac{\partial u_s}{\partial r} + \frac{u_s}{r}\right) + \phi_{f,0}\right]^3}{\phi_{f,0}^3\left(1 - \frac{\partial u_s}{\partial r} - \frac{u_s}{r}\right)^2} \tag{2.40b}$$

for the L-k_0 or L-k_{KC} models, respectively. Equation (2.40a) subject to $B^{a_0}[u_s] = B_i^{b_0}[u_s] = 0$, with $i = 1, 2$ now constitutes a closed IBVP. For the L-k_0 model driven by a fixed flux q, this problem is analytically tractable and we present solutions subsequently (*c.f.,* §4.1.2).

2.6.3 Q and N models

The conservation law for the Q and N models is

$$\frac{\partial u_s}{\partial t} = \frac{1}{\lambda_r} v_s = \left(1 - \frac{\partial u_s}{\partial r}\right)\left[\frac{q}{r} + k[u_s]\frac{\partial p}{\partial r}\right], \tag{2.41a}$$

where

$$k[u_s] \equiv 1 \quad \text{or} \quad k[u_s] = \frac{\left[(1-\phi_{f,0})\left(\frac{\partial u_s}{\partial r} + \frac{u_s}{r} - \frac{u_s}{r}\frac{\partial u_s}{\partial r}\right) + \phi_{f,0}\right]^3}{\phi_{f,0}^3\left(1 - \frac{\partial u_s}{\partial r} - \frac{u_s}{r} + \frac{u_s}{r}\frac{\partial u_s}{\partial r}\right)^2} \tag{2.41b}$$

for the '-k_0' or '-k_{KC}' models, respectively. Note that it can be shown that Equation (2.41a) is equivalent to Equation (2.15a). For the Q models, we pair Equation (2.41) with Equation (2.25) to obtain a PDE in terms of u_s. For the N models, we pair Equation (2.41) with Equation (2.22). Both of these cases, subject to Equation (2.30) and either Equation (2.33a) or Equation (2.33b), form the corresponding closed IBVPs.

2.7 Chapter summary

In §2.1, we have presented the kinematics for fluid injection from a line source into a cylinder in plane strain. These results are rigorous and applicable for any constitutive laws. In §2.2, we have discussed various constitutive choices and presented two different elasticity laws (Hencky and linear elasticity) and two different permeability laws (Kozeny-Carman

and constant permeability). Thus far we have only considered elastic deformations although elasto-plastic deformations will be the subject of Chapter 5. The material contained in this chapter (Chapter 2) has been published in *Proceedings of the Royal Society A*; it is a homogenisation of the model problem and governing equation summary contained within Auton and MacMinn [6, 7]. In Chapter 3, we consider the steady state solution to the model problems derived in this chapter. The full transient solution is the subject of Chapter 4.

Chapter 3

The poroelastic steady-state problem

In this chapter, we consider the steady-state deformation field of a poroelastic annulus driven by radially outward fluid flow using the six models, which range from classical linear poroelasticity (L-k_0) to a rigorous, fully nonlinear model (N-k_{KC}), developed in Chapter 2. Again, the majority of the material in this chapter has been published in *Proceedings of the Royal Society A* as part of Auton and MacMinn [6].

Firstly, in §3.1, we develop solutions to the steady-state problem analytically when tractable and numerically when not. We present analytical solutions to the L-k_0 and Q-k_0 models (§3.1.1) and an asymptotic solution for a thin-walled unconstrained cylinder with linear elasticity, constant permeability but rigorous kinematics (§3.1.2). We discuss the Chebyshev spectral collocation scheme used for the analytically intractable models (§3.1.3).

Secondly, in §3.2, we present the results. We focus, in particular, on the qualitative and quantitative implications of the simplifications of linear poroelasticity, the separate roles of nonlinear kinematics, nonlinear elasticity, and deformation-dependent permeability, and the nontrivial coupling of these with the geometry and boundary conditions. We show that both wall thickness and choice of outer boundary condition play crucial roles in controlling the mechanics of the problem.

3.1 Solutions and numerical solution techniques

At steady state, such that the fluid velocity is steady ($\partial v_f/\partial t \equiv 0$) and the solid is stationary ($v_s \equiv 0$), the governing equation for the L models, Equation (2.40a), simply becomes

$$\frac{\mathrm{d}^2 u_s}{\mathrm{d}r^2} + \frac{1}{r}\frac{\mathrm{d}u_s}{\mathrm{d}r} - \frac{u_s}{r^2} = -\frac{q}{rk[u_s]}, \tag{3.1}$$

with $k[u_s]$ defined in Equation (2.40b). For the Q models, Equation (2.41) also reduces to Equation (3.1) but now with $k[u_s]$ instead defined in Equation (2.41b). For the N models, Equation (2.41) is instead combined with Equation (2.22) which re-arranges to give

$$\frac{\mathrm{d}^2 u_s}{\mathrm{d}r^2} = \frac{(1-\lambda_\theta/\lambda_r)\left[\ln(\lambda_r) + \Gamma\ln(\lambda_\theta) - \Gamma\right] + (1-\Gamma)\ln\left(\lambda_\theta/\lambda_r\right) - q\lambda_r\lambda_\theta/k[u_s]}{\lambda_r r\{1 - [\ln(\lambda_r) + \Gamma\ln(\lambda_\theta)]\}}, \tag{3.2}$$

where the stretches λ_r and λ_θ are defined in Equation (2.4) and $k[u_s]$ is once again defined in Equation (2.41b). Note that Equations (3.1) and (3.2) are valid for any permeability law and either set of boundary conditions. Thus the BVP governing the behaviour of the annulus comprises a second-order ODE, Equation (3.1) or Equation (3.2), subject to Equation (2.30) and either (2.33a) (2.33b), and the appropriate kinematic conditions.

Note that q appears explicitly in Equations (3.1) and (3.2). Thus, for an imposed flow rate q, the above BVP is closed. As such, Δp can be calculated either via Equation (2.35) at steady state such that

$$\Delta p = q\int_a^b \frac{1}{rk(\phi_f)}\,\mathrm{d}r, \tag{3.3}$$

or directly from the resulting pressure field once u_s has been determined.

In contrast, an imposed pressure drop Δp will lead to a steady-state flow rate q that must be calculated as part of the solution via the re-arrangement of Equation (3.3). For constant permeability, this relationship becomes

$$\Delta p = q\ln(b/a). \tag{3.4}$$

Everything else being fixed, the same steady state can therefore be achieved by imposing either q or Δp. Clearly, the geometry and boundary conditions will have a strong impact on the relationship between q and Δp. We explore this relationship in the next section.

For the L-k_0 and Q-k_0 models, the ODE (Equation 3.1) can be solved analytically and we detail this below in §3.1.1. For the L-k_0 model, this provides the full solution to the problem. For the Q-k_0 model, the analytical solution leads to either an implicit equation for a or a pair of implicit equations for a and b, depending on the boundary condition. We can either solve for just the unknown(s) a (and b) with standard numerical root-finding techniques or we can solve the BVP entirely numerically using a Chebyshev spectral collocation method, as described in §3.1.3. We use both approaches at various points. For the other four models, the ODE cannot be solved analytically thus we also solve these via Chebyshev spectral collocation.

3.1.1 Linear elasticity with constant permeability (L-k_0 and Q-k_0)

In this section we provide solutions for the L-k_0 and Q-k_0 models subject to Equation (2.30) and either (2.33a) or Equation (2.33b); we first provide the general solution valid for linear elasticity and constant permeability and subsequently determine the constants for each combination of kinematics and boundary condition.

Assuming linear elasticity, we solve Equation (3.1) for constant permeability ($k[u_s] \equiv 1$) to arrive at a general expression for the displacement,

$$u_s = -\frac{qr\ln r}{2} + \frac{(2B_1+q)r}{2(1+\Gamma)} + \frac{B_2}{(1-\Gamma)r}, \tag{3.5a}$$

where the constants B_1 and B_2 are determined by the boundary conditions. This result is solely mechanical and constitutive, and is therefore valid for both the L-k_0 and Q-k_0

models. The general expressions for the effective stresses are then

$$\sigma'_r = -\frac{(1+\Gamma)}{2} q \ln r + B_1 - \frac{B_2}{r^2} \quad \text{and} \quad \sigma'_\theta = -\frac{(1+\Gamma)}{2} q \ln r + B_1 + \frac{B_2}{r^2} + \frac{q}{2}(1-\Gamma). \tag{3.5b}$$

From these expressions, we arrive at four distinct solutions by combining the two different treatments of the kinematics (rigorous Q and linearised L) with two distinct outer boundary conditions (Equation (2.33a) or Equation (2.33b)). The two L-k_0 solutions are classical solutions from linear poroelasticity [16]. An approximate version of the Q-k_0 solutions was derived by Barry and Aldis [10] and Barry and Mercer [11], who applied boundary conditions at the moving boundary but linearised the relationship between ϕ_f and u_s.

3.1.1.1 Solution for L-k_0 with a fixed outer boundary

For a fixed outer boundary, we derive expressions for B_1 and B_2 by applying Equations (2.30) and (2.33a) at a_0 and 1, respectively, to obtain

$$B_2 = -(1-\Gamma)\left\{\frac{q a_0^2[1+(1+\Gamma)\ln(a_0)]}{2[a_0^2(1+\Gamma)+(1-\Gamma)]}\right\} \tag{3.6a}$$

and

$$B_1 = -\left[\frac{q}{2} + \frac{B_2(1+\Gamma)}{1-\Gamma}\right] = \frac{B_2}{a_0} + \frac{q(1+\Gamma)\ln(a)}{2}. \tag{3.6b}$$

3.1.1.2 Solution for L-k_0 with an applied effective stress at the outer boundary

Similarly, for an applied effective stress at the outer boundary, applying Equations (2.30) and (2.33b) at a_0 and 1, respectively, yields

$$B_2 = \frac{a^2[2\sigma'_b - (1+\Gamma)q\ln(a_0)]}{2(1-a_0^2)} \quad \text{and} \quad B_1 = \sigma'_b + B_2. \tag{3.7}$$

All other quantities can be derived from the expressions for u_s. Thus, we have complete explicit solutions following classical linear poroelasticity for the two different sets of outer

boundary conditions. Note that for linearised kinematics, ϕ_f should be calculated from u_s according to Equation (2.17a).

3.1.1.3 Solution for Q-k_0 with a fixed outer boundary

For a fixed outer boundary, application of Equations (2.30) and (2.33a) yields

$$B_2(a) = -(1-\Gamma)\left\{\frac{qa^2[1+(1+\Gamma)\ln(a)]}{2[a^2(1+\Gamma)+(1-\Gamma)]}\right\} \quad \text{and} \quad B_1(a) = \frac{B_2(a)}{a^2} + \frac{q(1+\Gamma)\ln(a)}{2}, \tag{3.8}$$

where a is unknown. To close the problem we additionally use the kinematics condition (Equation 2.31a) to give the implicit relation for a

$$a - a_0 = \frac{2B_2(a)}{a(1-\Gamma^2)} + \frac{qa}{2(1+\Gamma)}. \tag{3.9}$$

3.1.1.4 Solution for Q-k_0 with an applied effective stress at the outer boundary

For an applied effective stress at the outer boundary, application of Equations (2.30) and (2.33b) yields

$$B_2(a,b) = \frac{a^2b^2[2\sigma'_b + (1+\Gamma)q\ln(b/a)]}{2(b^2-a^2)} \quad \text{and} \quad B_1(a,b) = \frac{B_2(a,b)}{a^2} + \frac{q(1+\Gamma)\ln(a)}{2}, \tag{3.10}$$

where both a and b are unknown. Applying the kinematics conditions Equations (2.31a) and (2.34a) leads to the coupled implicit relations for a and b

$$a - a_0 = \frac{2B_2(a,b)}{a(1-\Gamma^2)} + \frac{qa}{2(1+\Gamma)} \tag{3.11a}$$

and

$$b - b_0 = \frac{qb}{2}\left[\frac{1}{1+\Gamma} - \ln\left(\frac{b}{a}\right)\right] + \frac{B_2(a,b)\left[b^2(1-\Gamma)+a^2(1+\Gamma)\right]}{a^2b(1-\Gamma^2)} \tag{3.11b}$$

We may solve this numerically using a root-finding technique or instead opt to solve the full Q-k_0 BVP also via Chebyshev spectral collocation. Once a (and b) are determined, all other quantities can then be derived from the expressions for u_s. Note that for rigorous kinematics, ϕ_f should be calculated from u_s according to Equation (2.7).

3.1.2 Solution for Q-k_0 in the thin-walled limit

We now derive an approximate solution to the Q-k_0 model in the limit of vanishing wall thickness, starting from Equation (3.1) with $k[u_s] \equiv 1$. We do this for the case of an applied effective stress at the outer boundary since the case of no displacement at the outer boundary is ultimately limited to small displacements, and thus is well-captured by linear poroelasticity.

We begin by defining a new radial coordinate $\epsilon := r - a$ such that $\epsilon \in [0, \delta]$ where $\delta := b - a \ll 1$ is the wall thickness. We then rewrite Equation (3.1) in terms of ϵ and seek a solution under the assumption that $\epsilon \ll 1$. From these assumptions, and writing $u_s(r) = U(\epsilon)$, we obtain at leading order

$$\frac{\mathrm{d}^2 U}{\mathrm{d}\epsilon^2} + \frac{1}{a}\frac{\mathrm{d}U}{\mathrm{d}\epsilon} - \frac{U}{a^2} = -\frac{q}{a}. \tag{3.12}$$

Note that for asymptotic consistency these assumptions require that $q/a = O(1)$.

Equation (3.12) is a linear, second-order ODE with solution

$$U = A_1 \exp\left[-\left(\frac{\sqrt{5}+1}{2a}\right)\epsilon\right] + A_2 \exp\left[\left(\frac{\sqrt{5}-1}{2a}\right)\epsilon\right] + aq. \tag{3.13}$$

We now apply the relevant boundary conditions, Equations (2.30) and (2.33b) and the corresponding kinematic conditions, which results in four equations for four unknowns: the two integration constants, A_1 and A_2, and the inner and outer radii, a and $a + \delta$, respectively. We use the two conditions at the inner boundary to derive expressions for A_1 and

A_2 in terms of a,

$$A_1(a) = \frac{(a-a_0)(\Gamma-1)+q}{\sqrt{5}} \quad \text{and} \quad A_2(a) = \frac{(\sqrt{5}+1)[a(1-q)-a_0]-\Gamma(a-a_0)}{\sqrt{5}}. \tag{3.14}$$

The two conditions at the outer boundary then give

$$A_1(a)\exp\left[-\left(\frac{\sqrt{5}+1}{2a}\right)\delta\right] + A_2(a)\exp\left[\left(\frac{\sqrt{5}-1}{2a}\right)\delta\right] + aq = a+\delta-1 \tag{3.15a}$$

and

$$\left(\frac{\sqrt{5}-1}{2a}\right)A_2(a)\exp\left[\left(\frac{\sqrt{5}-1}{2a}\right)\delta\right] - \left(\frac{\sqrt{5}+1}{2a}\right)A_1(a)\exp\left[-\left(\frac{\sqrt{5}+1}{2a}\right)\delta\right] + \frac{\Gamma}{a}(a+\delta-1) = \sigma_b'. \tag{3.15b}$$

We can combine these to write δ as a function of a

$$\delta(a) = ag(a) - \frac{2a\sqrt{5}A_2(a)}{2\Gamma - a(1+\sqrt{5})}\mathcal{W}\left(\frac{A_2(a)(5-\sqrt{5})}{2\Gamma-a(1+\sqrt{5})}\exp\left[\frac{g(a)(\sqrt{5}-1)}{2}\right]\right), \tag{3.16}$$

with

$$g(a) := \frac{a^2(1+\sqrt{5})(1-q)+a(\sigma_b'-\Gamma-1-\sqrt{5})+2\Gamma}{2\Gamma-a(1+\sqrt{5})} \tag{3.17}$$

where $\mathcal{W}(x)$ is the Lambert-W function [25] which satisfies

$$\mathcal{W}(x) = -\ln\left(\frac{\mathcal{W}(x)}{x}\right). \tag{3.18}$$

This is now a root-finding problem for just a, which we solve numerically using the standard `MATLAB` function `fsolve`.

The pressure field is given by

$$\frac{\mathrm{d}p}{\mathrm{d}r} = -\frac{q}{r} \quad \mapsto \quad \frac{\mathrm{d}P}{\mathrm{d}\epsilon} = -\frac{q}{a} \quad \implies \quad P(\epsilon) = \frac{q}{a}(\delta - \epsilon). \tag{3.19}$$

This then leads to $\Delta p = (q/a)\delta$ and, since $q/a = O(1)$, we have that $\Delta p = O(\delta)$. This implies that a small pressure drop will drive a large flow rate when the walls are sufficiently thin.

3.1.3 Numerical solution

In this subsection we discuss numerous potential numerical solution schemes. We focus on the chosen Chebyshev spectral collocation numerical scheme and provide a review of the underlying theory following Trefethen [91]. We explain how the differentiation matrices used in this thesis are defined in line with Weideman and Reddy [107] and we discuss convergence of spectral methods following Trefethen [91, 92]; we then apply this theory by calculating the order of convergence for the L-k_0 subject to both sets of outer boundary conditions (either Equation (2.33a) or (2.33b)).

When the ODE cannot be solved analytically, it must instead be integrated using numerical methods for BVPs, such as direct finite differences or a shooting method. For a shooting method, one must guess the locations of the free boundaries, solve the ODE as an initial value problem (IVP) subject to two of the constraints, and then iterate on the guesses until the remaining constraints are satisfied. The structure of this method, with the pitfalls highlighted, is presented in Figure 3.1. For direct finite differences, two approaches are possible. One may follow the same approach as above by first guessing the solution domain, then solving the BVP directly using finite differences (*i.e.,* rather than treating it as an IVP) and finally using a root finding method to iterate the domain until all constraints are satisfied (*e.g.*, Newton's method). Alternatively, one may solve the BVP and all constraints simultaneously using finite differences and root finding.

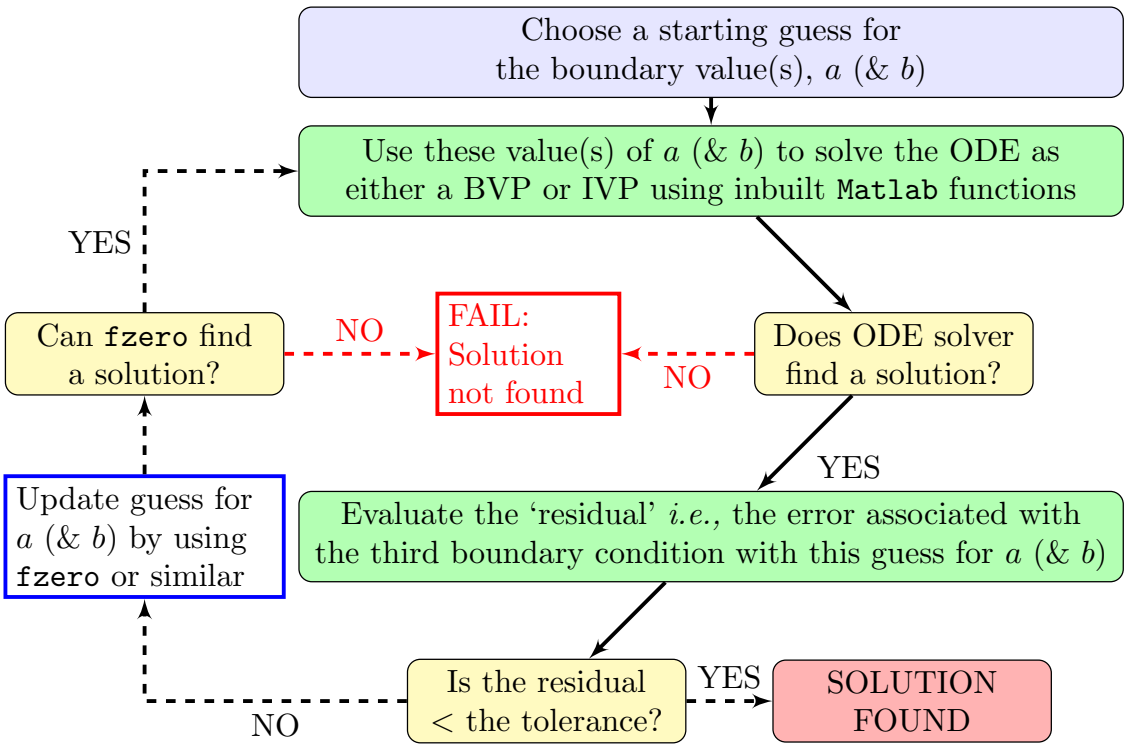

Figure 3.1: Procedure for a 'classical' shooting method for BVPs. We highlight the shortcomings of the method by indicating how this approach often fails to find a solution.

Although straightforward to implement, these approaches are unreliable in the present context because the iteration process can easily lead to a nonphysical state that prohibits further iteration (*cf.* Figure 3.1). To mitigate these difficulties, we instead use a direct method based on Chebyshev spectral collocation (*i.e.*, a Chebyshev pseudospectral method) [15, 71]. That is, we solve the BVP and all constraints simultaneously as described above, but replacing the sparse finite-difference differentiation matrix with a dense Chebyshev-pseudospectral differentiation matrix. This approach still requires Newton iteration for all but the L-k_0 model (which is linear in a fixed domain), but is more robust than finite differences because the density of the pseudospectral differentiation matrix directly couples the solution at each discrete point to the solution at every discrete point. Additionally, approximations of derivatives via Chebyshev differentiation matrices exhibit 'spectral accuracy' (see §3.1.3.2) which means that in general a far more accurate approximation can be obtained for a given number of discrete points compared to a classical finite difference

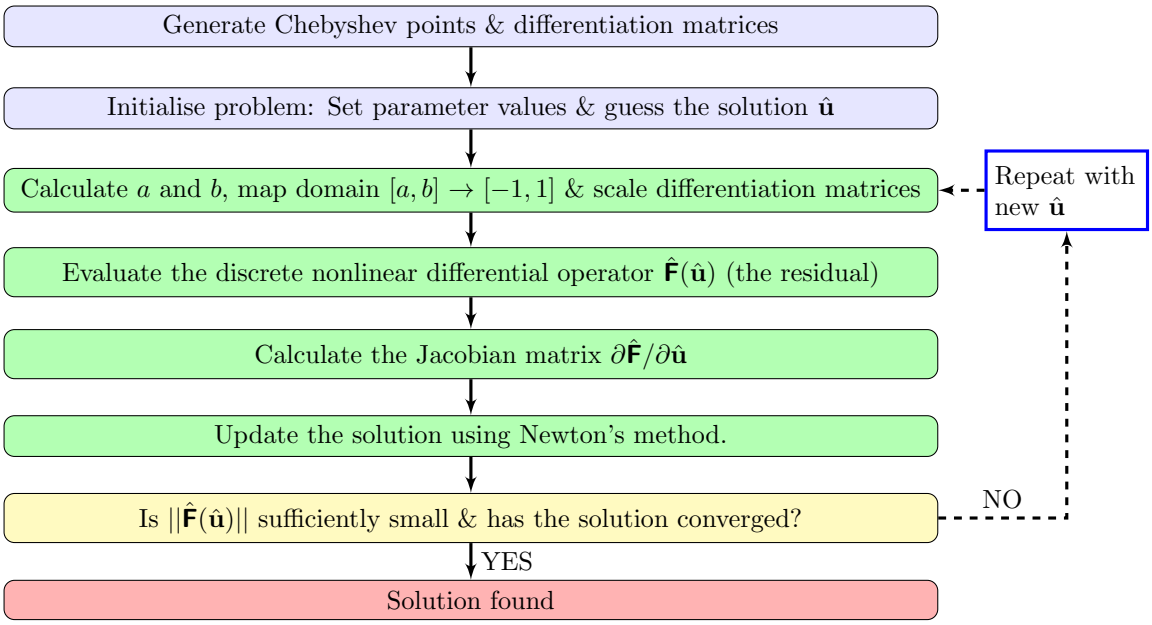

Figure 3.2: Procedure for a direct solution via Chebyshev spectral collocation.

approximation. As such, once the solution u_s has been determined, we are able to calculate the related quantities (*e.g.*, ϕ_f, σ_r', σ_θ' and p) from u_s without losing any further accuracy of the solution[1]. This Chebyshev pseudospectral approach also allows for the straightforward incorporation of additional unknowns and constraints, such as solving the problem for an imposed pressure drop Δp rather than for an imposed flow rate q. We illustrate the overall structure of the method in Figure 3.2. Spectral methods enable complex equations to be solved in just a few lines of code. To illustrate this we include the code to solve the L-k_0 and Q-k_{KC} numerically in Appendix A. Note that for purposes of Newton iteration, we calculate the Jacobian analytically for the L and Q models and numerically for the N models.

3.1.3.1 Chebyshev spectral collocation

Spectral collocation methods ('pseudospectral methods') involve discretising the solution domain into a set of N collocation points, $\{\hat{X}_k\}$, defining a global function that interpolates

[1]This is because u_s is simply the interpolant $\mathfrak{p}(x)$ which is a linear combination of the basis functions ω_k.

the solution at these collocation points (the interpolant, $\mathfrak{p}(x)$), and then approximating the derivatives of the solution as the derivatives of the interpolant. As discussed in Trefethen [91], for periodic domains the natural choice is to use a 'classical' Fourier pseudospectral method involving trigonometric polynomials on equispaced collocation points. In this case the collocation points are equispaced throughout the domain. However, for finite domains the trigonometric polynomials are replaced by algebraic polynomials and the collocation points must be irregularly spaced. Regularly spaced collocation points for algebraic polynomials on finite domains lead to the Runge phenomenon (a more extreme version of the Gibbs phenomenon) and may diverge as the grid is refined. Essentially, the spacing of the points must be chosen such that the relative size of the polynomial with roots at all N collocation points,

$$\prod_{k=1}^{N}\left(x-\hat{X}_k\right), \tag{3.20}$$

is approximately uniform across the domain [91]. For a finite domain $x \in [-1,1]$, this requires the density of points, Υ, to be distributed asymptotically as $N \to \infty$ by

$$\Upsilon \sim \frac{N}{\pi\sqrt{1-x^2}}. \tag{3.21}$$

The simplest example of a set of N points with the correct density are the N Chebyshev points or nodes $\hat{X}_k \in [1,-1]$, which can be defined as [71]

$$\hat{X}_k = \cos\left(\frac{(k-1)\pi}{N-1}\right), \quad k=1,\ldots,N. \tag{3.22}$$

These are the extreme points of the Chebyshev polynomial[2], $T_{N+1}(x) := \Re\left(z^{N+1}\right) \equiv \frac{1}{2}\left(z^{N+1}+z^{-N-1}\right)$ where z is the complex number on the unit circle with $z := x+iy$.

It is standard to compose the interpolant from a set of N basis functions $\{\omega_j\}$ with $j \in \{1,\ldots,N\}$ each of which is a polynomial of degree $N-1$ that satisfies the criterion

[2]This is the same as in Trefethen [91] but we map $N+1$ in Trefethen [91] to N here.

that it is equal to unity at exactly one collocation point — that is $\omega_j(\hat{X}_k) = \delta_{j,k}$ where $\delta_{j,k}$ is the Kronecker delta function. This is sufficient to prescribe $\{\omega_j\}$ via

$$\omega_j(x) \prod_{\substack{k=1 \\ k\neq j}} (\hat{X}_j - \hat{X}_k) = \prod_{\substack{k=1 \\ k\neq j}} (x - \hat{X}_k) \tag{3.23}$$

for all $k \in \{1, \ldots, N\}$. Hence, $\mathfrak{p}(x)$, a polynomial of degree $N-1$, can be constructed via a linear combination of the $\omega_k(x)$ such that it satisfies the differential equation at each interpolation point.

We define the differentiation matrix $\widehat{\boldsymbol{D}}_N$ for N collocation points. For $N \geq 2$ the $N \times N$ matrix $\widehat{\boldsymbol{D}}_N$ has leading diagonal entries given by

$$\left(\widehat{D}_N\right)_{11} = \frac{2(N-1)^2 + 1}{6} \tag{3.24a}$$

$$\left(\widehat{D}_N\right)_{jj} = \frac{-x_j}{2(1-x_j^2)}, \qquad j \in [2, N-1], \tag{3.24b}$$

$$\left(\widehat{D}_N\right)_{NN} = -\frac{2(N-1)^2 + 1}{6} \tag{3.24c}$$

$$\tag{3.24d}$$

and off-diagonal entries given by

$$\left(\widehat{D}_N\right)_{ij} = \frac{c_i(-1)^{i+j}}{c_j(x_i - x_j)}, \quad i \neq j, \quad i, j \in [1, N] \tag{3.24e}$$

where

$$c_k = \begin{cases} 2, & k = 1, N \\ 1, & \text{otherwise.} \end{cases} \tag{3.24f}$$

To obtain a differentiation matrix for a χth derivative, one may simply raise $\widehat{\boldsymbol{D}}_N$ to the power χ. That said, this is less computationally efficient than constructing the higher order differentials via explicit formulae [91]. For the definition given in Equation (3.22), Weide-

man and Reddy [107] provide a suite of MATLAB functions that generate the Chebyshev points $\{\hat{X}_k\}$ and differentiation matrices, and that perform interpolation on Chebyshev functions that are defined at $\{\hat{X}_k\}$.

3.1.3.2 Convergence study for the L-k_0 model

As well as the increased robustness provided by the Chebyshev pseudospectral method, in comparison to that of a classical finite difference approach for this problem, spectral methods in general also offer a significantly faster convergence rate. To investigate convergence we must define an error; we take the error, $\mathcal{E}$, to be the absolute maximum difference between the analytical solution and the numerical Chebyshev spectral approximation to the solution at any of the N Chebyshev points. As the number of collocation points increases we expect the error to decrease; the rate of convergence is how quickly $\mathcal{E}$ decays as N increases.

A classical finite difference or finite element method typically converges at a rate $O(N^{-m})$ for an m which depends both on the order of approximation and the smoothness of the solution. For example, a simple second order finite difference approximation of the derivative of a sufficiently smooth function converges to the derivative of said function at a rate $O(N^{-2})$. However, for a spectral method, provided the solution is smooth (*i.e.,* infinitely differentiable) a convergence rate $O(N^{-m})$ is achieved for *every* m. If the function is also suitably analytic then an exponential convergence rate $O(c^N)$ is achieved for some $c \in (0, 1)$. This is known as 'spectral accuracy' [91].

For a real function the convergence rate is related to how far we can analytically[3] continue the function into the complex plane around the line segment $[-1, 1]$. Specifically, we care about the ellipses with foci at ± 1 for which our function defined on the real line segment $[-1, 1]$ is analytically continuable. All these possible ellipses can be called Bernstein ellipses (a Bernstein ellipse is just an ellipse in the complex plane with foci at ± 1),

[3] A function is analytic in the open set in which it is holomorphic — that is, for each point at which it is given locally by a convergent Taylor series.

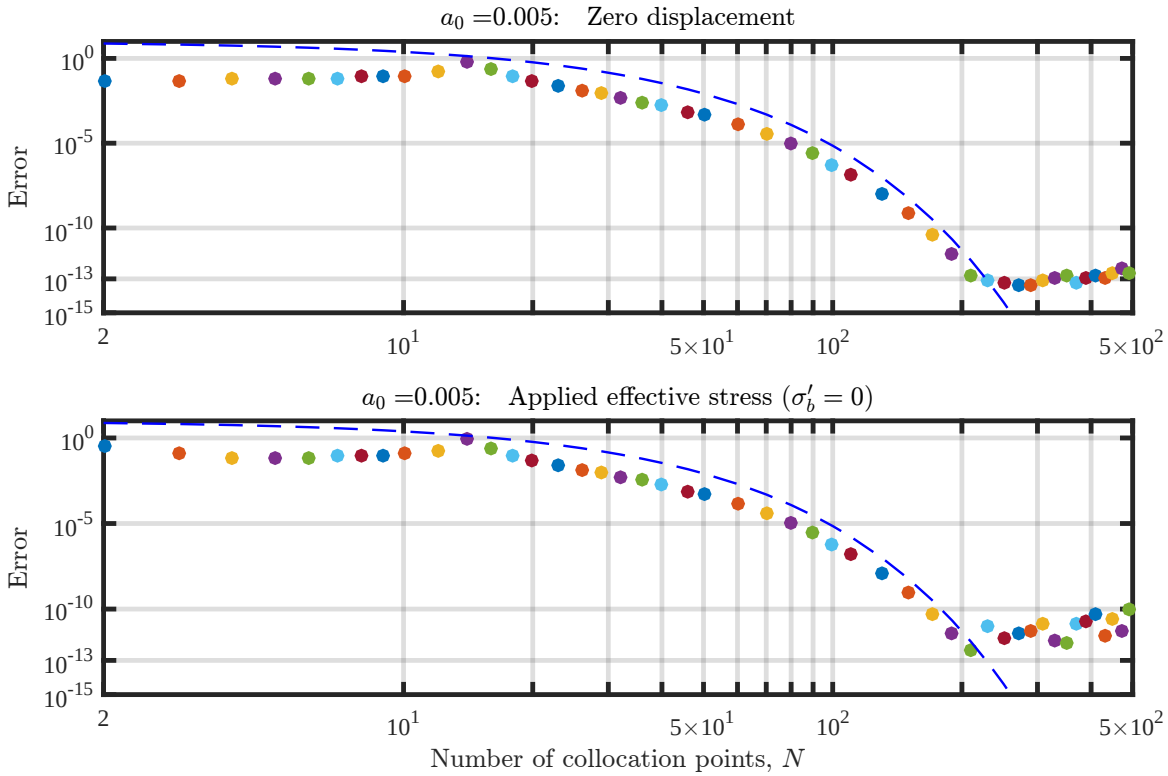

Figure 3.3: Convergence study of Chebyshev spectral collocation with $a_0 = 0.005$ for the L-k_0 model for both a constrained cylinder, $B_1^{b_0}[u_s] = 0$ (top) and an unconstrained cylinder, $B_2^{b_0}[u_s] = 0$ with $\sigma_b' = 0$ (bottom), for which we have analytical solutions. We plot the error, $\mathcal{E}$, against the number of Chebyshev nodes N. We additionally plot the curve $10(0.868)^N$ (blue dashed lines), which illustrates spectral accuracy in that the convergence rate is $O(c^N)$, until rounding errors dominate. We fix $\Gamma = 0.4$ and $q = 1$.

although commonly we define the largest such ellipse to be *the* Bernstein ellipse associated with that function. The Bernstein ellipse is characterised by a parameter c where $1/c$ is the sum of the length of the semimajor and semiminor axes. Hence from consideration of the singularities of the analytic continuation of the function we are able to determine c and hence the order of convergence, $O(c^N)$.

The physical domain in which we solve our model problem is $r \in [a, b]$; as such we linearly map this domain to the Chebyshev domain $x \in [-1, 1]$ via Equation A.1. The solution to the L-k_0 model given by Equation (3.5), is simply a linear combination of r, r^{-1} and $r\ln(r)$ which, for $r \in [a_0, b_0]$, are all smooth. To extend $\ln(r)$ to the complex plane a branch cut must be defined; it is convenient to take this to be the line segment

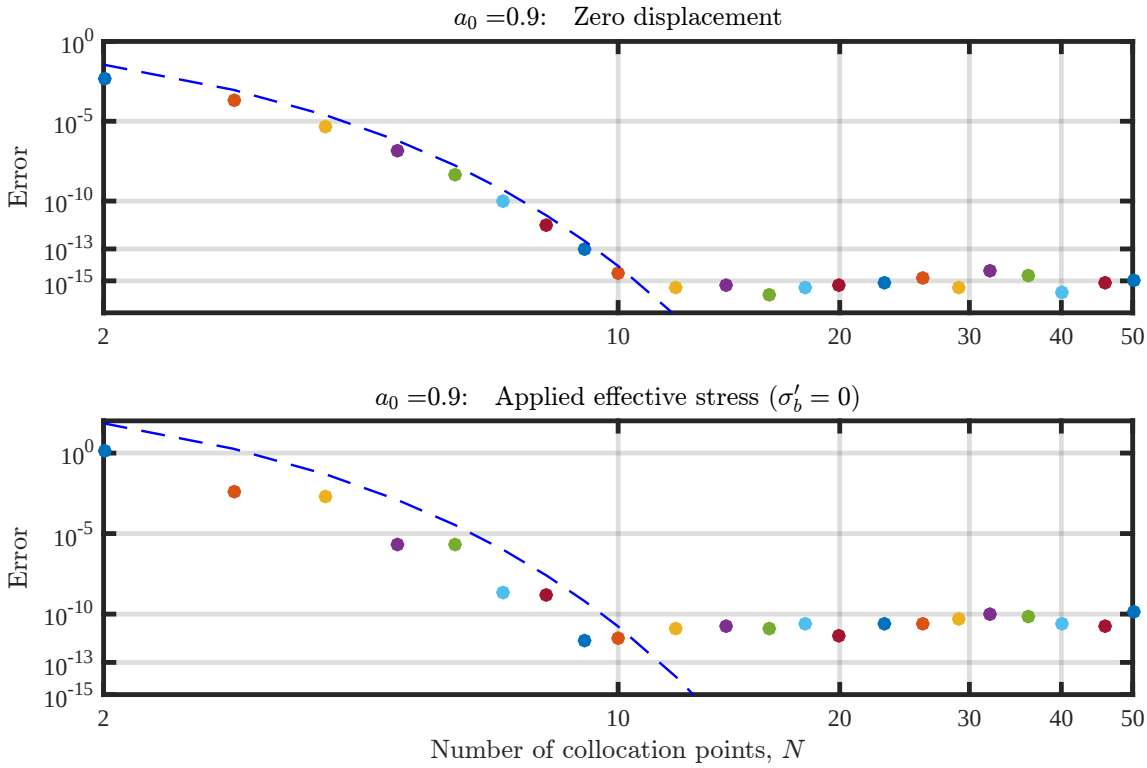

Figure 3.4: Convergence study of Chebyshev spectral collocation with $a_0 = 0.9$ for the L-k_0 model for both a constrained cylinder (top) and an unconstrained cylinder (bottom) on logarithmic axes, with Γ and q fixed as in Figure 3.3. We additionally plot the curves $50(0.0265)^N$ (blue dashed line, top) and $10^5(0.0265)^N$ (blue dashed line, bottom), which once again illustrates spectral accuracy and convergence at rate $O(c^N)$, until rounding errors dominate.

$(-\infty, 0]$. Both r^{-1} and $\ln(r)$ have singularities at $r = 0$ which corresponds to[4] $x = \pm\frac{1+a_0}{1-a_0}$. Thus, z is entire (that is, it is analytic for the entire complex plane), $1/z$ is defined in $\mathbb{C}\setminus\{0\}$ and $\ln(z) := \ln|z| + i\arg(z)$ is defined in $\mathbb{C} \setminus (-\infty, 0]$. As such, we find that

$$c = \frac{1 - a_0}{1 + a_0 + 2\sqrt{a_0}}. \tag{3.25}$$

For the Q-k_0 models, this becomes $c_Q = \frac{b-a}{b+a+2\sqrt{ab}}$. In the spectral context, we can be more precise than $O(c^N)$; in fact we can say that for all $N \geq 2$, $\mathcal{E} \leq 2M\left(c^N\right)$ where M is the supremum of the function (Equation 3.5) on the Bernstein ellipse. We omit any further calculation of the precise value of M and simply provide some constant $l \geq 2M$ for each

[4]Note that the $\pm$ depends on which mapping $r \mapsto x$ is chosen — see Appendices A and C

example in Figures 3.3 and 3.4 for which $\mathcal{E} \leq l\left(c^N\right)$ [92].

Figure 3.3 shows $\mathcal{E}$ of the Chebyshev pseudospectral solution for a thick walled cylinder ($a_0 = 0.005$) for the L-k_0 model for both the constrained (top) and unconstrained (bottom) cylinders, against the number of collocation points N. We expect the Chebyshev spectral collocation approximation to the L-k_0 solution to converge at a rate $O\left(\left[\frac{1-a_0}{1+a_0+2\sqrt{a_0}}\right]^N\right)$. For $a_0 = 0.005$, $c \approx 0.868$ and we plot the line $10(0.868)^N$ (blue dashed lines), which bounds $\mathcal{E}$ until rounding error takes over. From this we can say that for this value of $a_0 = 0.005$, $M \lesssim 5$, for both boundary condtions.

The parameter c is a monotonically decreasing function of a_0 for $a_0 \in (0, 1)$; as such we note that as a_0 increases we expect a faster rate of convergence, that is a smaller c (equivalently, a larger possible Berstein ellipse). To illustrate this we consider a thin-walled cylinder ($a_0 = 0.9$) in Figure 3.4. As in Figure 3.3 we plot $\mathcal{E}$ versus N for a constrained cylinder (top) and unconstrained cylinder (bottom). We include curves, $l(c^N)$, bounding the rate of convergence where we determine the value of c from the size of the Bernstein ellipse which gives $c \approx 0.0265$; additionally, for the constrained cylinder we take $l = 50$ and for the unconstrained cylinder we take $l = 10^5$. Here, of course the values of l for the constrained and unconstrained cylinders are vastly different. This is due to the significant impact of the boundary conditions on the solution in the thin-walled limit (*cf.* Figures 3.6 – 3.12).

3.2 Results

In §3.1 we have developed steady-state solutions for six different models, each for two distinct outer boundary conditions — constrained and an applied effective stress σ_b' at the outer boundary (see §2.6). As described in §2.5, these models are characterised by five dimensionless parameters: Γ, a ratio of elastic constants; $\phi_{f,0}$, the initial porosity; a_0, the ratio of the initial inner radius to the initial outer radius; σ_b', the applied effective stress; and

either q, the flow rate, or Δp, the pressure drop. To focus on the impact of model choice, boundary conditions and geometry, we adopt fixed values of $\Gamma = 0.4$ and $\phi_{f,0} = 0.5$ throughout the remainder of Chapter 3 and Chapter 4. Varying these two parameters across a moderate range of typical values does not lead to dramatic qualitative differences in the resulting behaviour. Similarly, we fix $\sigma_b' \equiv 0$, considering an unconstrained cylinder for simplicity.

3.2.1 Model comparison

In this section, we compare and contrast the six models for the two different boundary conditions (unconstrained and constrained) in the context of two end-member geometries: a thick-walled cylinder (Figure 3.5) and a thin-walled cylinder (Figure 3.6). This gives us a preliminary sense of how the geometry impacts the mechanics, which is in turn the focus of §3.2.2.

3.2.1.1 Unconstrained thick-walled cylinder

In Figure 3.5, we consider a thick-walled cylinder for flow driven by an imposed pressure drop of $\Delta p = 0.33$. For an unconstrained thick-walled cylinder (left column), the predictions of all models are qualitatively similar. The porosity ϕ_f (top row), azimuthal effective stress σ_θ' (fourth row), and pressure p (last row) all have maxima at the inner boundary and decrease monotonically from left to right. The porosity remains everywhere greater than $\phi_{f,0}$, the azimuthal effective stress is strictly tensile, and the pressure drops from $p(a,t) = \Delta p = 0.33$ to $p(b,t) = 0$ by construction. Additionally, the pressure profile is strongly nonlinear for the k_{KC} models, but closer to classical linear poroelasticity (L-k_0) for the k_0 models. In contrast to the behaviour of these quantities, the displacement u_s (second row) and the radial effective stress σ_r' (third row) are non-monotonic. The displacement has an interior maximum that is located in roughly the same place for all models. The radial effective stress vanishes at the inner and outer boundaries by construction. Between these

limits, it is purely tensile with an interior maximum, with the location of this maximum depending strongly on model choice.

3.2.1.2 Constrained thick-walled cylinder

For the same pressure drop, a constrained thick-walled cylinder (Figure 3.5, right column) exhibits a strikingly similar behaviour to that of the unconstrained cylinder. The maximum porosity across all models, located at the inner boundary, is lower than for the unconstrained cylinder, and the porosity now drops slightly below $\phi_{f,0}$ at the outer boundary where the material is slightly compressed. The displacement is qualitatively similar, but a factor of 2–3 smaller than in the unconstrained case. The radial and azimuthal effective stresses are now both slightly compressive at the outer boundary. This comparison between the unconstrained and constrained cylinders supports the intuition that the difference between these two cases becomes unimportant for thick walls (*i.e.,* $a_0 \ll 1$). In §4.2.4 we again consider thick-walled unconstrained and constrained cylinders to see if constraint makes little impact not only on the final deformation field but also on the transient evolution to their respective steady states (*cf.* Figure 4.10).

In all of the cases shown in Figure 3.5, the flow is driven by the same imposed pressure drop of $\Delta p = 0.33$. In addition to the above differences between the six models and the two boundary conditions, each of these twelve cases will result in a different flow rate[5] q (see legend, bottom of Figure 3.5). In all cases, q is lower for the constrained cylinder than for the unconstrained cylinder (again, except for the L-k_0 model[5]). This is because the inner radius of the constrained cylinder always expands less than that of the unconstrained cylinder, and q is very sensitive to the inner radius (*c.f.,*Equation (3.3)); the constrained cylinder is also slightly compressed against the outer boundary, which reduces its permeability in the k_{KC} models, amplifying the reduction in q.

All of the k_0 models produce quantitatively similar values of q. For each, q differs

[5]Except for the L-k_0 model, for which q is independent of the boundary condition— by Equation (3.4) with $a \equiv a_0$ and $b \equiv 1$.

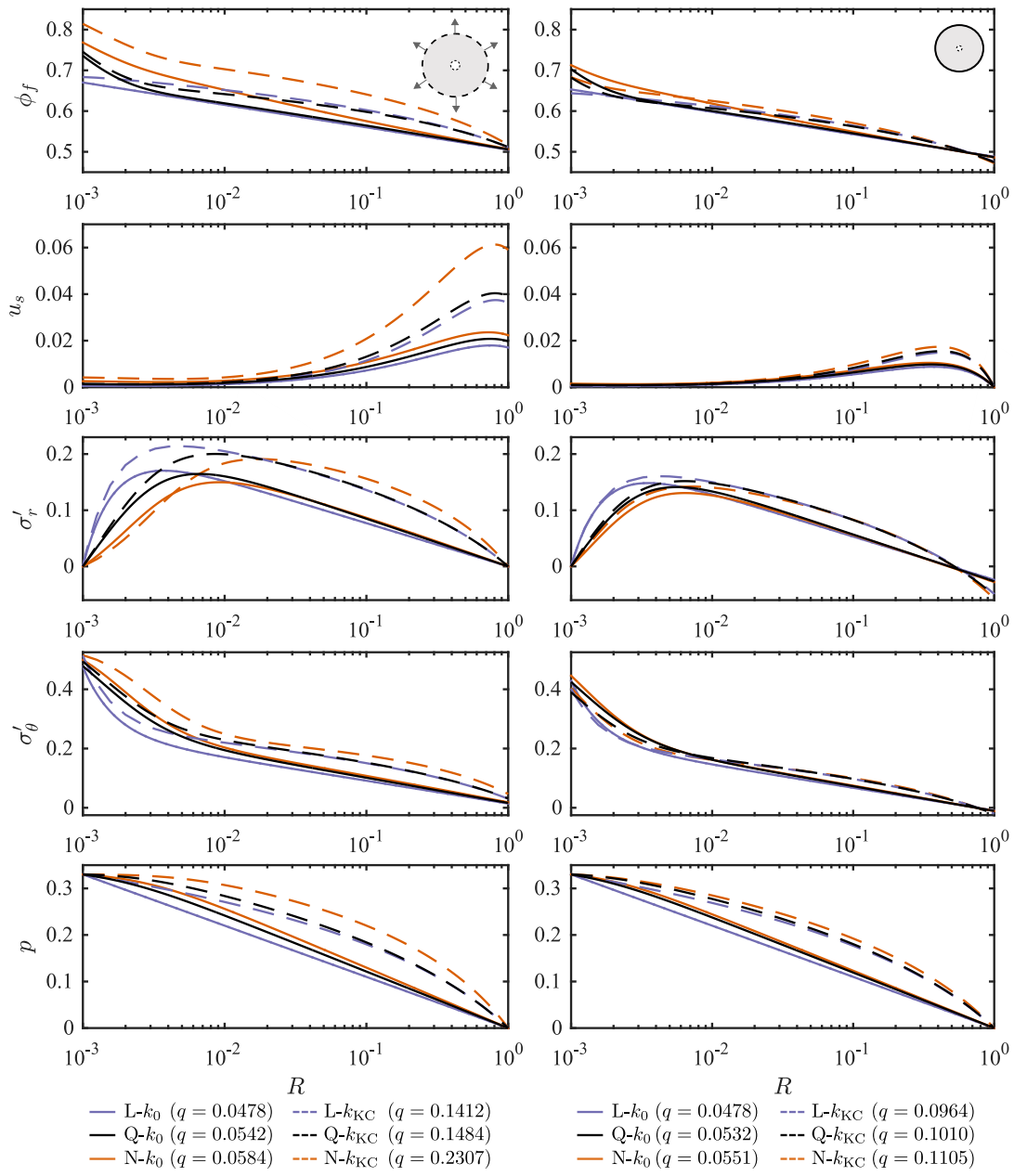

Figure 3.5: Six models at steady state for a thick-walled cylinder ($a_0 = 10^{-3}$). We consider an unconstrained cylinder (left column) and a constrained cylinder (right column), both for flow driven by an imposed pressure drop $\Delta p = 0.33$. For clarity, we plot the results against the Lagrangian coordinate $R(r,t) = r - u_s$ and on a logarithmic horizontal scale. The unconstrained and constrained cylinders exhibit very similar behaviour, implying that the distinction between these two outer boundary conditions is unimportant when the walls are very thick (*i.e.*, for small a_0). Additionally, note that in this case the permeability law has a stronger impact than the elasticity law or the treatment of the kinematics.

by only a few percent between the two boundary conditions; between the k_0 models for the same boundary condition, q differs by about 10–20%. By far the largest difference is between the corresponding k_0 and k_{KC} models, where the k_{KC} model produces a value of q that is roughly 2–4 times larger than the corresponding k_0 model. The permeability law makes a great difference since large deformations of a thick-walled cylinder lead to large and nonuniform changes in porosity. This substantial change in porosity leads to a substantial change in permeability for the k_{KC} models, but has no impact on the k_0 models. This effect leads to higher values of q for the k_{KC} models because the average porosity is in all cases larger than $\phi_{f,0}$, so the permeability increases. Comparing the N models to the Q models, and the Q models to the L models, reveals that both rigorous kinematics and nonlinear elasticity also lead to higher values of q relative to their linearised counterparts. However, these effects are noticeably weaker than the impact of changing the permeability law. Given that the values of q vary so widely, it is surprising that the behaviour illustrated in Figure 3.5 is otherwise so similar across the models and boundary conditions.

3.2.1.3 Unconstrained thin-walled cylinder

We now consider the other extreme geometry, a thin-walled cylinder, for a driving pressure drop of $\Delta p = 0.025$ (Figure 3.6). Note that this value of Δp is more than one order of magnitude less than the value used for the thick-walled cylinder (Figure 3.5). Despite this much smaller value of Δp, σ'_θ here is comparable in magnitude to the thick-walled case while u_s is much larger. We discuss these points in more detail in §3.2.2.

For the unconstrained thin-walled cylinder (left column), ϕ_f (first row) is almost uniform across the domain, with a weak and roughly linear decrease from left to right. This behaviour is mirrored in u_s (second row) and σ'_θ (fourth row). The pressure also decreases roughly linearly from left to right, from $p(a,t) = \Delta p = 0.025$ to $p(b,t) = 0$, following classical linear poroelasticity for all models. Unlike for the thick-walled case, the permeability law is relatively unimportant for these quantities, whereas the kinematics and the

elasticity law play much more prominent roles. Note that the kinematics consistently account for most of the difference between the L models and the N models (*i.e.*, the Q models are closer to the N models than they are to the L models).

Unlike these other quantities, σ_r' does show a strong dependance on the permeability law. This suggests that the most direct impact of the permeability law is on σ_r', and this propagates to all other quantities when σ_r' is mechanically important (*e.g.*, Figure 3.5). For the unconstrained thin-walled cylinder, σ_r' vanishes at the boundaries and has an intermediate tensile maximum of order 10^{-3}, whereas σ_θ' is uniformly of order 10^{-1}. As a result, the stark differences in σ_r' between the k_0 and k_{KC} models are ultimately unimportant.

3.2.1.4 Constrained thin-walled cylinder

For the same pressure drop, the constrained thin-walled cylinder exhibits strikingly different behaviour to the unconstrained thin-walled cylinder. Whereas the unconstrained cylinder expands almost uniformly by 20–70%, the constrained cylinder is prevented from doing so. This results in much smaller displacements, with a maximum of order 10^{-3}, making model choice essentially unimportant — all models approach their asymptotic limit of classical linear poroelasticity (L-k_0). Note also that most of the material is in compression, with the porosity decreasing roughly linearly from a value just above $\phi_{f,0}$ at the inner boundary to a value noticeably below $\phi_{f,0}$ at the outer boundary. The displacement is weakly nonlinear, decreasing monotonically from left to right.

With regard to the flow rate q, we first note that the values of q in this case are substantially larger than the corresponding values for the thick-walled cylinder, despite the fact that Δp is much smaller. To rationalise this, note that the relationship between q and a_0 for a given Δp is strongly nonlinear even for a rigid cylinder (*i.e.*, Equation (3.4) with $a = a_0$ and $b = 1$). The same is also true for classical linear poroelasticity, where the same expression also applies. In other words, this difference in q is due in large to the fact that a_0 is much larger.

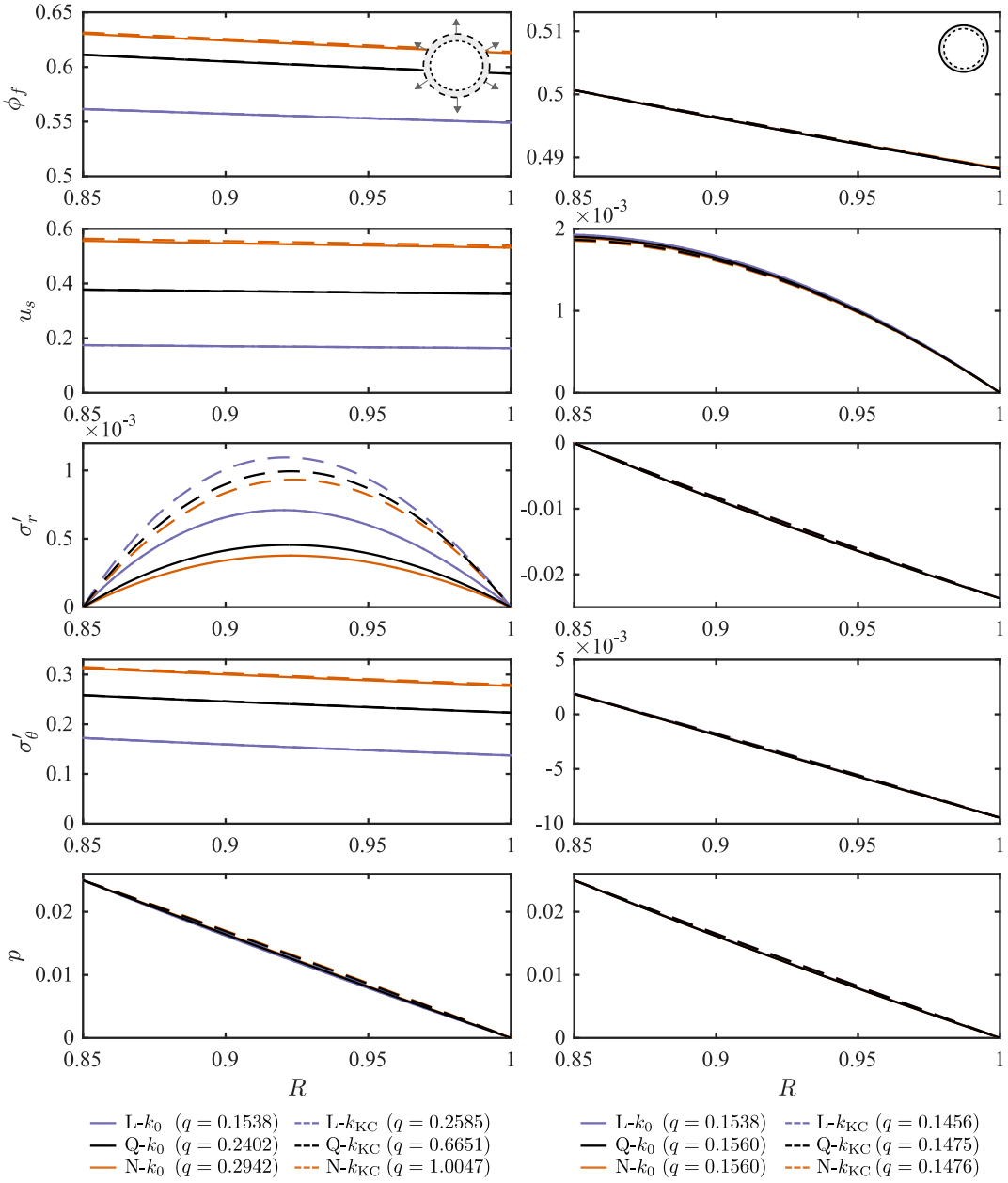

Figure 3.6: Six models at steady state for a thin-walled cylinder ($a_0 = 0.85$). We again consider an unconstrained cylinder (left column) and a constrained cylinder (right column), now for flow driven by an imposed pressure drop $\Delta p = 0.025$. For clarity, we plot the results against the Lagrangian coordinate $R(r,t) = r - u_s$ on a linear horizontal scale. Unlike for the thick-walled cylinder (Figure 3.5), the two different boundary conditions in this case result in strikingly different behaviour. For the unconstrained cylinder, the most important factors are the elasticity law and the treatment of the kinematics; the permeability law is relatively unimportant. For the constrained cylinder, all models exhibit nearly identical behaviour.

For the constrained thin-walled cylinder, q is considerably smaller than for the unconstrained thin-walled cylinder (except for the L-k_0 case, where, as for the thick-walled cylinder, q is independent of the boundary conditions). For the k_0 cases, the unconstrained cylinder expands substantially and almost uniformly, which decreases the ratio of b to a and increases the flow rate (see Equation (3.4)). This is true to a much lesser extent for the constrained cylinder since the displacements are much smaller. For the k_{KC} models, this increase in q is substantially enhanced for the unconstrained cylinder by the noticeable increase in porosity and therefore permeability. The reverse occurs for the constrained cylinder, where the porosity decreases, leading to a lower q for the k_{KC} models than for the k_0 models. As for the thick-walled cylinder, both rigorous kinematics and nonlinear elasticity also lead to higher values of q relative to their linearised counterparts. For the unconstrained cylinder, these effects are substantial; for the constrained cylinder, these effects are noticeably weaker than the impact of the permeability law. There is relatively little difference in q across the six different models for the constrained cylinder, again because the displacements are necessarily small.

In this section, we have considered the implications of model choice in the context of two end-member geometries (thick-walled and thin-walled). We have shown that the error associated with linearisation depends strongly on factors such as geometry and boundary conditions. In the next section, we study the mechanics of the problem over the full transition from $a_0 \ll 1$ to $1 - a_0 \ll 1$.

3.2.2 Impact of geometry

We now explore the parameter space more broadly, focusing on the importance of geometry (a_0) and driving (q or Δp) while again fixing $\Gamma = 0.4$ and $\phi_{f,0} = 0.5$. Although the N-k_{KC} model is arguably the most 'correct' of those considered above, it is much more computationally expensive than the other models. For simplicity, we restrict ourselves to the Q-k_{KC} model below. This model offers a good compromise between accuracy, ro-

bustness, and computational efficiency, demonstrating the same qualitative behaviour as the N-k_{KC} model for both end-member geometries and for both boundary conditions (see §3.2.4).

In Figure 3.7, we consider the evolution of several key quantities as the inner radius a_0 varies continuously from $a_0 \ll 1$ (thick walls) to $1 - a_0 \ll 1$ (thin walls). For a particular value of a_0, the flow can be driven by imposing either a fixed pressure drop Δp or a fixed flow rate q; the other quantity (q or Δp, respectively) is then calculated as part of the solution. We drive the flow with a fixed pressure drop Δp and plot the results for several values of Δp for unconstrained cylinders (left column) and constrained cylinders (right column). The resulting flow rate q varies along these contours of fixed Δp as shown in the last row. Essentially, Figure 3.7 considers the a_0, Δp, q parameter space such that fixing any two of these prescribes the third. As such one could instead impose both Δp and q and calculate a_0, which could be desirable in applications where a_0 is a design parameter to be used for targeting a particular combination of Δp and q, however we do not consider this case here. This parameter space is very complex and non-monotonic and although conceptually, continuously varying the initial inner radius and showing how each quantity changes for a discrete set of Δp, is not the most intuitive presentation of the data it does lead to the cleanest figures. That said, it is useful for interpretation to present the same results in several other configurations. Thus we present the quantities as shown in Figure 3.7 as contours of fixed q against a_0 (Figure 3.8), contours of fixed a_0 against Δp (Figure 3.9), and contours of fixed a_0 against q (Figure 3.10).

3.2.2.1 Unconstrained cylinders

For unconstrained cylinders (Figure 3.7, left column), the most striking feature is the double-valued nature of all quantities for a certain range of a_0. Specifically, our results suggest that there exists a Δp-dependent maximum initial inner radius $a_0^{\max}(\Delta p)$, above which the problem appears to have no solution, and below which the problem appears to

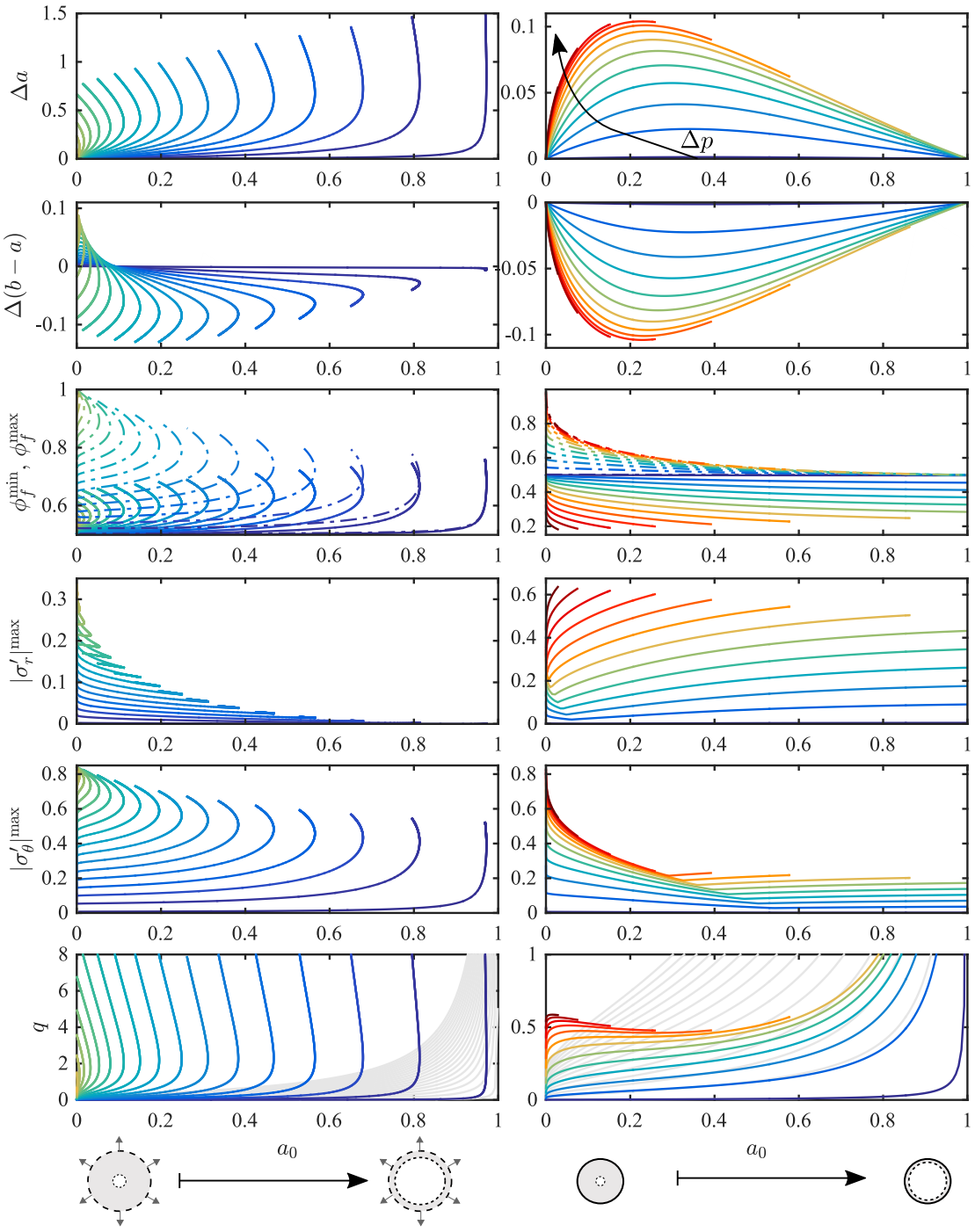

Figure 3.7: We explore the steady-state parameter space in more detail using the Q-k_{KC} model, plotting contours of fixed Δp against a_0 for several key quantities for unconstrained cylinders (left, $\Delta p \in [0.005, 0.5374]$, blue to yellow) and constrained cylinders (right, $\Delta p \in [0.005, 1.2]$, blue to red). We show the change in inner radius Δa (first row); change in wall thickness $\Delta(b-a)$ (second row); minimum porosity $\phi_f^{\min}$ and maximum porosity $\phi_f^{\max}$ (solid and dot-dashed lines, respectively; third row); maximum absolute radial effective stress $|\sigma_r'|^{\max}$ (fourth row) and maximum absolute azimuthal effective stress $|\sigma_\theta'|^{\max}$ (fifth row); and flow rate q (last row). We compare the latter with the reference flow rate q_0 that would occur for a rigid cylinder with the same initial geometry, $q_0 := -\Delta p / \ln(a_0)$ (grey lines). Note that the left and right columns use the same colour scale in Δp.

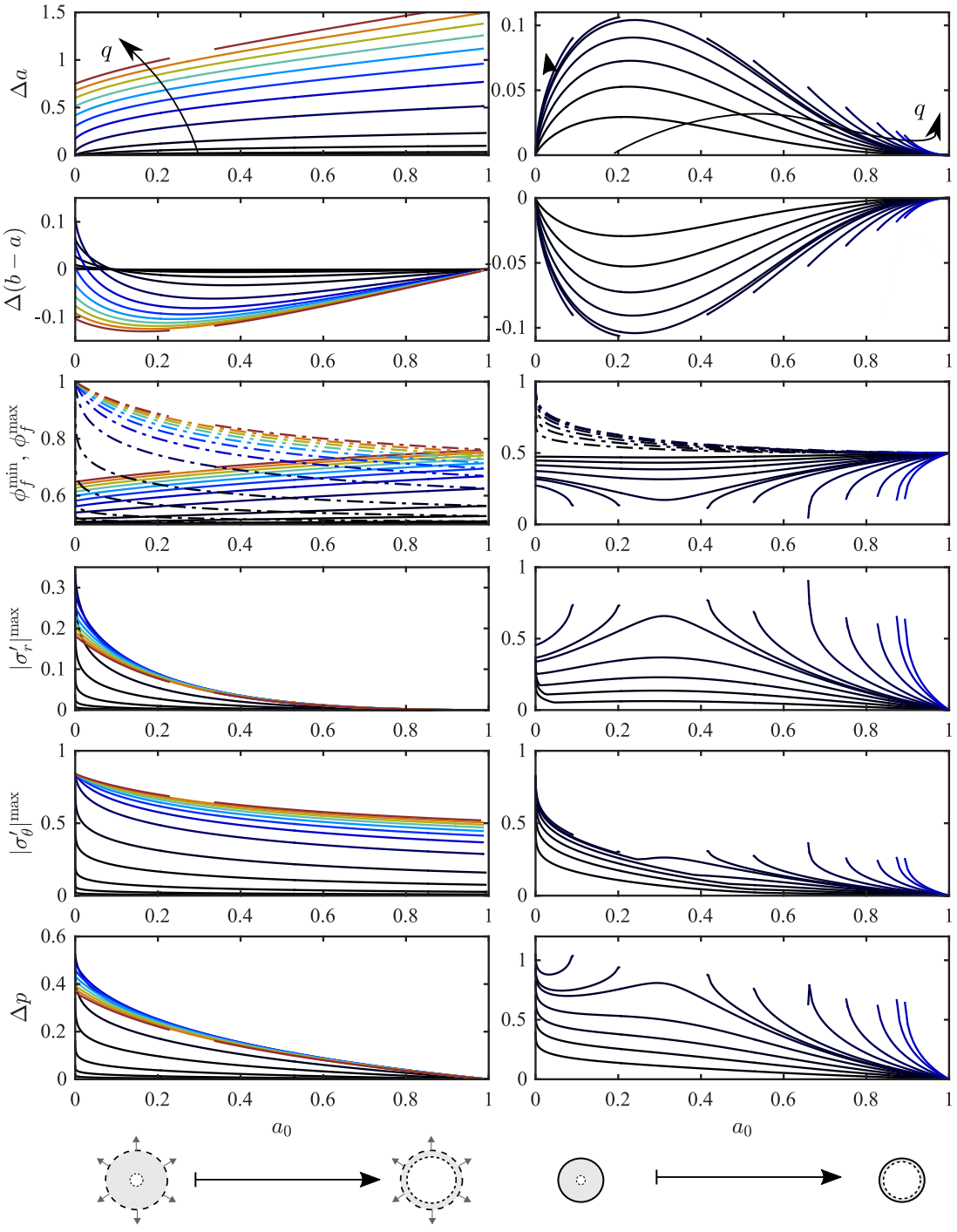

Figure 3.8: The results of Figure 3.7 plotted as contours of fixed q against a_0, with $q \in [0.001, 8]$ (left, black to red) and $q \in [0.001, 2]$ (right, black to blue).

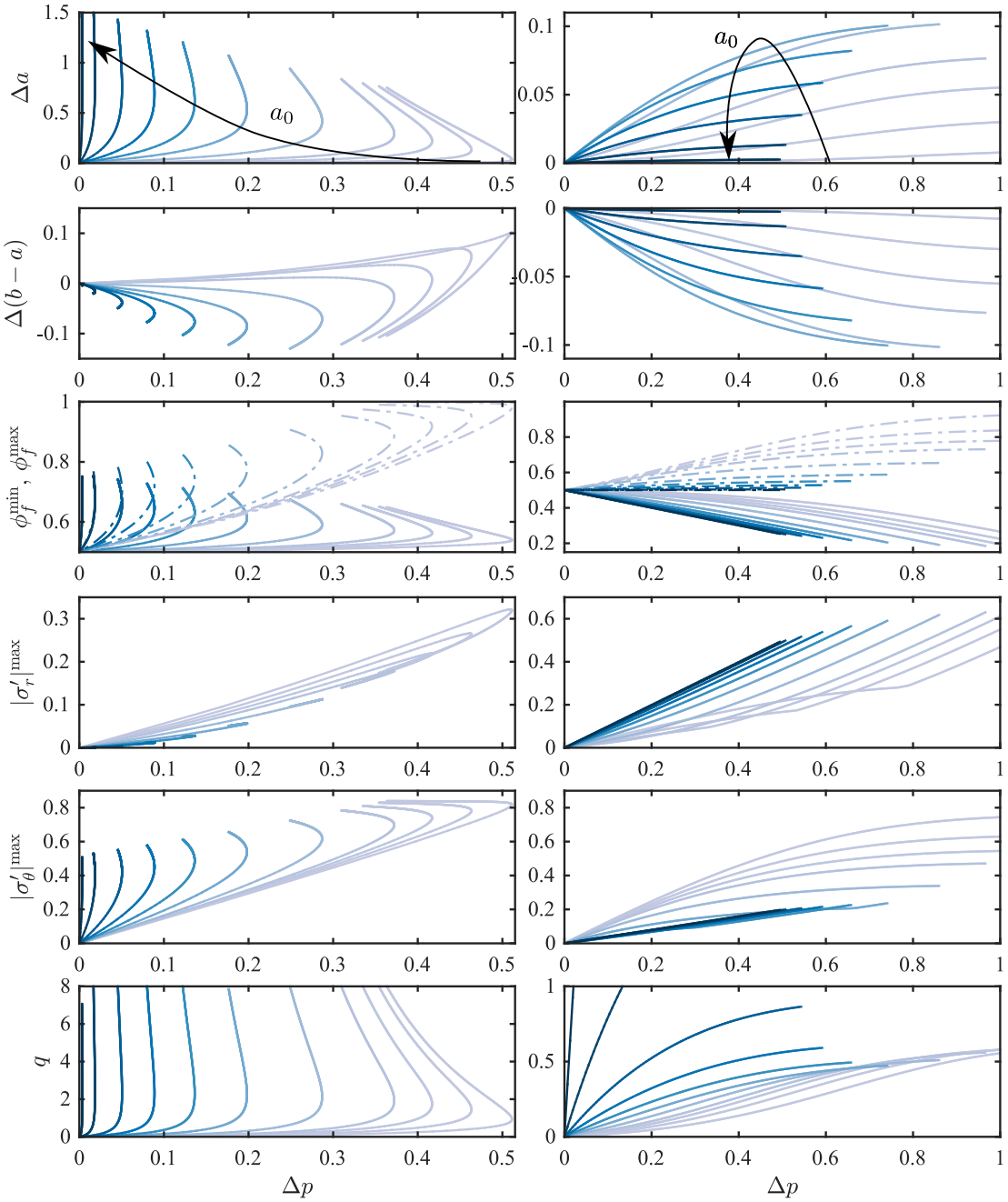

Figure 3.9: The results of Figure 3.7 plotted as contours of fixed a_0 against Δp, with $a_0 \in [0.001, 0.98]$ (light to dark).

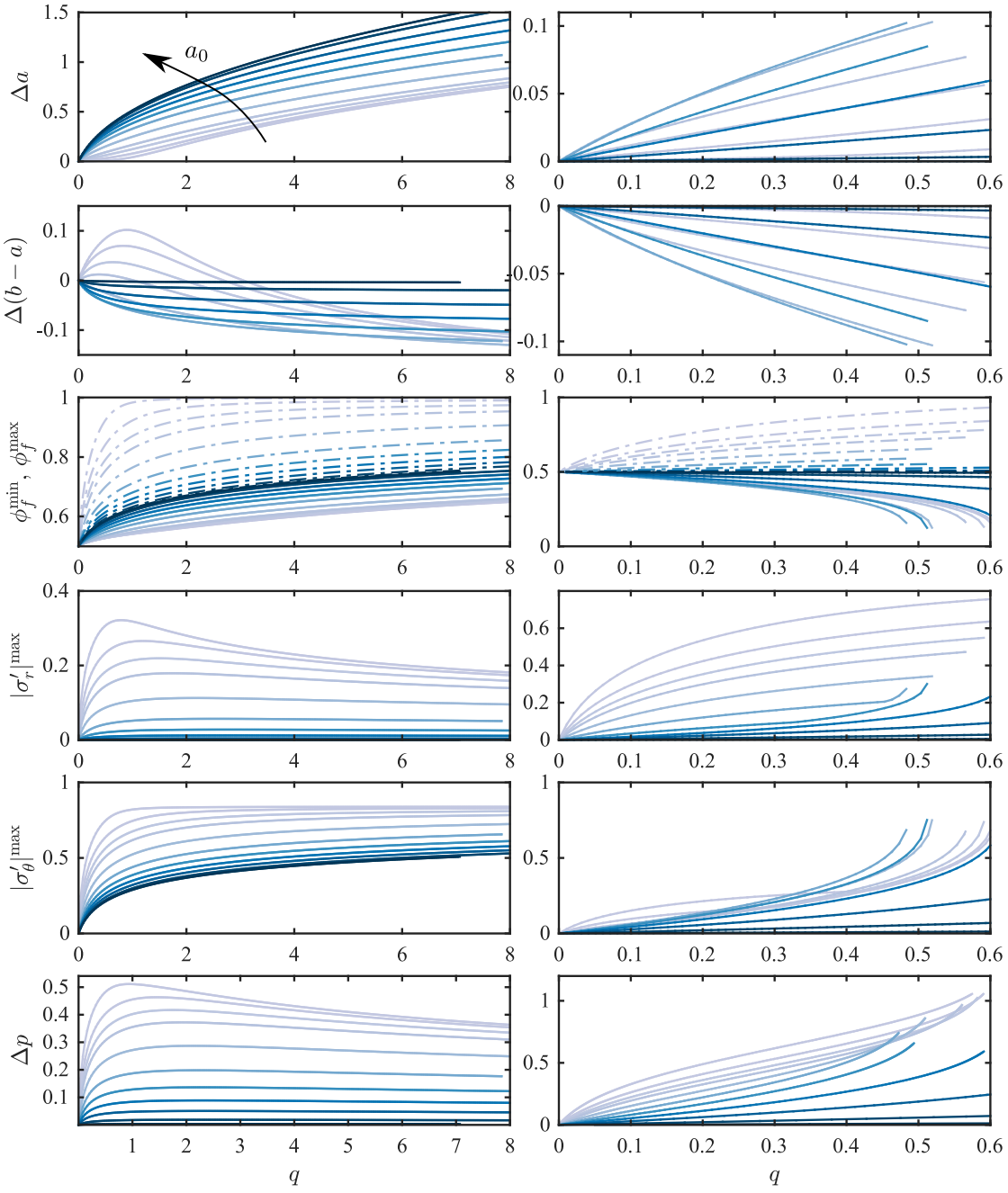

Figure 3.10: The results of Figure 3.7 plotted as contours of fixed a_0 against q, with $a_0 \in [0.001, 0.98]$ (light to dark).

have two distinct solutions for at least some range of a_0. Although most of these contours terminate at some value of a_0 beyond which our numerical scheme is no longer able to converge to a solution, the existence of complete branches for larger values of Δp suggests that all contours would continue smoothly back to $a_0 = 0$. For simplicity, we assume that this is indeed the case in the discussion below.

For $a_0 > a_0^{\max}(\Delta p)$, no steady-state solution exists. This suggests that, for a given value of a_0, there exists a maximum allowable driving pressure $\Delta p^{\max}(a_0)$ that can be supported (Figure 3.9). This maximum is an inherent feature of poromechanical coupling in a radial geometry. In the absence of a change in constitutive behaviour, applying a pressure drop larger than $\Delta p^{\max}(a_0)$ would lead to unbounded deformation and, ultimately, to material failure. The value of $\Delta p^{\max}$ is finite and positive for $0 < a_0 < 1$, diverging as a_0 tends to zero and vanishing as a_0 tends to one.[6]

For $a_0 < a_0^{\max}(\Delta p)$, two distinct steady-state solutions exist for a given a_0. These correspond to a less-deformed solution and a more-deformed solution, where the latter is characterised by more extreme values of all quantities except for $|\sigma_r'|^{\max}$. This implies that a given Δp can lead to one of two different flow rates for the same cylinder: a lower flow rate in the less-deformed state or a higher flow rate in the more-deformed state. The classical balloon-inflation problem in nonlinear elasticity famously also exhibits multiple solutions in certain regions of its parameter space; in that case, the effect is purely kinematic and nonlinear-elastic. Here, this effect results from the nontrivial coupling of kinematics and poromechanics, even for a linear elasticity law (L-k_{KC} model; see Figure 3.12). In the remainder of this section, we focus on the characteristics of these two solutions.

Flow drives all parts of the material radially outward ($u_r > 0$ for all r), so that the inner and outer radii of the cylinder always increase, $a > a_0$ and $b > b_0$ (*i.e.*, $\Delta a > 0$, first row; $\Delta b > 0$, not shown). The wall thickness $b - a$ may increase or decrease, depending on whether Δb exceeds Δa ($\Delta(b - a)$, second row). For $a_0 \gtrsim 0.1$, both solutions are

[6]The limit $a_0 \to 0$ corresponds to a line source in an infinite domain, for which no steady state exists. The limit $a_0 \to 1$ corresponds to vanishingly thin walls, which can support no load.

characterised by a decrease in wall thickness. For $a_0 \lesssim 0.1$, the less-deformed solution instead corresponds to an increase in wall thickness, while the more-deformed solution corresponds to a decrease in wall thickness. For $a_0 \lesssim 0.01$, both solutions correspond to an increase in wall thickness.

For all values of a_0 and Δp, both the minimum porosity $\phi_f^{\min}$ and the maximum porosity $\phi_f^{\max}$ exceed $\phi_{f,0}$ (third row; solid and dot-dashed lines, respectively). This implies that the porosity increases throughout the material ($\phi_f > \phi_{f,0}$ for all r), which further implies that the total cross-sectional area always increases, regardless of whether the wall thickness increases or decreases. For sufficiently small Δp, there exists a value of a_0 at which $\phi_f^{\min}$ and $\phi_f^{\max}$ intersect, implying the existence of a family of solutions with uniform porosity. The difference between $\phi_f^{\min}$ and $\phi_f^{\max}$ increases monotonically with Δp such that this intersection no longer exists at high Δp (Figure 3.9).

The maximum absolute azimuthal effective stress $|\sigma'_\theta|^{\max}$ (fourth row) and the maximum absolute radial effective stress $|\sigma'_r|^{\max}$ (fifth row) are relevant to material failure. The azimuthal component increases monotonically with Δp along the less-deformed solution branch; the radial component exhibits a more complex behaviour, but $|\sigma'_r|^{\max} < |\sigma'_\theta|^{\max}$ for all a_0 and Δp (Figure 3.9).

The flow rate q exhibits the same striking feature as most other quantities—a region $a_0 > a_0^{\max}(\Delta p)$ characterised by no solution, and a region $a_0 < a_0^{\max}(\Delta p)$ characterised by two solutions (last row; coloured lines). We compare the actual flow rate q with the reference flow rate q_0 that would occur for the same Δp for a rigid cylinder with the same initial geometry, $q_0 := -\Delta p / \ln(a_0)$ (last row; grey lines). This reference flow rate is equivalent to the prediction of classical linear poroelasticity (L-k_0), and it diverges for all Δp as a_0 tends to one. Note that $q > q_0$ for all a_0 and Δp—that is, a deformable unconfined cylinder (modelled here via the Q-k_{KC} model) will always conduct a higher flow rate than a rigid cylinder of the same initial geometry, and this is a nonlinear effect.

3.2.2.2 Constrained cylinders

Constrained cylinders exhibit qualitatively different behaviour (Figure 3.7, right column) — a single solution exists for all values of a_0, and all quantities vary monotonically with Δp. Note that we expect unconstrained and constrained cylinders to approach the same limiting behaviour for $a_0 \ll 1$, as noted above in the context of Figure 3.5.

The change in inner radius Δa is strictly positive, tending to zero for both small a_0 and large a_0. In the former limit, this is because Δa decreases with a_0 for fixed Δp; in the latter limit, this is because $b = 1$ is fixed and the material has nowhere to go. The change in wall thickness is equal and opposite to the change in inner radius, $\Delta(b - a) = -\Delta a$, and is therefore strictly negative. That is, the walls always get thinner. As a result, the cross-sectional area always decreases and the average porosity (and thus $\phi_f^{\min}$) must always be less than $\phi_{f,0}$. However, $\phi_f^{\max}$ is still always greater than $\phi_{f,0}$. The difference between $\phi_f^{\max}$ and $\phi_f^{\min}$ increases with Δp (Figure 3.9) and is roughly constant with a_0. For a thin-walled cylinder, $\phi_f^{\max}$ is close to $\phi_{f,0}$ while $\phi_f^{\min}$ is substantially below $\phi_{f,0}$. For a thick-walled cylinder, $\phi_f^{\min}$ is close to $\phi_{f,0}$ while $\phi_f^{\max}$ is substantially above $\phi_{f,0}$. Note that the latter scenario respects the constraint on the average porosity by virtue of the fact that the large porosities are localised to a small region near the inner radius while the rest of the cylinder (the vast majority) is weakly compressed. The azimuthal stress $|\sigma'_\theta|^{\max}$ decreases with a_0 for small a_0 and increases gently with a_0 for large a_0, tending to a finite, nonzero value as a_0 tends to one. The radial stress $|\sigma'_r|^{\max}$ exhibits a similar trend, with the transition from decreasing to increasing occurring at a much smaller value of a_0. For both stress components, this transition occurs at a corner that corresponds to a transition in the maximum absolute value of the stress from tensile near/at the inner radius (radial/azimuthal) to compressive at the outer radius (both).

The flow rate q is weakly non-monotonic in a_0 for small a_0 and large Δp, implying that two different values of a_0 can lead to the same combination of Δp and q. Comparing the actual flow rate q to the reference flow rate q_0 (rigid cylinder or L-k_0 model, grey lines),

we find that a constrained deformable cylinder will conduct a larger flow rate than a rigid cylinder if the walls are thick, but a smaller flow rate than a rigid one if the walls are thin; this is in contrast to an unconstrained deformable cylinder, which always conducts a larger flow rate than a rigid one. This effect is amplified as Δp increases, but its magnitude is relatively modest; q decreases from a few tens of percent above q_0 to a few tens of percent below q_0 over the full range of a_0. For an unconstrained cylinder, in contrast, deformation dominates the flow rate as a_0 approaches $a_0^{\max}$.

3.2.3 Force balance

Flow always forces the material radially outward. This loading must be supported through a combination of internal azimuthal stress and external radial traction. To investigate these mechanics in more detail, we consider a macroscopic balance of the 'vertical' components of the forces acting on one-half of the annular cross-section of the cylinder (see diagrams, top of Figure 3.11). The 'vertical' components of the forces due to fluid or pore-pressure loading F_p, internal azimuthal stress F_θ, and external radial traction F_r are given by

$$F_p = 2a\Delta p + 2\int_a^b p\,\mathrm{d}r\,, \quad F_\theta = 2\int_a^b \sigma'_\theta\,\mathrm{d}r\,, \quad \text{and} \quad F_r = -2b\sigma'_r(b), \tag{3.26}$$

and macroscopic force balance requires that $F_p = F_\theta + F_r$. We plot these quantities in Figure 3.11 for unconstrained cylinders (left column) and constrained cylinders (right column). Note that, as with Figure 3.7, these results can be presented in several different ways and as such the first row of Figure 3.11 has the same axes, line colours and constant contours as Figure 3.7; the second row of Figure 3.11 has the same axes, line colours and constant contours as Figure 3.8; the third row of Figure 3.11 has the same axes, line colours and constant contours as Figure 3.9 and the last row of Figure 3.11 has the same axes, line colours and constant contours as Figure 3.10 .

For unconstrained cylinders, $F_r \equiv 0$ and therefore $F_\theta \equiv F_p$. These two nontrivial

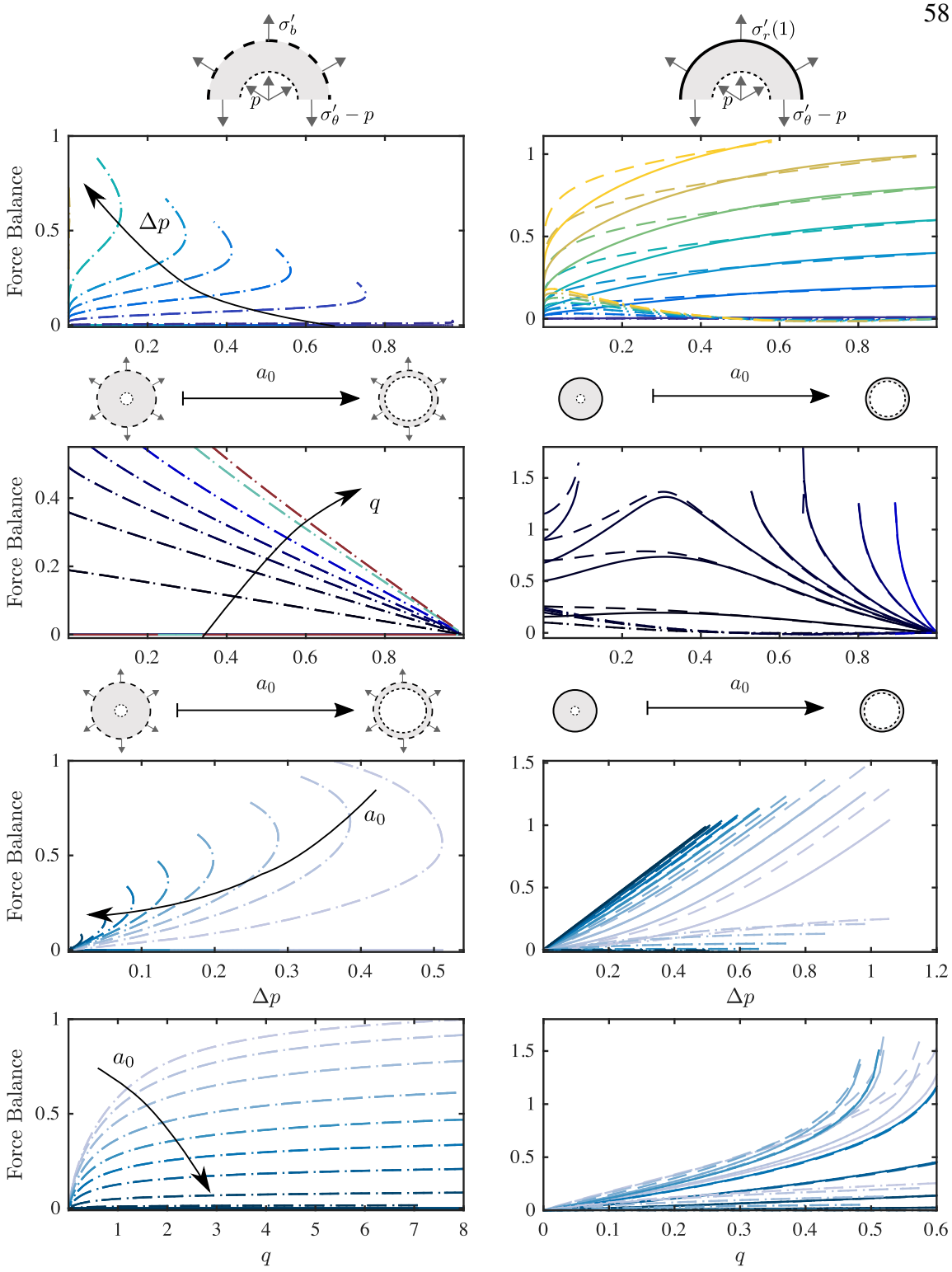

Figure 3.11: Flow leads to a net pressure force F_p (dashed lines) that must be supported by a combination of force due to internal azimuthal stress F_θ (dot-dashed lines) and force due to external radial traction F_r (solid lines). We plot these forces for unconstrained cylinders for $\Delta p \in [0.005, 0.5]$ (top row, left), and for constrained cylinders for $\Delta p \in [0.005, 0.6]$ (top row, right). The colour scale for Δp is the same as in Figure 3.7. For unconstrained cylinders, note that $F_r \equiv 0$ and $F_\theta \equiv F_p$. Additionally, we present the same data plotted in various combinations as we did for Figure 3.7 (*cf.* Figures 3.8–3.9). The colours in each row are the same as in the corresponding 'version' of Figure 3.7 — that is the second row corresponds to Figure 3.8, the third row to Figure 3.9 and the last row to Figure 3.10.

force components increase as Δp increases along the less-deformed solution branch. These quantities ultimately mirror the behaviour shown in Figures 3.7-3.9. That is two solutions exist for $a_0 < a_0^{\max}(\Delta p)$, one corresponding to less deformation and smaller forces and the other corresponding to more deformation and larger forces.

For constrained cylinders, F_r will be determined implicitly to satisfy the condition that $u_s(1) = 0$. For fixed Δp, both F_p and F_r increase monotonically with a_0. For $a_0 \lesssim 0.05$, F_θ is similar in magnitude to F_r and increases with a_0; for $a_0 \gtrsim 0.05$, however, F_θ decreases rapidly with a_0 and ultimately becomes weakly negative but negligible in the overall force balance. In other words, the outer boundary supports most of the fluid loading for a cylinder with moderate to thin walls. Note that $F_r < F_p$ for $a_0 \lesssim 0.5$ since $F_\theta > 0$, but $F_r > F_p$ for $a_0 \gtrsim 0.5$ since $F_\theta < 0$.

3.2.4 Effects of model choice

In §3.2.2 and §3.2.3 we focused on results from the Q-k_{KC} model because it provides a good compromise between rigour, robustness, and computational efficiency. We examine this choice in more detail in Figure 3.12 by plotting q against a_0 for contours of fixed Δp, as in the last row of Figure 3.7, for five different models: Q-k_{KC} (first row), L-k_{KC} (second row), Q-k_0 (third row), N-k_{KC} (last row), and L-k_0 (all rows, grey lines). Note that q appears to be much more sensitive to the permeability law than other aspects of the deformation (*cf.* data at bottom of Figures 3.5 and 3.6), making it a useful quantity for this comparison.

For unconstrained cylinders (left column), the Q-k_{KC} and N-k_{KC} models predict qualitatively similar behaviour, with the contours in the latter bending to the left somewhat more strongly. The latter model is also much more computationally expensive. The Q-k_0 model exhibits similar behaviour, but with much more extreme bending of the contours (note the different vertical scale). Our results for the L-k_{KC} model are inconclusive because this model is much less robust than either of the Q models; our method fails to find a solution

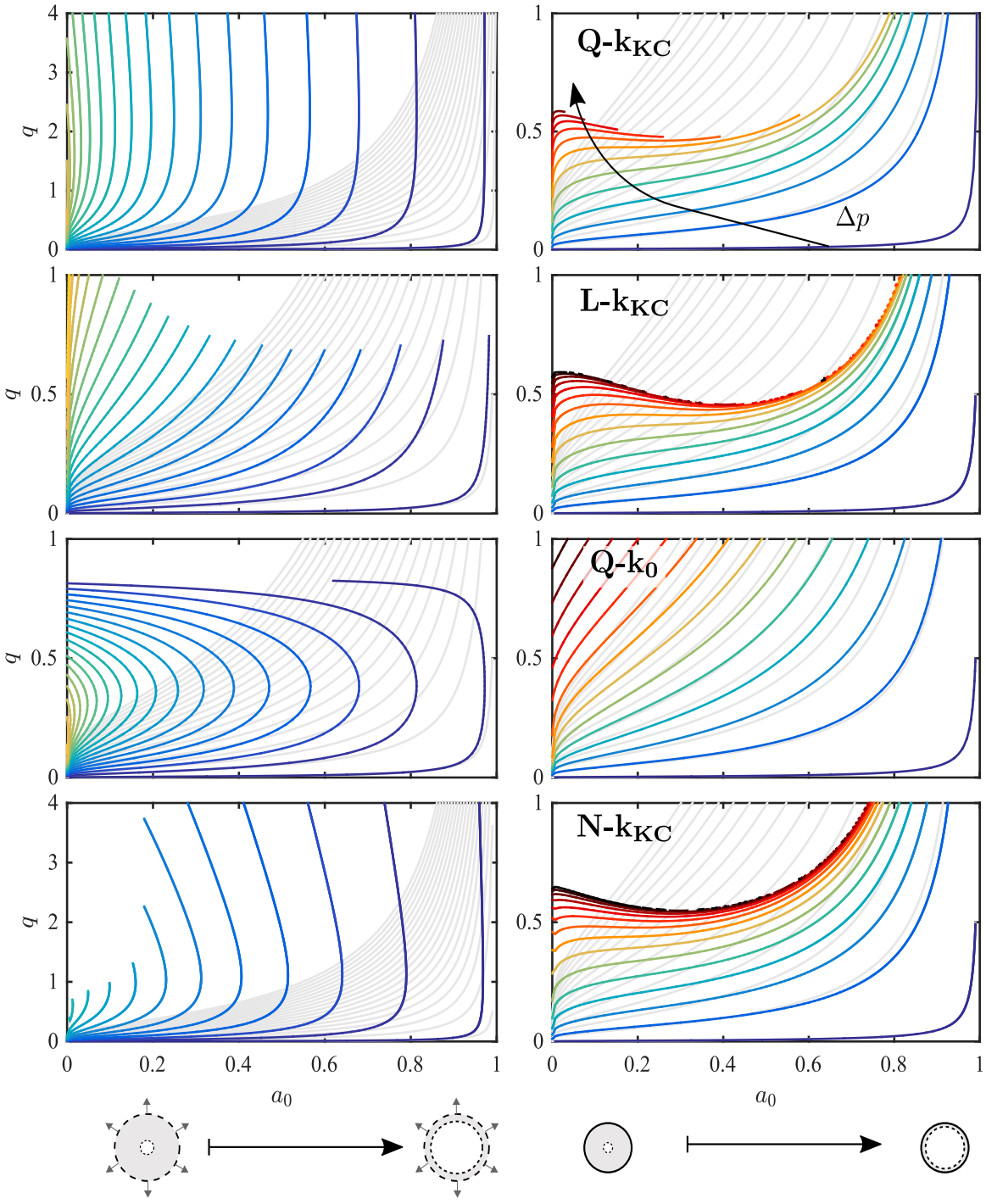

Figure 3.12: To illustrate the impact of model choice, we plot q against a_0 for contours of fixed Δp, as in the last row of Figure 3.7, for five different models: Q-k_{KC} (first row), L-k_{KC} (second row), Q-k_0 (third row), N-k_{KC} (last row), and L-k_0 (all rows, grey lines). The colour scale is the same as in Figure 3.7.

for even moderate values of q. This is likely because the L-k_{KC} model is asymptotically inconsistent and does not correctly capture the kinematic relationship between porosity and displacement. The Q-k_{KC} is much more rigorous in these regards, and is only slightly more computationally expensive in our Chebyshev pseudospectral framework.

For constrained cylinders (right column), all three of the k_{KC} models exhibit very similar behaviour despite the different elasticity laws (L and Q *vs.* N) and the different treatments of the kinematics (L *vs.* Q and N). This presentation does not constitute a careful quantitative comparison, but it suggests that deformation-dependent permeability plays a key role in the mechanics of the problem, particularly for high pressures (as for the constrained cylinder, right column), whereas large-deformation kinematics are less important. This is somewhat unsurprising since constrained cylinders generally deform much less than unconstrained cylinders.

These results suggest that rigorous large-deformation kinematics (including the relationship between porosity and displacement) are important for model robustness and are central to the double-valued behaviour of unconstrained cylinders. Deformation-dependent permeability appears to moderate (but not eliminate) the double-valued behaviour of unconstrained cylinders, and to be central to the behaviour of constrained cylinders.

As noted in §2.2.1 and §2.3, we have chosen Hencky elasticity and Kozeny-Carman permeability as relatively generic constitutive laws that capture the qualitatively important features of deformation-dependent permeability and large-deformation elasticity, respectively. Given the strong role of deformation-dependent permeability in our results, a comparison with results for other permeability laws would be an interesting topic for future work.

3.3 Conclusion

Despite being a classical topic in geomechanics and in biophysics, radial poroelastic deformation has not previously been systematically explored, particularly in the context of large deformations. To assess the qualitative and quantitative impacts of large deformations, we considered six different models in the context of two end-member geometries (thick-walled and thin-walled) and two different outer boundary conditions (unconstrained and constrained). We showed that the impacts of nonlinear kinematics, nonlinear elasticity, and deformation-dependent permeability depend strongly on geometry and boundary conditions, as does the relative importance of these facets of nonlinearity. For example, the mechanical response of an unconstrained thin-walled cylinder to an imposed pressure drop is dominated by kinematics and elasticity, although the permeability law exerts a strong control on the resulting flow rate through the material; for the same pressure drop, a constrained thin-walled cylinder is limited to much smaller deformations and exhibits what is essentially a linear-poroelastic response (Figure 3.6). In contrast, the mechanical response of a thick-walled cylinder is much less sensitive to constraint, although the outer boundary condition has a strong impact on the flow rate when the permeability is deformation-dependent (Figure 3.5).

To explore the importance of geometry and constraint in more detail, we then focused on a model that includes rigorous nonlinear kinematics and deformation-dependent permeability, but with the simplification of linear elasticity (Q-k_{KC}). This model captures the qualitative and quantitative impacts of large deformations, as heuristically shown in Figure 3.12, but is more computationally convenient than a fully nonlinear model. We showed that, for an unconstrained cylinder, a given initial inner radius can conduct an arbitrarily large flow rate but can only support a finite maximum pressure drop, and this maximum allowable pressure drop increases with the thickness of the walls (Figures 3.7, 3.9 and 3.11). For a pressure drop less than this maximum, our results suggest that two valid solutions exist—a less-deformed state with a lower flow rate and a more-deformed state with a

higher flow rate. A constrained cylinder, in contrast, can support an arbitrarily large pressure drop but can only conduct a finite maximum flow rate, and this maximum flow rate is non-monotonic in the wall thickness (see Figures 3.8–3.9). These behaviours are mirrored in the corresponding force balance (Figures 3.11).

We have assumed here that the constitutive response of the solid skeleton remains elastic for arbitrarily large deformations. This is relevant to biomedical applications such as fluid permeation through artery walls, and to the design of radial filters. In geomechanical applications, however, large deformations are typically the result of material failure through plasticity or fracture, which will lead to a fundamentally different constitutive behaviour in the solid. Additionally, it may be relevant for many biomedical and geophysical applications to couple the poroelastic domain to different surface phenomena, such as free external flows. Plastic failure in porous annuli is the focus of Chapter 5.

We conclude by noting that, in addition to providing fundamental physical insight, our results and numerical codes (see Electronic Supplementary Material of [6]) could serve as a useful benchmark for general numerical-simulation tools (*e.g.,* finite-element codes). Relatively few benchmarks are available in the context of large-deformation poroelasticity.

In Chapter 4 we consider the transient problem, focussing on the impact of model choice, driving mechanism and geometry on the evolution of the problem. We define a characteristic timescale and explore its complex dependence on geometry, model choice and driving mechanism.

Chapter 4

The full poroelastic transient problem

In this chapter we consider the transient response of a poroelastic cylinder to sudden, radially outward fluid injection. Specifically, we investigate the impact of geometry, permeability law, and outer boundary condition for the L Q and N models. The majority of the material in this chapter has been published in *Proceedings of the Royal Society A* as part of Auton and MacMinn [7]. The transient evolution is important in biomedical applications because these systems are inherently transient, as with the periodic pressure pulses in vascular flows, and in geophysical applications where the primary interest is in the time needed for a certain amount of consolidation or pressure dissipation to occur.

The transient aspects of large-deformation poroelasticity have been considered in some detail in a rectilinear (uni-axial) geometry in the context of fluid injection [8, 61], forced infiltration [74, 87], and transmural flow [56]. For example, MacMinn et al. [61] considered the effect of constant versus deformation-dependent permeability in a model problem where the deformation is strictly compressive, showing that deformation-dependent permeability can greatly increase the evolution timescale (slow the response) relative to constant permeability.

The radial geometry has attracted interest in a range of contexts, including biomedical applications such as subcutaneous injections and flow through arterial walls [*e.g*, 54, 96]

and geophysical applications such as borehole pressurisation or consolidation following pile driving [*e.g*, 76, 79]. For scenarios involving small deformations, it is appropriate to use classical linear poroelasticity; this leads to a linear partial differential equation (PDE) that can be solved analytically via various classical methods. Kenyon [55] and Jayaraman [54] considered fluid flow across arterial walls, in which the artery is modelled as a soft porous cylinder with a time-dependent inner fluid pressure and a constrained outer boundary. Kenyon [55] considered the transient response to a step change in the inner pressure and used a Laplace transform to derive an approximate solution for small times. Jayaraman [54] considered the transient response to an oscillatory inner fluid pressure, using normal modes to derive approximate long-time solutions for low- and high-frequency driving. Randolph and Wroth [76] considered consolidation after pile-driving, in which the insertion of the pile leads to locally elevated pore pressure that subsequently dissipates. They modelled the relaxation of the soil around the cylindrical pile, treating the pile as a rigid and impermeable boundary from which the soil could not separate and assumed that pore pressure was only perturbed from its initial value in a finite region around the pile. They used separation of variables to derive a solution in terms of an infinite series of Bessel functions. Jana [53] considered elastic deformations around a cylindrical cavity in an infinite medium, deriving solutions via Fourier Series and Laplace Transforms. Similarly, Detournay and Cheng [32] considered relaxation around an excavated or pressurised borehole by modelling the borehole as a cylindrical cavity in an infinite domain, with various modes of loading at the interface. They applied a Laplace transform in time, solved the spatial problem in terms of modified Bessel functions, and then inverted the Laplace transform numerically. Rice and Cleary [79] considered the internal pressurisation of annular rock specimens, modelling these as unconstrained cylinders in plane strain. They solved this problem using complex variable techniques, deriving an approximate solution for small times and a complete solution for the limiting case of a semi-infinite domain.

The introduction of nonlinearity leads to a problem that is less analytically tractable.

Barry and Aldis [9] and Barry and Mercer [10] accounted partially for large deformations by including moving boundaries and deformation-dependent permeability in a model that was otherwise linearised. Barry and Aldis [9] considered a similar model for a constrained cylinder, using perturbation methods to derive approximate solutions for small times and for slow compression rates. Barry and Mercer [10] again used a similar model to study constrained and unconstrained cylinders and develop approximate solutions for small times.

These previous works have considered a wide range of applications and model problems, but a systematic exploration of the transient mechanics of poroelastic cylinders is still lacking. We define the general parameter space and explore the effects of geometry, outer boundary condition, and driving method (fixed Δp or fixed q), as well as the impact of large deformations, on the transient response. For classical linear poroelasticity, we use separation of variables and Sturm-Liouville theory to derive analytical solutions for the fixed-flow rate problem in terms of an infinite series of Bessel and Struve functions. We solve the various nonlinear problems numerically using the method of lines with Chebyshev spectral collocation [71], a natural extension of the pseudospectral method developed in §3.1.3. Examining the transient evolution of the deformation we show that the evolution timescale exhibits a complex dependence on geometry, boundary condition and driving method, even for linear poroelasticity. For the range of cases considered here, nonlinear elasticity has a much smaller impact on the evolution timescale than nonlinear kinematics, deformation-dependent permeability, or the other factors mentioned previously.

4.1 Solutions and numerical solution techniques

In this section we first define some helpful notation for the boundary conditions (§4.1.1); we then present analytical solutions for classical linear poroelasticity (L-k_0) for a fixed flow rate q (§4.1.2), derive an early-time solution for the displacement at the inner boundary for all models for fixed q (§4.1.3) and discuss the extension of Chebyshev spectral collocation

that we use to solve the nonlinear transient problems (§4.1.4).

4.1.1 Boundary Conditions: Notation

For convenience, we define three operators

$$B^a[u_s] := \sigma_r'(a,t), \quad B_1^b[u_s] := u_s(b,t), \quad \text{and} \quad B_2^b[u_s] := \sigma_r'(b,t) - \sigma_b', \tag{4.1}$$

so that Equation (2.30) can be expressed as $B^a[u_s] = 0$ and Equation (2.33) can be expressed as $B_i^b[u_s] = 0$ for $i = 1, 2$, where $i = 1$ corresponds to a constrained cylinder and $i = 2$ corresponds to a cylinder subject to a fixed radial effective stress at the outer boundary[1]. When we linearise the kinematics of the problem by applying these at $r = a_0$ (rather than at a) and at $r = 1$ (rather than at b), respectively, we instead express Equation (2.30) via $B^{a_0}[u_s] = 0$ and Equation (2.33) via $B_i^{b_0}[u_s] = 0$ for $i = 1, 2$. In the limiting case of $\sigma_b' \equiv 0$, $i = 2$ corresponds to an unconstrained cylinder.

4.1.2 Analytical solutions: L-k_0 for fixed q

We now develop analytical solutions for the L-k_0 model for a fixed driving flow rate q. For clarity we first provide the complete solution for the constrained cylinder (§4.1.2.1) and subsequently present the solution for an arbitrary constant applied radial effective stress at the outer boundary (§4.1.2.2).

[1]Note that σ_r' is related to u_s via either Equation (2.21) or Equation (2.24). Thus the operators $B^a[u_s]$ and $B_2^b[u_s]$ are different for linear and Hencky elasticity.

4.1.2.1 Zero displacement

The IBVP for the constrained cylinder is

$$\frac{\partial u_s}{\partial t} - \frac{\partial}{\partial r}\left[\frac{1}{r}\frac{\partial}{\partial r}(ru_s)\right] = \frac{q}{r} \qquad a_0 < r < 1, \quad t > 0 \tag{4.2a}$$

$$u_s(r,0) = 0 \qquad a_0 < r < 1, \quad t = 0 \tag{4.2b}$$

$$B^{a_0}[u_s] = \frac{\partial u_s}{\partial r} + \Gamma\frac{u_s}{a_0} = 0 \qquad r = a_0, \qquad t > 0 \tag{4.2c}$$

$$B_1^{b_0}[u_s] = u_s(1,t) = 0 \qquad r = 1, \qquad t > 0. \tag{4.2d}$$

We approach this problem using separation of variables for a non-homogeneous PDE. We begin by substituting the separable ansatz

$$u_s = \mathcal{T}(t)\mathcal{R}(r) \tag{4.3}$$

into the associated homogeneous PDE

$$\frac{\partial u_s}{\partial t} - \frac{1}{r}\left[\frac{\partial}{\partial r}\left(r\frac{\partial u_s}{\partial r}\right) - \frac{u_s}{r}\right] = 0 \tag{4.4}$$

to obtain

$$\frac{\mathcal{T}'(t)}{\mathcal{T}(t)} = \frac{[r\mathcal{R}'(r)]' - \mathcal{R}(r)/r}{r\mathcal{R}(r)} = -\omega^2 \tag{4.5}$$

for some constant ω and where prime denotes differentiation with respect to the given variable. The spatial problem is thus

$$[r\mathcal{R}'(r)]' - \frac{\mathcal{R}(r)}{r} + r\omega^2\mathcal{R}(r) = 0 \tag{4.6a}$$

$$\mathcal{R}'(a_0) + \Gamma\frac{\mathcal{R}(a_0)}{a_0} = \mathcal{R}(1) = 0, \tag{4.6b}$$

which constitutes a Sturm-Liouville eigenvalue problem. This has two key advantageous properties: firstly, there exist a countably infinite number of strictly increasing real eigenvalues; secondly, the corresponding eigenfunctions constitute an orthogonal basis [73]. The solution to this eigenvalue problem can therefore be used to construct solutions to the original IBVP (4.2) in terms of an infinite series of eigenfunctions.

The boundary conditions are homogeneous (Robin at $r = a_0$ and Dirichlet at $r = 1$), allowing us to solve the spatial problem (4.6) in its current form. We rewrite Equation (4.6a) as

$$\mathcal{R}''(r) + \frac{\mathcal{R}'(r)}{r} + \mathcal{R}(r)\left(\omega^2 - \frac{1}{r^2}\right) = 0, \tag{4.7}$$

recognising this as Bessel's differential equation with solution

$$\mathcal{R}(r) = c_1 J_1(\omega r) + c_2 Y_1(\omega r), \tag{4.8}$$

where c_1 and c_2 are constants to be determined and $J_\mathfrak{v}$ and $Y_\mathfrak{v}$ are Bessel functions of the first and second kind, respectively, of order $\mathfrak{v}$. Using Equation (4.6b), we then obtain

$$\begin{pmatrix} J_1(\omega) & Y_1(\omega) \\ \frac{\omega}{2}[J_0(\omega a_0) - J_2(\omega a_0)] + \frac{\Gamma}{a_0} J_1(\omega a_0) & \frac{\omega}{2}[Y_0(\omega a_0) - Y_2(\omega a_0)] + \frac{\Gamma}{a_0} Y_1(\omega a_0) \end{pmatrix} \begin{pmatrix} c_1 \\ c_2 \end{pmatrix} = \begin{pmatrix} 0 \\ 0 \end{pmatrix}. \tag{4.9}$$

For non-trivial solutions, we set the determinant of the matrix to zero,

$$J_1(\omega)\left\{\frac{\omega}{2}\left[Y_0(\omega a_0) - Y_2(\omega a_0)\right] + \frac{\Gamma}{a_0} Y_1(\omega a_0)\right\} - Y_1(\omega)\left\{\frac{\omega}{2}\left[J_0(\omega a_0) - J_2(\omega a_0)\right] + \frac{\Gamma}{a_0} J_1(\omega a_0)\right\} = 0, \tag{4.10}$$

which provides an infinite number of solutions for the infinite set of distinct eigenvalues

$\omega = \omega_n$ that satisfy Equation (4.10). For the boundary condition at $\mathcal{R}(1)$, we have

$$c_2 = -c_1 \frac{J_1(\omega_n)}{Y_1(\omega_n)}, \tag{4.11}$$

and we further take $c_1 = 1$ without loss of generality. We then have an infinite number of eigenfunctions $\mathcal{R}_n(r)$ given by

$$\mathcal{R}_n(r) = J_1(\omega_n r) - \frac{J_1(\omega_n)}{Y_1(\omega_n)} Y_1(\omega_n r). \tag{4.12}$$

Note that as the ω_n are eigenvalues of a Sturm-Liouville problem, and by construction are positive, they must also satisfy

$$0 < \omega_1 < \omega_2 < \cdots \quad \text{with} \quad \omega_n \to \infty \quad \text{as} \quad n \to \infty, \tag{4.13}$$

The eigenfunctions are orthogonal with respect to a weighted inner product with associated weighting function $\mathfrak{W}(r) = r$ (the coefficient of $\omega^2 \mathcal{R}$ in Equation (4.6a)). The weighted inner product is therefore given by

$$\langle f, g \rangle_r = \int_{a_0}^{1} r f(r) g(r) \, \mathrm{d}r, \tag{4.14a}$$

so that

$$\frac{\langle \mathcal{R}_n, \mathcal{R}_m \rangle}{\langle \mathcal{R}_n, \mathcal{R}_n \rangle} = \begin{cases} 0 & \text{if } n \neq m; \\ 1 & \text{if } n = m. \end{cases} \tag{4.14b}$$

We must now determine the corresponding $\mathcal{T}_n(t)$ such that

$$u_s = \sum_{n=1}^{\infty} \mathcal{T}_n(t) \mathcal{R}_n(r) \tag{4.15}$$

satisfies the original IBVP (4.2), despite the fact that our initial separable ansatz was applied

to the homogeneous problem. Substituting Equation (4.15) into Equation (4.2a), we obtain

$$\frac{q}{r} = \frac{\partial u_s}{\partial t} - \frac{\partial}{\partial r}\left[\frac{1}{r}\frac{\partial}{\partial r}(u_s r)\right] = \sum_{n=1}^{\infty}\left[\mathcal{T}_n'(t) + \omega_n^2 \mathcal{T}_n(t)\right]\mathcal{R}_n(r). \tag{4.16}$$

This motivates decomposing q/r in terms of an infinite series of eigenfunctions,

$$\frac{q}{r} = \sum_{n=1}^{\infty} f_n \mathcal{R}_n(r), \tag{4.17}$$

for some infinite set of constants f_n. Combining Equations (4.16) and (4.17) leads to the ordinary differential equation (ODE)

$$\mathcal{T}_n'(t) + \omega_n^2 \mathcal{T}_n(t) = f_n, \tag{4.18}$$

which has solution

$$\mathcal{T}_n(t) = \frac{f_n}{\omega_n^2}\left(1 - e^{-\omega_n^2 t}\right). \tag{4.19}$$

We evaluate f_n from Equation (4.17) by invoking (4.14), yielding

$$f_n = \frac{q\int_{a_0}^{1}\mathcal{R}_n(r)\,\mathrm{d}r}{\int_{a_0}^{1} r[\mathcal{R}_n(r)]^2\,\mathrm{d}r} = \frac{q\left[Y_1(\omega_n)\right]^2 I_0}{\left[Y_1(\omega_n)\right]^2 I_1 + \left[J_1(\omega_n)\right]^2 I_2 - 2J_1(\omega_n)Y_1(\omega_n)I_3}, \tag{4.20}$$

where

$$I_0 := \frac{\Big[J_1(\omega_n)Y_0(\omega_n r) - Y_1(\omega_n)J_0(\omega_n r)\Big]_{a_0}^{1}}{\omega_n Y_1(\omega_n)}, \tag{4.21a}$$

$$I_1 := \left[\frac{r^2}{2}\Big\{J_1(\omega_n r)^2 - J_0(\omega_n r)J_2(\omega_n r)\Big\}\right]_{a_0}^{1}, \tag{4.21b}$$

$$I_2 := \left[\frac{r^2}{2}\Big\{Y_1(\omega_n r)^2 - Y_0(\omega_n r)Y_2(\omega_n r)\Big\}\right]_{a_0}^{1}, \tag{4.21c}$$

and

$$I_3 := \left[\frac{r^2}{2}\Big\{J_0(\omega_n r)Y_0(\omega_n r) + J_1(\omega_n r)Y_1(\omega_n r)\Big\} - \frac{r}{\omega_n}\Big\{J_0(\omega_n r)Y_1(\omega_n r)\Big\}\right]_{a_0}^{1}. \quad (4.21d)$$

Finally, the solution is given by

$$u_s = \sum_{n=1}^{\infty}\left[\frac{f_n}{\omega_n^2}\left(1 - e^{-\omega_n^2 t}\right)\right]\left[J_1(\omega_n r) - \frac{J_1(\omega_n)}{Y_1(\omega_n)}Y_1(\omega_n r)\right], \quad (4.22)$$

where the ω_n are the solutions to Equation (4.10) and the f_n are defined by Equations (4.20–4.21).

4.1.2.2 Applied radial effective stress

Now we present the analytical solution for a cylinder subjected to the linearised applied-stress conditions $B^{a_0}[u_s] = B_2^{b_0}[u_s] = 0$ for the general case $\sigma_b' \not\equiv 0$. A stress-free initial condition does not satisfy these boundary conditions, so we begin by solving the corresponding non-poroelastic ('drained') problem subjected to $B_2^{b_0}[u_s] = 0$. We then use this solution as a consistent initial condition for the evolution of the fluid-driven problem. For the L-k_0 model, this initial condition corresponds to a uniform porosity that is distinct from the reference porosity $\phi_{f,0}$ (*cf.* Equations (2.17a) and (4.24b)),

$$\phi_f(r,0) = \phi_{f,0} + \frac{2\sigma_b'(1-\phi_{f,0})}{(1-a_0^2)(1+\Gamma)}. \quad (4.23)$$

Equation (2.41a) with $k[u_s] \equiv 1$ subjected to $B^{a_0}[u_s] = B_2^{b_0}[u_s] = 0$ leads to the IBVP

$$\frac{\partial u_s}{\partial t} - \frac{\partial}{\partial r}\left[\frac{1}{r}\frac{\partial}{\partial r}(u_s r)\right] = \frac{q}{r} \qquad t > 0 \quad a_0 < r < 1, \tag{4.24a}$$

$$u_s(r,0) = u_{s,0} = \frac{\sigma_b'}{1-a_0^2}\left[\frac{r}{1+\Gamma} + \frac{a_0^2}{(1-\Gamma)r}\right] \qquad t = 0 \quad a_0 < r < 1, \tag{4.24b}$$

$$B^{a_0}[u_s] = \frac{\partial u_s}{\partial r} + \Gamma\frac{u_s}{a_0} = 0 \qquad t > 0 \quad r = a_0, \tag{4.24c}$$

$$B_2^{b_0}[u_s] = \frac{\partial u_s}{\partial r} + \Gamma u_s - \sigma_b' = 0 \qquad t > 0 \quad r = 1. \tag{4.24d}$$

Unlike for the constrained cylinder, the outer boundary condition in the above problem is not homogeneous. To address this, we begin by decomposing $u_s(r,t)$ into two functions $v(r,t)$ and $w(r,t)$, such that $u_s(r,t) = v(r,t) + w(r,t)$ and where $w(r,t)$ is chosen to satisfy the non-homogeneous boundary condition (Equation 4.24d),

$$w(r,t) = \frac{\sigma_b'}{a_0^2 - 1}\left(\frac{a_0^2}{\Gamma} - \frac{r^2}{2+\Gamma}\right). \tag{4.25}$$

Hence, $v(r,t)$ must then satisfy the IBVP

$$\frac{\partial v}{\partial t} - \frac{\partial}{\partial r}\left[\frac{1}{r}\frac{\partial}{\partial r}(vr)\right] = \frac{q}{r} - \frac{\sigma_b'}{a_0^2-1}\left(\frac{3}{2+\Gamma} + \frac{a_0^2}{r^2\Gamma}\right) \qquad t > 0 \quad a_0 \le r \le 1, \tag{4.26a}$$

$$v(r,0) = \frac{\sigma_b'}{1-a_0^2}\left[\frac{r}{1+\Gamma} + \frac{a_0^2}{(1-\Gamma)r} + \frac{a_0^2}{\Gamma} - \frac{r^2}{2+\Gamma}\right] \qquad t = 0 \quad a_0 \le r \le 1, \tag{4.26b}$$

$$\frac{\partial v}{\partial r} + \Gamma\frac{v}{a_0} = 0 \qquad t > 0 \quad r = a_0, \tag{4.26c}$$

$$\frac{\partial v}{\partial r} + \Gamma v = 0 \qquad t > 0 \quad r = 1, \tag{4.26d}$$

which comprises a non-homogeneous PDE with a spatially dependent initial condition and, importantly, two homogenous boundary conditions (both Robin). We can now solve the problem as in §4.1.2.1 via separation of variables. We begin with the separable ansatz

$$v = \mathcal{T}(t)\mathcal{R}(r) \tag{4.27}$$

on the associated homogeneous PDE

$$\frac{\partial v}{\partial t} - \frac{1}{r}\left[\frac{\partial}{\partial r}\left(r\frac{\partial v}{\partial r}\right) - \frac{v}{r}\right] = 0. \tag{4.28}$$

This allows us to consider the spatial problem as a Sturm-Liouville eigenvalue problem,

$$\mathcal{R}''(r) + \frac{\mathcal{R}'(r)}{r} + \mathcal{R}(r)\left(\omega^2 - \frac{1}{r^2}\right) = 0, \tag{4.29a}$$

$$\mathcal{R}'(a_0) + \frac{\Gamma}{a_0}\mathcal{R}(a_0) = \mathcal{R}'(1) + \Gamma\mathcal{R}(1) = 0, \tag{4.29b}$$

for some constant ω. From this, the weighting function for the associated orthogonality condition is, once again, $\mathfrak{W}(r) = r$. We solve for $\mathcal{R}(r)$ to obtain

$$\mathcal{R}(r) = c_1 J_1(\omega r) + c_2 Y_1(\omega r), \tag{4.30}$$

where c_1 and c_2 are constants to be determined. Using Equation (4.29b), we obtain

$$\begin{pmatrix} \mathcal{A} & \mathcal{B} \\ \mathcal{C} & \mathcal{D} \end{pmatrix} \begin{pmatrix} c_1 \\ c_2 \end{pmatrix} = \begin{pmatrix} 0 \\ 0 \end{pmatrix} \tag{4.31}$$

where

$$\mathcal{A} := \frac{\omega}{2}[J_0(\omega a_0) - J_2(\omega a_0)] + \frac{\Gamma}{a_0}J_1(\omega a_0), \tag{4.32a}$$

$$\mathcal{B} := \frac{\omega}{2}[Y_0(\omega a_0) - Y_2(\omega a_0)] + \frac{\Gamma}{a_0}Y_1(\omega a_0), \tag{4.32b}$$

$$\mathcal{C} := \frac{\omega}{2}[J_0(\omega) - J_2(\omega)] + \Gamma J_1(\omega), \tag{4.32c}$$

$$\mathcal{D} := \frac{\omega}{2}[Y_0(\omega) - Y_2(\omega)] + \Gamma Y_1(\omega). \tag{4.32d}$$

In order for Equation (4.31) to have a non-trivial solution, it must be the case that $\mathcal{AD} - \mathcal{BC} = 0$,

$$\left\{\frac{\omega}{2}\left[J_0(\omega a_0) - J_2(\omega a_0)\right] + \frac{\Gamma}{a_0}J_1(\omega a_0)\right\}\left\{\frac{\omega}{2}\left[Y_0(\omega) - Y_2(\omega b_0)\right] + \Gamma Y_1(\omega)\right\} - \left\{\frac{\omega}{2}[Y_0(\omega a_0) - Y_2(\omega a_0)] + \frac{\Gamma}{a_0}Y_1(\omega a_0)\right\}\left\{\frac{\omega}{2}\left[J_0(\omega) - J_2(\omega)\right] + \Gamma J_1(\omega)\right\} = 0. \quad (4.33)$$

Equation (4.33) suggests an infinite number of solutions for an infinite number of distinct eigenvalues $\omega = \omega_n$. The boundary condition at $r = a_0$ (Equation 4.26c) yields

$$c_2 = -c_1\frac{\omega a_0[J_0(\omega a_0) - J_2(\omega a_0)] + 2\Gamma J_1(\omega a_0)}{\omega a_0[Y_0(\omega a_0) - Y_2(\omega a_0)] + 2\Gamma Y_1(\omega a_0)} = -c_1\frac{\mathcal{A}}{\mathcal{B}}, \quad (4.34)$$

where we once again set $c_1 = 1$, giving the associated infinite number of eigenfunctions $\mathcal{R}_n(r)$ as

$$\mathcal{R}_n(r) = J_1(\omega_n r) - \frac{\mathcal{A}}{\mathcal{B}}Y_1(\omega_n r). \quad (4.35)$$

The general series solution for $v(r,t)$ is then

$$v(r,t) = \sum_{n=1}^{\infty}\mathcal{T}_n(t)\mathcal{R}_n(r), \quad (4.36)$$

where $\mathcal{T}_n(t)$ must be determined to satisfy Equation (4.26a). This requirement leads to

$$\frac{q}{r} - \frac{\sigma_b'}{a_0^2 - 1}\left(\frac{3}{2+\Gamma} + \frac{a_0^2}{r^2\Gamma}\right) = \frac{\partial v}{\partial t} - \frac{\partial}{\partial r}\left[\frac{1}{r}\frac{\partial}{\partial r}(vr)\right] = \sum_{n=1}^{\infty}\left[\mathcal{T}_n'(t) + \omega_n^2\mathcal{T}_n(t)\right]\mathcal{R}_n(r), \quad (4.37)$$

motivating the decomposition

$$\frac{q}{r} - \frac{\sigma_b'}{a_0^2 - 1}\left(\frac{3}{2+\Gamma} + \frac{a_0^2}{r^2\Gamma}\right) = \sum_{n=1}^{\infty} f_n\mathcal{R}_n(r) \quad (4.38)$$

for some infinite set of constants f_n. Equations (4.37) and (4.38) lead to

$$\mathcal{T}_n'(t) + \omega_n^2 \mathcal{T}_n(t) = f_n, \tag{4.39}$$

subject to $\mathcal{T}_n(0) = t_n$, where t_n is an infinite set of constants to be determined. This has solution

$$\mathcal{T}_n(t) = \frac{f_n}{\omega_n^2}\left(1 - e^{-\omega_n^2 t}\right) + t_n e^{-\omega_n^2 t}, \tag{4.40}$$

where, due to the properties developed in Equations (4.14), t_n is given by

$$t_n = \frac{\displaystyle\int_{a_0}^{1} r v(r,0)\mathcal{R}_n \mathrm{d}r}{\displaystyle\int_{a_0}^{1} [\mathcal{R}_n(r)]^2 r \mathrm{d}r} = \frac{\sigma_b'}{1-a_0^2}\left(\frac{\dfrac{1}{1+\Gamma}I_7 + \dfrac{a_0^2}{1-\Gamma}I_5 - \dfrac{1}{2+\Gamma}I_8 + \dfrac{a_0^2}{\Gamma}I_6}{I_1 + \dfrac{\mathcal{A}^2}{\mathcal{B}^2}I_2 - \dfrac{2\mathcal{A}}{\mathcal{B}}I_3}\right), \tag{4.41}$$

where I_1, I_2, and I_3 are defined in Equations (4.21) and

$$I_4 := \int_{a_0}^{1} \frac{\mathcal{R}_n(r)}{r}\mathrm{d}r = \left[\omega_n r\left\{J_0(\omega_n r) - \frac{\mathcal{A}}{\mathcal{B}}Y_0(\omega_n r)\right\} - J_1(\omega_n r) + \frac{\mathcal{A}}{\mathcal{B}}Y_1(\omega_n r)\right]_{a_0}^{1} + \omega_n \int_{a_0}^{1} r\mathcal{R}_n(r)\mathrm{d}r, \tag{4.42a}$$

$$I_5 := \int_{a_0}^{1} \mathcal{R}_n(r)\mathrm{d}r = \frac{\left[\mathcal{A}Y_0(\omega_n r) - \mathcal{B}J_0(\omega_n r)\right]_{a_0}^{1}}{\omega_n \mathcal{B}}, \tag{4.42b}$$

$$I_6 := \int_{a_0}^{1} r\mathcal{R}_n(r)\mathrm{d}r = \left[\frac{\pi r}{2\omega_n}\left\{\left[J_1(\omega_n r) - \frac{\mathcal{A}}{\mathcal{B}}Y_1(\omega_n r)\right]\mathbf{H}_0(\omega_n r) - \left[J_0(\omega_n r) - \frac{\mathcal{A}}{\mathcal{B}}Y_0(\omega_n r)\right]\mathbf{H}_1(\omega_n r)\right\}\right]_{a_0}^{1}, \tag{4.42c}$$

$$I_7 := \int_{a_0}^{1} r^2\mathcal{R}_n(r)\mathrm{d}r = \left[\frac{r^2}{\omega_n}\left\{J_2(\omega_n r) - \frac{\mathcal{A}}{\mathcal{B}}Y_2(\omega_n r)\right\}\right]_{a_0}^{1}, \tag{4.42d}$$

and

$$I_8 := \int_{a_0}^{1} r^3 \mathcal{R}_n(r)\mathrm{d}r = \left[\frac{3r^2}{\omega_n}\left\{J_1(\omega_n r) - \frac{\mathcal{A}}{\mathcal{B}}Y_1(\omega_n r)\right\} - \frac{r^3}{\omega_n}\left\{J_0(\omega_n r) - \frac{\mathcal{A}}{\mathcal{B}}Y_0(\omega_n r)\right\}\right]_{a_0}^{1} - \frac{3}{\omega_n}\int_{a_0}^{1} r\mathcal{R}_n(r)\mathrm{d}r, \tag{4.42e}$$

where $\mathbf{H}_{\mathfrak{v}}(r)$ is the Struve function of order $\mathfrak{v}$. Similarly,

$$f_n = \frac{qI_5 + \dfrac{\sigma_b'}{1-a_0^2}\left(\dfrac{3}{2+\Gamma}I_6 + \dfrac{a_0^2}{\Gamma}I_4\right)}{I_1 + \dfrac{\mathcal{A}^2}{\mathcal{B}^2}I_2 - \dfrac{2\mathcal{A}}{\mathcal{B}}I_3}. \tag{4.43}$$

The analytical solution is then finally given by

$$u_s(r,t) = w(r,t) + v(r,t) = \frac{\sigma_b'}{a_0^2-1}\left(\frac{a_0^2}{\Gamma} - \frac{r^2}{2+\Gamma}\right) + \sum_{n=1}^{\infty}\left\{\left[\frac{f_n}{\omega_n}\left(1-e^{-\omega_n t}\right) + t_n e^{-\omega_n t}\right]\left[J_1(\omega_n r) - \frac{\mathcal{A}}{\mathcal{B}}Y_1(\omega_n r)\right]\right\}, \tag{4.44}$$

where the ω_n are the solutions to Equation (4.33), $\mathcal{A}$ and $\mathcal{B}$ are defined in Equations (4.32), and the t_n and the f_n are defined by Equations (4.41) and (4.43), respectively.

4.1.3 Early-time evolution of $u_s(a,t)$: fixed q

When driven via a fixed q we find a simple expression for $u_s(a,t)$ at early times,

$$u_s(a,t) \sim (q/a_0)t \tag{4.45}$$

for fixed q which is true for all models for both the constrained and unconstrained cylinders — we show this below.

4.1.3.1 Classical linear poroelasticity (L-k_0 model)

We can derive this result for the constrained and unconstrained cylinders for the L-k_0 model by considering Equation (4.22) for the constrained cylinder, or Equation (4.44) for the unconstrained cylinder, at early times. In general, the displacement at the inner boundary is given by

$$u_s(t, a_0) = \sum_{n=1}^{\infty} \left[\frac{f_n}{\omega_n^2} \left(1 - e^{-\omega_n^2 t} \right) \right] \left[J_1(\omega_n a_0) + c_2(\omega_n) Y_1(\omega_n a_0) \right], \tag{4.46}$$

where c_2 is defined in Equation (4.11) for the constrained cylinder or by Equation (4.34) for the unconstrained cylinder. For early times, $t \ll 1$ and therefore

$$\exp(-\omega_n^2 t) \sim 1 - \omega_n^2 t + O(t^2), \tag{4.47}$$

so that

$$u_s(t, a_0) \sim \sum_{n=1}^{\infty} t\, f_n \left[J_1(\omega_n a_0) - \frac{J_1(\omega_n)}{Y_1(\omega_n)} Y_1(\omega_n a_0) \right] = t \sum_{n=1}^{\infty} f_n \mathcal{R}_n(a_0) = t \left(\frac{q}{a_0} \right), \tag{4.48}$$

where the last inequality is given by Equation (4.17) for the constrained cylinder or Equation (4.38) for the unconstrained cylinder (*i.e.,* when $\sigma_b' \equiv 0$).

4.1.3.2 The nonlinear models (L-k_{KC}, Q-k_0, Q-k_{KC}, N-k_0 & N-k_{KC} models)

Again, for the constrained and unconstrained cylinders, the nonlinear models lead to the same prediction for $t \ll 1$ and $u_s \ll 1$ since they are all asymptotically equivalent to the fully linear model for small strains. Letting $t = \epsilon T$ and $u = \epsilon U$ for some functions T and U that are strictly order one, Equations (2.40–2.41) subject to Equations (2.25) and (2.22) reduce at leading order to

$$\frac{\partial U}{\partial T} = \frac{q}{r}. \tag{4.49}$$

At $r = a = a_0 + u_s(a,t) = a_0 + \epsilon U$, Equation (4.49) becomes at leading order

$$\left.\frac{\partial U}{\partial T}\right|_a = \frac{q}{a_0} \quad \Longrightarrow \quad U(a,T) = T\left(\frac{q}{a_0}\right) \quad \Longrightarrow \quad u_s(a,t) = t\left(\frac{q}{a_0}\right), \tag{4.50}$$

where we have applied the initial condition that $u_s(a,0) = 0$ which is the appropriate initial condition for both the unconstrained and constrained cylinders. Note that we assumed that $t \sim u_s \ll 1$ in the above after showing it to be the case for the L-k_0 model. However, since we know that for infinitesimal strains all models are asymptotically equivalent to the L-k_0 model, this is a valid assumption. Figure 4.7 shows the early-time behaviour for all models is well approximated by Equation (4.45).

4.1.4 Numerical solution method

We solve all of the nonlinear problems, as well as the L-k_0 model for fixed Δp, numerically. We do so by extending the method presented in Auton and MacMinn [6] by combining Chebyshev spectral collocation with the method of lines. That is, we discretise the spatial domain into the N Chebyshev points and then approximate spatial derivatives using a Chebyshev differentiation matrix [6]. We then integrate the resulting system of differential algebraic equations (DAEs) in time with `MATLAB` using `ode15s` [71, 72]. This Chebyshev pseudospectral method has proven to be more robust and accurate than classical finite volumes or finite differences, as well as more convenient for handling certain combinations of boundary and driving conditions (*e.g.*, fixed Δp with fixed radial effective stress at the outer boundary).

4.1.4.1 Fixed q

We next outline the implementation of the numerical scheme for fixed q. We denote the general form of Equations (2.40a) and (2.41a) via

$$M[u_s]\frac{\partial u_s}{\partial t} = F[u_s] + c[u_s]\frac{q}{r}, \tag{4.51}$$

where M, F, and c are continuous partial-differential operators in r. In Appendix B, we provide expression for M, F, and c for all models and boundary conditions for fixed q. Following the method of lines, we discretise u_s and r in space and, using first and second order Chebyshev differentiation matrices $\widehat{\boldsymbol{D}}_N$ and $\widehat{\boldsymbol{D}}_N^2$ of size $N \times N$ as defined in Equation (3.24), we discretise the operators M, F, and c. Below, we denote spatially discretised quantities with hats; vectors and matrices are additionally in bold.

For $a < r < b$, we then have a system of coupled ODEs in time. At $r = a$ and $r = b$, we enforce the spatially discretised boundary conditions, $\hat{B}^a(\hat{\boldsymbol{u}}) = \hat{B}_i^b(\hat{\boldsymbol{u}}) = 0$ for $i = 1, 2$ (*c.f.,* Equation (4.1)), which are algebraic in t. Together, these equations constitute a system of DAEs. At each time step, the domain deforms and we use Equations (2.31a) and (2.34a) as appropriate to update the grid. It is clear that $\hat{\boldsymbol{F}}(\hat{\boldsymbol{u}})$, $\hat{\boldsymbol{c}}(\hat{\boldsymbol{u}})$, and thus the right-hand side of Equation (4.51), are all vectors of length N. To enforce the boundary conditions, the first and last entries of the right-hand side must be $\hat{B}^a(\hat{\boldsymbol{u}})$ and $\hat{B}_i^b(\hat{\boldsymbol{u}})$, respectively. We express this system of DAEs using a mass matrix $\hat{\boldsymbol{M}}(\hat{\boldsymbol{u}})$, which is the Chebyshev spatial discretisation of $M[u_s]$. The mass matrix pre-multiplies the time derivative $\partial u_s/\partial t$ and enables us to enforce the boundary conditions ($\hat{B}^a(\hat{\boldsymbol{u}}) = \hat{B}_i^b(\hat{\boldsymbol{u}}) = 0$) by setting the first and last rows of $\hat{\boldsymbol{M}}(\hat{\boldsymbol{u}})$ identically equal to zero.

We integrate this system of DAEs in time in `MATLAB` using `ode15s`. When tractable, we provide the solver with an analytical Jacobian, $\hat{\boldsymbol{J}}$

$$\hat{\boldsymbol{J}} = \frac{\mathrm{d}}{\mathrm{d}\hat{\boldsymbol{u}}}\left(\hat{\boldsymbol{F}}(\hat{\boldsymbol{u}}) + \hat{\boldsymbol{c}}(\hat{\boldsymbol{u}})\frac{q}{\hat{\boldsymbol{r}}}\right), \tag{4.52}$$

accounting appropriately for the moving boundaries. Note that as the problem becomes more nonlinear, it is numerically beneficial to initialise the problem with a flow rate of zero and ramp this to the desired value of q over a short time (at most 10^{-5}). It is clear from the results that this does not impact the transient evolution for times greater than the ramping time. We use the same spatial discretisation as for the steady state problem, which has spectral accuracy, so the overall accuracy will be determined by the accuracy of the time-stepping performed by `ode15s`.

4.1.4.2 Fixed Δp

Driving with a fixed pressure difference Δp leads to an integro-PDE as q appears explicitly in the PDE (4.51) and q is related to Δp via Equation (2.35), which contains a spatial integral of $\partial u_s/\partial t$. In our Chebyshev framework, we discretise these integrals using Lobatto's integral formula, which allows us to incorporate them into the system of DAEs. From Lobatto's integration formula for Chebyshev polynomials[2] we derive

$$\int_a^b g(r)\,\mathrm{d}r \approx \frac{\pi}{N-1}\left(\frac{b-a}{2}\right)\sum_{k=1}^{N}(1-\hat{X}_k^2)^{\frac{1}{2}}\hat{g}_k(\hat{\boldsymbol{r}}) \tag{4.53}$$

for some function $g(r)$, $r \in [a,b]$, where $\hat{X}_k \in [-1,1]$ is the k^{th} Chebyshev point defined in Equation (3.22) and $\hat{\boldsymbol{r}}$ is the vector comprising $\hat{r}_j$ where

$$\hat{r}_j = \frac{b+a}{2} - \frac{b-a}{2}\hat{X}_j. \tag{4.54}$$

This derivation is detailed in Appendix C.

Rewriting Equation (4.51) using Equation (2.35) gives

$$M[u_s]\frac{\partial u_s}{\partial t} = F[u_s] + c[u_s]\left(\frac{\Delta p}{r\int_a^b \frac{1}{kr}\,\mathrm{d}r} + \frac{\int_a^b \frac{v_s}{k}\,\mathrm{d}r}{r\int_a^b \frac{1}{kr}\,\mathrm{d}r},\right). \tag{4.55}$$

[2]Note that this expression is derived from a generalised version of Chebyshev-Gauss quadrature as detailed in Appendix C

The solid velocity v_s is related to $\partial u_s/\partial t$ via Equations (2.17) for the L models and Equations (2.15b) and (2.16) for the Q and N models, and we again discretise these relations in terms of $\hat{\boldsymbol{u}}$, $\hat{\boldsymbol{r}}$, $\widehat{\boldsymbol{D}}_N$ and $\widehat{\boldsymbol{D}}_N^2$. Using Equation (4.53), we then express the relevant integral in Equation (4.55) as a finite sum of $\mathrm{d}\hat{\boldsymbol{u}}/\mathrm{d}t$. Similarly, the other integral in Equation (4.55) is readily approximated with Lobatto's integral formula. We incorporate the resulting sum of $\mathrm{d}\hat{\boldsymbol{u}}/\mathrm{d}t$ into a new mass matrix $\hat{\boldsymbol{m}}$, whose first and last rows are once again identically equal to zero. We then write the fully discretised system in the form $\hat{\boldsymbol{m}}(\hat{\boldsymbol{u}})\mathrm{d}\hat{\boldsymbol{u}}/\mathrm{d}t = \hat{\boldsymbol{f}}(\hat{\boldsymbol{u}})$, where $\hat{\boldsymbol{f}}(\hat{\boldsymbol{u}})$ is a vector of length N whose first and last entries are $\hat{B}^a(\hat{\boldsymbol{u}})$ and $\hat{B}_i^b(\hat{\boldsymbol{u}})$, respectively.

We use this method for all of the fixed Δp cases. As the problem becomes more nonlinear, $\hat{\boldsymbol{m}}$ becomes more complicated and it is again numerically beneficial to ramp Δp from zero to the desired value over a short time (at most 10^{-5}).

4.2 Results

We now consider the transient evolution of the deformation for different driving method (fixed Δp *vs.* fixed q), confinement (confined *vs.* unconfined), and geometry (varying a_0) for the six poroelastic model combinations derived in Chapter 2: L-k_0, L-k_{KC}, Q-k_0, Q-k_{KC}, N-k_0, and N-k_{KC}.

4.2.1 Fixed Δp *vs.* fixed q for a constrained thick-walled cylinder

We begin by considering the impact of driving method for the constrained thick-walled cylinder ($a_0 = 0.1$). To do so, we solve the problem for a fixed Δp and then again for the fixed value of q that results in the same steady state. We consider the time evolution of the deformation for this scenario in Figures 4.1–4.4. In Figure 4.1, we show the time evolution of all key quantities for the Q-k_{KC} model. In Figure 4.2, we examine the impact of model choice by considering the evolution of the displacement at the inner boundary for all six models; in Figure 4.3 we additionally show the evolution of the azimuthal effective stress

at the inner boundary for all six models. In Figure 4.4, we examine the time evolution of q when Δp is fixed, and of Δp when q is fixed, again for all six models. In Figure 4.5, we consider both the absolute characteristic evolution timescale, $t^\star$, and the characteristic evolution timescale normalised with the classical linear poroelastic characteristic evolution timescale, $t^\star/t^\star_{Lk0}$, for this geometry and boundary condition over a wide range of Δp and q values, again for all six models.

In Figure 4.1, we plot the evolution of all key quantities to steady state for the Q-k_{KC} model for fixed $\Delta p = 0.1$ (left column), and for the fixed $q \approx 0.052$ that leads to the same steady state (right column). For fixed Δp, ϕ_f (first row), u_s (second row), and σ'_θ (fourth row) show similar qualitative behaviours: for the majority of the Lagrangian radius $R := r(t) - u_s(r,t)$, these quantities evolve monotonically towards their steady-state values. Additionally, all of these quantities overshoot their steady-state values near the inner and outer boundaries. Near $R = a_0$, they overshoot once before relaxing towards their steady states; near $R = 1$, they overshoot once at early times and then again at intermediate times before relaxing towards their steady states. The cylinder effectively 'over-deforms' near both the free inner boundary and the confined outer boundary; as time progresses, this deformation relaxes. This overshoot implies that the largest stresses (*e.g.*, the maximum value of σ'_θ) occur at some intermediate time, rather than at steady state, which has implications for problems concerning material failure such as hydraulic fracturing. Note, however, that this overshoot does not occur for all values of a_0 (*cf.* Figures 4.6 and 4.10). The radial effective stress σ'_r (third row) mirrors this behaviour near $R = 1$. Near $R = a_0$, however, σ'_r initially decreases into strong compression before increasing to its tensile steady-state value. The pressure p has a fixed value at both boundaries by construction, $p(a) \equiv \Delta p$ and $p(b) \equiv 0$, and exhibits an approximately uniform interior value bracketed by sharp boundary layers at $R = a_0$ and $R = 1$ that spread with time, which is consistent with classical consolidation theory. These boundary layers imply that the deformation is initially focused near the boundaries, which is linked to the overshoot in deformation through mechanical

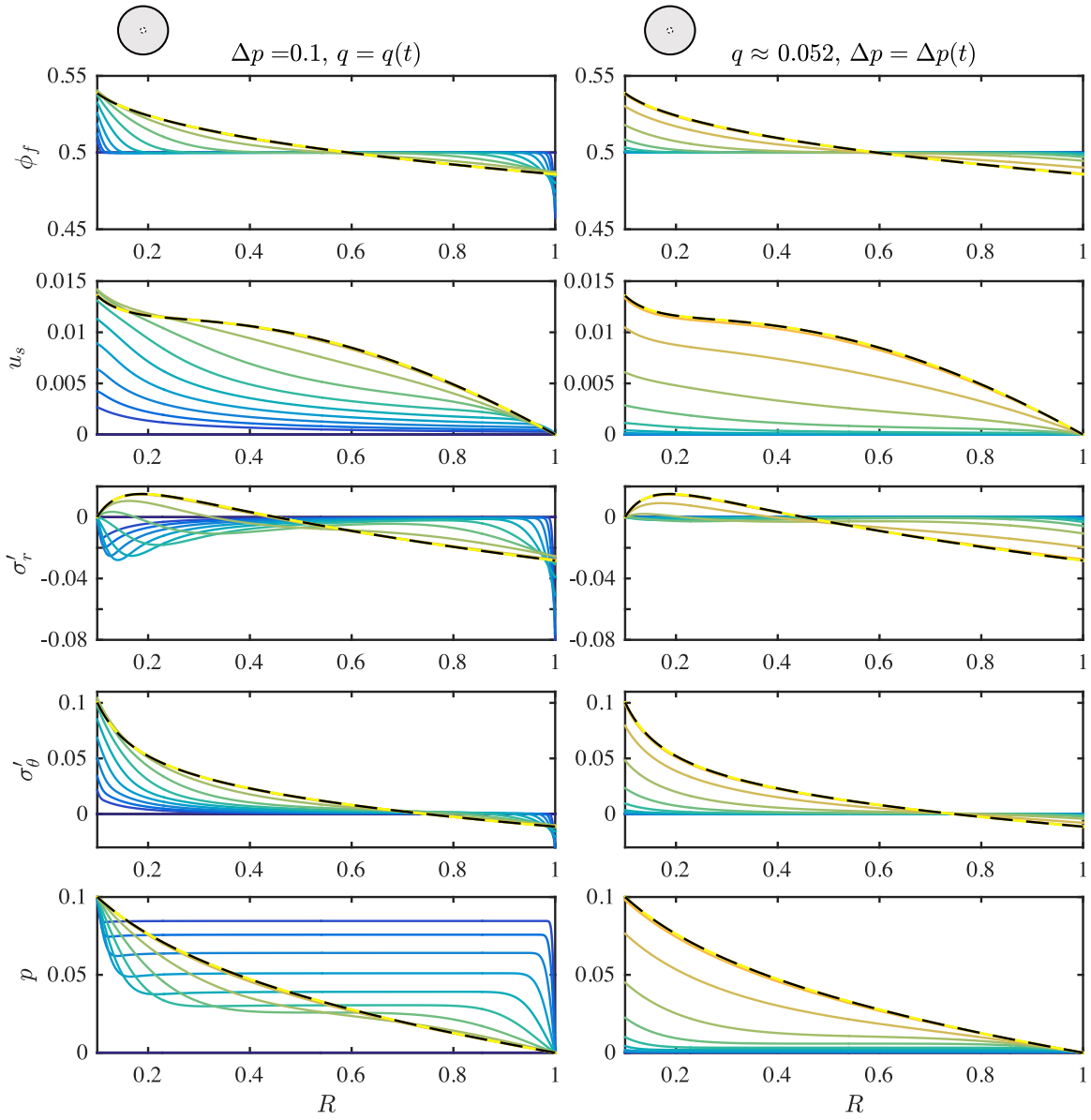

Figure 4.1: The time evolution of a constrained thick-walled cylinder ($a_0 = 0.1$) for the Q-k_{KC} model, where the flow is driven by fixed $\Delta p = 0.1$ (left column) or by the fixed $q \approx 0.052$ that leads to the same steady state (right column). We show the solution at twelve times, logarithmically spaced from $t = 10^{-5}$ (blue) to $t = 2.5$ (yellow). We also include the initial condition and the steady state for reference (solid and dashed black lines, respectively). We plot all quantities against the Lagrangian radial coordinate $R := r(t) - u_s(r, t)$. For this scenario, the evolution to the common steady state occurs much more quickly for fixed Δp than for fixed q. Additionally, some degree of non-monotonicity in time is evident in every quantity for fixed Δp, whereas all quantities except for σ'_r evolve monotonically for fixed q.

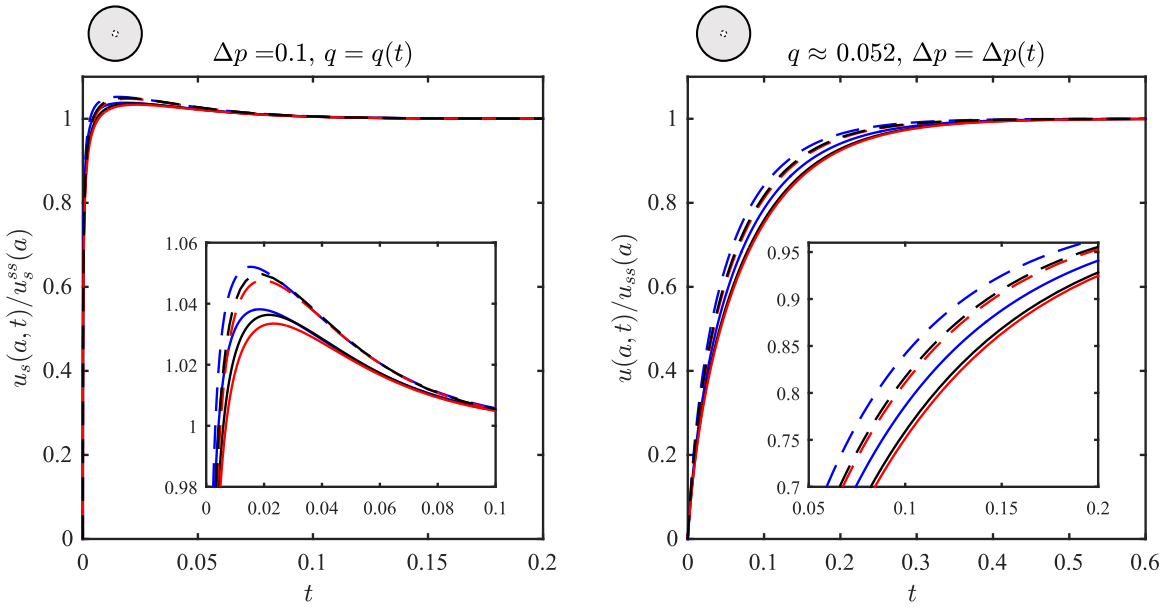

Figure 4.2: The time evolution of the normalised displacement at the inner boundary for all six models for the same scenario and parameter values as in Figure 4.1. We plot the L models (blue), Q models (black), and N models (red) for both constant permeability (solid lines) and Kozeny-Carman permeability (dashed lines). The insets highlight the differences between models at early times. All models exhibit the same qualitative behaviour, and the deformation evolves much more quickly in the fixed Δp case than in the fixed q case. In the fixed Δp case, nonlinear kinematics and nonlinear elasticity moderate the relative overshoot, whereas Kozeny-Carman permeability exacerbates it.

equilibrium (*cf*, Equation (2.12) and §3.2.3).

For fixed q, in contrast, the evolution is much slower and all quantities except for σ_r' evolve monotonically in time. The radial effective stress σ_r' decreases initially, such that it becomes strictly non-positive for some time before evolving towards its steady state by increasing into tension near the inner boundary and by decreasing further into compression near the outer boundary. The slower evolution timescale is a result of the fact that driving with fixed Δp leads to an initially large value of q that decreases towards its steady-state value, driving the material very aggressively at early times (*cf.* Figure 4.4, left); driving with fixed q, in contrast, leads to a initially small value of Δp that increases to steady state, driving the material more gently at early times (*cf.* Figure 4.4, right).

In Figure 4.2, we consider the normalised displacement at the inner boundary $\bar{u}^a := u_s(a,t)/u_s^{\text{ss}}(a)$ for all six models, where u_s^{ss} denotes the displacement at steady state such

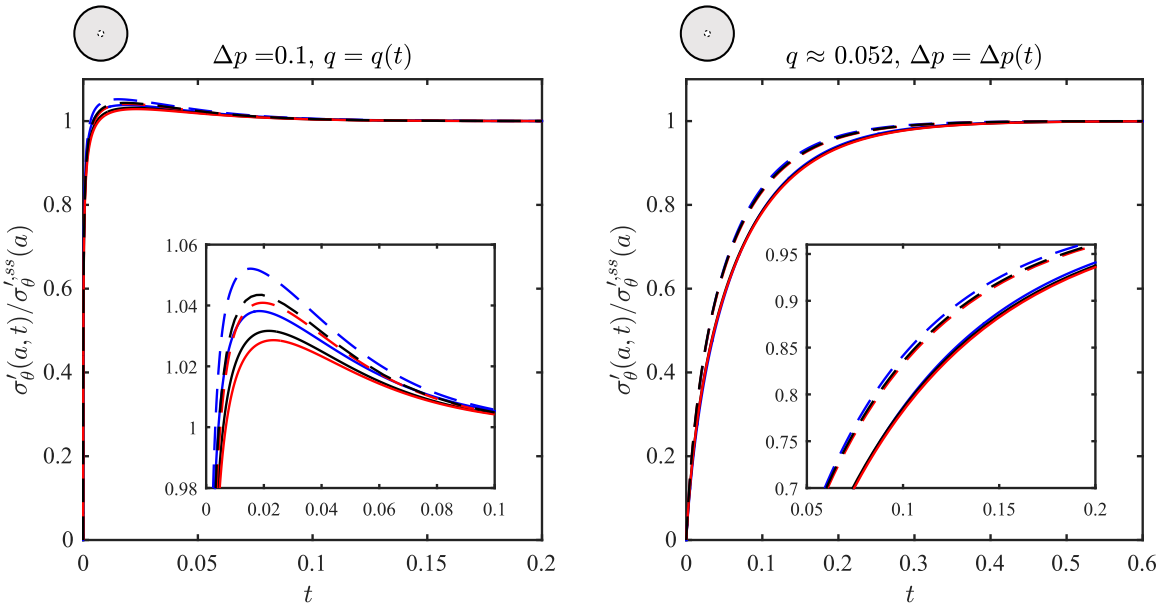

Figure 4.3: We reproduce Figure 4.2 but for the normalised azimuthal effective stress at the inner boundary for all six models and the same parameter values as in Figures 4.1 & 4.2. Line colours and styles are the same as those in Figure 4.2. Once again the inset highlights the differences between models at early times; all models exhibit the same qualitative behaviour as can be seen for $\bar{u}^a$ — an overshoot of $\sigma'_\theta(a,t)/\sigma'^{,ss}_\theta(a)$ for early times when the model is driven by a fixed Δp but with a monotonic approach to steady state when driven via a fixed q.

that $\bar{u}^a \to 1$ as $t \to \infty$. Note that we compare each model to *its own* steady state, and the six steady states are not the same (*cf* §3.2). We also compare the evolution of $\bar{u}^a$ for fixed Δp (left) *vs.* fixed q (right). For fixed Δp, all six models exhibit the overshoot noted above. This overshoot is most pronounced in the -k_{KC} models. Within each permeability grouping, the L models show the most relative overshoot and the N models the least, implying that both rigorous kinematics and nonlinear elasticity moderate the relative overshoot, while deformation-dependent permeability exacerbates it. For fixed q, the ordering of the models is the same as for fixed Δp, but the evolution timescale is clearly much slower. These results suggest that, for a constrained thick walled cylinder, driving method has much stronger impact than model choice on both the qualitative nature and the timescale of the transient evolution.

Similarly, in Figure 4.3, we present the transient evolution of the azimuthal effective stress, $\sigma'_\theta(a,t)$ at the inner boundary for a constrained cylinder, once again normalised

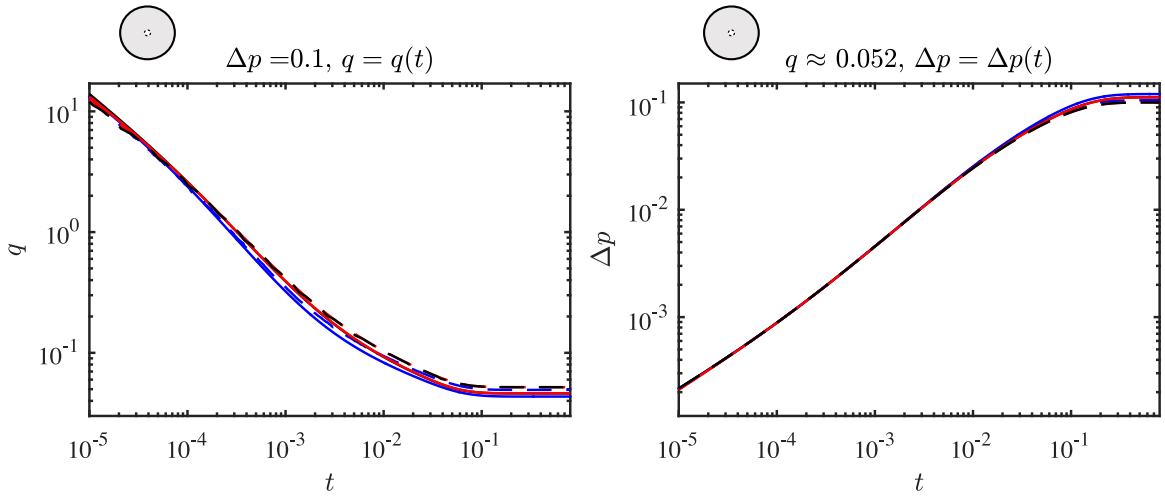

Figure 4.4: The time evolution of q for fixed Δp (left), and of Δp for fixed q (right), for all six models and for the same scenario and parameter values as in Figures 4.1 and 4.2. Line colours and styles are also the same as in Figure 4.2. For fixed Δp, $q(t)$ is initially very large and decreases towards steady state; for fixed q, $\Delta p(t)$ is initially very small and gradually increases towards steady state. These opposite evolutions result from the same physics.

by each model's steady state value, $\sigma'^{,ss}_\theta(a)$. The normalised azimuthal effective stress at the inner boundary $\bar{\sigma}^a_\theta := \sigma'_\theta(a,t)/\sigma'^{,ss}_\theta(a)$ exhibits the same behaviour as $\bar{u}^a$ for these parameters, in the sense that both are non-monotonic in time for fixed Δp for all models, with a maximum at some intermediate time, and both are monotonic in time for fixed q. Unlike for $\bar{u}^a$, for fixed q, the choice of permeability law is the most significant factor contributing to the evolution of $\bar{\sigma}^a_\theta$, with the k_{KC} models all evolving quicker than the k_0 models.

In Figure 4.4, we examine the time evolution of q for fixed Δp (left), and of Δp for fixed q (right). For fixed Δp, $q(t)$ is initially very large and then decreases towards steady state; this behaviour is qualitatively the same for all models. The flow rate $q(t)$ decreases with time because the solid moves radially outward at early times, so a relatively large fluid velocity is needed to generate the required pressure difference. The solid slows over time as deformation increasingly resists further motion, and the fluid velocity slows accordingly. This leads to an initially large flow rate that decays towards the steady-state value, for which the solid is stationary. For fixed q, the reverse occurs: the solid and the fluid both

contribute to the fixed total flux at early times, moving together such that only a relatively small Δp is needed. As the solid slows, the relative velocity of the fluid must increase to preserve the fixed total flux and the necessary Δp increases. At steady state, the solid is stationary, the fluid provides the entire flux, and Δp is largest.

In Figure 4.5, we consider the absolute characteristic evolution timescale of the various models shown in Figures 4.1–4.4 (top row) and to highlight the degree to which nonlinearity accelerates or decelerates the evolution relative to the L-k_0 model we consider the characteristic evolution timescale normalised by the characteristic evolution timescale of the L-k_0 model (bottom row). We define the evolution timescale as the time $t^\star$ at which the root-mean-square of the relative difference from steady state is equal to 0.2 — that is, we use interpolation to find the value $t^\star$ such that

$$\sqrt{\frac{1}{N}\sum_{j=1}^{N}\left[\frac{u_s^{ss}(\hat{r}_j)-u_s(\hat{r}_j,t^\star)}{u_s^{ss}(\hat{r}_j)}\right]^2}=0.2, \tag{4.56}$$

where the steady state $u_s^{ss}(\hat{r}_j)$ is determined via the method as presented in Chapter 3. Note that this metric is weakly influenced quantitatively by the fact that our solutions are defined on a Chebyshev grid, but this is consistent across all cases and makes no qualitative difference in the results. Similarly we define $t^\star$ for the L-k_0 model to be $t^\star_{Lk0}$ such that $t^\star$ normalised by $t^\star_{Lk0}$ is denoted $t^\star/t^\star_{Lk0}$.

For the L-k_0 model, the timescale is independent of driving strength for both fixed Δp and fixed q. This is due to our definition of $t^\star$ in terms of the relative difference from steady state and the fact that, for the L-k_0 model, $u_s(r,t)$ and $u_s^{ss}(r)$ are proportional to Δp for fixed Δp, and proportional to q for fixed q. In the latter case, this is obvious from the transient analytical solutions for the constrained and unconstrained cylinders (§4.1.2). Although $t^\star$ is independent of driving strength for the L-k_0 model, the driving method, boundary condition, and geometry (*i.e.*, a_0) all have significant impacts on the timescale (*cf.* Figure 4.9, top row).

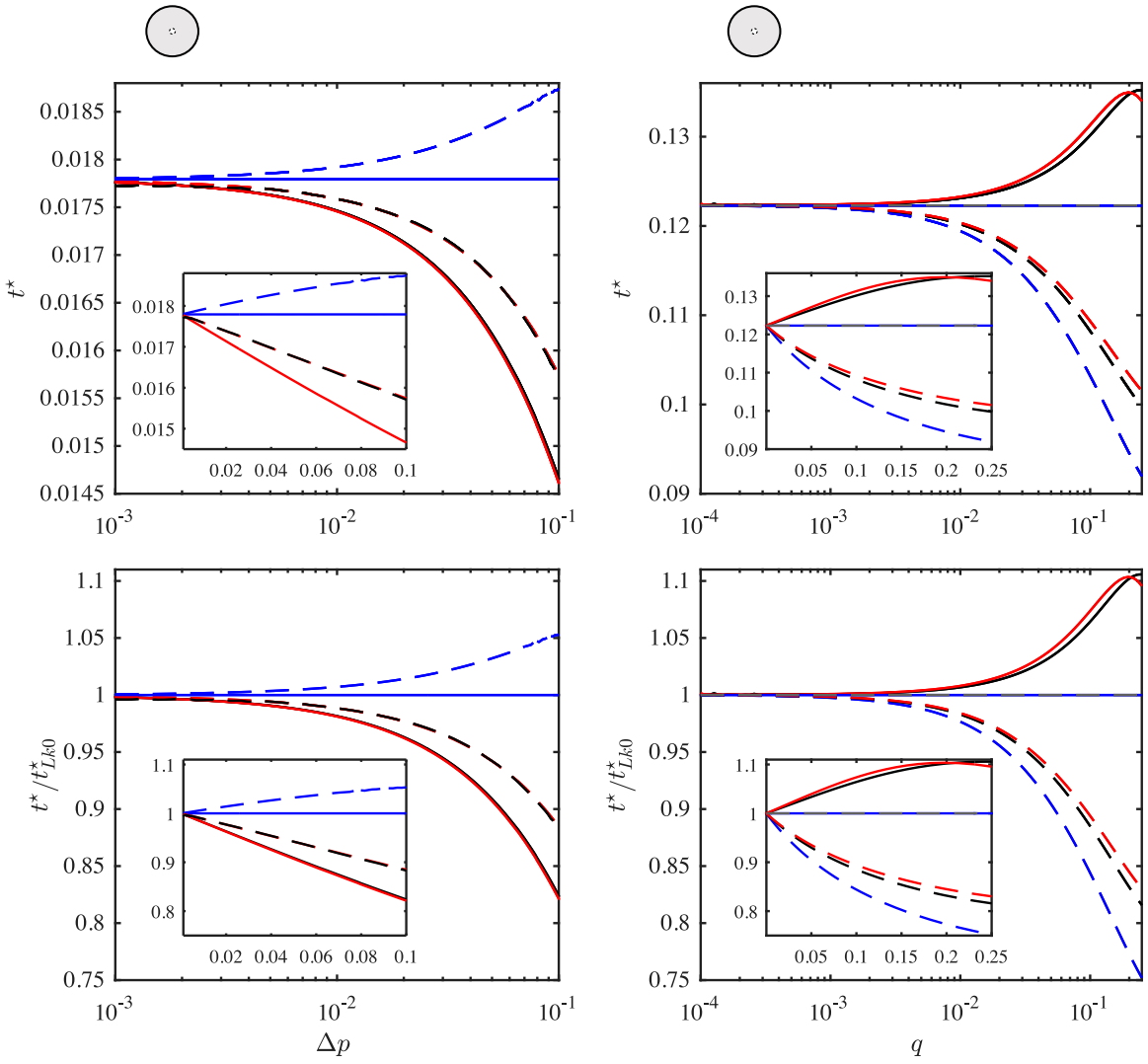

Figure 4.5: The absolute characteristic evolution timescale $t^\star$ (top row), and the characteristic evolution timescale normalised by the characteristic evolution timescale for the L-k_0 model $t^\star/t^\star_{Lk0}$ (bottom row) of the constrained thick-walled cylinder ($a_0 = 0.1$) for all six models as a function of Δp (left column), and of q (right colum). Line colours and styles are the same as in Figures 4.2–4.4; we additionally show the analytical dynamic L-k_0 fixed q solution (right, dashed grey lines). For the L-k_0 model, $t^\star$ is independent of driving strength in both cases. For the Q and N models, $t^\star$ is very similar. For the fixed Δp cases, $t^\star$ is roughly one order of magnitude smaller than for the fixed q cases. The direct comparison of $t^\star$ to $t^\star_{Lk0}$ explicitly highlights the extent to which nonlinearity accelerates or decelerates the transient evolution in each case relative to classical linear poroelasticity.

For the other models, $t^\star$ is determined by the complex combination of many different competing mechanisms. For example, Figure 4.5 shows that the inclusion of Kozeny-Carman permeability increases $t^\star$ relative to the corresponding constant-permeability models for the fixed Δp cases, but that the opposite is true for the fixed q cases (*i.e.*, the -k_{KC} models evolve slower than the corresponding -k_0 models for fixed Δp, but faster for fixed q).

In general, we expect an increase or decrease in the effective permeability of the medium to lead to a faster or slower evolution (a decrease or increase in $t^\star$), respectively, because the characteristic poroelastic timescale is inversely proportional to permeability, $\tilde{T}_{\mathrm{pe}} \propto 1/\tilde{k}$ (*cf.* §2.5). However, the permeability field is transient and non-uniform. The development of localised regions with significantly reduced permeability can act as a global bottleneck because of the harmonic nature of combining permeabilities in series, leading to a slower evolution (increase in $t^\star$) even when the permeability increases in most of the domain. In the fixed q case, the effective permeability of the medium increases monotonically in time and therefore the impact of deformation-dependent permeability is to speed up the evolution (decrease $t^\star$). In the fixed Δp case, in contrast, the sudden development of a sharp, low-porosity boundary layer at the outer boundary dominates the effective permeability of the medium, leading to a strong transient decrease, and this slows the evolution (increases $t^\star$). This effect is particularly strong because the boundary layer significantly overshoots the steady-state porosity.

Nonlinear kinematics enter the problem in several ways competing ways. One major difference between the L models (linearised kinematics) and the Q and N models (rigorous kinematics) is the relationship between $\partial u_s/\partial t$ and v_s. The linearised relationship is $\partial u_s/\partial t = v_s$, whereas the exact relationship is $\partial u_s/\partial t = (1/\lambda_r)v_s$. Since $v_s = q/r + k(\phi_f)(\partial p/\partial r)$ in all models, the additional factor of $1/\lambda_r = 1 - \partial u_s/\partial r$ typically accelerates the deformation in the Q and N models relative to the L models because, in most cases, $\partial u_s/\partial r < 0$ (*cf.* Figures 4.1 and 4.6), and therefore $1/\lambda_r > 1$. That is, lin-

earisation leads to an underestimation of $\partial u_s/\partial t$ in the L models and we would therefore expect the introduction of nonlinear kinematics to speed up the evolution (decrease $t^\star$). A second effect is that the inner boundary condition is applied at the moving inner boundary in the Q and N models, but at the original position of the inner boundary in the L models. For the fixed Δp case, the outward motion of the inner boundary should increase the flow rate q (applying the same Δp across a thinner wall leads to a larger q), which would imply a faster evolution (smaller $t^\star$) in the Q and N models relative to the L models. For the fixed q case, the outward motion of the inner boundary should lead to a lower Δp across the material (driving the same q through a thinner wall requires a smaller Δp), which would imply a slower evolution (larger $t^\star$) in the Q and N models relative to the L models. These latter effects, although clearly weak, are visible in Figure 4.4. A third effect is simply that the Q and N models deform more than the L models for this scenario (*cf.* Chapter 3); as a result, it takes longer for the Q and N models to reach a certain relative difference from their respective steady states (larger $t^\star$). These three effects combine such that nonlinear kinematics speed up the deformation for fixed Δp (the first effect dominates), but slow down the deformation for fixed q (the second and third effects dominate) (Figure 4.5).

Finally, we consider the role of nonlinear elasticity. The L and Q models use linear elasticity, whereas the N models uses Hencky elasticity. The elasticity law determines the relationship between u_s and $\partial p/\partial r$, and also plays a role in the boundary conditions. Under uniform uniaxial deformation, Hencky elasticity is stiffer than linear elasticity in compression and softer than linear elasticity in tension (*cf.* Figure 2.2). The classical poroelastic timescale is inversely proportional to stiffness, $\tilde{T}_{\mathrm{pe}} \propto 1/\tilde{\mathcal{M}}$ (*cf.* §2.5), so we would expect the N models to deform more quickly than the L and Q models in uniaxial scenarios dominated by compression, and more slowly than the L and Q models in uniaxial scenarios dominated by tension. It is not straightforward to extrapolate these expectations to a biaxial problem featuring a mix of tension and compression, but we note that the N models do evolve slightly more quickly than the Q models in the fixed Δp case, which

features strong transient compression in σ_r' near both boundaries; this is consistent with the general explanation above.

Although the precise value of q that corresponds to a given Δp is dependant on the model choice, we note that for all models $\Delta p = 0.1$ approximately corresponds to $q \approx 0.05$. For these values of Δp and q, for both driving mechanisms the slowest model evolves in $\sim 90\%$ of the time of its classical linear poroelastic counterpart and the fastest evolving $\sim 5\%$ quicker. For all models for $\Delta p < 0.1$, $t^\star$ increases (or decreases) approximately linearly with Δp, and for $q < 0.05$, $t^\star$ increases (or decreases) approximately linearly with q. Hence we infer that for a fixed driving strength the overall relative acceleration or deceleration of $t^\star$ due to model choice is approximately the same whether the system is driven via fixed q or Δp.

4.2.2 Impact of constraint on thin-walled cylinders for fixed q

We now consider the impact of the outer boundary condition on the transient evolution of the problem. We do so by comparing the behaviour of an unconstrained thin-walled cylinder to that of a constrained thin-walled cylinder ($a_0 = 0.85$) for fixed q. In Figure 4.6, we show the time evolution of all key quantities for the Q-k_{KC} model. In Figure 4.7, we examine the impact of model choice by considering the evolution of the displacement at the inner boundary for all six models. In Figure 4.8, we consider the characteristic evolution timescale, $t^\star$, and the normalised characteristic evolution timescale, $t^\star/t^\star_{Lk0}$, for this geometry by comparing these boundary conditions over a wide range of q values for all six models.

In Figure 4.6, we plot the evolution of all key quantities to steady state for the Q-k_{KC} model for fixed $q = 0.25$ for an unconstrained thin-walled cylinder (left column) and for a constrained thin-walled cylinder (right column) ($a_0 = 0.85$). For the unconstrained cylinder, all quantities except for σ_r' evolve monotonically in time. The radial effective stress σ_r' initially decreases into compression throughout the entire interior of the cylinder,

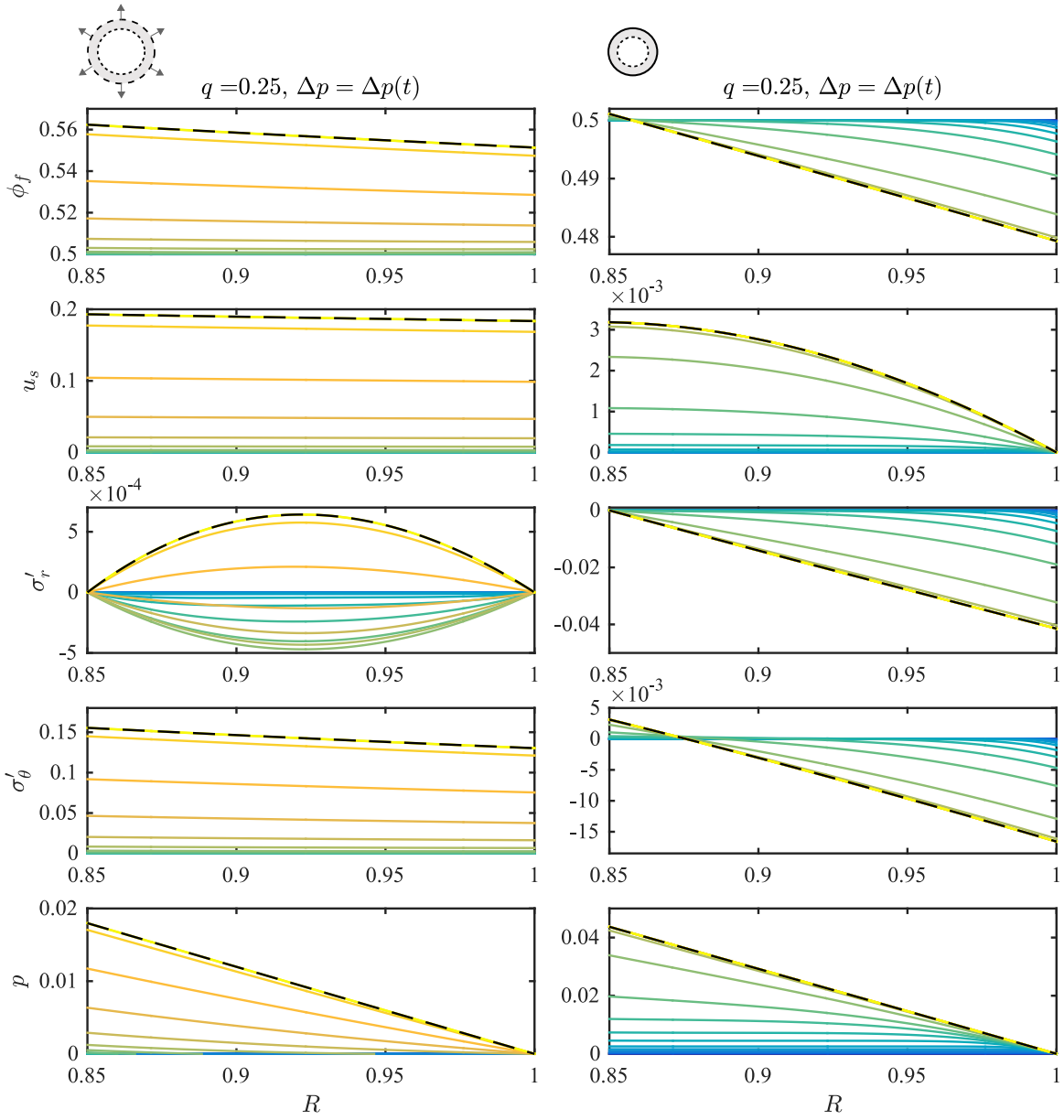

Figure 4.6: The time evolution of an unconstrained thin-walled cylinder (left column) and a constrained thin-walled cylinder (right column), for the Q-k_{KC} model ($a_0 = 0.85$), where the flow is driven by fixed $q = 0.25$. We show the solution at a range of times, logarithmically spaced from $t = 10^{-7}$ (blue) to $t = 10$ (yellow). We also show the initial condition and the steady state for reference (solid and dashed black lines, respectively). The constrained cylinder reaches steady state much more quickly than the unconstrained cylinder.

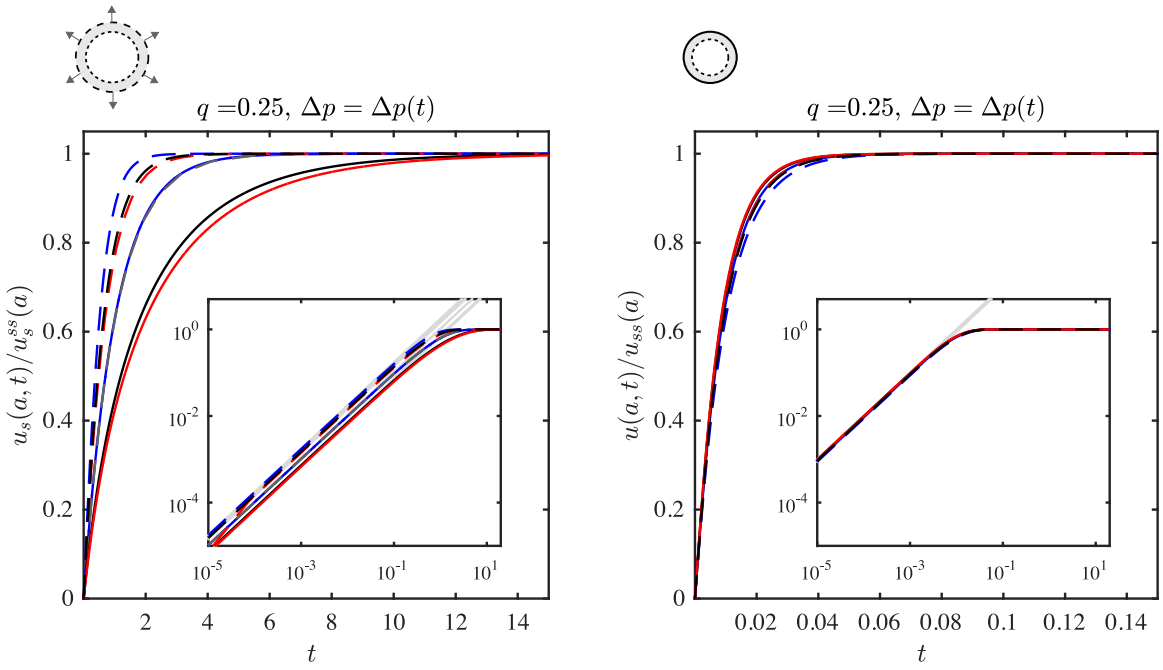

Figure 4.7: The time evolution of the normalised displacement at the inner boundary for all six models for the same scenario and parameter values as in Figure 4.6. Line colours and styles are the same as in Figure 4.2–4.5, although we additionally show the analytical dynamic L-k_0 solution (dashed grey lines). The insets show the evolution on a logarithmic scale, clearly demonstrating that $u_s(a,t) \sim (q/a_0)t$ for $t \ll 1$ (solid grey lines) in all cases. Note that the time evolution of the unconstrained cylinder is about two orders of magnitude slower than that of the constrained cylinder, and that model choice is much more important for the unconstrained cylinder than for the constrained cylinder for these parameters.

before eventually increasing to its tensile steady state. Note, however, that $||\sigma'_r||$ is several orders of magnitude smaller than $||\sigma'_\theta||$. For the constrained cylinder, all quantities except for σ'_θ evolve monotonically in time, and σ'_θ evolves monotonically except in a small region near the transition from tension to compression. More importantly, all quantities evolve much more quickly than for the unconstrained cylinder.

In Figure 4.7, we again consider the normalised displacement at the inner boundary $\bar{u}^a$ for all six models, comparing the evolution of $\bar{u}^a$ for the unconstrained (left) and constrained (right) cylinders. The evolution is monotonic for all models in both cases, but about two orders of magnitude faster for the constrained cylinder than for the unconstrained cylinder. Plotting $\bar{u}^a$ on a logarithmic scale (insets) highlights its early-time evolution, which is shown to be $u_s(a,t) \sim (q/a_0)t$ for $t \ll 1$ for all a_0 (see §4.1.3). For the unconstrained

cylinder, the Q-k_0 and N-k_0 models clearly evolve much more slowly than the L-k_0 model and all -k_0 models are much slower than the -k_{KC} models. Note also that the models are in the same relative order as in Figure 4.2. For the constrained cylinder, in contrast, the rate is relatively insensitive to model choice and the ordering of the models is reversed.

In Figure 4.8, we consider the characteristic evolution timescale $t^\star$ (top row) and the normalised characteristic evolution timescale $t^\star/t^\star_{Lk0}$ (bottom row) for a thin-walled cylinder for all six models as a function of q. For the unconstrained cylinder (left column), $t^\star$ increases with q for the Q-k_0 and N-k_0 models, but decreases with q for the -k_{KC} models. This suggests that, for an unconstrained cylinder, nonlinear kinematics speed up the deformation whereas deformation-dependent permeability slows down the deformation. The underlying physical mechanisms are the same as those discussed in regard to Figure 4.5. The various impacts of these mechanisms are easier to interpret in this case because the permeability increases strongly throughout the material, $\partial u_s/\partial r$ is strictly negative, and the inner radius moves substantially. These various impacts are also much stronger in this case because the deformation is much larger, and they are further amplified as q increases— for models except the L-k_0 model, $t^\star$ changes by several-fold over this range of q. The Q and N models are again very similar, suggesting that the elasticity law again plays a relatively minor role. For the constrained cylinder (right column), all of these effects are reversed in direction and much smaller in magnitude, with $t^\star$ changing by up to about 10% over this range of q, again for models except the L-k_0 model. This is straightforward to interpret: the permeability decreases strongly almost everywhere, and the displacement is two orders of magnitude smaller than for the unconstrained cylinder. For the L-k_0 model, $t^\star$ is independent of q for both unconstrained and constrained cylinders. Note that the constrained cylinder evolves about two orders of magnitude faster than the unconstrained cylinder, which is simply due to the fact that the unconstrained cylinder deforms substantially more in total. Via consideration of $t^\star/t^\star_{Lk0}$ it is unequivocal that model choice impacts $t^\star$ far more for the unconstrained cylinder than for the constrained cylinder. For example, for the

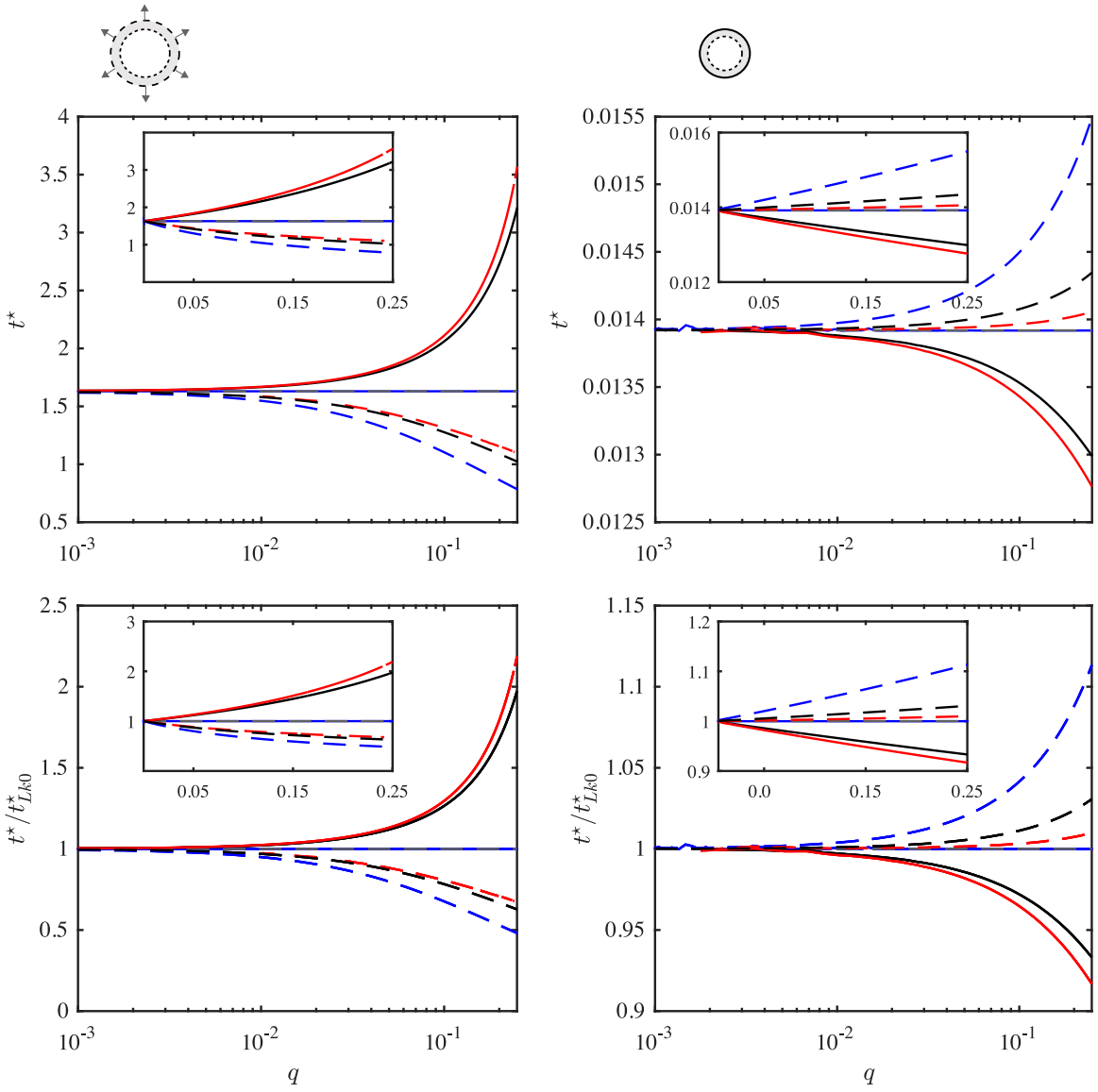

Figure 4.8: The evolution timescale $t^\star$ of the thin-walled cylinder ($a_0 = 0.85$) for all six models for unconstrained (left column) and constrained (right column) cases (top row) and the normalised evolution timescale $t^\star/t^\star_{Lk0}$ (bottom row). Line colours and styles are the same as in Figures 4.2–4.5 and 4.7. The evolution timescale of the L-k_0 model is again independent of driving strength (*c.f.*, Figure 4.5). For the unconstrained cylinder, $t^\star$ increases strongly with q for the Q-k_0 and N-k_0 models and decreases strongly with q for all of the -k_{KC} models; for the constrained cylinder, these effects are reversed in direction and much smaller in magnitude. We note that for the unconstrained cylinder model choice impacts the timescale to a far greater extent than for the constrained cylinder.

largest driving $q = 0.25$, the slowest unconstrained model takes more than twice as long to evolve as its classical linear poroelastic counterpart, while the slowest constrained model takes only $\sim 11\%$ longer than its classical linear poroelastic counterpart.

4.2.3 Impact of geometry and driving method on time evolution

In Figure 4.9, we plot the characteristic evolution timescale $t^\star$ (top row) and the normalised characteristic evolution timescale $t^\star/t^\star_{Lk0}$ (bottom row) against a_0 for all six models for constrained cylinders for fixed Δp (left column) and fixed q (centre column), and for unconstrained cylinders for fixed q (right column). Note, firstly, that $t^\star$ is a strong function of a_0 even for classical linear poroelasticity (the L-k_0 model). This is evident from the time-dependent component of the analytical solution, which is a nontrivial function of a_0. For the constrained cylinder for fixed Δp, model choice appears to be relatively unimportant relative to geometry; the evolution is slowest for thick walls and fastest for thin walls, but $t^\star$ has a modest local maximum around $a_0 \approx 0.2$. For the constrained cylinder for fixed q, model choice is more important; the evolution is still fastest for thin walls, but $t^\star$ now has a global maximum for some intermediate wall thickness and the amplitude and position of this maximum varies strongly from model to model. Importantly, the relative roles of deformation-dependent permeability, nonlinear kinematics, and nonlinear elasticity are nontrivial and depend strongly on a_0—this suggests that the conclusions drawn above for constrained cylinders are valid only for thick walls. It is clear that even given $t^\star_{Lk0}$ the different facets of nonlinearity added to attain each of the other models combined with the precise a_0 impact $t^\star$ in a non-trivial way, which is not the case for the unconstrained cylinder. For the unconstrained cylinder for fixed q, $t^\star$ increases monotonically with a_0 for all models except the N-k_0 model, which exhibits a weak interior minimum at $a_0 \approx 0.05$. The fast evolution occurs for thick-walled cylinders and the slowest for thin-walled cylinders, and the ordering of the models is independent of a_0. As a result, the conclusions drawn above for unconstrained cylinders should be qualitatively valid for all a_0. Finally,

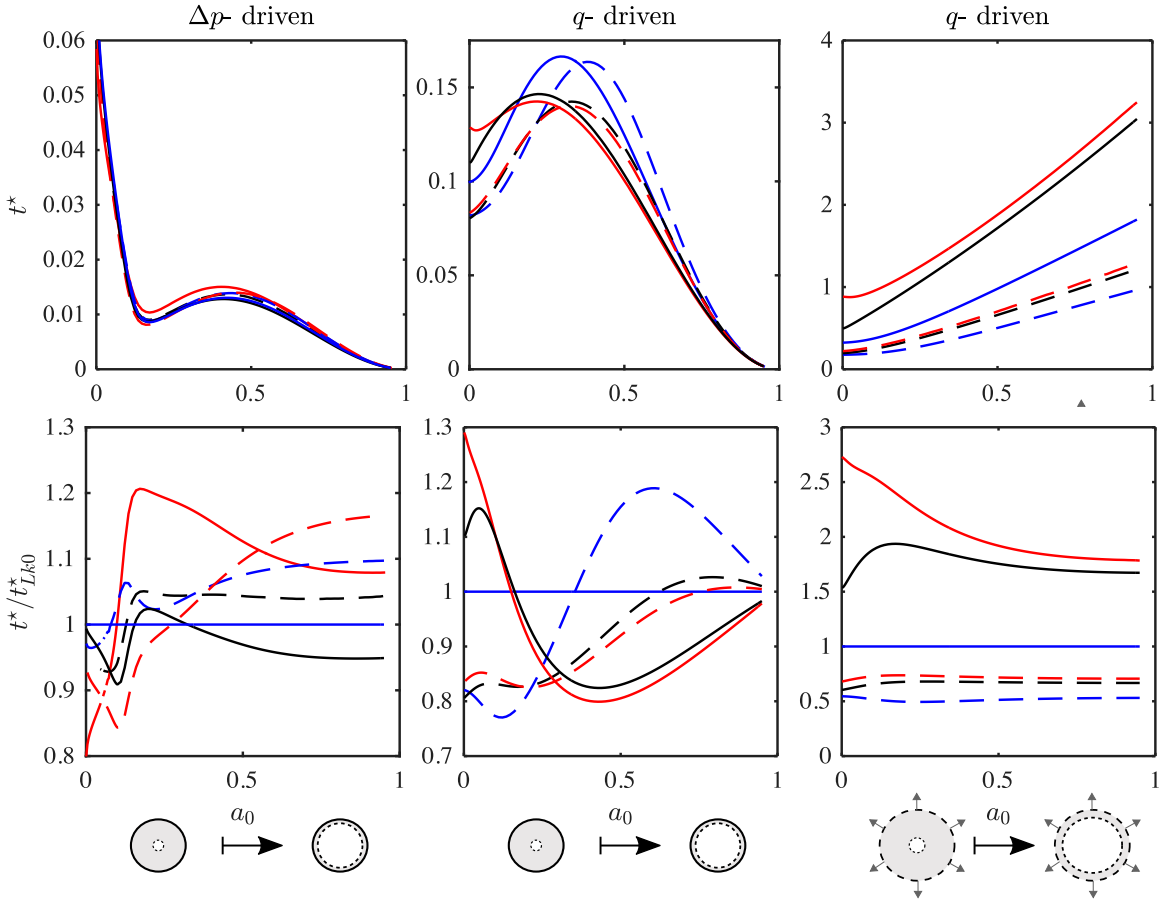

Figure 4.9: The impact of a_0 on $t^\star$ (top row) and on $t^\star/t^\star_{Lk0}$ (bottom row) for a constrained cylinder driven by fixed $\Delta p = 0.05$ (left column), a constrained cylinder driven by fixed $q = 0.2$ (centre column), and an unconstrained cylinder driven by fixed $q = 0.2$ (right column), and for all six models in both cases. Line colours and styles are the same as in Figures 4.2–4.5 and 4.7–4.8. For the constrained cylinder, the evolution is fastest for thin walls; for the unconstrained cylinder, it is fastest for thick walls. Note also that $t^\star$ depends non-monotonically on a_0 for the constrained cylinder, and is particularly sensitive to model choice for fixed q. Plotting $t^\star/t^\star_{Lk0}$ against q and Δp highlights the extent to which nonlinearity accelerates or decelerates the transient evolution in each case relative to the L-k_0 model.

note that $t^\star$ is about an order of magnitude larger for constrained cylinders for fixed q than for constrained cylinders for fixed Δp, and about an order of magnitude larger again for unconstrained cylinders for fixed q (except when the walls are very thick, in which case the dynamics of constrained and unconstrained cylinders for fixed q are very similar see §4.2.4 below).

4.2.4 Impact of constraint on a thick-walled cylinder for fixed q

In Figure 4.10, we show the time evolution of an unconstrained thick-walled cylinder (left column) and a constrained thick-walled cylinder (right column), both for $a_0 = 10^{-4}$ and driven by fixed $q = 0.25$. We present this figure to complement Figure 3.5 where we noted very similar steady state behaviour for the constrained and unconstrained thick-walled cylinders — the evolution in these two cases is also very similar; as such, applications that would be naturally modelled with an unconstrained annulus could be approximated with a constrained annulus provided the radius is sufficiently large, simplifying the problem by reducing the number of free/moving boundaries.

4.3 Conclusion

Despite being central to important problems in a variety of fields, radial poroelastic deformations remain relatively poorly understood. Here, we have presented the first systematic exploration of the effects of nonlinearity, driving method, and geometry on the transient evolution of these deformations. We have shown that the radial geometry results in non-trivial biaxial deformations and a strong dependence on wall thickness that render this problem much more complex and nuanced than the corresponding uniaxial scenario [61].

We first illustrated the strong qualitative and quantitative impacts of driving method (fixed Δp *vs.* fixed q). For a constrained cylinder with thick walls, we showed that driving with fixed Δp can lead to non-monotonicity in the time evolution of the displacement at

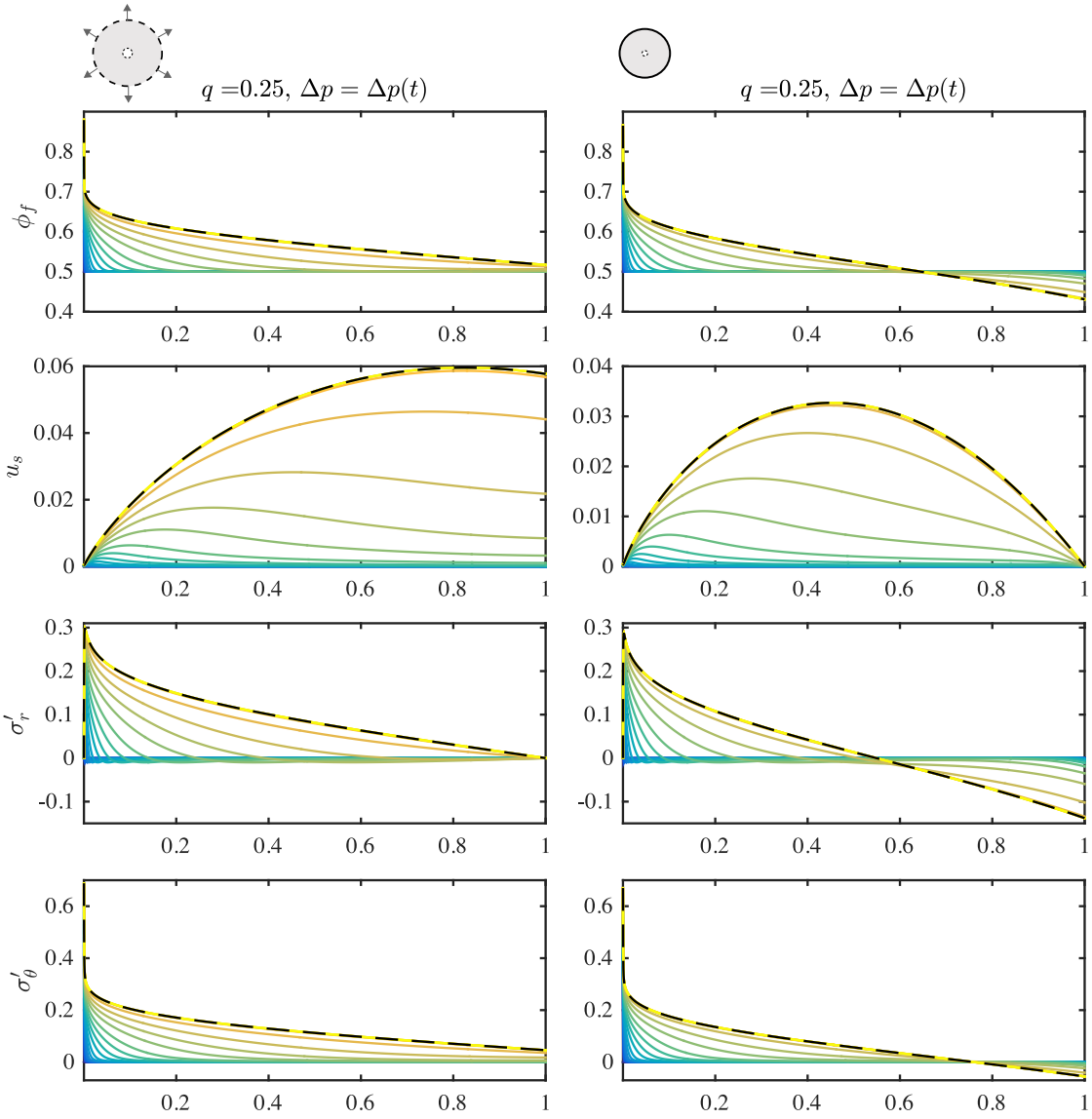

Figure 4.10: The time evolution of a very thick-walled unconstrained cylinder (left column) and a very thick-walled constrained thick-walled cylinder (right column) for the Q-k_{KC} model. Both cylinders have $a_0 = 10^{-4}$ and are driven by fixed $q = 0.25$. We show the solutions at times logarithmically spaced from $t = 10^{-7}$ (blue) to $t = 10$ (yellow). For reference, we also show the steady state (black dashed lines). The evolution is qualitatively very similar, as are the steady states.

the inner boundary for all models, even classical linear poroelasticity (Figure 4.2). This does not occur when driving with fixed q. We found that this non-monotonicity was also reflected in the azimuthal effective stress, again even for linear poroelasticity, which has implications for applications involving material failure such as hydraulic fracturing. We considered the details of these deformations in the context of a model that includes rigorous nonlinear kinematics and deformation-dependent permeability, but with the simplification of linear elasticity (Q-k_{KC}) (Figure 4.1). We found that this scenario evolves much more quickly when driven by fixed Δp as opposed to fixed q, and that this is true for all models across a wide range of driving values (Figure 4.5). We also found that, when Δp is fixed, $q(t)$ is initially very high and decreases towards the steady-state value; when q is fixed, in contrast, $\Delta p(t)$ is initially very small and increases towards the steady-state value (Figure 4.4).

We also investigated the impact of constraint at the outer boundary (unconstrained *vs.* constrained). For a thin-walled cylinder, we found that a constrained cylinder evolves about two orders of magnitude more quickly than an unconstrained cylinder (Figures 4.6–4.8). We also found that the evolution timescale of an unconstrained thin-walled cylinder is dominated by kinematics and deformation-dependent permeability (Figures 4.7- 4.8), despite the fact that the steady state is dominated by kinematics and elasticity (§3.2).

Finally, we showed that the evolution timescale depends strongly on wall thickness for all models, for both driving conditions, and for both constrained and unconstrained cylinders (Figure 4.9). For constrained cylinders, the evolution timescale is non-monotonic in wall thickness for all models and for both driving conditions. For unconstrained cylinders driven by fixed q, the relative contributions of nonlinear kinematics, deformation-dependent permeability, and nonlinear elasticity also depend very strongly on wall thickness.

Having extensively studied the poroelastic response of an annulus to fluid injection in Chapters 3 and 4, in Chapter 5 we extend the model to consider the poroelasto-plastic response of a cylinder to fluid injection. Additionally we introduce a simple mechanism

to smoothly transition between an impermeable material and a fully permeable material. Unlike for the poroelastic case, where we systematically explored the parameter space considering a wide range of geometries, we now limit our consideration to geomechanical applications and as such a very thick-walled annulus ($a_0 = 10^{-4}$). Additionally, we restrict our considerations to the resulting (poro)elasto-plastic steady-state problem.

Chapter 5

Large poroelasto-plastic deformations due to fluid injection from a borehole

A clear understanding of the failure of granular materials due to fluid injection has direct relevance to a variety of applications in geomechanics, including borehole stability, cavity expansion and 'fracking' for the recovery of oil or natural gas from shales. These problems involve injecting fluid into a long cylindrical hole in the shallow subsurface; modelling this scenario requires consideration of the constitutive and kinematic behaviour of the soil or rock. Due to the granular nature of soils and sedimentary rocks, these are often modelled as plastic solids, although purely elastic deformations are sometimes assumed for simplicity. Similarly, soils and rocks are intrinsically porous and are usually saturated making a permeable model most appropriate; that said, the effect of fluid flow is often neglected with the material being modelled as undrained. Granular materials are likely to undergo large deformations and as such the kinematics of the material play a key role and their linearisation under a small strain assumption is likely to be invalid. An additional complicating factor is that during the creation of these cavities, fine grains may be forced into the surrounding pore space, reducing the local permeability. This reduction in local permeability is often helpful as it enables a fixed fluid volume to occupy the opening and keep the cavity open.

Special wall-building chemicals are often injected into newly formed boreholes to coat the walls for this purpose.

A borehole is a long cylindrical cavity in the subsurface from which the original material has been removed by drilling. Typically, boreholes are drilled in soils, sands, clays or poorly consolidated sedimentary rock such as sandstone, which are inherently ductile and porous. Their walls can be cased with metal, either with or without perforations, or uncased and self-supporting. Problems in borehole integrity are concerned with predicting and preventing borehole collapse after drilling or during subsequent operations (*e.g.*, during fluid injection or extraction). The stability of a borehole depends on many factors, including the state of stress in the material before drilling, the orientation of the borehole, and the loading to which the borehole is subjected. This problem has been considered in numerous studies [*e.g*, 32, 33, 81, 102–106] although all the studies make some modelling simplifications. Detournay and Fairhurst [33] and Wang and Dusseault [103] assume the boreholes are drilled in an impermeable material while Detournay and Cheng [32] assume that the soil or rock surrounding the cavity behaves purely poroelastically. Wang [102], Wang and Dusseault [105] and Risnes et al. [81] do all account for ductility and permeability, the latter two additionally allowing the permeable material to fail plastically in one plane and then in another plane, according to two distinct ratios of the induced stresses. That said, all these studies linearise under an infinitesimal strain assumption despite the inclusion of plasticity which intrinsically enables large displacements and strains in the plastic region.

In cavity expansion, a borehole-like cavity is created by radially-outward mechanical displacement of material around the insertion point. Cavity expansion is a classical problem in geotechnical engineering, with relevance to pile-driving and penetrometer testing. Since soils are weak and the deformations are large, this is typically modelled with plasticity theory [23, 28, 47, 99, 111, 112]. Carter et al. [23], Vesic [99] and Yu and Houlsby [112] all model the problem of cavity expansion in a semi-infinite domain while Yu [111] extends the model to that of a finite domain. All these studies treat the kinematics of the material near

the cavity wall rigorously, but focus on strictly mechanical loading, essentially modelling the material as impermeable despite the fluid saturated pore space of most soils, sands and clays in the subsurface.

In fracking, fluid is injected into hydrocarbon-bearing rocks, usually shales, in order to induce fractures around the injection point which provide hydraulic access deeper into the reservoir, allowing gas to be collected from a larger region of the rock [34, 39, 75]. Fracking relies on the brittle failure of shale, but the mechanical properties of shale depend strongly on the composition [21, 34, 80]; many hydrocarbon-bearing shales are known to have high clay content and may behave in a ductile manner [26, 89, 95, 97]. Both laboratory and field data suggest that the ductility of shales can have an important impact on the success of fracking, but this is currently poorly understood [21, 39]. Models for fracking almost always neglect the impact of ductility within the shales and model the rock as either elastic or poroelastic. Although shales have an extremely low permeability, they are nonetheless permeable and despite this, many classical models for fracking assume the rock to be impermeable [*e.g.,* 31, 48, 103, 106]. There is a significant qualitative difference between fluid-driven deformation in porous materials and mechanically driven deformation due to the fact that mechanical loads act only at the boundary, whereas the fluid pressure acts throughout the material [70].

In this chapter, we develop a kinematically rigorous model for fluid injection from a borehole into an elastic–perfectly-plastic cohesive granular medium. Specifically, we consider a cylinder subject to fluid pressurisation in the central cavity and within this context we develop a mechanism for transitioning smoothly between a fully permeable and an impermeable material by essentially including a skin or coating of varying permeability at the cavity wall. We isolate the effect of fluid injection from the pre-existing compressive stress state that exists in the subsurface by subtracting a compressive reference state from the model. We study the effect that both the inclusion of plastic failure and partial permeability have on the resulting deformation field. We find that plastic failure enables larger

deformations which in turn result in a divergence of the nonlinear models from the models whose kinematics are linearised in the plastic region. The elastic region is insensitive to these changes. We find that for a given total stress, the solid deformation is maximised in the fully permeable limit. As such, even for the poroelasto-plastic models for a cavity pressurisation, the various constitutive and kinematic nonlinearities only become significant as the loading mechanism transitions away from mechanical loading towards an effective fluid-induced body force felt throughout the material.

5.1 Theoretical Model

We provide a simplified model for the fluid-driven expansion of a borehole in the subsurface. We model the subsurface as a cylinder of uniform cohesive granular material and the borehole as a concentric cylindrical hole within the material. The subsurface is subjected to a compressive pre-existing tectonic stress field, which is typically characterised via its principal values and directions. In relatively flat areas, it is common to assume that one of these is vertical and due to the weight of the overburden (the material above). This means that the other mutually perpendicular stresses are horizontal. It is likely that the three principal stresses will differ and that the ordering of their magnitudes will be dictated by the tectonic behaviour in the area. That said, the largest and smallest principal stresses typically differ by less than one order of magnitude [12, 48]. Thus for simplicity, we assume each circular cross-section of the domain of uncompressed radius b_0 to be in plane strain and subject to a compressive radial stress such that the in-plane principal stresses are isotropic and of magnitude σ_b'.

To model the reference state (*i.e.,* the transition $A1 \mapsto A3$, Figure 5.1) we simply remove a cylinder of material of radius a^{ref} (such that if $\sigma_b' \equiv 0$ then $a^{\text{ref}} \equiv a_0$) from the stressed cylindrical domain of radius b^{ref}, and case the resulting hole with a permeable casing such that fluid flow into the cylinder from the borehole is unobstructed and the

stresses in the remaining material are unchanged.

To model the effects of fluid injection we consider the fluid-driven expansion of a borehole in a stressed granular material (Figure 5.1, $M1 \mapsto M3$). We assume that the effects of the injection are felt only locally, such that the pressure vanishes and the stresses tend to a constant far-field value for finite b. Thus, as before, we consider fluid injection into the annulus $a \leq r \leq b$ subject to plane strain. The inner (borehole) radius, elastic-plastic interface and outer radius at $r = a$, $r = s$ and $r = b$, respectively, all expand (or contract) due to fluid injection and imposed σ_b' so that the positions of a, s and b at steady state are a priori unknown. We assume that the material yields from the inner boundary such that the material behaves plastically in the region $a \leq r \leq s$ and elastically for $s < r \leq b$.

We present the radially symmetric plane-strain model in dimensionless form, now denoting *dimensional* quantities with a breve $\breve{\cdot}$ (see §2.5 and §5.1.1). The presentation of the model decomposes into kinematics and constitutive laws, the former of which is presented in full in §2 and briefly discussed below in §5.1.2; the latter we present in §5.1.3 in relative detail. We only consider the steady state problem and thus neglect time-dependence.

5.1.1 Scaling

We adopt the same scalings and dimensionless parameters as detailed in §2.5, characterising the model by Equations (2.36) and (2.38) and additionally by the friction φ and dilation ψ angles (see §5.1.4) and the dimensionless cohesion between grains of the solid skeleton (see §5.1.4)

$$c := \frac{\breve{c}}{\breve{\mathcal{M}}}, \tag{5.1}$$

where the p-wave modulus is now denoted by $\breve{\mathcal{M}}$ in lieu of just $\mathcal{M}$ for consistency. Similarly, from now we will denote Lamé's first parameter by $\breve{\Lambda}$ in lieu of just Λ. Note that as well as characterising the line source via a fixed dimensionless flow rate q or fixed dimensionless pressure difference Δp, we may now also fix a dimensionless applied total stress

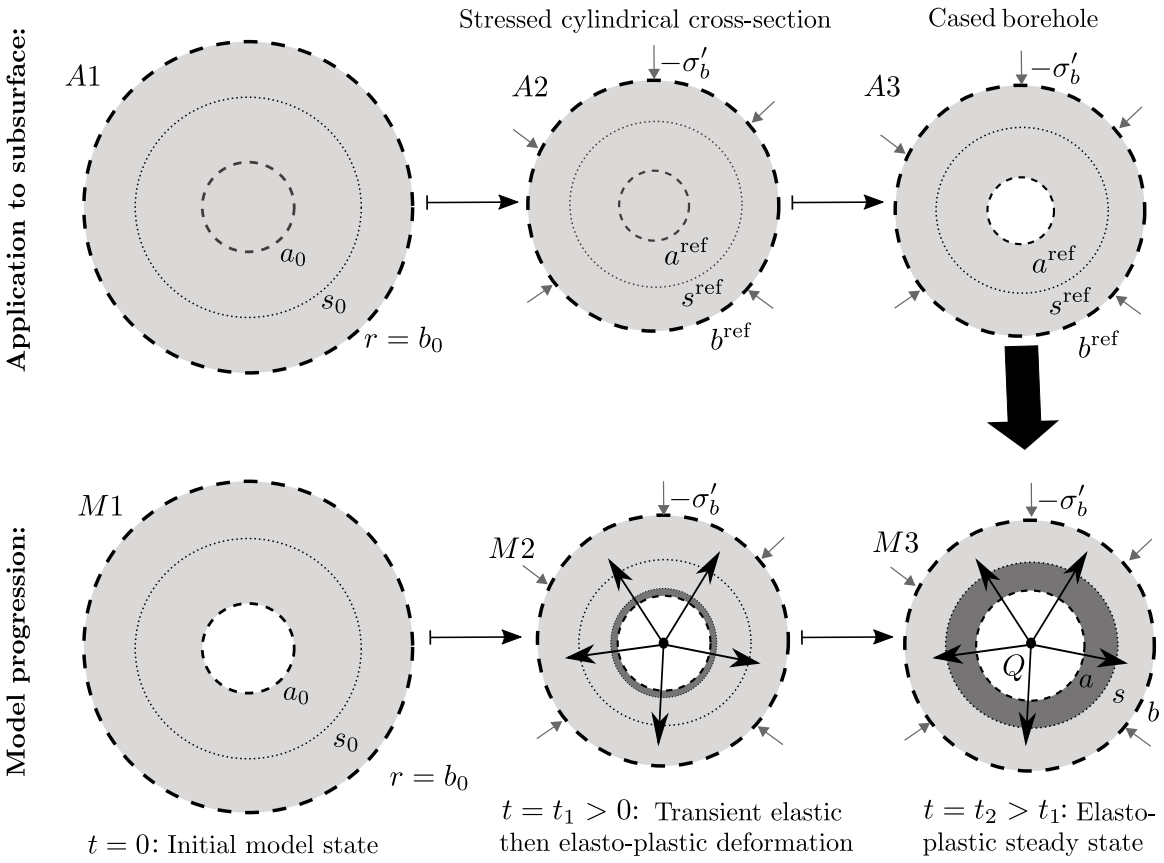

Figure 5.1: $A1$–$A3$: A simple model of the subsurface — a cylinder in plane strain. We first depict each circular cross-section 'at the point of sedimentation' (*i.e.,* an unstressed, undeformed circle — $A1$), which is then subjected to a uniform radial compressive effective stress of magnitude σ_b', such that the material is assumed to deform purely elastically ($A2$). A concentric cylindrical section is then removed and replaced with a permeable casing such that the flow into the remaining annulus of material is unobstructed and the stresses and deformation are unchanged from $A2$ ($A3$). $M1$–$M3$: Elasto-plastic expansion of a borehole (white) driven by radially outward fluid flow. Here, we show the initial configuration ($M1$), the deformed configuration at some intermediate time t_1, for which the annulus has just begun to yield plastically ($M2$), and the configuration at a later time t_2 such that the annulus is in steady state ($M3$). The initial configuration is not physical but is the 'initial state' for the plastic model. The inner and outer radii $a(t)$ and $b(t)$ expand or contract over the course of the deformation, and the inner plastic (dark grey) and outer elastic (light grey) regions are separated by a sharp boundary at $r = s(t)$. As in $A2$ and $A3$, we subject the outer radius $b(t)$ to an axisymmetric radial effective stress of $-\sigma_b'$, where we take tension to be positive. We also include the reference and initial positions for a and s (dashed and dotted lines, respectively). We focus on the transition $A3 \mapsto M3$.

at the inner cavity wall,

$$\sigma_a := \frac{\breve{\sigma}_a}{\breve{\mathcal{M}}}. \tag{5.2}$$

5.1.2 Kinematics, Darcy's law and mechanical equilibrium

Due to the inclusion of plasticity, we need to consider the governing kinematic equation in terms of the stress, since we do not have a direct relationship between stress and strain in the plastic region as we do within the elastic region. At steady state Equations (2.13) and (2.35) combine and simplify to give

$$\frac{\mathrm{d}p}{\mathrm{d}r} = -\frac{q}{r}, \tag{5.3}$$

and hence we can re-write Equation (2.12) as

$$\frac{\mathrm{d}\sigma'_r}{\mathrm{d}r} + \frac{\sigma'_r - \sigma'_\theta}{r} = -\frac{q}{r}. \tag{5.4}$$

This is purely a result of kinematics, mechanical equilibrium and Darcy's law and thus holds throughout the entire domain.

5.1.3 Constitutive laws: elasticity

Elastic deformations are quasi-static and reversible. Although plasticity allows for large deformations, the criteria for plastic yield (§5.1.4) restricts the magnitude of allowable stresses in the elastic region; thus it makes sense to consider small elastic displacements (§5.5). Hence we assume linear elasticity as defined in §2.2.2 (Equations 2.23 –2.25).

5.1.4 Constitutive laws: plasticity

Plastic deformations are path-dependent and irreversible. Plastic failure implies that, once the state of stress exceeds a threshold, some fraction of any additional strain energy will

be dissipated through irreversible rearrangements as opposed to being stored elastically. The simplest form of plasticity is perfect plasticity, in which the material properties are assumed to remain constant after yield and all additional strain energy is dissipated [46]. The threshold that defines the transition from elastic to plastic behaviour is known as a yield criterion. For granular materials, this is typically based on the idea of internal Coulomb-like friction. This implies that the effective shear stress τ' anywhere within the material must be strictly less than a specified fraction of the corresponding effective normal stress σ' for the deformation to remain elastic. For perfect plasticity, τ' is enforced to be equal to this fraction of σ' after yield. For a cohesive granular material, it is standard to additionally include a yield strength c due to the cohesion between the grains. The simplest cohesive-frictional yield criterion is the cohesive Mohr-Coulomb criterion, $|\tau'| \leq -\sigma \tan' \varphi + c$, where φ is the friction angle [28]. Through basic geometry, we can express this in terms of the principal effective stresses[1] ($\sigma'_1 \geq \sigma'_2 \geq \sigma'_3$) via a yield function

$$\mathcal{F}_{1,3} := \alpha\sigma'_1 - \sigma'_3 - y \tag{5.5}$$

where

$$\alpha := \frac{1+\sin(\varphi)}{1-\sin(\varphi)} \quad \text{and} \quad y := \frac{2c\cos(\varphi)}{1-\sin(\varphi)}. \tag{5.6}$$

such that if $\mathcal{F}_{1,3} < 0$ the material remains elastic while if $\mathcal{F}_{1,3} = 0$ the material flows plastically; as soon as equality is first achieved, we enforce $\mathcal{F}_{1,3} \equiv 0$ locally thereafter. Taking $\varphi = 0$ ($\alpha = 1$) provides the Tresca yield criterion (see Appendix D for explicit analytical Tresca solutions).

We take the three principal stresses to be σ'_r, σ'_θ, and σ'_z and we assume that before injection the material is uniformly, isotropically stressed in plane strain, such that[2] $\sigma'_r = \sigma'_\theta = \sigma'_b$ and $\sigma'_z = \frac{2\Gamma\sigma'_b}{1+\Gamma} \leq \sigma'_b$.

[1]The principal effective stresses are the eigenvalues of the effective stress tensor, with σ'_1 and σ'_3 being largest (most tensile) and the smallest (least tensile), respectively.

[2]For all physically reasonable parameters $\Gamma \in (0,1)$ which gives $\frac{\Gamma}{1+\Gamma} < \frac{1}{2}$ (see Appendix G).

It is commonly assumed that a cylinder in plane strain yields according to

$$\mathcal{F}_{\theta,r} := \alpha\sigma'_\theta - \sigma'_r - y \leq 0, \tag{5.7}$$

which requires that locally $\sigma'_\theta > \sigma'_z > \sigma'_r$ [103, 104]. This has been heuristically justified for an impermeable annulus [112]. We examine this assumption in detail in Appendix F and find that for a sufficiently 'strong' annulus relative to the compressive state to which it is subject — that is, $y(b^2 - a^2) > -2b^2\sigma'_b$— and for $\alpha\nu > 1$, where ν is Poisson's ratio, and additionally subject to some common assumptions, that the cylinder will fail exclusively subject to Equation (5.7).

Further, we assume the strain everywhere can be additively decomposed into elastic and plastic components [28],

$$\varepsilon = \varepsilon^{\mathrm{e}} + \varepsilon^{\mathrm{p}}, \tag{5.8}$$

where the superscripts e and p denote the elastic and plastic components of the strain, respectively. Stored elastic energy is associated with the elastic component of the strain, which is related directly to the effective stress via the elasticity law. The energy that has been dissipated is associated with the plastic component of the strain which has no direct connection to the effective stress; instead, the evolution of the plastic strain is described by a plastic flow law. Note that although strain decomposes into elastic and plastic components, there is one unique stress field.

For a perfectly-plastic metal under a Tresca yield condition, an associated flow law leads to plastic flow that is volume-conservative. However, the associated flow law for a Mohr-Coloumb material dictates that the material will undergo volumetric expansion (dilation) at the constant angle that induced yield, φ. Granular materials do dilate, but associated flow typically overestimates this dilation [111, 114]. We therefore adopt a non-associated flow law under which the material dilates at a constant angle $\psi < \varphi$ after yield

[111]. We express the flow law as

$$\beta\dot{\varepsilon}_r^{\mathrm{p}} + \dot{\varepsilon}_\theta^{\mathrm{p}} = 0, \tag{5.9}$$

where

$$\beta = \frac{1+\sin(\psi)}{1-\sin(\psi)} \tag{5.10}$$

and the overdot denotes the material time derivative (*i.e.*, $\dot{\varepsilon}_r = \partial\varepsilon_r/\partial t + \boldsymbol{v}_s \cdot \nabla\varepsilon_r$). Taking $\beta = \alpha$ ($\psi = \varphi$) provides the associated flow law for the cohesive Mohr-Coulomb yield criterion; taking $\beta = 1$ ($\psi = 0$) provides the associated flow law for the Tresca yield criterion.

5.1.5 Initial and boundary conditions $(M1 \mapsto M3)$

We once again assume that prior to injection the fluid pressure p_0 is uniform taking $p_0 = 0$. We take the initial porosity to be uniform and equal to the reference porosity $\phi_{f,0}$ and the solid to be relaxed, with both the solid and the fluid at rest.

5.1.5.1 Inner boundary

At the inner cavity wall, we enforce the partial permeability mechanism via the introduction of the 'permeability-load' parameter ζ, which allows us to control how the total applied stress at the inner cavity wall $\sigma_a := \sigma_r(a) = \sigma_r'(a) - \Delta p$ is being supported by the fluid and solid continuum. We liken this to considering a partially permeable thin weak skin or coating on the cavity wall, whose permeability we can control; the presence of the skin leads to a partitioning of this pressure between the fluid and the solid, such that the fluid pressure drops by some amount across the skin and the skin then exerts an effective stress on the solid at the cavity wall. We define $\zeta \in [0,1]$ such that we may continuously vary the boundary from impermeable ($\zeta \equiv 0$) to fully permeable ($\zeta \equiv 1$) (*i.e.,* the hypothetical skin mentioned above goes from impermeable, $\zeta \equiv 0$, to 'infinitely permeable', $\zeta \equiv 1$). Note

that ζ is distinct to the constant permeability k_0.

We drive this system with fluid via either a fixed flow rate q or fixed total stress σ_a. For a fully permeable material it is easiest to drive the deformation via a fixed q; however for $\zeta \not\equiv 1$ it is better to prescribe σ_a in lieu of q. Subsequently, we only present the solution for the general case $\zeta \not\equiv 1$ for fixed σ_a — the fully-permeable fixed-q case can be reproduced via setting $\zeta \equiv 1$ and $\sigma_a \equiv -q \ln\left(\frac{b}{a}\right)$, but is also presented in full in Appendix E.

A fixed total applied stress at the inner cavity wall leads to two conditions at the inner boundary,

$$\sigma_r'(a) = \sigma_a' = (1-\zeta)\sigma_a \tag{5.11a}$$

and

$$p(a) = \Delta p = -\zeta \sigma_a, \tag{5.11b}$$

as we take $p(b) = p_0 \equiv 0$. Note that q appears explicitly in Equation (5.4) and thus we use Equation (3.4) and Equation (5.11b) to express q in terms of σ_a with

$$q = -\frac{\zeta \sigma_a}{\ln\left(\frac{b}{a}\right)}. \tag{5.12}$$

Note that we expect $\sigma_a < 0$ when a fluid is being injected.

As before, the inner boundary is also a material boundary, and as such we have a kinematic condition on the displacement given by

$$u_s(a) = a - a_0. \tag{5.13}$$

5.1.5.2 The elastic-plastic interface

We assume that $a \leq s < b$, so that the annulus is not entirely plastic and hence the outer boundary conditions will always be applied to the elastic region[3]. We must also impose

[3]Note that the problem becomes over-constrained and thus ill-defined once the material has yielded entirely.

boundary conditions at the elastic-plastic interface to enforce continuity of radial stress and displacement,

$$u_s(s^+) = u_s(s^-) \quad \text{and} \quad \sigma_r'(s^+) = \sigma_r'(s^-), \tag{5.14a}$$

where s^- denotes $r = s$ as approached from within the plastic region ($a \leq r \leq s$) and, likewise, s^+ denotes $r = s$ as approached from within the elastic region ($s \leq r \leq b$). Finally, the effective stresses in the elastic region must be at the point of yield at $r = s^+$,

$$\alpha\sigma_\theta'(s^+) - \sigma_r'(s^+) = y. \tag{5.14b}$$

5.1.5.3 Outer boundary

At the outer boundary we impose a constant radial effective stress[4],

$$\sigma_r'(b) = \sigma_b', \tag{5.15a}$$

which means that the outer boundary is also a free boundary requiring the kinematic condition given by Equation (2.34a). We also present the solution for a fully permeable material subject to a no displacement outer boundary condition (Equation (2.33a) —see Appendix E.2.2).

5.2 Governing equations and model summary

5.2.1 The transition $M1 \mapsto M3$: ODE & boundary conditions for u_s in elastic region

In the elastic region, we use Equation (2.24) to eliminate the stresses in Equation (5.4), and additionally use Equation (5.12) to eliminate q in lieu of σ_a, leading to an ordinary

[4]Also note that this is equivalent to $B_2^b[u_s] \equiv 0$, as defined in Equation (4.1), because this condition is always applied to the elastic solution for which we have an explicit relationship between stress and strain.

differential equation (ODE) in u_s for the elastic region

$$\frac{\mathrm{d}^2 u_s}{\mathrm{d}r^2} + \frac{1}{r}\frac{\mathrm{d}u_s}{\mathrm{d}r} - \frac{u_s}{r^2} = \frac{\zeta\sigma_a}{r\ln\left(\frac{b}{a}\right)} \quad s < r < b. \tag{5.16}$$

This second order ODE is to be solved on a domain with two free boundaries, a material boundary at $r = b$ and a non-material boundary at $r = s$, and two constants of integration. As before we define a 'Q' class of models subject to the four boundary conditions:

$$\alpha\sigma'_\theta(s^+) - \sigma'_r(s^+) = y, \tag{5.17a}$$

$$u_s(s^+) = u_s(s^-), \tag{5.17b}$$

$$\sigma'_r(b) = \sigma'_b \tag{5.17c}$$

and

$$u(b) = b - 1. \tag{5.17d}$$

We also define a strain-linearised or 'L' class of models (*cf.* §2.1.4, §2.2.4 and §2.6). This is a common simplification in borehole integrity works [*e.g.,* 81, 102, 104, 105]. Note that as before for this class of models we take $b \equiv 1$, such that Equation (5.17c) is applied at $b = 1$ and Equation (5.17d) is no longer imposed.

5.2.2 The transition $M1 \mapsto M3$: ODE & boundary conditions for u_s in plastic region

We next consider the plastic region: combining the yield condition (Equation (5.7) — for which we have equality in the plastic region) with mechanical equilibrium (Equation 5.4) leads to

$$\frac{\mathrm{d}\sigma'_r}{\mathrm{d}r} + \frac{\sigma'_r(\alpha - 1)}{\alpha r} = \frac{y\ln\left(\frac{b}{a}\right) + \alpha\zeta\sigma_a}{\alpha r\ln\left(\frac{b}{a}\right)} \qquad a < r < s, \tag{5.18}$$

which has solution

$$\sigma'_r = C_1 + C_2\left(\frac{r}{a}\right)^K \quad \text{and} \quad \sigma'_\theta = \frac{y+\sigma'_r}{\alpha} = \frac{1}{\alpha}\left[y + C_1 + C_2\left(\frac{r}{a}\right)^K\right], \tag{5.19}$$

where

$$K := \frac{1-\alpha}{\alpha}, \quad C_1(a,b) := \frac{y\ln\left(\frac{b}{a}\right) + \alpha\sigma_a\zeta}{(\alpha-1)\ln\left(\frac{b}{a}\right)}, \quad \text{and} \quad C_2(a,b) := -C_1 + (1-\zeta)\sigma_a. \tag{5.20}$$

To determine the displacement we integrate the plastic flow law (Equation 5.9) with respect to time which leads to

$$\beta\varepsilon_r^{\mathrm{p}} + \varepsilon_\theta^{\mathrm{p}} = f, \tag{5.21}$$

where f is such that $\left(\frac{\partial}{\partial t} + \boldsymbol{v}_s \cdot \nabla\right) f = 0$. Prior to the injection of fluid, we have an undeformed and unstressed material (*cf.* Figure 5.1, $M1$) so that initially there is no plastic strain in any direction. Equation (5.9) is a statement that the quantity $\beta\varepsilon_r^{\mathrm{p}} + \varepsilon_\theta^{\mathrm{p}}$ must be conserved; hence as $f = 0$ in the undeformed initial state, it must be the case that $f \equiv 0$. Thus, by Equation (5.8)

$$\beta\varepsilon_r + \varepsilon_\theta = \beta\varepsilon_r^{\mathrm{e}} + \varepsilon_\theta^{\mathrm{e}} \qquad a < r < s. \tag{5.22}$$

The elastic strains are always directly related to the effective stresses via the elasticity law. As such using Equation (5.19), Equation (5.22) becomes

$$\beta\varepsilon_r^{\mathrm{e}} + \varepsilon_\theta^{\mathrm{e}} = \frac{\sigma'_r(\beta-\Gamma) + \sigma'_\theta(1-\beta\Gamma)}{1-\Gamma^2} = D_1 + D_2\left(\frac{r}{a}\right)^K, \tag{5.23a}$$

where

$$D_1(a,b) := \frac{\alpha C_1(\beta-\Gamma) + (y+C_1)(1-\beta\Gamma)}{\alpha(1-\Gamma^2)} \tag{5.23b}$$

and

$$D_2(a,b) := \frac{C_2\left[\alpha(\beta-\Gamma)+1+\beta\Gamma\right]}{\alpha(1-\Gamma^2)} \equiv \frac{C_2}{C_1}\left[D_1 - \frac{y(1-\beta\Gamma)}{\alpha(1-\Gamma^2)}\right], \tag{5.23c}$$

and C_1 and C_2 are defined in Equations (5.20)

Strains in the plastic region can, in general, be large. Hence, it may be reasonable to adopt a Hencky (logarithmic) constitutive model for the total strains in the plastic region [11, 111]. In this case, the left hand side of Equation (5.22) becomes

$$\beta\varepsilon_r + \varepsilon_\theta = -\ln\left[\left(1-\frac{\mathrm{d}u_s}{\mathrm{d}r}\right)^{\beta}\left(1-\frac{u_s}{r}\right)\right], \tag{5.24}$$

which, on combining Equation (5.24) with Equations (5.22) and (5.23a), leads to

$$\frac{\mathrm{d}u_s}{\mathrm{d}r} = 1-\left(1-\frac{u_s}{r}\right)^{-\frac{1}{\beta}}\exp\left(-\frac{D_1a^K + D_2r^K}{a^K\beta}\right). \tag{5.25}$$

The model using these constitutive strains will be denoted by ‘N’.

Additionally, for simplicity, we adopt a linear constitutive model for the total strains in the plastic region

$$\beta\varepsilon_r + \varepsilon_\theta = \beta\frac{\mathrm{d}u}{\mathrm{d}r} + \frac{u}{r}. \tag{5.26}$$

Note that under the assumption of small strains, Equation (5.24) linearises to give Equation (5.26). Combining Equation (5.26) with Equations (5.22) and (5.23a), yields

$$\beta\frac{\mathrm{d}u_s}{\mathrm{d}r} + \frac{u_s}{r} = D_1 + D_2\left(\frac{r}{a}\right)^K. \tag{5.27}$$

We denote these models by ‘L’ or ‘Q’, depending on the associated kinematic treatment.

5.2.3 The transition $M1 \mapsto M3$: model summary of the full free-boundary BVP

For rigorous kinematics throughout, and Hencky strains in the plastic region, the full boundary value problem (BVP) is

$$\frac{\mathrm{d}u_s}{\mathrm{d}r} = 1 - \left(1 - \frac{u_s}{r}\right)^{-\frac{1}{\beta}} \exp\left(-\frac{D_1 a^K + D_2 r^K}{a^K \beta}\right) \qquad a < r < s, \tag{5.28a}$$

$$\frac{\mathrm{d}^2 u_s}{\mathrm{d}r^2} + \frac{1}{r}\frac{\mathrm{d}u_s}{\mathrm{d}r} - \frac{u_s}{r^2} = \frac{\zeta \sigma_a}{r \ln\left(\frac{b}{a}\right)}, \qquad s < r < b, \tag{5.28b}$$

$$u_s(s^+) = u_s(s^-), \tag{5.28c}$$

$$\sigma_r'(s^+) = \sigma_r'(s^-), \tag{5.28d}$$

$$\alpha \sigma_\theta'(s^+) - \sigma_r'(s^+) = y, \tag{5.28e}$$

$$\sigma_r'(b) = \sigma_b', \tag{5.28f}$$

$$u_s(a) = a - a_0, \tag{5.28g}$$

$$u_s(b) = b - 1, \tag{5.28h}$$

and we denote this model 'NQ-k_0' where the first letter corresponds to the treatment of the kinematics and plastic strain decomposition in the plastic region, and the second the treatment of the kinematics in the elastic region. Note that the boundary conditions Equations (5.11a) and (5.11b) have already been used in derivation of the above.

To consider linear strains in the entire domain, we couple Equation (5.27), in lieu of Equation (5.28a), with Equations (5.28b —5.28h). This is still rigorous from a kinematic perspective and we denote this model 'QQ-k_0'.

Although deformations and strains in the plastic region are liable to be large, deformations and strains in the elastic region are likely to remain small. Thus, to provide a simplified version of the QQ-k_0 model, we linearise under a small strain assumption in the elastic region only, to provide a mixed intermediate model defined by Equation (5.27) and

Equations (5.28b —5.28g) where Equation (5.28f) is applied at $b = 1$. This model now has only two free boundaries and is denoted by 'QL-k_0'.

Finally we consider a fully linearised model. This reduces the problem to a coupled BVP with only one free boundary. Also, as this can be solved analytically, with s determined via an implicit relation which is numerically straightforward to solve via conventional root finding techniques, this solution provides a good first guess for the Newton iteration for the other three models (see §5.4.4). This model is defined by Equation (5.27) and Equations (5.28b —5.28f), with Equation (5.28f) evaluated at $b = 1$. We denote this model 'LL-k_0'.

5.2.4 Reference state ($A1 \mapsto A3$)

For physical applications in the subsurface we are concerned with the effect of fluid flow on an elastically pre-stressed state (*i.e.,* Figure 5.1 $A3 \mapsto M3$). We consider two separate models: the transition $M1 \mapsto M3$ as summarised in §5.2.3 and denoted as u_s and the transition $A1 \mapsto A3$ denoted by u_s^{ref}. We develop the solution to the latter below.

Purely mechanical linear-elastic deformation is governed by

$$\frac{\mathrm{d}^2 u_s^{\text{ref}}}{\mathrm{d}r^2} + \frac{1}{r}\frac{\mathrm{d}u_s^{\text{ref}}}{\mathrm{d}r} - \frac{u_s^{\text{ref}}}{r^2} = 0 \tag{5.29}$$

subject to

$$\sigma_r'^{,\text{ref}}(b) = \sigma_b' \tag{5.30}$$

and the requirement of boundedness at the origin. This has solution

$$u_s^{\text{ref}}(r) = \frac{\sigma_b' r}{1 + \Gamma}, \tag{5.31}$$

which gives $\sigma_r^{\text{ref}} = \sigma_\theta^{\text{ref}} = \sigma_b'$ and $p^{\text{ref}} = 0$. For 'Q' elasticity (*i.e.,* rigorous kinematics),

$$\phi_f^{Q,\text{ref}} = \phi_{f,0} + \frac{\sigma_b'(1-\phi_{f,0})[2(1+\Gamma) - \sigma_b']}{(1+\Gamma)^2}. \tag{5.32}$$

Using the kinematic condition $u_s^{\text{ref}}(r) = r - R$ at every point to eliminate r from Equation (5.31) we obtain

$$u_s^{Q,\text{ref}} = \frac{\sigma_b' R}{1 + \Gamma - \sigma_b'}. \tag{5.33}$$

For the Q model the kinematic boundary condition at the inner cavity wall leads to

$$a_Q^{\text{ref}} = \frac{(1+\Gamma)a_0}{1 + \Gamma - \sigma_b'}. \tag{5.34}$$

We use this Q reference state for the NQ-k_0 and QQ-k_0 poroelasto-plastic models.

However, it would be inconsistent to use this kinematically rigorous framework as a reference state for the LL-k_0 model and for the elastic region of the QL-k_0 model. Thus we develop different reference states. For the 'L' model (*i.e.,* linearised kinematics) we linearise in[5] σ_b' so that Equations (5.32)–(5.34) become

$$\phi_f^{L,\text{ref}} = \phi_{f,0} + \frac{2(1-\phi_{f,0})\sigma_b'}{1+\Gamma}, \quad u_s^{L,\text{ref}}(R) = \frac{\sigma_b' R}{1+\Gamma} \quad \text{and} \quad a_L^{\text{ref}} = a_0\left(\frac{\sigma_b' + 1 + \Gamma}{1+\Gamma}\right), \tag{5.35}$$

respectively. Due to the inherent inconsistencies of the mixed QL-k_0 model, that is treating the kinematics as linearised in the elastic region but rigorously in the plastic region, there are two distinct values of s_0 and hence s^{ref}. However under the small strain assumption these are approximately equal (see §5.5 Figure 5.2). We consider the effect of flow on the background compressive state and define $\delta u_s^{\text{fl}} := u_s - u_s^{\text{ref}}$.

[5]Note that this is equivalent to linearising under an infinitesimal strain assumption.

5.3 Physical parameters: ductile yet prospective shales

Despite the high clay content of many shales, the resulting ductility is often neglected with shales being modelled as purely elastic or poroelastic materials that fail via fracture [17, 21, 26, 41, 82, 89, 95, 97, 113]. Fracture is a mechanism of brittle failure in which the bonds between the particles of the material are broken by large tensile stresses; fracking for shale-gas relies on the fact that fluid injection will lead to sufficiently high tensile stresses to initiate fractures. The often overlooked ductility of shales is important as the tensile stress in the plastic region will be much less than that predicted by the theory of elasticity, which could delay or prevent the onset of fracture [21, 30, 40, 80, 95] (see §5.5). Here, in particular, we consider a range of parameters that broadly describe a ductile shale. We consider this in more detail in Appendix G. Since shales are intrinsically anisotropic[6] this makes evaluation of elastic parameters particularly challenging.

In general, the higher the Poisson's ratio $\nu = \frac{\breve{\Lambda}}{\breve{\mathcal{M}}+\breve{\Lambda}}$ or the lower the Young's Modulus $\breve{E} = \frac{(\breve{\mathcal{M}}-\breve{\Lambda})(\breve{\mathcal{M}}+2\breve{\Lambda})}{\breve{\mathcal{M}}+\breve{\Lambda}}$ the more ductile the shale, yet for a shale to be generally considered a candidate for fracking the Young's modulus must be sufficiently large ($\gtrsim 24$ GPa) [21]. Thus we take $\breve{\mathcal{M}} \sim 50$ GPa and $\breve{\Lambda} \sim 27$ GPa ($\breve{E} \sim 25$ GPa, $\nu \sim 0.36$). We characterise the shale as having moderate internal friction and cohesion, taking $\varphi \sim 35°$ and $\breve{c} \sim 120$ MPa, but very little dilation taking $\psi \sim 0.3°$ [16, 17, 62, 98]. High confining pressures ($\sim$ 20 MPa) can cause usually brittle shales to become ductile [38] and as such we take $-\sigma_b' \sim 50$ MPa. The porosity of shales can vary greatly; we take $\phi_{f,0} \sim 20\%$ [16, 17, 35, 38, 67]. These values correspond to the dimensionless parameters, $\Gamma = 0.55$, $\alpha = 4$, $\beta = 1.01$, $y = 10^{-2}$, $a_0 = 10^{-4}$, $\phi_{f,0} = 0.2$ and $\sigma_b' = -1 \times 10^{-3}$. Note that $\alpha\nu = \frac{\alpha\Gamma}{1+\Gamma} \sim 1.4 > 1$ and $y(1-a_0^2) + 2\sigma_b' \sim 0.008 > 0$ and as such with these parameters yield will occur exclusively subject to $\mathcal{F}_{\theta,r}$ (see Appendix F). We vary the driving strength (σ_a or q) and additionally consider the transition from impermeable to fully permeable via varying the permeability-load parameter ($\zeta \in [0,1]$).

[6] They are sedimentary rocks made from layers of deposits of organic materials and mineral particles.

5.4 Solutions and numerical solution techniques

For a given model and set of parameters, the model will not be well posed for all values of σ_a. Specifically, for a given ζ, the material will remain elastic if σ_a is sufficiently small — this purely poroelastic problem for the limiting case $\zeta \equiv 1$ is the subject Chapters 2–4. Alternatively, for a given ζ, the material will yield entirely for a sufficiently large σ_a and this problem becomes ill posed. We denote the minimum σ_a for which the material yields by $\sigma_a^{\min}(\zeta)$ and the maximum allowable σ_a by $\sigma_a^{\max}(\zeta)$. In this section, firstly we consider the minimum and maximum allowable σ_a for all models (§5.4.1 and §5.4.2, respectively); secondly we consider the solution for the LL-k_0 model (§5.4.3) and finally, we discuss the numerical scheme developed to solve the QL-k_0, QQ-k_0 and NQ-k_0 models (§5.4.4).

5.4.1 Minimum $\sigma_a = \sigma_a^{\min}(\zeta)$

To determine $\sigma_a^{\min}(\zeta)$, we consider the purely elastic problem. Solving Equation (5.16), we obtain the general solution for the linear elastic displacement,

$$u_s = \frac{\sigma_a \zeta r \ln(r)}{2\ln\left(\frac{b}{a}\right)} + \frac{\mathfrak{B}_1 r}{1+\Gamma} + \frac{\mathfrak{B}_2}{(1-\Gamma)r} - \frac{\zeta \sigma_a r}{2(1+\Gamma)\ln\left(\frac{b}{a}\right)}, \tag{5.36a}$$

where $\mathfrak{B}_1$ and $\mathfrak{B}_2$ are functions of a and b to be determined. This leads to the general form of the stresses in the elastic region,

$$\sigma'_r = \frac{(1+\Gamma)\zeta\sigma_a \ln(r)}{2\ln\left(\frac{b}{a}\right)} + \mathfrak{B}_1 - \frac{\mathfrak{B}_2}{r^2} \tag{5.36b}$$

$$\sigma'_\theta = \sigma'_r + \frac{2\mathfrak{B}_2}{r^2} - \frac{\zeta\sigma_a(1-\Gamma)}{2\ln\left(\frac{b}{a}\right)}. \tag{5.36c}$$

We assume that yield will first occur at $r = a = a_{\min}$ and that the yield function (Equation 5.7) is maximised at steady state. This is consistent with previous work [103,

104, 112]. Hence, this assumption requires that

$$\alpha\sigma'_\theta(a_{\min}) - \sigma'_r(a_{\min}) = y. \tag{5.37}$$

Applying the boundary conditions $\sigma'_r(a) = (1-\zeta)\sigma_a$ and $\sigma'_r(b) = \sigma'_b$ to the poroelastic radial stress as given in Equation (5.36b), we obtain

$$\mathfrak{B}_2(a,b) := \frac{b^2a^2\left\{\sigma_a\left[\zeta(1-\Gamma)-2\right]+2\sigma'_b\right\}}{2(b^2-a^2)}. \tag{5.38}$$

Applying Equation (5.37) gives

$$(\alpha-1)(1-\zeta)\sigma_a + \alpha\left[\frac{2\mathfrak{B}_2}{a^2} - \frac{\zeta\sigma_a(1-\Gamma)}{2\ln\left(\frac{b}{a}\right)}\right] = y \quad \text{at} \quad r = a_{\min} \equiv s \tag{5.39}$$

so that

$$\sigma_a^{\min}(\zeta; a_{\min}, b_{\min}) = \frac{2\ln\left(\frac{b_{\min}}{a_{\min}}\right)\left[y\left(\frac{b_{\min}^2}{a_{\min}^2}-1\right) - 2\alpha\sigma'_b\left(\frac{b_{\min}^2}{a_{\min}^2}\right)\right]}{2\ln\left(\frac{b_{\min}}{a_{\min}}\right)\left\{\left(\frac{b_{\min}^2}{a_{\min}^2}\right)\Big[\zeta(1-\Gamma\alpha)-\alpha-1\Big] - (\alpha-1)(1-\zeta)\right\} - \alpha\zeta(1-\Gamma)\left(\frac{b_{\min}^2}{a_{\min}^2}-1\right)}. \tag{5.40}$$

Note that if $\sigma_a \geq \sigma_a^{\min}$, no yield will occur (*i.e.,* $|\sigma_a| \leq |\sigma_a^{\min}|$). For the LL-$k_0$ model we take $a_{\min} = a_0$ and $b_{\min} = 1$ and hence $\sigma_a^{\min}$ is fully determined. For the QL-k_0 model we have that $b_{\min} = 1$ and $a_{\min}$ can be found via enforcing the kinematic condition from the implicit relation

$$a_{\min} - a_0 = a_{\min}\left[\frac{(1-\zeta)(1-\alpha\Gamma)\sigma_a^{\min}(\zeta, a_{\min}, 1) + y}{\alpha(1-\Gamma^2)}\right]. \tag{5.41}$$

Unfortunately, as there is not an analytically tractable solution for $a_{\min}$ for all ζ, as there is

for the fixed $\zeta \equiv 1$ cases (see Appendix E.1), for the QQ-k_0 and NQ-k_0 cases we have a double root finding problem for $a_{\min}$ and $b_{\min}$:

$$a_{\min} - a_0 = a_{\min}\left[\frac{(1-\zeta)(1-\alpha\Gamma)\sigma_a^{\min}(\zeta, a_{\min}, b_{\min}) + y}{\alpha(1-\Gamma^2)}\right] \tag{5.42}$$

and

$$b_{\min} - 1 = \frac{b_{\min}\sigma_b'}{1+\Gamma} + \frac{2b_2(a_{\min}, b_{\min})}{b_{\min}(1-\Gamma^2)} - \frac{\zeta b_{\min}\sigma_a^{\min}(\zeta, a_{\min}, b_{\min})}{2(1+\Gamma)\ln\left(\frac{b_{\min}}{a_{\min}}\right)} \tag{5.43}$$

with $\mathfrak{B}_2(a_{\min}, b_{\min})$ and $\sigma_a^{\min}(\zeta; a_{\min}, b_{\min})$ defined in Equations (5.38) and (5.40), respectively

5.4.2 Maximum $\sigma_a = \sigma_a^{\max}(\zeta)$

When $\sigma_a = \sigma_a^{\max}(\zeta)$, $s \equiv b_{\max}$ by construction, and as such we enforce the constraint $\sigma_r'(b_{\max}) = \sigma_b'$ on Equation (5.19) which gives

$$\sigma_a^{\max}(\zeta) = \frac{\ln\left(\frac{b_{\max}}{a_{\max}}\right)\left[\sigma_b' a_{\max}^K(\alpha-1) - y(a_{\max}^K - b_{\max}^K)\right]}{\alpha\zeta(a_{\max}^K - b_{\max}^K) + b_{\max}^K(1-\zeta)(\alpha-1)\ln\left(\frac{b_{\max}}{a_{\max}}\right)}. \tag{5.44}$$

As for $\sigma_a^{\min}(\zeta)$ for the LL-k_0 model we take $a_{\max} = a_0$ and $b_{\max} = 1$, while for the QL-k_0 and the QQ-k_0 models we need to evaluate $u_s^{\mathrm{e}}(r = s = b_{\max})$. Note that the above conditions are limited to the *first* $\sigma_a^{\max}(\zeta)$ for which the entire material is yielded— for all $\sigma_a > \sigma_a^{\max}(\zeta)$ the problem has no solutions as it is over-prescribed (we have a first order ODE for σ_r' with two boundary conditions).

In general, for the LL-k_0, QL-k_0 and QQ-k_0 models the solution of Equation (5.27), given by

$$u_s^{\mathrm{p}} = \frac{D_1 r}{\beta+1} + \frac{\alpha a D_2}{\beta+\alpha}\left(\frac{r}{a}\right)^{\frac{1}{\alpha}} + \mathcal{D}_1 r^{-\frac{1}{\beta}}, \tag{5.45a}$$

where we use continuity of displacement at the elastic-plastic interface to determine $\mathcal{D}_1$

such that

$$\mathcal{D}_1 := s^{\frac{1}{\beta}} \left[u_s^{\mathrm{e}}(s) - \frac{D_1 s}{\beta+1} - \frac{\alpha a D_2}{\beta+\alpha} \left(\frac{s}{a}\right)^{\frac{1}{\alpha}} \right] \tag{5.45b}$$

with D_1 and D_2 defined in Equation (5.23b), governs the displacement in the plastic region.

For the QL-k_0 model we do not a priori know the value of u_s at the outer boundary, but we do know that $s = b_{\max} \equiv 1$. In this case $u_s(1)$ must be calculated via the elastic solution, Equation (5.36), subject to $\sigma_r'(1) = \sigma_b'$ and $\alpha\sigma_\theta'(1) - \sigma_b' = y$. This gives

$$u_s(1) = \frac{y + (1-\alpha\Gamma)\sigma_b'}{\alpha(1-\Gamma^2)}, \tag{5.46}$$

and hence

$$u_s = \frac{D_1}{\beta+1}\left[r - \left(\frac{1}{r}\right)^{\frac{1}{\beta}}\right] + \frac{\alpha D_2}{a^K(\beta+\alpha)}\left[r^{\frac{1}{\alpha}} - \left(\frac{1}{r}\right)^{\frac{1}{\beta}}\right] + \left[\frac{y+(1-\alpha\Gamma)\sigma_b'}{\alpha(1-\Gamma^2)}\right]\left(\frac{1}{r}\right)^{\frac{1}{\beta}}, \tag{5.47}$$

so that $\sigma_a^{\min}(\zeta)$ is fully determined once $a_{\max}$ is found via the implicit relation

$$a_{\max} - a_0 = \frac{D_1(a_{\max})}{\beta+1}\left[a_{\max} - \left(\frac{1}{a_{\max}}\right)^{\frac{1}{\beta}}\right] + \frac{\alpha D_2(a_{\max})}{a_{\max}^K(\beta+\alpha)}\left[a_{\max}^{\frac{1}{\alpha}} - \left(\frac{1}{a_{\max}}\right)^{\frac{1}{\beta}}\right] + \left[\frac{y+(1-\alpha)\sigma_b'}{\alpha(1-\Gamma^2)}\right]\left(\frac{1}{a_{\max}}\right)^{\frac{1}{\beta}}. \tag{5.48}$$

For the QQ-k_0 model, the rigorous treatment of the kinematics gives $u_s(b) = b - 1$ and hence

$$u_s = \frac{D_1}{\beta+1}\left[r - b_{\max}\left(\frac{b_{\max}}{r}\right)^{\frac{1}{\beta}}\right] + \frac{\alpha D_2}{a^K(\beta+\alpha)}\left[r^{\frac{1}{\alpha}} - b_{\max}^{\frac{1}{\alpha}}\left(\frac{b_{\max}}{r}\right)^{\frac{1}{\beta}}\right] + (b_{\max}-1)\left(\frac{b_{\max}}{r}\right)^{\frac{1}{\beta}}. \tag{5.49}$$

To find $b_{\max}$ we once again appeal to the elastic problem at $r = b$; solving Equation (5.36) subject to $\sigma_r'(b_{\max}) = \sigma_b'$ and $\alpha\sigma_\theta'(r = s = b_{\max}) - \sigma_b' = y$ and equating this to $u_s(b_{\max}) =$

$b_{\max} - 1$ yields

$$b_{\max} := \frac{\alpha(1-\Gamma^2)}{\alpha(1-\Gamma^2) + (\alpha\Gamma - 1)\sigma_b' - y}. \tag{5.50a}$$

Note that this is also true for the NQ-k_0 model as we have not used the plastic flow law anywhere in this calculation. Hence, $\sigma_a^{\min}(\zeta)$ is fully determined once $a_{\max}$ is found via the implicit relation

$$\begin{aligned} a_{\max} - a_0 = \frac{D_1(a_{\max}, b_{\max})}{\beta+1}\left[a_{\max} - b_{\max}\left(\frac{b_{\max}}{a_{\max}}\right)^{\frac{1}{\beta}}\right] + \\ \frac{\alpha D_2(a_{\max}, b_{\max})}{a_{\max}^K(\beta+\alpha)}\left[a_{\max}^{\frac{1}{\alpha}} - b_{\max}^{\frac{1}{\alpha}}\left(\frac{b_{\max}}{a_{\max}}\right)^{\frac{1}{\beta}}\right] + (b-1)\left(\frac{b_{\max}}{a_{\max}}\right)^{\frac{1}{\beta}}, \end{aligned} \tag{5.50b}$$

with $b_{\max}$ a known constant as defined in Equation (5.50a). Due to the nonlinearity of Equation (5.25) it is not tractable to work out the value of $a_{\max}$ for the NQ-k_0 model.

5.4.3 LL-k_0 solution for prescribed σ_a and varying ζ

We obtain analytical solutions to the displacement in both the elastic ($s < r < b \equiv 1$) and plastic ($a \equiv a_0 < r < s$) regions, while the position of the interface at s is the solution to an implicit relation. Solving the problem defined by Equations (5.27) and (5.28b) subject to conditions (5.28c) – (5.28h) leads to

$$u_s = \begin{cases} \dfrac{D_1 r}{\beta+1} + \dfrac{\alpha a D_2}{\beta+\alpha}\left(\dfrac{r}{a_0}\right)^{\frac{1}{\alpha}} + \mathcal{D}_1 r^{-\frac{1}{\beta}} \quad a_0 < r < s \\ \\ -\dfrac{\sigma_a \zeta r \ln(r)}{2\ln(a_0)} + \dfrac{\mathfrak{D}_1 r}{1+\Gamma} + \dfrac{\mathfrak{D}_2}{(1-\Gamma)r} + \dfrac{\zeta\sigma_a r}{2(1+\Gamma)\ln(a_0)}, \quad s \le r < 1, \end{cases} \tag{5.51a}$$

where D_1 and D_2 are functions of s defined in Equation (5.23b),

$$\mathcal{D}_1(s) := s^{\frac{1}{\beta}} \left[\underbrace{-\frac{\sigma_a \zeta s \ln(s)}{2\ln(a_0)} + \frac{\mathfrak{D}_1 s}{1+\Gamma} + \frac{\mathfrak{D}_2}{(1-\Gamma)s} + \frac{\zeta \sigma_a s}{2(1+\Gamma)\ln(a_0)}}_{u_s^e(s)} - \frac{D_1 s}{\beta+1} - \frac{\alpha a D_2}{\beta+\alpha}\left(\frac{s}{a_0}\right)^{\frac{1}{\alpha}} \right] \tag{5.51b}$$

with

$$\mathfrak{D}_1(s) := \mathfrak{D}_2(s) + \sigma_b' \tag{5.51c}$$

and

$$\mathfrak{D}_2(s) := \frac{s^2\left\{2\ln(a_0)[y - \sigma_b'(\alpha-1)] - \alpha\zeta\sigma_a(1-\Gamma) + \zeta\sigma_a(\alpha-1)(1+\Gamma)\ln(s)\right\}}{2\ln(a_0)[1+\alpha+(\alpha-1)s^2]} \tag{5.51d}$$

where s is then determined to be the solution of the implicit expression

$$C_1(s) + C_2(s)\left(\frac{s}{a_0}\right)^K - \sigma_b' + \frac{(1+\Gamma)\sigma_a\zeta\ln(s)}{2\ln(a_0)} + \frac{1-s^2}{s^2}\mathfrak{B}_2(s) = 0 \tag{5.52a}$$

such that $C_1(s)$ and $C_2(s)$ are defined in Equation (5.20) or, explicitly, as the solution to

$$\begin{aligned} &\frac{y\ln(a_0) - \alpha\sigma_a\zeta}{(\alpha-1)\ln(a_0)} + \frac{(1+\Gamma)\sigma_a\zeta\ln(s)}{2\ln(a_0)} - \left[\frac{y\ln(a_0) - \alpha\sigma_a\zeta - (\alpha-1)(1-\zeta)\ln(a_0)\,\sigma_a}{a_0^K(\alpha-1)\ln(a_0)}\right] s^K \\ &+ \frac{(1-s^2)\left\{2\ln(a_0)[y-\sigma_b'(\alpha-1)] - \alpha\zeta\sigma_a(1-\Gamma) + \zeta\sigma_a(\alpha-1)(1+\Gamma)\ln(s)\right\}}{2\ln(a_0)[1+\alpha+(\alpha-1)s^2]} = \sigma_b'. \end{aligned} \tag{5.52b}$$

Note that s can take any value from a_0 to 1 — this is in contrast to the fixed outer boundary case presented in Appendix E.2.2. The implicit relation Equation (5.52b) for one unknown, s, must be solved numerically via a root finding scheme; we use `MATLAB`'s `fzero`. Once this value is determined the solution is fully prescribed by Equation (5.51).

5.4.4 QL-k_0, QQ-k_0 and NQ-k_0— models ($M1 \mapsto M3$): numerical solution method

For all models, the problem (Figure 5.1 $M1 \mapsto M3$) is defined as a closed, coupled, free-boundary BVP in terms of one independent variable u_s in Equations (5.28) for the NQ-k_0 model and Equation (5.27) and Equations (5.28b) – (5.28h) for the other three models. Despite the analytical tractability of the governing ODE in both the elastic region (Equation 5.28b) and the 'L' or 'Q' ODE in the plastic region, (Equation 5.27), we choose not to solve these ODEs analytically as we have done above for the LL-k_0 models, as doing so leads to a triple root finding problem for $\{a, s, b\}$ where we do not know s_0. Instead we adapt the Chebyshev spectral collocation method developed in §3.1.3.

We map both the plastic region, $r \in [a, s]$, and the elastic region, $r \in [s, b]$, to separate Chebyshev grids, each with N Chebyshev nodes. Note that both domains include the boundary point $r = s$, meaning that the entire space $r \in [a, b]$ will be discretised by $2N - 1$ nodes (or collocation points); we use the dense Chebyshev differentiation matrices to discretise any derivatives and thus convert this coupled free boundary BVP into a system of algebraic equations. We solve for the displacement at the $2N - 1$ nodes and also for the position of the non-material free boundary point s; thus we require a system of $2N$ equations, and we must enforce all boundary conditions with the exception of $\sigma_r'(a) = 0$ (which has already been enforced in the derivation of the closed, coupled BVP in terms of u_s). As the governing equation in the plastic region (Equation 5.28a) is a first order ODE, it must be enforced at exactly $N - 1$ nodes. Hence we enforce this for the first $N - 1$ nodes of the discretised domain, essentially enforcing this for $r \in [a, s)$ which produces a system of $N - 1$ equations. The governing equation (Equation 5.28b) in the elastic region is, however, a second order ODE; thus this must be enforced at precisely $N - 2$ nodes, essentially for $r \in (s, b)$ resulting in a system of $N - 2$ equations. Hence we require: one equation governing the displacement at $r = s$ — we enforce continuity of displacement (Equation 5.28c); another equation governing the displacement at $r = b$ — we enforce

the effective stress condition (Equation 5.28f); and finally an equation to determine the position of s (*i.e.,* an equation in which s appears explicitly) — we enforce the condition that the elastic stresses are at the point of yield at $r = s$ (Equation 5.28e). This forms the system of $2N$ equations we solve for the $2N$ unknowns (the displacement at $2N - 1$ Chebyshev nodes and the position of s). This system is solved via Newton iteration; note that the kinematic conditions (Equations 5.28g & 5.28h), along with the current values of s, are used to update the domains after each iteration and as such Equations (5.28g) and (5.28h) are not included in our coupled system of $2N$ equations, but are enforced. Not only is this numerical scheme possible for the analytically intractable NQ-k_0 model, also as for the purely poroelastic problem, it allows for a solution for an imposed Δp (or, equivalently, fixed σ_a) in lieu of a fixed q.

The main structural difference between the models presented here and the models presented in Chapters 2–4 is the domain. Here, we have a coupled free-boundary domain $r \in [a, s]$ and $r \in [s, b]$, such that s is a non-material boundary— a significant complication from the domain in the purely poroelastic problem, which is simply bounded by two material points. At steady state, the distinction between the material points at a and b and the non-material point at s, is just that whilst we know a_0 and $b_0 \equiv 1$, we do not a priori know s_0, only that $s_0 \in [a_0, 1]$. Given this, ideally we would use an analytical Jacobian matrix to update the Newton iteration at each step because it is more robust, allowing for a starting guess further away from the solution than would be possible if a numerical Jacobian was used instead. That said, although it is possible to determine the analytical Jacobian for this problem, it is certainly nontrivial to account for the moving boundaries[7]; as such, we opt for a numerical Jacobian instead, ensuring that the initial starting guess is sufficiently close to the appropriate steady-state solution. We do this by chaining the models — that is we use the analytical solution of the LL-k_0 model as a guess for the QL-k_0

[7]Note that a 'first-pass' analytical solution (*i.e.,* an analytical expression for the Jacobian that does not account for the hidden dependence on displacement due to the deforming grid), is actually worse than a simple numerical calculation.

model, whose solution we use as a guess for the QQ-k_0 model, and this solution we use as a guess for the NQ-k_0 model. Alternatively, if we are solving for a range of q or σ_a we instead use the above chain to initialise the solutions for each of the four models for the lowest driving strength; then for subsequent larger driving strengths, we use the previous solutions as guesses for their respective models. This allows for the fact that as driving strength increases the model behaviours diverge from one another (see Figure 5.5). This same procedure can also be used for increasing ζ, as small ζ has a less deformed solution and hence in general less difference between the models for a given σ_a (see Figures 5.7 — 5.9).

5.5 Results

We present steady-state solutions for the poroelasto-plastic deformation of a cohesive granular annulus, subject to fluid injection through the inner cavity. We have developed solutions for four distinct model combinations: LL-k_0, QL-k_0, QQ-k_0 and NQ-k_0 as detailed in §5.2.3. To investigate the impact of fluid injection into the pre-stressed subsurface, we isolate the effect of fluid injection into the stressed background state, that is we consider $\delta u_s^{\text{fl}} := u_s - u_s^{\text{ref}}$ (*i.e.,* the transition $A3 \mapsto M3$, Figure 5.1) in Figures 5.2, 5.5 – 5.7 and 5.9. In Figures 5.3 and 5.8 we plot the solutions without the reference state for comparison. Figure 5.4 also uses the 'raw' quantities for simplicity. All figures are such that the outer boundary of the annulus subject to a fixed compressive radial effective stress and all parameter values, with the exception of driving strength and ζ, are fixed as discussed in §5.3.

Additionally, we extend the purely poroelastic L-k_0 (linear elasticity, linearised kinematics and constant permeability) and Q-k_0 (linear elasticity, rigorous kinematics and constant permeability) steady-state solutions as developed in Chapters 2 and 3 to incorporate the permeability-load parameter ζ, and present these in companion with the poroelasto-

plastic model developed in this chapter. This enables direct comparison between these constitutive behaviours which clearly highlights the impact of plasticity and varying ζ.

5.5.1 Fully permeable: fixed q

In Figures 5.2 – 5.6 we restrict our considerations to the fully permeable model ($\zeta \equiv 1$). For this model we consider driving the system with a fixed flow rate q in lieu of driving via a fixed pressure difference $\Delta p \equiv -\zeta\sigma_a = -\sigma_a$. Although we consider only the steady state solution such that a fixed Δp corresponds to a value of q, this value is dependant on model choice, so the relative behaviour of the models is different (*cf.* $\delta\sigma_r'^{,\text{fl}}$ Figure 5.2 *vs* Figure 5.7). Note that q must be bounded by the minimum q that leads to yield, q_{min}, and the maximum q that leads to an entirely yielded domain, q_{max}. This minimum q is derived directly in Appendix E.1.1 and given by Equation (E.4), although it is reproduced via $q_{\text{min}} = -\sigma_a^{\text{min}}(1)/\ln\left(\frac{b}{a}\right)$ where $\sigma_a^{\text{min}}(1)$ is defined in Equation (5.40). Similarly, q_{max} is derived in Appendix E.1.2 and given by Equation (E.9); this is reproduced via $q_{\text{max}} = -\sigma_a^{\text{max}}(1)/\ln\left(\frac{b}{a}\right)$ where $\sigma_a^{\text{min}}(1)$ is defined in Equation (5.44). In Appendix E.2.1 the full solution for the transition $M1 \mapsto M3$ is explicitly presented. Additionally, in Appendix E.2.2 we also present the solution for a relaxed, undeformed annulus subject to fluid injection at the inner boundary and a fixed outer boundary — a modified version of the transition $M1 \mapsto M3$. Figures 5.2 – 5.6 provide a qualitative comparison between the poroelastic and the poroelasto-plastic solutions to illustrate the impact of plasticity.

In Figures 5.2 and 5.3 we drive with fixed $q = 0.0012$; for the LL-k_0 model for these parameters $q_{\text{min}} \approx 3.1 \times 10^{-4}$ and $q_{\text{max}} \approx 3.3 \times 10^{-3}$, so that the fixed driving q is approximately one third of the q required to yield the material entirely. Note that Figure 5.3, produced for reference, is the same as Figure 5.2 but the transition $M1 \mapsto M3$ is plotted without the subtraction of the reference state.

For the poroelastic response (Figures 5.2, left column) the L-k_0 and Q-k_0 models are practically indistinguishable. The porosity $\delta\phi^{\text{fl}}$ (first row), azimuthal effective stress, $\delta\sigma_\theta'^{,\text{fl}}$

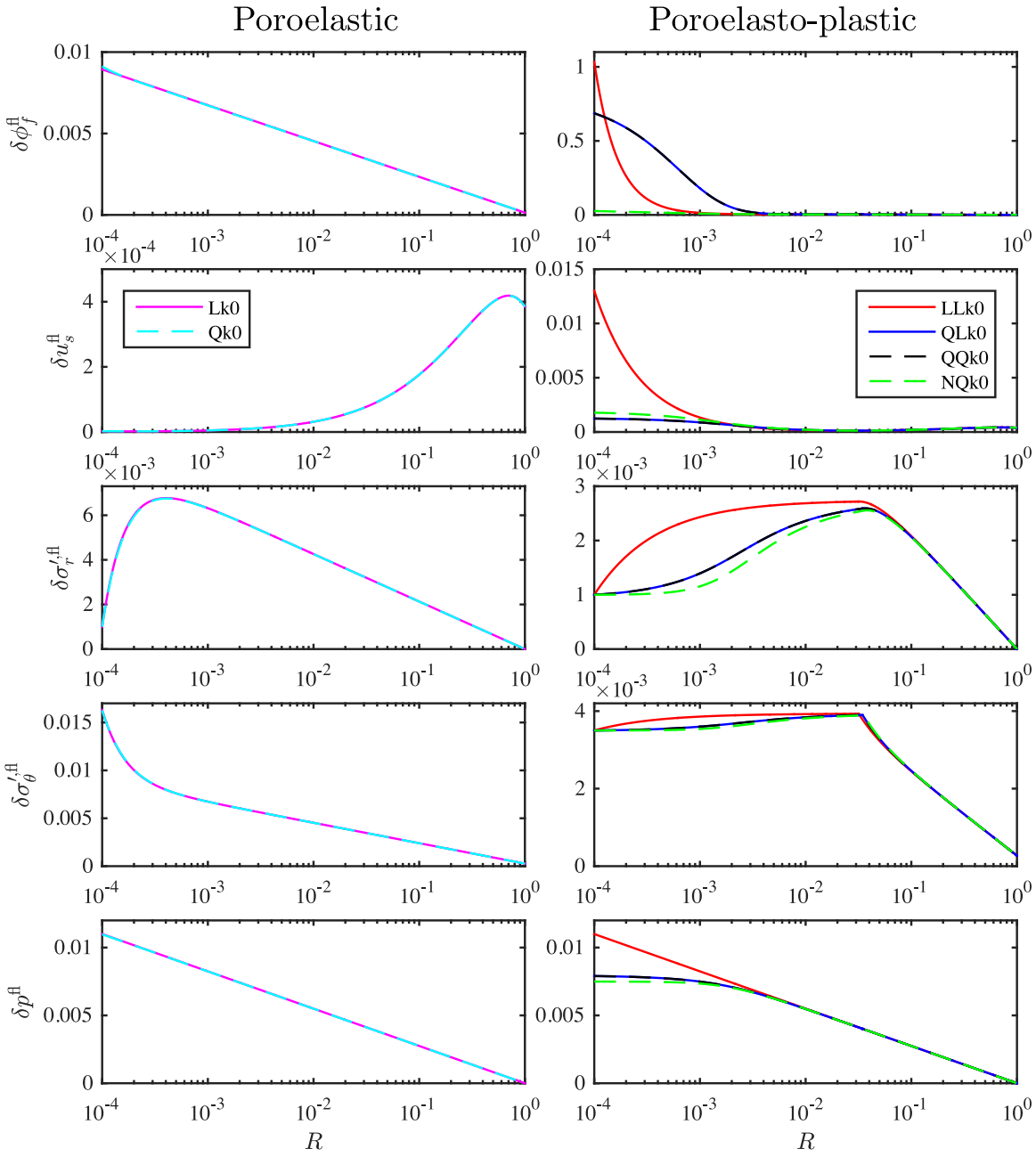

Figure 5.2: Two poroelastic models (left column) and four poroelasto-plastic models (right column), all fully permeable, at steady state and driven via fixed flow rate $q \approx 0.0012$. We show only the change in the key quantities due to fluid injection in relation to a pre-stressed state (*i.e.,* Figure 5.1, $A3 \mapsto M3$). The key quantities shown are the porosity $\delta\phi^{\mathrm{fl}}$ (first row), the displacement δu_s^{fl} (second row), the radial and azimuthal effective stresses $\delta\sigma_r'^{,\mathrm{fl}}$ and $\delta\sigma_\theta'^{,\mathrm{fl}}$ (third and fourth rows, respectively) and the pressure δp^{fl} (last row). For clarity we plot the results against the Lagrangian coordinate $R(r) = r - u_s$ and on a logarithmic horizontal scale. Note the significant effect of plasticity and how model choice, in particular the inclusion of rigorous kinematics in the plastic region, makes a key difference to the resulting deformation in the plastic region, but yet has very little impact in the elastic region.

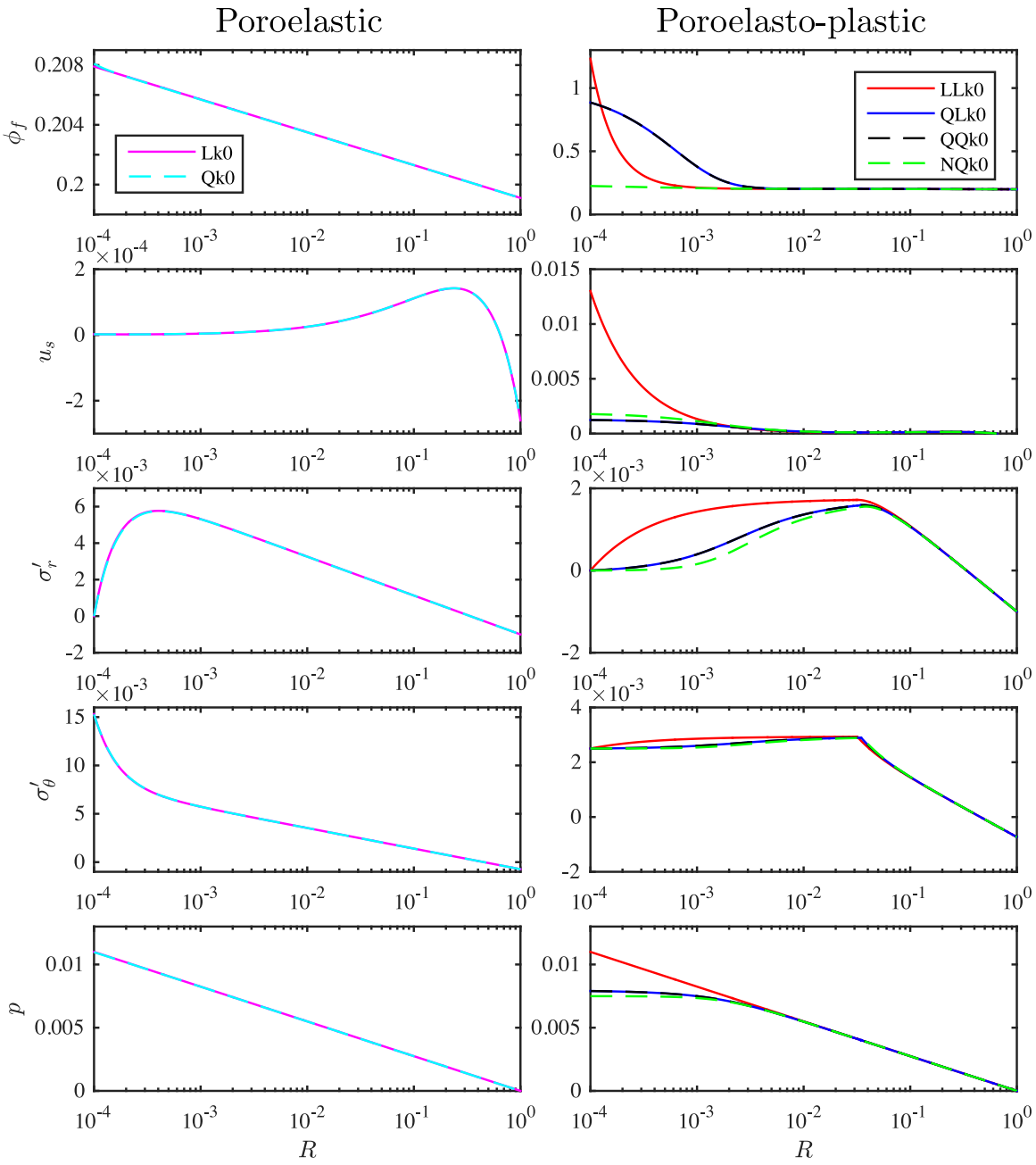

Figure 5.3: Figure 5.2 plotted for the transition $M1 \mapsto M3$ as opposed to $A3 \mapsto M3$.

(fourth row) and pressure δp^{fl} (last row) all have maxima at the inner cavity; δp^{fl} decays logarithmically with increasing Lagrangian radius R as does $\delta\phi^{\text{fl}}$ for the L-k_0 model, while for the Q-k_0 model $\delta\phi^{\text{fl}}$ decays approximately logarithmically with increasing R. Note that $\delta\phi^{\text{fl}}$ is strictly positive signifying that fluid injection has increased the porosity everywhere relative to the compressed reference state. Near the cavity wall, the azimuthal effective stress decays faster than logarithmically with increasing R; for sufficiently large R, both the radial and azimuthal effective stresses (third and fourth rows, respectively) appear to also decay logarithmically. Both the displacement and the radial effective stress (second and third rows, respectively) have internal maxima; $\delta\sigma_r'^{;\text{fl}}$ is pinned at the inner radius to the value of $-\sigma_b'$ by construction due to the reference state, but rapidly increases to its maximum value close to the borehole. The displacement however does not decay with R; in fact, the maximum displacement is reached near the outer boundary at $R \sim 0.7$.

On the addition of perfect plasticity (Figure 5.2, right column), we see that the behaviour of all quantities, with the exception of δp^{fl}, is drastically altered and now model choice clearly becomes significant. That said, although the behaviour of the different models is quite varied in the plastic region this has a negligible impact on the respective elastic behaviours. Similarly, the inclusion of kinematic nonlinearity in the elastic region has little impact on the deformation field. In general the LL-k_0 model predicts the largest values for every quantity and the NQ-k_0 model is the most conservative. The QL-k_0 and QQ-k_0 models are generally intermediate to the other models and are effectively indistinguishable from each other for all quantities. For all quantities with the exception of $\delta\phi^{\text{fl}}$, the NQ-k_0 model predicts similar behaviour as for the QL-k_0 and QQ-k_0 models with very minimal discrepancy between these three models.

As for the poroelastic case, $\delta\phi^{\text{fl}}$ achieves its maximum value at the inner radius for all models, with all models decreasing monotonically from the inner cavity wall to the outer boundary, becoming indistinguishable for sufficiently large R; $\delta\phi^{\text{fl}}$ also remains strictly positive. However, the quantitative behaviour of these models in the plastic region is sig-

nificantly different from the poroelastic models for R near the inner cavity wall. Not only this, but the poroelasto-plastic models behave quite differently from one another, with the exception of the QQ-k_0 and QL-k_0 models. For the NQ-k_0 model we have the least change in porosity at the inner cavity, and for R approximately greater than 10^{-3} the NQ-k_0 and LL-k_0 models are indistinguishable. The QQ-k_0 and QL-k_0 models do predict the intermediate maximum-value, with the LL-k_0 model predicting the largest increase. For R close to the inner cavity, approximately in the region $(1.3 \times 10^{-4}, 1.2 \times 10^{-2})$, the QL-$k_0$ and QQ-k_0 models predict a significantly higher porosity than the other models. For R greater than 1.2×10^{-2} once again all models become indistinguishable, so that for a larger section of the cylinder the NQ-k_0 and LL-k_0 models predict the same behaviour which is not entirely expected. That said, for the LL-k_0 model we see immediately that the maximum change in porosity due to fluid injection is greater than unity which is clearly nonphysical; in fact we need $\delta\phi_f^{\text{fl}} \lesssim 0.8$ (*cf.* Figure 5.3)[8]. Thus for the LL-k_0 model it is clearly evident that linearising the kinematics in the plastic region can and has lead to unphysical solutions (see Figure 5.4 and surrounding discussion). If we compare this to the QL-k_0 model, where we have linearised the kinematics in the elastic region while treating them rigorously in the plastic region, we have a well-behaved solution which is practically indistinguishable from the QQ-k_0 model in which we have not linearised the kinematics in either region. This illustrates nicely the reason why the L-k_0 and Q-k_0 models are indistinguishable while there is such a drastic difference between the LL-k_0 and other poroelasto-plastic models; it is all due to the magnitude of the displacement.

On consideration of the second row of Figure 5.2 we see the difference in the orders of magnitude of the respective displacements. For any model the maximum poroelastic displacement is nearly two orders of magnitude less than the maximum poroelasto-plastic displacement. The linearisation of kinematics relies on the assumption that the strain $\frac{\mathrm{d}u_s}{\mathrm{d}r}$ and $\frac{u_s}{r} \ll 1$; hence the magnitude and location of the maximum displacement and nature

[8]Recall $\delta\phi^{\text{fl}} := \phi_f - \phi_f^{\text{ref}} = \phi_f - \phi_{f,0} - \frac{2\sigma_b'(1-\phi_{f,0})}{1+\Gamma} \approx \phi_f - 0.2 \approx 0.8$, or, equivalently, $\phi_f < 1$.

of the entire displacement field are all important in ensuring that both strains remain small. For the poroelastic case the maximum value of $\left(\frac{u_s}{r}\right)_{\max} \approx 0.02$ at the inner boundary, while for the LL-k_0 model in the poroelasto-plastic case $\left(\frac{u_s}{r}\right)_{\max} \approx 130$ also at the inner boundary. Thus, clearly, neglecting the nonlinearity inherent to the kinematics during plastic flow is not valid. However the maximum azimuthal strain in the elastic region of the poroelasto-plastic solution $\left(\frac{u_s}{r}\right)^{\mathrm{e}}_{\max} \approx 0.003 \ll 1$. This is merely an illustrative example, yet we see that because the displacements and associated strains present in the elastic region of the poroelasto-plastic solution are small and there are no regions of rapid change (and R is relatively large), linearising in the strains seems reasonable. The validity of this 'mixed model' is further supported by Figures 5.2–5.3 and Figure 5.5 – 5.9 (solid blue and dashed black lines, respectively) in which the QL-k_0 and QQ-k_0 models are indistinguishable. Unlike the poroelastic case, all poroelasto-plastic models predict that the maximum displacement occurs at the inner boundary and the minimum displacement is now an interior point $R \approx 0.05$. The displacement at the inner cavity wall for the LL-k_0 model is almost one order of magnitude larger than for the other models; this decays for increasing R and at around $R = 1.1 \times 10^{-3}$ the LL-k_0 model predicts the least displacement. For R bigger than approximately 10^{-2} all models once again become essentially indistinguishable predicting the same displacement. Contrary to the general relationship between the models, the NQ-k_0 model actually predicts the intermediate maximum-displacement at the cavity wall.

As for the poroelastic case, $\delta\sigma_r'^{;\mathrm{fl}}$ is pinned to $-\sigma_b'$ at the inner boundary, vanishes at the outer boundary and has an internal maximum. However, the location of the internal maximum is at $s \approx 0.032$ which is significantly further into the material than the maximum in the poroelastic case. Note that for the poroelasto-plastic case the magnitude of σ_r' is smaller than for the poroelastic models— the maximum value obtained is approximately one half of that in the poroelastic case. For all models the stress increases monotonically within the plastic region and then decreases approximately logarithmically for sufficiently

large $R \approx 0.1$ in the elastic region, in line with the poroelastic model. That said, the four models do not appear to converge until R is sufficiently greater than s_0, that is for R sufficiently far into the elastic region. Following the general trend, the LL-k_0 model predicts the greatest stress and the NQ-k_0 model the least, with the QL-k_0 and QQ-k_0 models being intermediate but closer to NQ-k_0 models than the LL-k_0.

Unlike the poroelastic case in which $\delta\sigma'^{,\mathrm{fl}}_\theta$ decreases monotonically from its maximum at the inner cavity wall, the poroelasto-plastic $\delta\sigma'^{,\mathrm{fl}}_\theta$ has an interior maximum at $r = s$. At s, this is the only quantity that exhibits a sharp transition, requiring the elastic stresses to be at the point of yield (*i.e.,* $\mathcal{F}_{\theta,r} = 0$) at s gives $\alpha\sigma'^{,\mathrm{e}}_\theta - \sigma'^{,\mathrm{e}}_r = \alpha\sigma'^{,\mathrm{p}}_\theta - \sigma'^{,\mathrm{p}}_r$ and enforcing continuity of σ'_r implies σ'_θ must also be continuous. As σ'_r and σ'_θ are continuous by Equation (5.4), which must hold throughout the material, $\frac{\mathrm{d}\sigma'_r}{\mathrm{d}r}$ must also be continuous as the flow rate is continuous. Finally in the elastic region $\sigma'_r = \mathfrak{f}(\frac{\mathrm{d}u_s}{\mathrm{d}r}, \frac{u_s}{r})$, in general, ($\mathfrak{f} \equiv \frac{\mathrm{d}u_s}{\mathrm{d}r} + \Gamma\frac{u_s}{r}$ for all models considered here) with $\mathfrak{f}$ a continuous function; therefore $\frac{\mathrm{d}u_s}{\mathrm{d}r} = \hat{\mathfrak{f}}(\sigma'_r, \frac{u_s}{r})$ (for the elasticity law considered here $\hat{\mathfrak{f}} \equiv \sigma'_r - \Gamma\frac{u_s}{r}$). Thus as both σ'_r and u_s are continuous at s, and $\frac{\mathrm{d}u_s}{\mathrm{d}r}$ is a continuous function of these in the elastic region, $\frac{\mathrm{d}u_s}{\mathrm{d}r}$ must itself be continuous at s.

Note that $\delta\sigma'^{,\mathrm{fl}}_\theta$ is nearly an order of magnitude less than its poroelastic counterpart. This is an artefact of plasticity which allows energy to be dissipated through an irreversible structural rearrangement of the grains and reduces the stress via enforcing the combination of stresses, as defined by the yield function $\mathcal{F}_{\theta,r} := \alpha\sigma'_\theta - \sigma'_r - y = \alpha\delta\sigma'^{,\mathrm{fl}}_\theta - \delta\sigma'^{,\mathrm{fl}}_r - y + \sigma'_b(\alpha - 1)$, to be identically zero in the plastic region and strictly negative in the elastic region. As for $\delta\sigma'^{,\mathrm{fl}}_r$, for sufficiently large $R \gtrsim 0.1$ in the elastic region, $\delta\sigma'^{,\mathrm{fl}}_\theta$ decays approximately logarithmically with increasing R. For R slightly greater still, all models once again become practically indistinguishable. In the plastic region the general trend of the QL-k_0 and the QQ-k_0 models being intermediate to the LL-k_0 and NQ-k_0 models is followed; however these two models are far closer to the NQ-k_0 model than the LL-k_0 model. At the elastic-plastic interface the ordering of models changes such that in the

elastic region, near $R = s_0$. The LL-k_0 model now predicts the smallest stress and the NQ-k_0 the largest.

The poroelasto-plastic pressure field bears a significant resemblance to its poroelastic counterpart. For all models the pressure field decays monotonically with increasing R; for the LL-k_0 model δp^{fl} is independent of the inclusion of plasticity decaying logarithmically with increasing R. However, for the models with rigorous kinematics, the pressure field is altered near the inner cavity but tends to the LL-k_0 model, and hence poroelastic pressure fields, for sufficiently large $R \gtrsim 10^{-2}$. Near the inner cavity once again the QL-k_0 and QQ-k_0 models are indistinguishable and both are very similar to the NQ-k_0 model which offers a more conservative prediction. This is due to the fact that the pressure field ($p \equiv \delta p^{\text{fl}} = q \ln\left(\frac{b}{r}\right)$) only depends on the values of r and for the LL-k_0 model there is essentially no distinction between the Lagrangian and Eulerian spatial coordinates, so that despite the LL-k_0 model predicting the most displacement at the inner radius, which should lead to the smallest predicted value for Δp, the pressure field is independent of the actual displacement at the cavity wall and thus the LL-k_0 yields the highest prediction of $\Delta\delta p^{\text{fl}}$. This becomes significant in §5.5.2 when we instead enforce σ_a at the inner cavity, which in the limit $\zeta \equiv 1$ is equivalent to prescribing Δp, since for a fixed σ_a the NQ-k_0 model experiences the highest steady-state q and the LL-k_0 model the lowest.

In Figure 5.4 we show the total thickness of the annulus (magenta) and the thickness of both the elastic and plastic regions (green and blue, respectively) for the fully permeable, perfecly-plastic case ($\zeta \equiv 1$). Note that for the LL-k_0 (top left), QL-k_0 (top right) and QQ-k_0 (bottom left) models q is between $q_{\text{min}} \approx 3 \times 10^{-4}$, the smallest q that induces yield in all models, and $q_{\text{max}} \approx 3.3 \times 10^{-3}$, the first value of q for which the material is entirely yielded. However, for the NQ-k_0 model(bottom right), it is only between $q_{\text{min}} \approx 3 \times 10^{-4}$ and $q \approx 1.1 \times 10^{-3}$. Note also that while even the 'mixed' QL-k_0 model predicts sensible results for all q, effectively indistinguishable from those of the QQ-k_0 model, the LL-k_0 model predicts a negative annulus thickness with a negative plastic region, which is

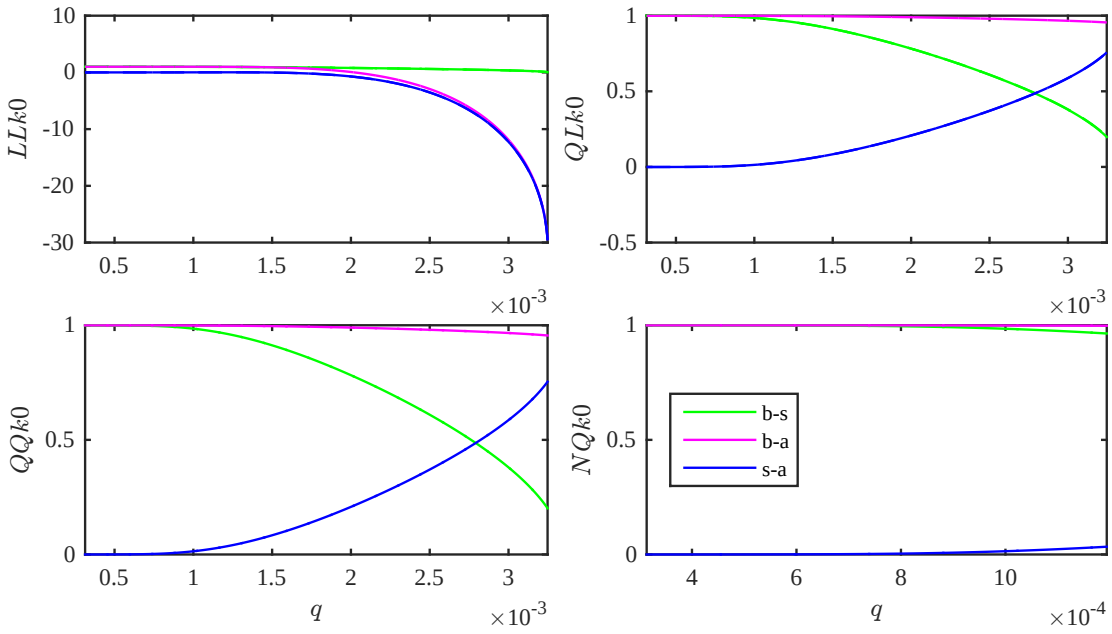

Figure 5.4: For all four models – the LL-k_0 model (top left), QL-k_0 model (top right), QQ-k_0 model (bottom left) and NQ-k_0 model (bottom right), we plot the thickness of the elastic region (green), the total thickness of the annulus (magenta) and the thickness of the plastic region (blue) against increasing flow rate q. Note the range of q is the same for the LL-k_0, QL-k_0 and QQ-k_0 models but reduced for the NQ-k_0. For this range of q the LL-k_0 model predicts an annulus with a plastic region of negative area and overall negative area — that is, it inverts itself.

clearly non-physical. This is further evidence that for even moderate driving flow rates the kinematic treatment is key when plasticity is present; linearising the plastic region of model under the infinitesimal strain assumption can lead to unphysical solutions simply because this underlying assumption is violated.

In Figure 5.5, we present summary quantities for a range of fixed q. We start with a very small q, such that the material will not have yielded (*i.e.,* $q < q_{\min}$); as such, the LL-k_0 and the QL-k_0 models behave according to the L-k_0 model, while the QQ-k_0 and NQ-k_0 models behave according to the Q-k_0 model for all $q \leq q_{\min}$. We increase q up to the maximum value as shown in Figure 5.5 of $q \approx 0.0012$ which is about one third of the rate required to yield the material entirely. In the main figure we focus on the poroelasto-plastic behaviour, while in the insets we focus on the poroelastic behaviour. As one would expect, all the quantities, for both the poroelastic and poroelasto-plastic cases, increase monotonically

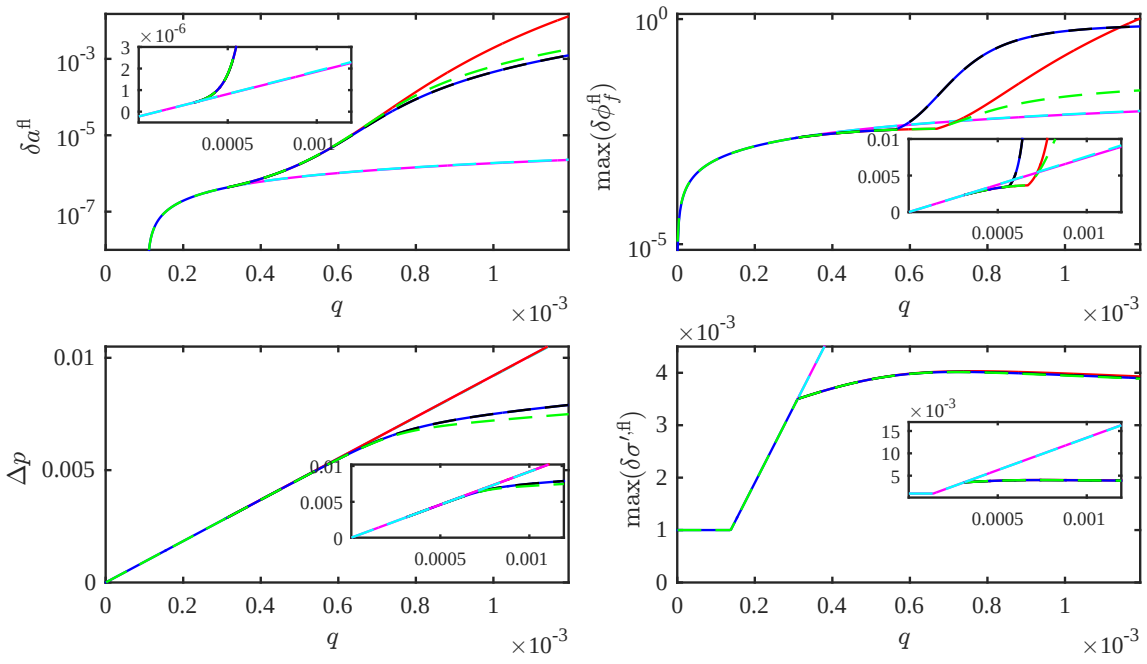

Figure 5.5: Four summary quantities for varying fixed flow rate $q \in (\sim 0, \sim 0.0012)$, once again for the fully permeable case $\zeta \equiv 1$, with the same colour scheme as in Figure 5.2 and 5.3; the displacement at the inner cavity wall due to fluid injection δa^{fl} (top left), the maximum increase in porosity due to fluid injection $\delta\phi^{\mathrm{fl}}$ (top right), the bottom-hole pressure Δp, (bottom left) and the maximum increase in (tensile) effective stress (bottom right). In each main subplot we focus on the four poroelasto-plastic models and in each inset we focus on the poroelastic solution. The main plots on the top row are plotted on a logarithmic vertical scale for clarity. For values of q less than each models respective q_{min} we have the LL-k_0 and QL-k_0 models behave as the L-k_0 model and the QQ-k_0 and NQ-k_0 models behave as Q-k_0 model. Note how once again model choice is insignificant for the poroelastic models but model choice, in particular the kinematics chosen in the plastic region of the poroelasto-plastic model, is overall a very significant factor as is the inclusion of plasticity.

with increasing q.

First we consider δa^{fl} (Figure 5.5, top left). For very small flows, when the material is still behaving poroelastically, $\delta a^{\mathrm{fl}} < 0$. For this range of q our simple model for transitioning from $A3$ to $M3$ is not realistic. As the model $A3$ is for a *cased* borehole, a negative δa^{fl} means the flow rate is not sufficient to support the pre-existing stress in the rock and that in reality the casing would still be supporting the solid; this simplified model therefore only makes sense for flows sufficient to separate the solid body from the permeable casing. We denote the value of q such that the entire solid stress is being supported by the fluid not the

casing but is still in contact with the casing q_{crit}. We have not accounted for the behaviour of the solid for $q < q_{\text{crit}} \approx 10^{-4}$ because the focus of this study is the impact of plasticity for which we require $q > q_{\text{min}} > q_{\text{crit}}$. For $q > q_{\text{crit}}$ the fluid flow pushes the inner cavity radially outwards and continues to expand the opening monotonically as q increases. Once q_{min} is reached, all the poroelasto-plastic models start to deform more than the poroelastic models, as is to be expected by consideration of Figure 5.2. Mirroring the behaviour of the deformation seen in Figure 5.2, the LL-k_0 model predicts the largest inner cavity and the QL-k_0 and QQ-k_0 models the least. In comparison to the poroelastic models in which δa^{fl} increases approximately linearly with q, for the poroelasto-plastic case δa^{fl} increases much more rapidly.

The other kinematic quantity considered is the maximum $\delta\phi^{\text{fl}}$ (Figure 5.5, top right). As expected for very small flow rates $\max\left(\delta\phi^{\text{fl}}\right)$ is very small; the poroelastic $\max\left(\delta\phi^{\text{fl}}\right)$ increases approximately linearly with increasing q, while the poroelasto-plastic maximum $\delta\phi^{\text{fl}}$ increases rather differently. From the models' respective q_{min} until around $q \approx 5.5 \times 10^{-4}$, the QL-$k_0$ and QQ-k_0 models predict a lower maximum $\delta\phi^{\text{fl}}$ than the poroelastic models; for q greater than this, the QL-k_0 and QQ-k_0 models predict a greater maximum $\delta\phi^{\text{fl}}$ than any of the other four models. This remains the case until $q \approx 1.1 \times 10^{-3}$ at which flow rate the LL-k_0 model predicts a greater maximum. The LL-k_0 and NQ-k_0 models predict a lower maximum $\delta\phi^{\text{fl}}$ than the poroelastic models from their respective q_{min} to $q \approx 7.3 \times 10^{-4}$, at which point the LL-$k_0$ model predicts that $\max\left(\delta\phi^{\text{fl}}\right)$ increases approximately logarithmically with q. The NQ-k_0 model however, does not predict such an extreme growth rate with increasing q, and predicts $\max\left(\delta\phi^{\text{fl}}\right)$ that is far closer to the poroelastic predictions than it is to the other poroelasto-plastic models.

Next we consider Δp (Figure 5.5, bottom left); this is a quantity that can be measured on site as the bottom-hole injection pressure. All models increase monotonically with increasing q; note that for moderate $q > q_{\text{min}}$ all models behave rather similarly with a noticeable difference only becoming visible around $q \gtrsim 6 \times 10^{-4}$. After this point the LL-k_0 model

increases linearly, as expected from Figure 5.2, with the other models predicting less of an increase. Again as inferred from Figure 5.2, the NQ-k_0 model predicts the lowest value and the QL-k_0 and QQ-k_0 models predict the intermediate value, although their behaviour is much more similar to the NQ-k_0 model than the LL-k_0 model.

Finally, we consider the maximum tensile effective stress due to fluid injection, $\max\left(\delta\sigma'^{,fl}\right)$ (Figure 5.5, bottom right). Firstly, note the two sharp transitions (discontinuities of the gradient) in the line; the first is within the poroelastic region; for small q the maximum value is given by $\delta\sigma_r'^{,\text{fl}}(a)$ which is fixed at 10^{-3}, then at $q \approx 10^{-4}$ the maximum switches $\delta\sigma_\theta'^{,\text{fl}}(a)$. The latter transition is unique to the poroelasto-plastic solution and this is when the maximum switches from being at the internal radius of the azimuthal effective stress to the elastic-plastic interface.

In Figure 5.6 we show the same four output quantities as presented in Figure 5.5 but for a fixed q and varying $-\sigma_b' \in (0, 2\times10^{-3})$. This shows the transition from an unconstrained cylinder to a cylinder subject to a compressive radial effective stress of magnitude 2×10^{-3}. This provides a direct link with the purely poroelastic cylinder that was the focus of Chapters 3–4, in which we considered only constrained and unconstrained cylinders, for the transition $M1 \mapsto M3$. With the exception of $\max(\delta\phi_f^{\text{fl}})$, the ordering of the respective models within each quantity is preserved. For $\max(\delta\phi_f^{\text{fl}})$, note that the internal ordering of the poroelasto-plastic and the poroelastic models is preserved and it is simply the case for $-\sigma_b' \approx 1.5\times10^{-3}$ that the LL-k_0 and NQ-k_0 models cross the two poroelastic models. From this plot we are able to see that as the model transitions from less (closer to zero) to more (increasingly negative) confining stress, the models all behave monotonically. Thus, we may use the results presented in Chapters 3–4 to infer the behaviours that we may expect for a poroelasto-plastic cylinder modelled with a varying permeability, for example. In Figure 3.5 we see all quantities for an unconstrained poroelastic cylinder subject to a fixed pressure difference. Although we see that all quantities are exacerbated by the addition of a deformation-dependent permeability law, consider the flow rate; the respective q for

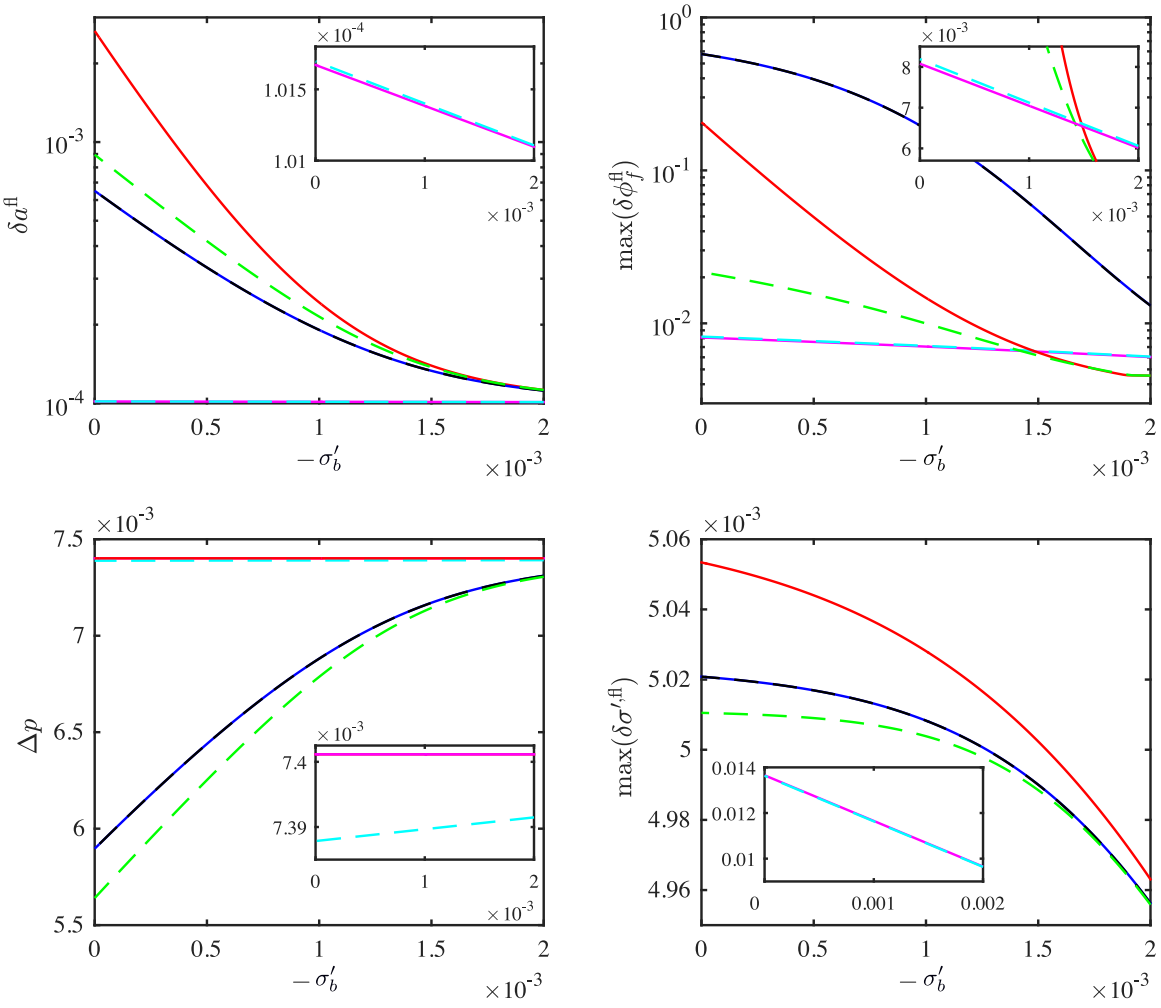

Figure 5.6: The four output quantities as presented in Figures 5.5, with the same line colours as Figures 5.2–5.3 and 5.5, plotted against varying $-\sigma'_b$. The main figure focusses on the poroelasto-plastic solution while the inset focuses on the poroelastic behaviour. This figure provides a direct link with the fully permeable poroelastic unconstrained cylinder that was the focus of Chapters 3–4. Since these quantities are well behaved as σ'_b transitions from zero to -2×10^{-3} we are able to infer that conclusions drawn about the unconstrained poroelastic cylinder in Chapters 3–4 are likely to be true for all relevant σ'_b.

given a Δp is 3–4 times larger for varying permeability compared to constant permeability. Therefore for a fixed q, as is the case in this section, we expect the varying permeability to reduce the effective pressure difference, as has the addition of nonlinear plastic flow. Hence, for the combination of plastic flow and varying permeability we would expect less deformation, stress and porosity accordingly.

5.5.2 Impermeable to fully permeable: fixed σ_a

In Figures 5.7–5.9 we consider varying the permeability-load parameter $\zeta \in [0, 1]$ which transitions the model from being impermeable ($\zeta \equiv 0$) to fully permeable ($\zeta \equiv 1$) for a fixed total applied stress at the inner boundary of $\sigma_a = -0.0075$. This value is chosen so that for all ζ it remains between $\sigma_a^{\min}$ and $\sigma_a^{\max}$. Once again we focus on the change in the displacement due to fluid injection by subtracting a reference state that is independent of ζ. Note that once again the QL-k_0 and QQ-k_0 models are indistinguishable.

In Figure 5.7 and 5.8 we fix four values of ζ ranging from near impermeable ($\zeta \approx 0$) to almost fully permeable ($\zeta \approx 1$). We conceptualise this by imagining a membrane on the inner cavity wall that increases in permeability as ζ increases, effectively spreading the total load between a mechanical stress at the inner cavity wall and an effective body force throughout the material. Once again we produce Figure 5.8 for reference — Figure 5.8 is the same as Figure 5.7 but plotted without the subtraction of the reference state.

For the poroelastic model (left column) there is a significant qualitative and quantitative change in the model as ζ is varied; every quantity increases as ζ increases, implying that loading via a pore-pressure gradient is a far more effective loading mechanism than purely mechanical loading. For every quantity the L-k_0 and Q-k_0 models are practically indistinguishable. The displacement δu_s^{fl} (second row) attains a very similar value at the cavity wall for all ζ, implying that the loading mechanism makes very little difference to the size of the cavity. However, for larger R the magnitude of δu_s^{fl} strongly increases with ζ. For the smallest $\zeta \approx 0.002$ the displacement attains its maximum at the inner cavity wall and

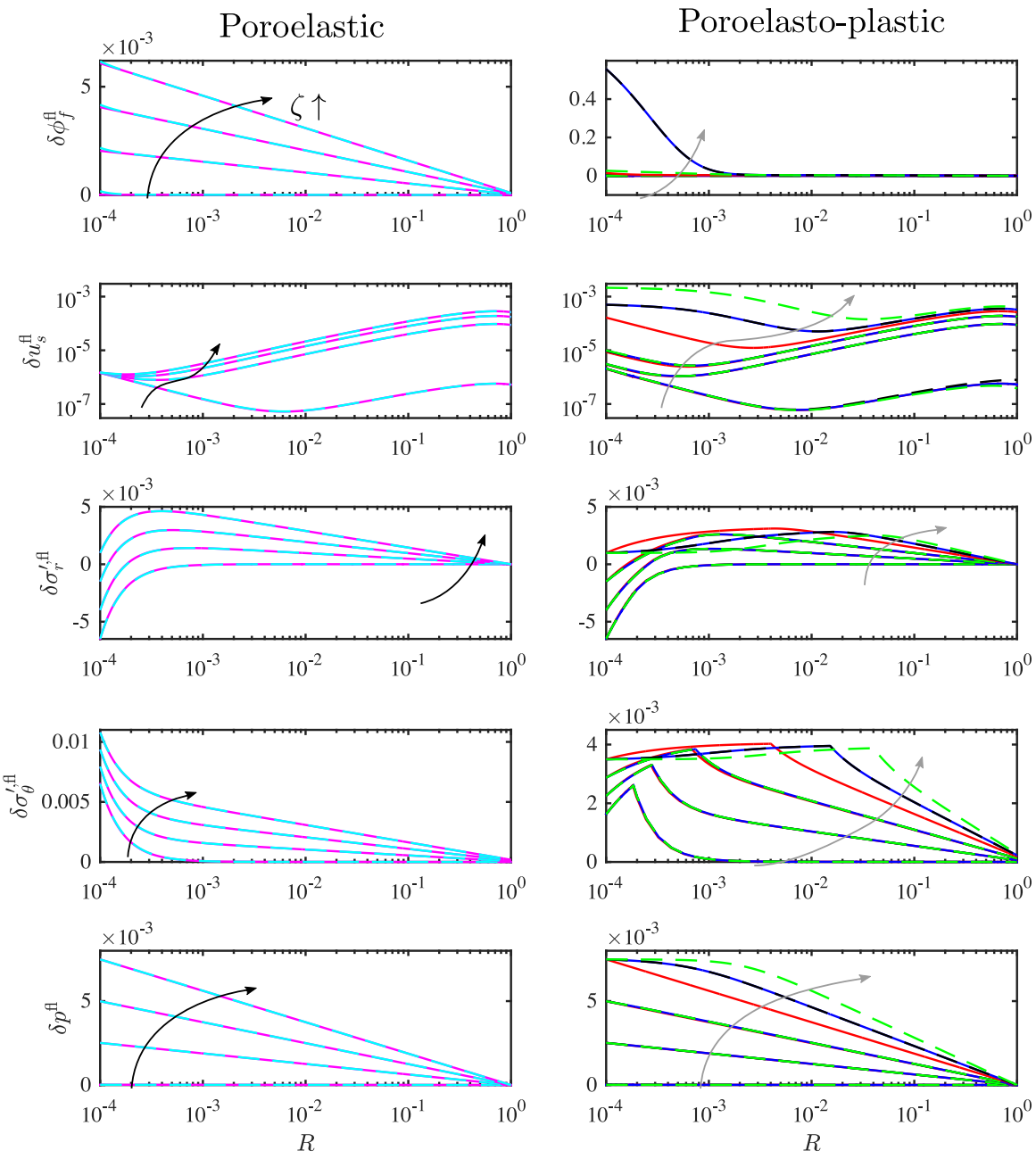

Figure 5.7: As in Figure 5.2 we plot two poroelastic (left column) and four poroelasto-plastic models (right column); we plot these for four values of increasing $\zeta \in \{0.002, 0.335, 0.665, 0.998\}$ for fixed $\sigma_a = -7.5 \times 10^{-3} \in (\sigma_a^{\max}, \sigma_a^{\min})$ for all ζ. The line colours are the same as in Figures 5.2–5.3 and 5.5–5.6. Note that while there is no discernible difference between the two poroelastic models there is a significant difference between the poroelasto-plastic models but only for sufficiently large ζ. Also note that driving via a body force is a more efficient driving mechanism than purely mechanical driving.

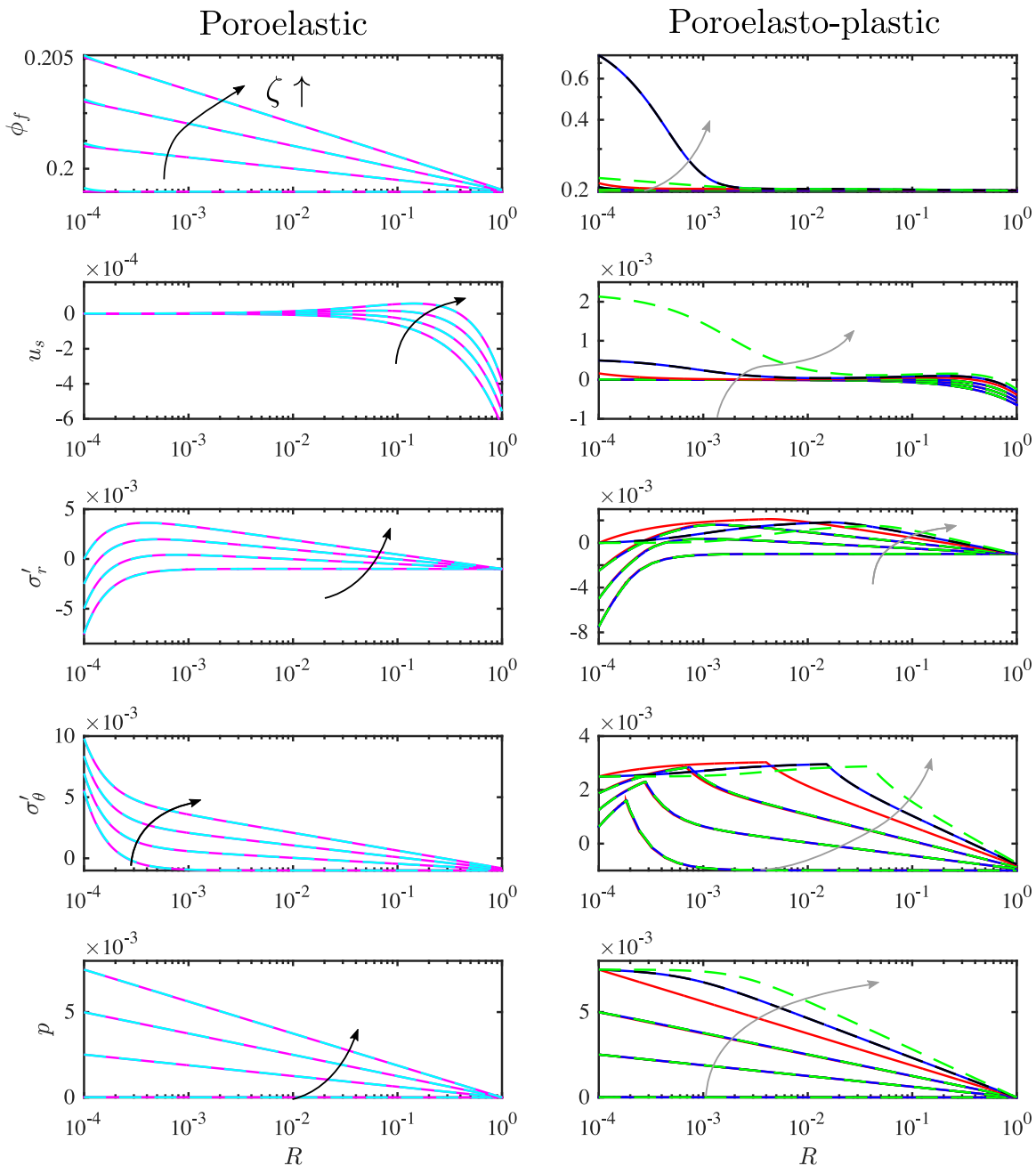

Figure 5.8: Figure 5.7 plotted for the transition $M1 \mapsto M3$ as opposed to $A3 \mapsto M3$. The line colours are the same as those defined in Figures 5.2 – 5.3 and 5.5–5.7. The porosity is plotted logarithmically in an attempt to view the behaviour near the inner boundary for all values of ζ.

interior minimum, while for the other values of ζ, there is a qualitative change in δu_s^{fl} such that both maxima become interior points, as is the case in the fully permeable limit (*cf.* Figure 5.2, left column, second row). As ζ increases the internal minimum moves closer to the cavity wall while the internal maximum located near the outer boundary remains in roughly the same place. Although it appears that the displacement fields get closer together as ζ increases this is an artefact of the logarithmic vertical scale. The radial effective stress due to fluid driving (third row) vanishes at the outer boundary by construction. At the inner boundary $\delta\sigma_r'^{,\text{fl}}$ is fixed, courtesy of the boundary condition and reference state, to be $(1-\zeta)\sigma_a - \sigma_b'$ and this increases (transitions from negative to positive) as ζ increases because $\sigma_a, \sigma_b' < 0$. As ζ increases the graph effectively pivots about the constant outer boundary value such that for small ζ the maxima is at the outer boundary but for some $\zeta \in (0.002, 0.335)$ this transitions to an internal maxima and, similarly, for some $\zeta \in (0.665, 0.998)$ the minima transitions from the inner boundary to the outer boundary. For all values of ζ, $\delta\sigma_\theta'^{,\text{fl}}$ (fourth row) exhibits the same qualitative behaviour as observed for the fully permeable case (*cf.* Figure 5.2, left column, fourth row). By construction, $\delta\Delta p^{\text{fl}}$, the value of δp^{fl} at the inner radius, is given by $-\zeta\sigma_a$ and δp^{fl} vanishes at the outer boundary. For all values of ζ the pressure decays logarithmically for increasing R.

In comparison for the poroelasto-plastic case (right column) there is a noticeable difference in models as ζ approaches unity. The porosity grows suddenly as zeta increases; note that $\delta\phi_f^{\text{fl}}$ is actually negative for small ζ signifying that the pressure induced in the cavity by the fluid causes less of an increase in porosity than the purely mechanical deformation of the rock due to the external applied effective stress. We plot the raw quantities, that is the quantities without the subraction of the reference state, in Figure 5.8 for reference. For $\zeta \approx 0.998$, the QL-k_0 and QQ-k_0 models both attain a significantly higher $\delta\phi_f^{\text{fl}}$ than the NQ-k_0 model which is the next highest, and LL-k_0 model the smallest. This is different from the behaviour seen in Figure 5.2 due to the fact that this model is driven via a fixed σ_a at the inner boundary and not fixed q. From Figure 5.9 note that the NQ-k_0 model predicts

the highest flow rate for given σ_a and the LL-k_0 model the least, although this effect only becomes significant as ζ approaches 1.

For small ζ, the poroelasto-plastic displacements are not very large, minimising the importance of model choice, whereas as ζ increases, the magnitude of the displacement near the inner cavity wall increases significantly, which means that model choice, in particular kinematics, becomes significant (see Figure 5.2 second row). This is not the case for the poroelastic models where, for all ζ, displacements near the cavity remain small. The increase in deformation as ζ increases manifests itself as a larger plastic region as can be clearly seen from $\delta\sigma'^{,\text{fl}}_{\theta}$ (right column, fourth row). In general, the displacement due cavity pressurisation for small ζ is very similar both qualitatively and quantitatively to the poroelastic model. For $\zeta \in \{0.002, 0.334, 0.665\}$ we have the an internal minimum for all models and for $\zeta \approx 0.002$ the maximum is at the inner boundary, while for the intermediate values of ζ the maximum is internal and close to the outer boundary. For $\zeta \approx 0.997$, there is a large discrepancy between the models for small R which decreases with increasing R. The NQ-k_0 model predicts the largest $\delta u^{\text{fl}}_s(a)$ and the LL-k_0 model the least, again due to the fact that for a fixed σ_a the associated q for the NQ-k_0 model is greatest and the associated q for the LL-k_0 model is the smallest.

The radial and azimuthal effective stresses due to fluid injection both depict a non-monotonicity as ζ increases, for the QL-k_0, QQ-k_0 and NQ-k_0 models, but not the LL-k_0 model. In both cases for the first three values of ζ we observe monotonicity for all R for increasing ζ. Note that for the elastic region of the poroelasto-plastic solution, the models are monotonic in ζ. For $\delta\sigma'^{,\text{fl}}_{r}$, the overall qualitative behaviour of the models is similar for the first three values of ζ; increasing from the minimum value, which is once again prescribed by the boundary condition and subtraction of the reference state, to an internal maximum and then decreasing approximately logarithmically towards the outer cavity. For $\zeta \approx 0.997$ in the plastic region there exists a range of R such that $\delta\sigma'^{,\text{fl}}_{r}(\zeta \approx 0.997) < \delta\sigma'^{,\text{fl}}_{r}(\zeta \approx 0.665)$.

Via consideration of $\delta\sigma_\theta'^{,\text{fl}}$, we can clearly see the location of s, the elastic-plastic interface. As noted above, s increases with increasing ζ, reinforcing that stress applied as an effective body force through the pore structure is more efficient than mechanical loading at the inner boundary. Note also that for $\zeta \approx 0.997$ the predicted location of s is significantly nearer the outer cavity wall for the more nonlinear models; between the LL-k_0 predication of $R = s_0$ and the NQ-k_0 predication of s_0 there is one full order of magnitude difference.

The poroelasto-plastic pressure field is similar to the poroelastic pressure field. For all but the largest value of ζ there is no visible difference between the six models, and for $\zeta \approx 0.997$ the LL-k_0 model is the same as the poroelastic L-k_0 model. By construction $\delta\Delta p^{\text{fl}}$ is once again fixed. For $\zeta \approx 0.997$ for the QL-k_0, QQ-k_0 and the NQ-k_0 models their pressure fields do not decay approximately logarithmically for all R but rather stays at a higher pressure for more of the annulus, the effect being increased as more facets of nonlinearity are added to the model.

In Figure 5.9 we depict the same four summary quantities as presented in Figures 5.5 and 5.6; now, instead of varying the driving strength or confining stress, which are fixed ($\sigma_a = -0.0075$ and $\sigma_b' = -10^{-3}$), we now vary ζ from impermeable ($\zeta \equiv 0$) to fully permeable ($\zeta \equiv 1$). The main figures focus on the poroelasto-plastic solution while the insets focus on the poroelastic behaviour. Note that for q and $\max\left(\delta\sigma'^{,\text{fl}}\right)$ as their relative sizes are quite different for the poroelasto-plastic and poroelastic models, they do not appear on the same axis. As inferred from Figure 5.7, but now seen for a continuous range of ζ values and output quantities in Figure 5.9, it is clear that poroelasto-plastic model choice is insignificant for sufficiently small ζ, which, for this set of parameters, is $\zeta \lesssim 0.55$.

We consider δa^{fl} (Figure 5.9, top left), the increase in cavity size due to fluid injection, as a measure of the displacement for varying ζ in each of the six models. Note that both the poroelastic and poroelasto-plastic models have the same general trend — δa^{fl} increases with increasing ζ, although this effect is clearly more pronounced in the poroelasto-plastic case. Also the difference between the Q-k_0 and L-k_0 model remains approximately con-

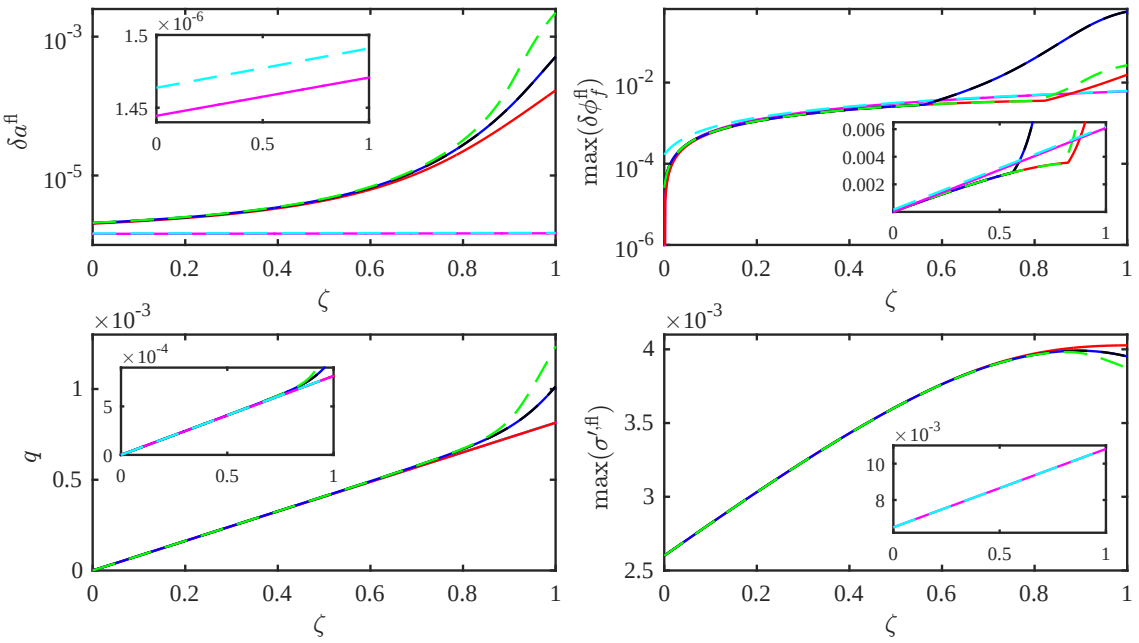

Figure 5.9: The same four quantities shown in Figure 5.5, but now for fixed $\sigma_a = -0.0075$ and varying ζ from impermeable ($\zeta = 0$) to fully permeable ($\zeta = 1$); once again the main figure focusses on the poroelasto-plastic response and the insets on the poroelastic behaviour. The line colours are the same as in Figures 5.2–5.3 and 5.5–5.8. Note that displacement is not only significantly greater with the inclusion of plasticity but an increased ζ also significantly increases the deformation. Note that while δa^{fl}, $\max(\delta\phi_{f,0}^{\mathrm{fl}})$ and q increase monotonically with ζ for all six models, $\max(\delta\sigma'^{,\mathrm{fl}})$ is in fact maximised for $\zeta < 1$ for the three nonlinear poroelasto-plastic models.

stant with both models increasing approximately linearly with increasing ζ, although this increase is not significant. In line with the general trend, for the poroelasto-plastic case model choice becomes significant for sufficiently large ζ with the NQ-k_0 model predicting the most displacement and the LL-k_0 the least. Note that unlike the poroelastic case δa^{fl} increases quicker than exponentially with increasing ζ.

The maximum increase in porosity due to fluid injection (Figure 5.9, top right) exhibits the most significant difference between the L-k_0 and Q-k_0 poroelastic models and this difference is at its greatest in the limit $\zeta \to 0$. For $\zeta = 0$, the value $\max\left(\delta\phi_f^{\mathrm{fl}}\right)$ differs by seven orders of magnitude. This discrepancy between linearised kinematics and rigorous kinematics is also apparent for the poroelasto-plastic models which have six orders of mag-

nitude difference between the two extremum (the NQ-k_0 and the LL-k_0) models. For the poroelastic models, unlike the poroelasto-plastic models, this visible discrepancy between model choices is not isolated to limiting behaviour $\zeta \to 0$, but the models remain clearly distinguishable until $\zeta \sim 0.2$. Both poroelastic solutions increase approximately linearly with increasing ζ and in fact predict a greater $\max\left(\delta\phi_f^{\text{fl}}\right)$ than any poroelasto-plastic model until $\zeta \approx 0.6$, at which point the QL-k_0 and QQ-k_0 models predict a significantly greater value which only diverges further as ζ increases; unlike the general trend these two models predict the greatest value of $\max\left(\delta\phi_f^{\text{fl}}\right)$. For $0.1 \lesssim \zeta \lesssim 0.6$ all the poroelasto-plastic models are practically indistinguishable and the NQ-k_0 and LL-k_0 models remain essentially indistinguishable until $\zeta \approx 0.8$. It is only for $\zeta \gtrsim 0.8$ that the LL-k_0 and NQ-k_0 models predict a larger value of $\max\left(\delta\phi_f^{\text{fl}}\right)$ than the poroelastic models, after which the LL-k_0 model grows approximately exponentially with ζ; the NQ-k_0 model predicts a larger value than the LL-k_0 model for all $\zeta \gtrsim 0.8$.

We consider how q varies with ζ and the effect model choice has on this (Figure 5.9, bottom left). For the majority of $\zeta \lesssim 0.55$ all models are essentially the same; q increases (approximately) linearly with ζ. For all models, $q = -\frac{\zeta\sigma_a}{\ln\left(\frac{b}{a}\right)}$ and thus by construction, the flow rate vanishes in the limit $\zeta \to 0$ and is pinned to $q = \frac{\Delta p}{\ln\left(\frac{b}{a}\right)} = -\frac{\sigma_a}{\ln\left(\frac{b}{a}\right)}$ in the fully permeable limit. Note that in general q is a function of a and b and thus is effected by the displacement field and hence model choice. However, the flow rate predicted by the L-k_0 and LL-k_0 models is identical for all ζ by the definition of $q = \frac{\zeta\sigma_a}{\ln(a_0)}$. Similarly for small strains, such as occur in the Q-k_0 model, the value of q will be very close to these linearised models. As discussed earlier the NQ-k_0 model experiences the largest flow rate for a fixed stress or pressure drop; this is because the displacement at the inner cavity is the greatest as is the ratio of outer radius to inner radius and the LL-k_0 model the lowest as $a \equiv a_0$ and $b \equiv 1$.

The maximum tensile effective stress induced by fluid flow (Figure 5.9, bottom right), demonstrates one of the key differences between the poroelastic and poroelasto-plastic

models: the magnitude of the stress. The poroelastic maximum tensile effective stress is around three times greater than the maximum poroelasto-plastic tensile effective stress for all ζ. The poroelasto-plastic stress is significantly lower as energy is allowed to dissipate through rearrangements of the skeleton structure and does not solely have to be stored as elastic potential energy. The poroelastic maximum tensile effective stress induced by fluid flow increases approximately linearly with increasing ζ. For $\zeta \lesssim 0.7$ poroelasto-plastic model choice has no visible impact on $\max(\delta\sigma'^{,\mathrm{fl}})$; for $\zeta \gtrsim 0.7$ model choice impacts the behaviour not only quantitatively but qualitatively too. The LL-k_0 model is the only model that predicts a monotonic increase in $\max(\delta\sigma'^{,\mathrm{fl}})$ for all ζ; the QL-k_0 QQ-k_0 and NQ-k_0 models all have an interior maximum for $\zeta \approx 0.9$ with the NQ-k_0 model's maximum arising for slightly smaller ζ than for the QL-k_0 and QQ-k_0 models. Note that the ordering of models is reversed for the stress quantity considered here compared to the the displacement quantity (Figure 5.9, top right), which reinforces the link that as larger displacements are enabled by the inclusion of plasticity, more energy is dissipated and therefore the lower the stress. This also leads to an optimum value of ζ for which the maximum tensile effective stress in a poroelasto-plastic material is achieved, which could either be desirable for applications like hydraulic fracturing into ductile shales, or avoided for borehole integrity applications.

5.6 Conclusion

Despite the clear importance of fluid-driven deformation from a borehole to problems in borehole integrity and cavity expansion, a kinematically rigorous poroelasto-plastic model has not previously been examined in detail. To assess the importance of plasticity and of large deformations, we developed four poroelasto–perfectly-plastic models: classical linear poroelasto-plasticity (LL-k_0) (*i.e.,* with linear elasticity, linear strains and linearised kinematics in both regions); linear elasticity with linear strains coupled with rigorous kine-

matics in either just the plastic or both regions (QL-k_0 and QQ-k_0, repectively); and a nonlinear model in which the strain-displacement relationship is logarithmic and the kinematics are treated rigorously in both regions coupled with linear elasticity (NQ-k_0). These we compare with each other as well as two poroelastic models: classical linear poroelasticity (L-k_0); and linear elasticity coupled with rigorous kinematics (Q-k_0).

We fix a set of parameter values that broadly describe a ductile but prospective shale (*i.e.*, a shale that is a good candidate for fracking) and vary the flow rate. Figures 5.2–5.3 and 5.5–5.6 illustrate that the inclusion of plasticity makes model choice more important — for the same driving flow rate there is no visible difference between the poroelastic L-k_0 and Q-k_0 models, while for the poroelasto-plastic models there is considerable difference between the models, most notably between the LL-k_0 and QL-k_0 models. This is because plasticity allows for large deformations which inherently violate the small-strain linearisation. However, we see that this is isolated to the plastic region and, as such, linearising the kinematics in the elastic region is valid, demonstrated clearly by the fact that the QL-k_0 and QQ-k_0 models are indistinguishable (Figures 5.2–5.9), while linearising in the plastic region leads to unphysical solutions (Figure 5.2–5.3 and 5.4). Note also that the elastic region remains relatively insensitive to large perturbations within the plastic region. Figure 5.6 allows us to make links between an unconstrained cylinder and the case $\sigma_b' \not\equiv 0$, as all quantities are well-behaved, increasing monotonically with decreasing magnitude of σ_b'.

Currently, models for low permeability materials such as shale are either treated as fully permeable or impermeable; here we propose a permeability-load parameter ζ that allows for a smooth transition between these limiting states —we liken this mechanism to applying a thin weak skin at the cavity wall of varying permeability. For a fixed applied total stress, as we vary the loading mechanism from purely mechanical ($\zeta \equiv 0$) to a pore-pressure gradient ($\zeta \equiv 1$), the material undergoes more deformation (Figures 5.7 – 5.9). That said, the maximum tensile effective stress attained does not mirror this and is at its greatest for an intermediate value of ζ, such that the scenario of a borehole with a slight

reduction in permeability at the cavity wall experiences the greatest effective stress. Since the deformation increases monotonically as ζ increases, the choice of poroelasto-plastic models becomes increasingly significant as the loading mechanism transitions from mechanical to a pore-pressure gradient. Specifically for the parameters considered here, for a fixed applied total stress, it is only when $\zeta \sim 0.8$ that there is any noticeable difference between the four poroelasto-plastic models. This study shows there is a significant qualitative and quantitative difference, for the given parameters, in the behaviour of a material subject to mechanical loading versus a material deformed by fluid flow. As such, boreholes that have been treated with wall-building chemicals and extremely low permeability rocks (which currently are modelled as either impermeable or fully permeable), are probably best modelled with an intermediate ζ.

Chapter 6

Overall discussion and conclusions

In this thesis we have developed and solved ten distinct models for fluid injection into the central cavity of a porous cylinder in plane strain. We have presented the first systematic analysis of the effects of driving method, geometry and numerous facets of nonlinearity on the resulting solid deformation. We have considered two different constitutive laws for permeability (constant *vs.* Kozeny-Carman), two constitutive solid behaviours (elasticity *vs.* elasto-plasticity); within the purely poroelastic scenario we considered two distinct elastic constitutive laws (Hencky *vs.* linear) and within the poroelasto-plastic scenario we considered two stress-strain relationships in the plastic region (logarithmic or 'Hencky' *vs.* linear), while retaining linear elasticity in the elastic region. Nonlinear effects manifest themselves within the kinematics, permeability, and elastic or plastic stress-strain relations, and by isolating the effects of each of these we have gained extensive insight into the validity of various simplifying assumptions. For example, in a poroelasto-plastic thick-walled annulus subject to a constant compressive far-field radial effective stress, which is a well-established model for soils, linearising the kinematics in the plastic region leads to unphysical results for even moderate driving strengths, while linearising them in the elastic region makes little difference while simplifying the model by reducing the number of free boundaries. Additionally we introduced a permeability-load parameter ζ that smoothly

transitions the model from impermeable to 'fully' permeable, likening this addition to the inclusion of a thin, weak skin at the inner cavity.

This thesis highlights the global physical factors that are present across all models and are thus applicable to the full range of applications from arteries to boreholes. A key contribution of the models presented here is the insight they provide into the physics of radially outward flow and resulting poromechanical deformations. Additionally, the relative simplicity of each model allows us to examine the implications of these numerous different constitutive and modelling choices in detail by running thousands of different simulations across a wide range of scenarios which is tractable only as these models are much less computationally expensive than detailed material-specific simulations.

In Chapter 2, we first developed the theory of poromechanics in plane strain for axisymmetric deformations subject to fluid injection from a line source. We coupled this to mechanical equilibrium, neglecting body forces and inertia, and to Darcy's law which is the iconic relation for modelling flow through a porous medium. Thus far, the equations are independent of the constitutive choices of permeability law and of stress-strain relations. In the latter half of Chapter 2 we then focussed the purely poroelastic problem and considered two different elastic constitutive relations. We introduced two distinct sets of boundary and driving conditions and culminated the chapter with the presentation of the closed poroelastic IBVP in terms of the displacement for six distinct model combinations which is the focus of Chapters 3 and 4. We find that the relative importance of these facets of nonlinearity is nontrivially linked to the wall-thickness. As such, it is very difficult to draw general quantitative or even qualitative conclusions about the impacts of various simplifications on the transient evolution and resulting steady-state.

In particular in Chapter 3, we focused on the steady-state response of a fully permeable poroelastic annulus to sudden fluid injection; we focussed in particular on one model (rigorous kinematics, linear elasticity and Kozeny-Carman permeability) which exhibits the same qualitative behaviour as the most complex poroelastic model considered in this the-

sis. We believe this model demonstrates the best balance between computational efficiency, accuracy and robustness. We used this model to examine the full range of geometries (very thin walls to very thick walls), for both a constrained and an unconstrained cylinder. For the unconstrained cylinder we found the existence of two steady states attained for the same pressure difference for two distinct flow rates, and through consideration of the transient evolution of the system as developed in Chapter 4, we hypothesise that only one of these is stable; note that details of this are not included in this thesis. For the constrained cylinder we found that there exists an intermediate cylinder thickness for which the most displacement is achieved.

The focus of Chapter 4 was on the transient evolution of fully permeable poroelastic annuli subject to sudden fluid injection. We first illustrated the strong qualitative and quantitative impacts of driving method by once again considering the intermediate model which coupled rigorous kinematics and Kozeny-Carman permeability with the simplification of linear elasticity. For a constrained cylinder we showed that certain wall thicknesses lead to a non-monotonic time evolution of the displacement and resulting azimuthal stress for all models, even classical linear poroelasticity, when driven by a fixed pressure difference. We also examined in great detail the effect both model choice and driving mechanism has on the evolution timescale. We find that for all but the thinnest constrained cylinders, driving with a fixed pressure difference is far quicker than driving via a fixed flow rate. Additionally, we illustrated the complex impact of model choice and geometry on the evolution timescale.

In Chapter 5, we introduced plasticity into the model via perfect plasticity, a simple cohesive Mohr-Columb yield condition and a non-associated flow law. We combined this with the pre-existing kinematic framework developed in Chapter 2 to study steady-state poroelasto-plastic deformation of a cohesive granular annulus subject to fluid injection through the inner cavity. We developed solutions for four distinct (poro)elasto-plastic model combinations: LL-k_0, QL-k_0, QQ-k_0 and NQ-k_0, as detailed in §5.2.3. The in-

troduction of ζ is useful for modelling boreholes that have a clogged damage zone local to the cavity wall, or for situations where wall-building chemicals have been used to artificially create a low permeability zone local to the cavity wall and allow the cavity to be propped open with fluid pressure. We used these models to investigate the relative importance of plasticity, kinematic nonlinearity and the permeability-load parameter. We found that the inclusion of plasticity enables larger deformations and as such linearising the kinematics in the plastic region can lead to unphysical solutions, while the linearisation of the kinematics in the elastic region makes little difference. In general, we found that the elastic region is quite insensitive to even significant changes in the plastic region. Transitioning the permeability-load parameter from impermeable to fully permeable leads to larger deformations in both the purely poroelastic and poroelasto-plastic models, making model choice more significant.

Throughout this thesis, we developed analytical solutions where tractable while consistently using Chebyshev spectral collocation to solve the free- or moving-boundary (I)BVPs. In Chapter 3, we introduced spectral collocation and in particular Chebyshev spectral collocation. We discussed the use of Chebyshev points versus equispaced collocation points and defined the Chebyshev differentiation matrices used throughout. We explained the numerical solution method of using a Chebyshev-pseudospectral framework to discretise the BVP, reducing it to a system of nonlinear algebraic expressions (the residual) which we solved via Newton iteration. We presented a convergence study for classical linear poroelasticity and summarised the complex analysis used to determine the rate of convergence. In Chapter 4, we discussed the extension of our Chebyshev collocation method to solve a moving-boundary IBVP. We approached the transient problem via the method of lines, that is we discretised the domain in space using Chebyshev nodes and solved the resulting system of differential algebraic equations with an inbuilt `MATLAB` ODE solver (`ode15s`). We used quadrature with Lobatto's integral formula to incorporate the integral constraint that arises from driving the system via a fixed pressure difference as opposed to a fixed

flow rate. In Chapter 5, we applied the Chebyshev spectral collocation framework to this problem, now consisting of a coupled free-boundary domain with two distinct governing ODEs. In doing so, we once again used Newton iteration with one residual function and associated Jacobian, but also solved for the position of the elastic-plastic interface within this structure as opposed to simply using a constraint on the interface to update the solution domain as we did for the two material boundaries.

The relatively generic and simple models we have developed are valid for arbitrarily large deformations, which is relatively rare within the field of poromechanics. As such, the codes developed here will be a useful resource for benchmarking more complex, material- and application-specific numerical simulations. Below, we discuss some possible extensions of the body of work presented in this thesis with some thought given to a couple of particular applications.

As discussed above, the two main simplifications used here are plane strain and axisymmetry. Relaxing either simplification leads to a coupled system of PDEs, even for the purely poroelastic case in steady state. Conveniently, such systems can also be solved via pseudospectral methods. In Chapter 5, we constructed a simple model for a cylindrical section of the subsurface and used this to isolate the effects of fluid injection from a cavity into the surrounding pre-stressed soil or rock. The pre-existing principal stresses typically differ by less than one order of magnitude so we assumed the stresses in plane to be equal while the out of plane stress was determined by the constraint of plane strain. Of course it makes little physical sense to assume that the direction of drilling must be in the direction of the distinct principal stress, while the two in plane principal stresses are equal. Ideally, we would like to assume an arbitrary pre-existing stress state, which could prove very fruitful in examining the behaviour in various areas subject to different pre-existing tectonic stress fields.

There are of course, many obvious extensions leading on from this kinematically rigorous framework. As discussed, we chose to consider relatively generic constitutive laws

that would be applicable to many materials across a wide range of applications. If one wished to address a specific application then there are many constitutive choice that could be made to more aptly describe the specific material. For example, most soils exhibit some strain-softening or -hardening behaviours and as such perfect plasticity classically over- or under-estimates the resulting stresses, respectively. In fact rocks, concrete and soils in compression typically all exhibit qualitatively the same triaxial test results characterised by a weak elastic behaviour followed by initial strain hardening and then resulting strain softening behaviour [98]. This is most pronounced in densely packed sands and rocks subject to small confining stresses while somewhat suppressed in loosely packed sands or rocks subject to high confining stresses, and as a result, perfect-plasticity is a better model for the latter scenario as opposed to the former [98]. To deal with this Vermeer and Borst [98] present a hardening-softening model unifying granular materials. As well as considering whether a soil or rock undergoes any strain-softening or hardening, the choice of yield criterion is heavily influenced by the specific material to be modelled. On generalisation to three-dimensions, alternative yield criteria include a Drucker-Prager model, which is an appropriate model choice for soft clays with low friction angles but not sands, or a Cam-Clay or modified Cam-Clay model both of which are readily used to model soft soils or clays [20, 98]. Similarly, more material specific permeability and elasticity laws can be considered for particular materials and applications.

Even with the relative simplicity of the chosen yield criterion and the use of perfect plasticity, a poroelasto-plastic model is structurally quite challenging, having two distinct constitutive behaviours in distinct domains coupled by a free boundary. As such, it would be interesting to see if a damage model could be developed that satisfactorily described the behaviour of a poroelasto-plastic model to simplify this aspect. The results presented here could be used to inform the development of such a model. As the domain would be significantly simplified by use of such a damage model one may then be able to investigate more complicated geometries or background stress states that may bear more direct relevance to

boreholes, due to the increased numerical simplicity of the problem. Additionally, using the damage model requires fewer assumptions to be made about the shape and location of the elastic-plastic transition region enabling more complex behaviour which would be intractable for a classical plasticity model.

Although poroelastic and poroelasto-plastic models have been relatively widely used in the contexts of subsurface flows and biomechanics they are very rarely used in the design of filters, with filters being commonly modelled as rigid structures. Optimising filter design is an active area of research across a huge spectrum of fields. Additionally, radial filter design has had relatively little attention, but could prove promising [24, 43, 44] and this will be the focus of my next research project.

Appendix A

MATLAB codes for L-k_0 and Q-k_{KC} models: constrained cylinder

```
% Set number of grid points
N = elasticpar.N;
%%%%%%%%%%%%%%%%%%%%%%%%%%%%%%%%%%%%%%%%%%%%%%%%%%%%%%%%%%%%%%%%%%%%%%%%%%%%
% Unpack physical parameters
a0 = elasticpar.a0; b0 = 1; Gamma = elasticpar.gamma;
q = elasticpar.q; dp = elasticpar.dp;
% Determine q if dp is prescribed instead
if strcmp(elasticpar.qVSdp,'dp')
    q = dp/log(1/a0);
end
%%%%%%%%%%%%%%%%%%%%%%%%%%%%%%%%%%%%%%%%%%%%%%%%%%%%%%%%%%%%%%%%%%%%%%%%%%%%
% Build Chebyshev differentiation matrices
[X,D] = chebdif(N,2);
i = [2:N-1];
I = eye(N);
%%%%%%%%%%%%%%%%%%%%%%%%%%%%%%%%%%%%%%%%%%%%%%%%%%%%%%%%%%%%%%%%%%%%%%%%%%%%
r = -(1-a0)/2*X + (1+a0)/2; %Map Chebyshev domain to
% [a0, 1] such that when X=1, r=a_0 and X=-1 r=1
dXdr = -2/(1-a0);
E1 = dXdr*D(:,:,1);%Scale differentiation matrices
E2 = (dXdr^2)*D(:,:,2);
% Solve Lk0 BVP (zero disp) in one line with `\'
u = [ E1(1,:)+(Gamma/a0)*I(1,:); ...
    (E2(i,:)+diag(1./r(i))*E1(i,:)-diag(1./r(i).^2)*I(i,:)); ...
    I(N,:)]\[0;-q./r(i);0];
```

Published with MATLAB® R2015a

Here we show the MATLAB code used to numerically solve the L-k_0 model (above) and the Q-k_{KC} model (below) for the constrained cylinder. We solve both models numerically

via Chebyshev spectral collocation. The L-k_0 model is solved like this for merely illustrative purposes as, of course, we have an explicit analytical solution (see §3.1.1). Note that `chebdif`, provided by Weideman and Reddy [107], produces the differentiation matrices `D` and the Chebyshev points `X`$\in [1, -1]$ in line with their definitions provided in Equations (3.24) and (3.22), respectively. Since these Cheybshev nodes run from 1 to -1 we use the scaling

$$x \mapsto r = \frac{b+a}{2} - \frac{b-a}{2}x, \tag{A.1}$$

in lieu of the scaling $r = \frac{b+a}{2} + \frac{b-a}{2}x$ as provided in Abramowitz and Stegun [1] and used in Bjørnarå and Mathias [15], so that $r \in [a, b]$ and not $[b, a]$ (*i.e.,* $x = 1$ maps to a and not b; see Appendix C).

The code loads the parameter values, determines q if Δp is prescribed instead, loads and scales the Chebyshev nodes and differentiation matrices, before solving the problem with a simple backslash. We construct a residual for Equation (3.1) for the L-k_0 model, by discretising the continuous variables and replacing the derivatives with the scaled differentiation matrices. We enforce the boundary conditions by replacing the first and last entries with the discretised boundary conditions. Note that the problem is solved in one line of code (last line of code — split across the last three lines in the above to aid presentation).

For the highly nonlinear Q-k_{KC} code we can no longer solve the BVP in one line and must instead use iteration to determine the solution. At each time step we re-map the Chebyshev domain $[1, -1]$ to the updated radial domain $[a, b]$, rescaling the differentiation matrices accordingly. As before we define a residual `F`(u_j) and its Jacobian matrix $\frac{\mathrm{d}}{\mathrm{d}u_i}\big(\texttt{F}(u_j)\big)$. We do this analytically and note that as we have a free boundary this causes a 'hidden' dependency on `u` for which the Jacobian must account — that is every time `a` appears explicitly in the equation we must write `a=u(1)+a0` and treat it accordingly. Once these quantities have been calculated, we update `u` via the use of backslash on the Jacobian and residual, subtracting this result this from the current `u`. This process repeats until `u` has both converged sufficiently and satisfies the residual to within a specified tolerance.

```
% Constrained QkKC model: Set number of grid points
N = elasticpar.N;
%%%%%%%%%%%%%%%%%%%%%%%%%%%%%%%%%%%%%%%%%%%%%%%%%%%%%%%%%%%%%%%%%%%%%%%%%%%%
% Unpack physical parameters
a0 = elasticpar.a0; b0 = 1; n0 = elasticpar.n0;
Gamma = elasticpar.gamma ;
dp = elasticpar.dp; q = elasticpar.q;
%%%%%%%%%%%%%%%%%%%%%%%%%%%%%%%%%%%%%%%%%%%%%%%%%%%%%%%%%%%%%%%%%%%%%%%%%%%%
% Extract control parameters
minchange = elasticpar.minchange; tol = elasticpar.tol;
maxresid = elasticpar.maxresid; maxnoit = elasticpar.maxnoit;
%%%%%%%%%%%%%%%%%%%%%%%%%%%%%%%%%%%%%%%%%%%%%%%%%%%%%%%%%%%%%%%%%%%%%%%%%%%%
% Build Chebyshev differentiation matrices and initialise problem
[X,D] = chebdif(N,2);
i = [2:N-1];
I = eye(N);
u = zeros(N,1)+elasticpar.uguess; % initial guess
res = 1; change = 1; noit = 0; stop = false;
%%%%%%%%%%%%%%%%%%%%%%%%%%%%%%%%%%%%%%%%%%%%%%%%%%%%%%%%%%%%%%%%%%%%%%%%%%%%
% Start iteration loop
while ~stop % Newton iterations /Criterion for convergence
    if  change<minchange && res < tol
        stop = true;
    end
    noit = noit + 1;
    a = u(1) + a0;
    r = -(1-a)/2*X + (1+a)/2;
    dXdr = -2/(1-a);
    E1 = dXdr*D(:,:,1);
    E2 = (dXdr^2)*D(:,:,2);
    if strcmp(elasticpar.qVSdp,'dp')
        n = (1-n0)*(diag(1./r)*E1)*(r.*u-u.^2/2)+n0;
        K = (1-n0)^2/n0^3*n.^3./(1-n).^2;
        int = (1-a)/2*pi/(N-1)*sqrt(1-X.^2)'*(1./(r.*K));
        q = dp/int ;
    end
    %%%%%%%%%%%%%%%%%%%%%%%%%%%%%%%%%%%%%%%%%%%%%%%%%%%%%%%%%%%%%%%%%%%%%%%%%%%%
    % Analytically build Kozeny-Carman element of the residual & Jac
    T = zeros(size(1:N-1)); B = T; A = B;
    dT1 = zeros(N-1,N);dB1 = dT1; dA = zeros(N,N);
    j = 2:N-1;
    T(j) = (n0^3)*((1-(diag(1./r(j))*E1(j,:))*(r.*u-u.^2/2))).^2;
    B(j) = r(j).*((1-n0)*(diag(1./r(j))*E1(j,:))*(r.*u-u.^2/2)+n0).^3;
    A(j) = T(j)./B(j);
    for k = 1:N
       dT1(j,k) =  2*(n0^3)*(1-(diag(1./r(j))*E1(j,:))* ...
                 (r.*u-u.^2/2)).*E1(j,k)*(1-u(k)/r(k));
       dB1(j,k) = 3*((1-n0)*E1(j,:)*(r.*u-u.^2/2)+n0*r(j)).^2 ...
                 *(1-n0).*(E1(j,k)*(1-u(k)/r(k)));
       dA(j,k) = (B(j)'.*dT1(j,k)-T(j)'.*dB1(j,k))./(B(j)'.^2);
    end
    %%%%%%%%%%%%%%%%%%%%%%%%%%%%%%%%%%%%%%%%%%%%%%%%%%%%%%%%%%%%%%%%%%%%%%%%%%%%
```

```
    % Calculate residual (analytical)
    F = [ E1(1,:)*u+(Gamma/a)*u(1) ;...
        (E2(i,:)+diag(1./r(i))*E1(i,:)-diag(1./r(i).^2)*I(i,:))*u ...
        + q*A(i)' ; ...
          u(N) ];
    %%%%%%%%%%%%%%%%%%%%%%%%%%%%%%%%%%%%%%%%%%%%%%%%%%%%%%%%%%%%%%%%%%%%
    % Calculate Jacobian (analytical)
    dF = [ E1(1,:)+(Gamma/a)*I(1,:); ...
           E2(i,:)+diag(1./r(i))*E1(i,:)-diag(1./r(i).^2)*I(i,:)...
           +q*dA(i,:); ...
           I(N,:) ];
    % Include contributions of a = u(1)+a0
    drdu_a = (X+1)/2;
    dF(i,1) = dF(i,1) + (2/(b0-a))*E2(i,:)*u - ...
            ((-a+(b0-a)*X(i))./((r(i).^2)*(b0-a))).*(E1(i,:)*u) - ...
            (1./(r(i).^3)).*drdu_a(i).*u(i);
    dndu_a = (1-n0)*(-((-a+(b0-a)*X(i))./((r(i).^2)*(b0-a))).*...
        (E1(i,:)*(r.*u-(u.^2)/2)) + ...
        (1./r(i)).*(E1(i,:)*(drdu_a.*u)) );
    n = (1-n0)*(diag(1./r)*E1)*(r.*u-u.^2/2) + n0;
    dA_a = ((n0^3)/((1-n0)^2))*( 2*(n(i).^3).*r(i).*(1-n(i))...
         .*dndu_a -((1-n(i)).^2).*...
         ((n(i).^3).*drdu_a(i)+r(i).*3.*(n(i).^2).*dndu_a));
    dF(i,1) = dF(i,1) + q*dA_a;
    dF(1,1) = E1(1,1) + (1/(b0-a))*E1(1,:)*u + ...
        (1/a -(1/(a^2))*u(1))*Gamma;
    %%%%%%%%%%%%%%%%%%%%%%%%%%%%%%%%%%%%%%%%%%%%%%%%%%%%%%%%%%%%%%%%%%%%
    % Update solution and calculate residual
    Unew = max(0,u-dF\F);
    res = norm(F,inf)/N+norm(imag(Unew),inf);
    change = norm(Unew-u,inf)+norm(imag(Unew),inf);
    u = Unew;
end
```

Published with MATLAB® R2015a

Note that although the Q-k_{KC} code looks significantly longer than the L-k_0 code, the majority of this is simply due to the increasingly complex analytical expressions contained within it; structurally, the only additions are the Jacobian and `while`-loop which facilitates the iteration.

The full versions of the poroelastic steady-state codes are included in the Electronic Supplementary material of Auton and MacMinn [6].

Appendix B

Numerical implementation of transient poroelastic problem: M, F, and c for fixed q

Here, as in the Electronic Supplementary Material of Auton and MacMinn [7], we list the $F[u_s]$, $M[u_s]$ and $c[u_s]$ for all models for fixed q. Note that, although it is often preferable to simplify the mass matrix as much as possible, handling of the nonlinearity of $k[u_s]$ sometimes benefits from a more complicated mass matrix. We use the simplest possible mass matrices for all fixed q cases except for applied-stress Q-k_{KC}, applied-stress N-k_{KC}, and constrained N-k_{KC}. These three cases benefit from including $k[u_s]$ as a component in M and c rather than F.

For the L models, we have

$$M = 1, \quad F = k[u_s]\frac{\partial}{\partial r}\left[\frac{1}{r}\frac{\partial}{\partial r}(u_s r)\right] \quad \text{and} \quad c = 1. \tag{B.1a}$$

For the Q-k_0 models, we have

$$M = 1, \quad F = \left(1 - \frac{\partial u_s}{\partial r}\right)\left(\frac{\partial^2 u_s}{\partial r^2} + \frac{1}{r}\frac{\partial u_s}{\partial r} - \frac{u_s}{r^2}\right) \quad \text{and} \quad c = 1 - \frac{\partial u_s}{\partial r}. \tag{B.1b}$$

For the Q-k_{KC} model subjected to $B^a[u_s] = B_1^b[u_s] = 0$, we have

$$M = 1, \quad F = k[u_s]\left(1 - \frac{\partial u_s}{\partial r}\right)\left(\frac{\partial^2 u_s}{\partial r^2} + \frac{1}{r}\frac{\partial u_s}{\partial r} - \frac{u_s}{r^2}\right) \quad \text{and} \quad c = 1 - \frac{\partial u_s}{\partial r}. \tag{B.1c}$$

For the Q-k_{KC} model subjected to $B^a[u_s] = B_2^b[u_s] = 0$, we have

$$M = \frac{1}{k[u_s]}, \quad F = \left(1 - \frac{\partial u_s}{\partial r}\right)\left(\frac{\partial^2 u_s}{\partial r^2} + \frac{1}{r}\frac{\partial u_s}{\partial r} - \frac{u_s}{r^2}\right) \quad \text{and} \quad c = \frac{1 - \dfrac{\partial u_s}{\partial r}}{k[u_s]}. \tag{B.1d}$$

For the N models, we first write the PDE explicitly in terms of u_s in the following form:

$$\frac{\partial u_s}{\partial t} = \frac{k[u_s]\left[1 - \ln\left(\lambda_r \lambda_\theta^\Gamma\right)\right]}{\lambda_r \lambda_\theta}\left(\frac{\partial^2 u_s}{\partial r^2} + \frac{\dfrac{q\lambda_r\lambda_\theta}{k[u_s]} - \mathrm{T}}{\mathrm{B}}\right), \tag{B.1ea}$$

$$\mathrm{T} := \left[\ln\left(\lambda_r \lambda_\theta^\Gamma\right) - \Gamma\right]\left(1 - \frac{\lambda_\theta}{\lambda_r}\right) + (1 - \Gamma)\ln\left(\frac{\lambda_\theta}{\lambda_r}\right), \tag{B.1eb}$$

$$\mathrm{B} := \lambda_r r\left[1 - \ln\left(\lambda_r \lambda_\theta^\Gamma\right)\right]. \tag{B.1ec}$$

For the N-k_0 model, we have

$$M = 1, \quad F = \frac{\left[1 - \ln\left(\lambda_r \lambda_\theta^\Gamma\right)\right]}{\lambda_r \lambda_\theta}\left(\frac{\partial^2 u_s}{\partial r^2} - \frac{\mathrm{T}}{\mathrm{B}}\right) \quad \text{and} \quad c = \frac{1}{\lambda_r r}, \tag{B.1f}$$

and, finally, for the N-k_{KC} model, we have

$$M = \frac{\lambda_r \lambda_\theta}{k[u_s]\left[1 - \ln\left(\lambda_r \lambda_\theta^\Gamma\right)\right]}, \quad F = \frac{\partial^2 u_s}{\partial r^2} - \frac{\mathrm{T}}{\mathrm{B}} \quad \text{and} \quad c = \frac{\lambda_r \lambda_\theta}{k[u_s]\mathrm{B}}. \tag{B.1g}$$

Appendix C

Manipulation of Lobatto's integral formula

Although Clenshaw-Curtis quadrature is the classical approach for approximating definite integrals involved in the solution of differential equations by Chebyshev spectral collocation [91], we use Lobatto's integral formula [15]. Consider Lobatto's integration formula for Chebyshev polynomials of the second kind [1, p889, 25.4.41].[1] Note that direct use of [1, p889, 25.4.40] on the unscaled domain $x \in [1, -1]$ is often referred to as Chebyshev-Gauss quadrature; here we re-arrange [1, p889, 25.4.41] to evaluate $\int_a^b g(r)dr$ in lieu of $\int_a^b \sqrt{(y-a)(b-y)}f(y)dy$.

$$\int_a^b \sqrt{(y-a)(b-y)}f(y)dy = \left(\frac{b-a}{2}\right)^2 \sum_{j=2}^{N-1} \hat{W}_j \hat{f}(\hat{Y}_j) + Res_n \tag{C.1}$$

where the abscissas (*i.e.,* the set of Chebyshev collocation points) $\hat{X}_j$ is defined in Equation (3.22) and $y \in [a, b]$ is the mapped domain with corresponding mapped coordinates $\hat{Y}_j$ such that $\hat{X}_j \mapsto \hat{Y}_j$, the weights, $\hat{W}_i$, and the error term, Res_n, are defined, as:

[1] Note that for consistency with the notation used throughout the thesis, i and n in [1, p889, 25.4.41] are mapped according to $i \mapsto j-1$, $n \mapsto N-2$ and $R_n \mapsto Res_N$. Additionally, we have added hats to discretised quantities and capitalised x, y and w.

$$\hat{Y}_j = \frac{b+a}{2} + \frac{b-a}{2}\hat{X}_j \tag{C.2a}$$

$$\hat{W}_j = \frac{\pi}{N-1}\sin^2\left(\frac{(j-1)\pi}{N-1}\right) = \frac{\pi\left(1-\hat{X}_j^2\right)}{N-1} \tag{C.2b}$$

$$Res_N = \frac{\pi}{(2N-4)!2^{2N-3}} f^{(2N-4)}(\xi) \tag{C.2c}$$

respectively, for *some* $\xi \in (-1, 1)$ and where $\cdot^{(m)}$ denotes 'differentiated m times'.

We now relate Equation (4.54) to Equation (C.1). Firstly, note that $\hat{Y}_j = \hat{r}_{N-j}$; secondly, since $\sin(\gamma)$ is symmetrical about $\gamma = 0$ and the N Chebyshev points are symmetrical about $x = 0$, we have that $\hat{W}_j = \hat{W}_{N-j}$. Lastly, due to the fact that we have a finite sum in Equation (C.1), the order of summation is unimportant and thus we may re-write Equation (C.1) as

$$\int_a^b \sqrt{(r-a)(b-r)} f(r)dr = \left(\frac{b-a}{2}\right)^2 \sum_{k=2}^{N-1} \hat{W}_k \hat{f}(\hat{r}_k) + Res_n, \tag{C.3}$$

where $k = j - N$. Making the substitution

$$g(r) = \sqrt{(r-a)(b-r)} f(r) \tag{C.4}$$

into Equation (C.3) then leads to

$$\int_a^b g(r)dr = \left(\frac{b-a}{2}\right)^2 \sum_{k=2}^{N-1} \frac{\hat{W}_k \hat{g}(\hat{r}_k)}{\hat{h}(\hat{r}_k)} + \tilde{Res}_N \tag{C.5}$$

where

$$[\hat{h}(\hat{r}_k)]^2 = (\hat{r}_k - a)(b - \hat{r}_k) = \left(\frac{b+a}{2}\right)^2 - \left(\frac{b-a}{2}\right)^2 \hat{X}_k - ab = \left(\frac{b-a}{2}\right)^2 \left(1 - \hat{X}_k^2\right) \tag{C.6}$$

and

$$\tilde{R}es_N = \frac{\pi}{(2N-4)!2^{2N-3}} \left[\frac{g(r)}{\sqrt{(r-a)(b-r)}} \right]^{(2N-4)} . \tag{C.7}$$

We neglect the residual $\tilde{R}es_N$, which we assume decays rapidly as $N \to \infty$ [1, 15]. As $\hat{X}_1 = 1$ and $\hat{X}_N = -1$, we have that $\left(1 - \hat{X}_i^2\right) = 0$ for $i = 1, N$; Equation (4.53) follows.

Appendix D

Analytical Tresca solutions

The Tresca yield criterion is commonly used to model cohesive soils subject to *undrained* loading because it is volume conservative. The Tresca model is useful not only because it allows for fully analytical solutions, but also from the Tresca solution the corresponding solutions for a von Mises material can be derived. Von Mises yield criterion is extremely useful in cases of multi-axial loading and is often used to model metals. Firstly, we present the LL-k_0 solution for a zero displacement outer boundary condition. For the elastic region we solve

$$\frac{\mathrm{d}^2 u_s}{\mathrm{d}r^2} + \frac{1}{r}\frac{\mathrm{d}u_s}{\mathrm{d}r} - \frac{u_s}{r^2} = -\frac{q}{r}, \qquad s < r < b, \tag{D.1}$$

subject to

$$u_s(1) = 0 \quad \text{and} \quad \sigma'_\theta(s^+) - \sigma'_r(s^+) = y \tag{D.2}$$

for $r \in (s, 1]$. This leads to

$$u_s = -\frac{qr\ln(r)}{2} + \frac{(2F_1 + q)r}{2(1+\Gamma)} + \frac{F_2}{(1-\Gamma)r}, \tag{D.3a}$$

such that

$$\sigma'_r = -\frac{1+\Gamma}{2} q \ln(r) + F_1 - \frac{F_2}{r^2} \quad \text{and} \quad \sigma'_\theta = y + \sigma'_r \tag{D.3b}$$

where

$$F_2(s) := \frac{s^2}{4}\left[2y - q(1-\Gamma)\right] \quad \text{and} \quad F_1(s) := -\frac{F_2(s)(1+\Gamma)}{1-\Gamma} - \frac{q}{2}. \tag{D.3c}$$

For the plastic region we solve

$$\frac{\mathrm{d}\sigma_r'}{\mathrm{d}r} = \frac{y-q}{r} \tag{D.4}$$

subject to

$$\sigma_r'(a_0) = 0 \tag{D.5}$$

which leads to

$$\sigma_r' = (y-q)\ln\left(\frac{r}{a_0}\right). \tag{D.6}$$

To determine the value of s we equate Equations (D.3b) and (D.6) for $r = s$, which gives

$$G_1 = G_2 \ln\left(s^2\right) + G_3 s^2 \tag{D.7a}$$

where

$$G_1 := 4(y-q)\ln(a_0) - q(1+\Gamma) - 2y, \quad G_2 := 2y - q(1-\Gamma) \quad \text{and} \quad G_3 := \frac{1+\Gamma}{1-\Gamma}G_2, \tag{D.7b}$$

Solving for s gives

$$s = \sqrt{\frac{G_2}{G_3}\mathcal{W}\left(\frac{G_3}{G_2}e^{\frac{G_1}{G_2}}\right)} = \sqrt{\frac{1-\Gamma}{1+\Gamma}\mathcal{W}\left(\frac{1+\Gamma}{1-\Gamma}\exp\left(\frac{4(y-q)\ln(a_0) - q(1+\Gamma) - 2y}{2y - q(1-\Gamma)}\right)\right)} \tag{D.8}$$

where $\mathcal{W}(x)$ is the Lambert-W function defined in Equation (3.18). From the flow law (Equation 5.26) we determine the ODE for the displacement in the plastic region

$$\beta\frac{\mathrm{d}u_s}{\mathrm{d}r} + \frac{u_s}{r} = \sigma_r'\frac{1+\beta}{1+\Gamma} + \frac{y(1-\beta\Gamma)}{1-\Gamma^2} = \left[\frac{(y-q)(1+\beta)}{1+\Gamma}\right]\ln\left(\frac{r}{a_0}\right) + \frac{y(1-\beta\Gamma)}{1-\Gamma^2} \tag{D.9}$$

with solution

$$u_s = r\ln\left(\frac{r}{a_0}\right)\frac{y-q}{1+\Gamma} + \frac{\Gamma}{1+\beta}\left[\frac{y(1-\beta)+q\beta(1-\Gamma)}{1-\Gamma^2}\right] + F_3(s)r^{-\frac{q}{\beta}}, \tag{D.10}$$

where, from continuity of displacement at $r = s$,

$$F_3(s) := s^{\frac{1}{\beta}}\left\{-\frac{qs\ln(s)}{2} + \frac{(2F_1(s)+q)s}{2(1+\Gamma)} + \frac{F_2(s)}{(1-\Gamma)s} - s\ln\left(\frac{s}{a_0}\right)\frac{y-q}{1+\Gamma} - \frac{s}{1+\beta}\left[\frac{y(1-\beta]+q\beta(1-\Gamma)}{1-\Gamma^2}\right]\right\}. \tag{D.11}$$

Hence the LL-k_0 Tresca solution given explicitly by

$$u_s = \begin{cases} r\ln\left(\frac{r}{a_0}\right)\frac{y-q}{1+\Gamma} + \frac{\Gamma}{1+\beta}\left[\frac{y(1-\beta)+q\beta(1-\Gamma)}{1-\Gamma^2}\right] + F_3(s)r^{-\frac{q}{\beta}} & a_0 < r < s, \\ -\frac{qr\ln(r)}{2} + \frac{[2F_1(s)+q]r}{2(1+\Gamma)} + \frac{F_2(s)}{(1-\Gamma)r}, & s \le r < 1, \end{cases} \tag{D.12}$$

where $F_2(s)$, $F_1(s)$ and $F_3(s)$ are given in Equations (D.3c) and (D.11), respectively, and s is defined in Equation (D.8).

For the 'N_LL-k_0' model, the only change is the flow law, now given by Equation (5.23a); in lieu of Equation (D.9) we now have

$$\ln\left[\left(1-\frac{\mathrm{d}u_s}{\mathrm{d}r}\right)^{-\beta}\left(1-\frac{u_s}{r}\right)^{-1}\right] = \left[\frac{(y-q)(1+\beta)}{1+\Gamma}\right]\ln\left(\frac{r}{a_0}\right) + \frac{y(1-\beta\Gamma)}{1-\Gamma^2} \tag{D.13}$$

which rearranges to

$$\frac{\mathrm{d}u_s}{\mathrm{d}r} = 1 - \frac{r^{\frac{\beta+1-\mathfrak{F}_2}{\beta}}}{\mathfrak{F}_1}\left(1-\frac{u_s}{r}\right)^{-\frac{1}{\beta}} \tag{D.14a}$$

where

$$\mathfrak{F}_1 := a_0^{\dfrac{(q-y)(1+\beta)}{(1+\Gamma)\beta}} \exp\left(\frac{y(1-\beta\Gamma)}{(1-\Gamma^2)\beta}\right) \quad \text{and} \quad \mathfrak{F}_2 := \frac{(1+\beta)(1+\Gamma+q-y)}{1+\Gamma}. \tag{D.14b}$$

This has solution

$$u_s = r - \left[F_3^\star(s) + \frac{(\beta+1)r^{\dfrac{\mathfrak{F}_2}{\beta}}}{\mathfrak{F}_1\mathfrak{F}_2}\right]^{\dfrac{\beta}{1+\beta}} \tag{D.15a}$$

where

$$F_3^\star(s) := \left[s + \frac{qs\ln(s)}{2} - \frac{(2F_1(s)+q)s}{2(1+\Gamma)} - \frac{F_2(s)}{(1-\Gamma)s}\right]^{\dfrac{\beta+1}{\beta}} - \frac{\beta+1}{\mathfrak{F}_1\mathfrak{F}_2} s^{\dfrac{\mathfrak{F}_2}{\beta}}. \tag{D.15b}$$

Thus, the full solution for the N$_L$L-k_0 model for Tresca yield is given by

$$u_s = \begin{cases} r - \left[F_3^\star(s) + \dfrac{(\beta+1)r^{\dfrac{\mathfrak{F}_2}{\beta}}}{\mathfrak{F}_1\mathfrak{F}_2}\right]^{\dfrac{\beta}{1+\beta}} & a_0 < r < s, \\ -\dfrac{qr\ln(r)}{2} + \dfrac{(2F_1(s)+q)r}{2(1+\Gamma)} + \dfrac{F_2(s)}{(1-\Gamma)r}, & s \le r < 1, \end{cases} \tag{D.16}$$

where $F_2(s)$, $F_1(s)$ and $F_3^\star(s)$ are given in Equations (D.3c) and (D.15b), respectively, and s is once again defined in Equation (D.8).

The problems solved here in the linearised Tresca limit could, of course, be trivially generalised to consider varying ζ, as well as an applied stress at the outer boundary, because no additional presence of s will appear due to either of these changes. This is omitted for the sake of brevity.

Appendix E

The fully permeable ($\zeta \equiv 1$) poroelasto-plastic solution for fixed q

Here we derive the poroelasto-plastic solutions driven via a fixed flow rate q for the fully permeable limit in which $\zeta \equiv 1$ for both a cylinder subject to a constant applied radial effective stress at the outer boundary and a constrained cylinder. Following the structure of Chapter 5, firstly in §E.1 we present the smallest flow rate $q = q_{\min}$ that induces yield and the largest flow rate for which the model remains well posed $q = q_{\max}$ (*i.e.,* the first q such that the material is entirely yielded). Note that these values of q and the corresponding values of a will be effected by the linearisation (*e.g.,* 'LL' *vs* 'QQ' models). In §E.2 we present the corresponding analytic LL-k_0 solution where the position of the elastic-plastic interface is the solution to an implicit relation.

E.1 Minimum $q = q_{\min}$ and maximum $q = q_{\max}$

To determine the $q = q_{\min}$ such that an infinitesimal amount of the material has yielded plastically at steady state, we consider the purely poroelastic problem (*cf.* Chapters 2–4).

Equations (3.5), which govern the poroelastic displacement and stress fields, are

$$u_s = -\frac{qr\ln r}{2} + \frac{(2B_1+q)r}{2(1+\Gamma)} + \frac{B_2}{(1-\Gamma)r}, \tag{E.1a}$$

$$\sigma'_r = -\frac{(1+\Gamma)}{2}q\ln r + B_1 - \frac{B_2}{r^2}, \tag{E.1b}$$

$$\sigma'_\theta = -\frac{(1+\Gamma)}{2}q\ln r + B_1 + \frac{B_2}{r^2} + \frac{q(1-\Gamma)}{2} = \sigma'_r + \frac{2B_2}{r^2} + \frac{q}{2}(1-\Gamma), \tag{E.1c}$$

where B_1 and B_2 are to be determined. We assume that yield will first occur at $r = a = a_{\min}$ (*i.e.,* that yield first occurs at the inner cavity wall), and that the material will yield positively subject to $\mathcal{F}_{\theta,r}$ and that the maximum value of $\mathcal{F}_{\theta,r}$ is attained at steady state and not during the transient evolution. The conditions for the former assumption to be valid are derived in Appendix F. This is consistent with previous work [103, 104, 112]. Under these assumptions we have the additional conditions

$$\alpha\sigma'_\theta(s=a_{\min}) - \sigma'_r(s=a_{\min}) = y \quad\Longrightarrow\quad \sigma'_\theta(s=a_{\min}) = \frac{2B_2}{a_{\min}^2} + \frac{q_{\min}}{2}(1-\Gamma) = \frac{y}{\alpha}, \tag{E.2}$$

since $\sigma'_r(a) = 0$.

E.1.1 Applied stress: $q_{\min}$

Firstly, we consider the outer boundary conditions as defined in Equations (5.15a). Applying no radial effective stress at the inner boundary and constant applied effective radial stress at the outer boundary, we eliminate B_1 to determine

$$B_2(a,b) = \frac{b^2a^2\left[2\sigma'_b + q(1+\Gamma)\ln\left(\frac{b}{a}\right)\right]}{2(b^2-a^2)}. \tag{E.3}$$

Using Equation (E.3) we eliminate B_2 from Equation (E.2) which gives

$$q_{\min}(a_{\min},b_{\min}) = \frac{2\left[y(b_{\min}^2 - a_{\min}^2) - 2\sigma'_b b_{\min}^2\alpha\right]}{\alpha\left[2b_{\min}^2(1+\Gamma)\ln\left(\frac{a_{\min}}{b_{\min}}\right) + (b_{\min}^2 - a_{\min}^2)(1-\Gamma)\right]}. \tag{E.4}$$

For the LL-k_0 model $q_{\min}$ is fully determined with $a_{\min} = a_0$ and $b_{\min} = 1$. For the QL-k_0 model we take $b_{\min} = 1$ and $a_{\min}$ is found via elimination of $q_{\min}\ln(a_{\min})$ between Equations $\sigma_r'(a_{\min}) = 0$ and $u_s(a_{\min}) = a_{\min} - a_0$, which leads to

$$a_{\min} - a_0 = \frac{q_{\min}a_{\min}}{2(1+\Gamma)} + \frac{2B_2}{a_{\min}(1-\Gamma^2)}. \tag{E.5}$$

Finally Equation (E.2) is used to eliminate B_2 from Equation (E.5) giving

$$a_{\min} = a^\star_{\min} := \frac{a_0(1-\Gamma^2)\alpha}{(1-\Gamma^2)\alpha - y}. \tag{E.6}$$

Note that $a^\star_{\min}$ is independent of the outer boundary condition while $q_{\min}$ is not. For the QQ-k_0 and NQ-k_0 models $a_{\min}$ is also given by Equation (E.6) as $a^\star_{\min}$, but for these models we need also evaluate $b_{\min}$. The kinematic condition $u_s(b_{\min}) = b_{\min} - 1$ leads to the implicit relation

$$\begin{aligned}\frac{q_{\min}(a^\star_{\min}, b_{\min})}{4b_{\min}}\left\{b^2_{\min}\left[1 - 2\ln\left(\frac{b_{\min}}{a^\star_{\min}}\right)\right] - (a^\star_{\min})^2\right\} \\ + \frac{y}{2\alpha b_{\min}}\left[b^2_{\min}(1-\Gamma) + (a^\star_{\min})^2(1+\Gamma)\right] + 1 - b_{\min} = 0,\end{aligned} \tag{E.7}$$

which we must solve numerically for $b_{\min}$.

E.1.2 Applied stress: $q_{\max}$

We evaluate $q_{\max}$ as the first value of q for which the material has entirely yielded *i.e.,* the value of q such that

$$\sigma_r'(b_{\max}) = \frac{y - q\alpha}{\alpha - 1}\left[1 - \left(\frac{b_{\max}}{a_{\max}}\right)^K\right] = \sigma_b' \tag{E.8}$$

with K defined in Equation (5.20). This rearranges to give

$$q_{\max}(a_{\max}, b_{\max}) = \frac{y\left[1 - \left(\frac{b_{\max}}{a_{\max}}\right)^K\right] - \sigma_b'(\alpha - 1)}{\alpha\left[1 - \left(\frac{b_{\max}}{a_{\max}}\right)^K\right]}. \tag{E.9}$$

Note that again the above conditions are limited to the *first* $q_{\max}$ for which the material yields, after which the problem becomes over prescribed. For the LL-k_0 model $a_{\max} = a_0$ and $b_{\max} = 1$.

For all other models we must invoke the kinematic conditions and thus need an expression for the displacement. Solving the linear plastic-flow ODE (Equation 5.27) gives

$$u_s = \frac{H_1}{\beta + 1}\left[r - b\left(\frac{b}{r}\right)^{\frac{1}{\beta}}\right] + \frac{\alpha H_2}{\beta + \alpha}\left[r^{\frac{1}{\alpha}} - b\left(\frac{b}{r}\right)^{\frac{1}{\beta}}\right] + [u_s(b)]\left(\frac{1}{r}\right)^{\frac{1}{\beta}}, \tag{E.10a}$$

where

$$H_1 := \frac{y(1 - \beta\Gamma)}{\alpha(1 - \Gamma^2)} - H_2 a^K \tag{E.10b}$$

with

$$H_2(a) := -\frac{(y - \alpha q)\left[\alpha(\beta - \Gamma) + 1 - \beta\Gamma\right]}{\alpha a^K(\alpha - 1)(1 - \Gamma^2)}. \tag{E.10c}$$

Note that while H_2 is a function of both $q(a, b)$ and a, H_1 is just a function of $q(a, b)$.

For the QL-k_0 model we do not a priori know the value of $u_s(b_{\max} \equiv 1)$. In this case we calculate $u_s(1)$ from the elastic solution (Equation E.1a) subject to $\sigma_r'(1) = \sigma_b'$ and $\alpha\sigma_\theta'(s = 1) - \sigma_b' = y$. This gives

$$u_s(1) = \frac{y + (1 - \alpha\Gamma)\sigma_b'}{\alpha(1 - \Gamma^2)} \tag{E.11}$$

so that the plastic displacement is given by

$$u_s = \frac{H_1}{\beta + 1}\left[r - \left(\frac{1}{r}\right)^{\frac{1}{\beta}}\right] + \frac{\alpha H_2}{\beta + \alpha}\left[r^{\frac{1}{\alpha}} - \left(\frac{1}{r}\right)^{\frac{1}{\beta}}\right] + \left[\frac{y + (1 - \alpha\Gamma)\sigma_b'}{\alpha(1 - \Gamma^2)}\right]\left(\frac{1}{r}\right)^{\frac{1}{\beta}}. \tag{E.12}$$

Hence the QL-k_0 model is fully specified with $b_{\max} = 1$ and $a_{\max}$ the solution to the implicit relation

$$a_{\max} - a_0 = \frac{H_1}{\beta+1}\left[a_{\max} - \left(\frac{1}{a_{\max}}\right)^{\frac{1}{\beta}}\right] + \frac{\alpha H_2(a_{\max})}{\beta+\alpha}\left[a_{\max}^{\frac{1}{\alpha}} - \left(\frac{1}{a_{\max}}\right)^{\frac{1}{\beta}}\right] + \left[\frac{y + (1-\alpha\Gamma)\sigma_b'}{\alpha(1-\Gamma^2)}\right]\left(\frac{1}{a_{\max}}\right)^{\frac{1}{\beta}}. \quad \text{(E.13)}$$

For the QQ-k_0 model we once again appeal to the elastic problem at $r = b$ to determine $b_{\max}$. Firstly, we solve Equations (E.1) subject to $\sigma_r'(s = b_{\max}) = \sigma_b'$ and $\alpha\sigma_\theta'(b_{\max}) - \sigma_b' = y$ which gives

$$u_s(b_{\max}) = \frac{\alpha(1-\Gamma^2)}{(\alpha\Gamma - 1)\sigma_b' - y}. \quad \text{(E.14)}$$

Additionally $u_s(b_{\max}) = b_{\max} - 1$ and equating this with Equation (E.14) yields

$$b_{\max} = \frac{\alpha(1-\Gamma^2)}{\alpha(1-\Gamma^2) + (\alpha\Gamma - 1)\sigma_b' - y}. \quad \text{(E.15)}$$

Note that this is also true for the NQ-k_0 model as this expression is independent of plastic flow law. Hence the QQ-k_0 model is fully prescribed with $a_{\max}$ the solution to the implicit relation

$$a_{\max} - a_0 = \frac{H_1}{\beta+1}\left[a_{\max} - b_{\max}\left(\frac{b_{\max}}{a_{\max}}\right)^{\frac{1}{\beta}}\right] + \frac{\alpha H_2}{\beta+\alpha}\left[a_{\max}^{\frac{1}{\alpha}} - b_{\max}^{\frac{1}{\alpha}}\left(\frac{b_{\max}}{a_{\max}}\right)^{\frac{1}{\beta}}\right] + (b-1)\left(\frac{b_{\max}}{a_{\max}}\right)^{\frac{1}{\beta}}, \quad \text{(E.16)}$$

with $b_{\max}$ a known constant as defined in Equation (E.15). Due to the nonlinearity of Equation (5.28a) it is not tractable to work out the value of $a_{\max}$ for the NQ-k_0 model, thus the solution is omitted as conceptually trivial but computationally heavy.

E.1.3 Zero displacement: $q_{\min}$

We now consider the constrained cylinder; that is, we simply replace Equations (5.15a) with a zero displacement condition at $b \equiv 1$ as given in Equation (2.34a). Note that there is no distinction between the QL-k_0 and QQ-k_0 models, when determining u_s, (ϕ_f is the only quantity that is different), thus we refer to the model using linear elastic constitutive relations in both regions and a rigorous treatment of kinematics as the QQ-k_0 model.

For the constrained cylinder we must re-evaluate B_2 from Equations (E.1) now subject to Equation (2.34a) and no effective radial stress at the inner boundary (Equation 2.30). As such B_2 is given by

$$B_2(a_{\min}) = \frac{q_{\min} a_{\min}^2 (\Gamma - 1)[(1+\Gamma)\ln(a_{\min}) + 1)}{2[1 - \Gamma + a_{\min}^2(1+\Gamma)]}. \tag{E.17}$$

Using Equation (E.17) we eliminate B_2 from Equation (E.2) which gives

$$q_{\min}(a_{\min}) = \frac{2y[a_{\min}^2(1+\Gamma) + (1-\Gamma)]}{\alpha(1-\Gamma^2)(a_{\min}^2 - 1 - 2\ln a_{\min})}. \tag{E.18}$$

Once again, for the LL-k_0 model we take $a_{\min} = a_0$. For the QQ-k_0 and NQ-k_0 models $a_{\min} = a_{\min}^\star$ as defined in Equation (E.6). For a physically reasonable solution, we need $a_{\min} > a_0$ and also $a_{\min} < 1$. It emerges that both conditions are satisfied when $0 < y \leq (1 - a_0)(1 - \Gamma^2)\alpha$.

E.1.4 Zero displacement: the existence of $q_{\max}$

For a constrained cylinder there does not exist a maximum value of q for which the material has fully yielded; instead $q \to \infty$ $s \to s_{\max}$. This value of $s_{\max}$ can be found to be the solution of the implicit equation,

$$\frac{\alpha(1-\Gamma^2)(2\ln s + s^2 - 1)}{2\left[s^2(\alpha-1)(1+\Gamma) - (1-\Gamma)(\alpha+1)\right]} + \frac{\alpha}{\alpha - 1}\left[\left(\frac{s}{a_0}\right)^{\frac{1-\alpha}{\alpha}} - 1\right] = 0. \tag{E.19}$$

E.2 Implicit analytical solution: LL-k_0 model

We present analytical solutions for the displacement in both the elastic ($s < r < b = 1$) and plastic ($a = a_0 < r < s$) regions, while the interface $r = s$ is the solution to an implicit relation. The full displacement field (Equations (E.10a) and (E.1a)) is

$$u_s = \begin{cases} \dfrac{H_1}{\beta+1}\left[r - b\left(\dfrac{b}{r}\right)^{\frac{1}{\beta}}\right] + \dfrac{\alpha H_2}{\beta+\alpha}\left[r^{\frac{1}{\alpha}} - b\left(\dfrac{b}{r}\right)^{\frac{1}{\beta}}\right] + \mathcal{H}\left(\dfrac{1}{r}\right)^{\frac{1}{\beta}}, & a_0 < r < s \\ \\ -\dfrac{qr\ln r}{2} + \dfrac{(2B_1+q)r}{2(1+\Gamma)} + \dfrac{B_2}{(1-\Gamma)r} & s \le r < 1, \end{cases} \tag{E.20a}$$

where H_1 and H_2 are defined in Equation (5.23b),

$$\mathcal{H}(s) = u_s^{\mathrm{e}}(s) = -\frac{qs\ln s}{2} + \frac{(2B_1+q)s}{2(1+\Gamma)} + \frac{B_2}{(1-\Gamma)s}, \tag{E.20b}$$

s is the solution to the implicit relation

$$\frac{y-q\alpha}{\alpha-1}\left[1 - \left(\frac{s}{a_0}\right)^{\frac{1-\alpha}{\alpha}}\right] + \frac{q\ln s(1+\Gamma)}{2} - B_1(s) + \frac{B_2(s)}{s^2} = 0, \tag{E.20c}$$

and where $B_1(s)$ and $B_2(s)$ are still to be determined from Equation (5.28e) and the outer boundary condition.

E.2.1 LL-k_0: Applied Stress

For an applied radial effective stress at the outer boundary condition we obtain

$$B_2(s) = \frac{s^2\left[2y + q\ln s(1+\Gamma)(\alpha-1) - 2\sigma_b'(\alpha-1) - q(1-\Gamma)\right]}{2\left[s^2(\alpha-1)+\alpha+1\right]}, \tag{E.21a}$$

and

$$B_1(s) = B_2 + \sigma_b'. \tag{E.21b}$$

Note that this is well defined for all s as $\alpha \geq 1$ for all physically plausible parameters (see Appendix G).

E.2.2 LL-k_0: Zero displacement

For the constrained cylinder, applying Equations (5.28e) and (2.34a) to Equation (E.20a) leads to

$$B_1(s) = \frac{s^2(1+\Gamma)\left[2y - q\alpha(1-\Gamma) + q(1+\Gamma)(\alpha-1)\ln s\right] + q(1-\Gamma)(1+\alpha)}{2\left[s^2(\alpha-1)(1+\Gamma) - (1-\Gamma)(\alpha+1)\right]}, \tag{E.22a}$$

and

$$B_2(s) = -\frac{s^2(1-\Gamma)\left\{q\left[\alpha\Gamma - 1 + (1+\Gamma)(\alpha-1)\ln s\right] + 2y\right\}}{2\left[s^2(\alpha-1)(1+\Gamma) - (1-\Gamma)(\alpha+1)\right]}. \tag{E.22b}$$

Note that these constants become ill-defined for $s^2 = s_T^2 := \dfrac{(1-\Gamma)(\alpha+1)}{(\alpha-1)(1+\Gamma)}$. We can determine the value of $q = q_T$ that corresponds to this troublesome value of s. This is the q_T that satisfies

$$\left[s_T^2(\alpha-1)(1+\Gamma) - (1-\Gamma)(\alpha+1)\right]\left[\frac{B_2(s_T)}{s_T^2} - B_1(s_T)\right] = 0 \tag{E.23}$$

which yields

$$q_T = \frac{2y}{1 - \alpha\Gamma - (1+\Gamma)(\alpha-1)\ln(s_T)}. \tag{E.24}$$

Note that q_T is independent of a_0 and that for given α and Γ, s_T is uniquely determined and the corresponding value of q_T is only additionally dependent on y.

Appendix F

Which yield condition?

We now consider all six possible cohesive Mohr-Coloumb yield criteria for a cylinder in plane strain with principal stresses σ'_r, σ'_θ and σ'_z. As discussed in §5.1.4, we assume that yield first occurs at the inner radius $r = a_{\min}$ and that, prior to yield, the yield function $\mathcal{F}_{1,3}$ is maximised at the poroelastic steady-state and not during the transient evolution to steady-state[1]. We adorn $\sigma_a^{\min}$ with a superscript '$1,3$' where σ'_1 is the maximum principal stress and σ'_3 is the minimum principal stress to associate the various $\sigma_a^{\min}$ with their corresponding yield functions (*cf.* Equation F.2). Additionally we assume that once a yield criterion has been selected the material will fail according to this and only this criterion.

For plane strain

$$\sigma'_z = \frac{\Gamma}{1+\Gamma}\left(\sigma'_r + \sigma'_\theta\right) \equiv \nu\left(\sigma'_r + \sigma'_\theta\right). \tag{F.1}$$

Note that the dimensionless constant $\frac{\Gamma}{1+\Gamma} \equiv \nu$, where ν is Poisson's ratio (*cf.* §5.3 and Appendix G). For all physical material considered[2] $\nu \in (0, \frac{1}{2})$. Since $\sigma'_1 \geq \sigma'_2 \geq \sigma'_3$, there are three distinct possibilities based on the signs of σ'_r and σ'_θ. If $\sigma'_r, \sigma'_\theta > 0$ this implies that $\sigma'_z \neq \sigma'_1$. Similarly if $\sigma'_r, \sigma'_\theta < 0$ then $\sigma'_z \neq \sigma'_3$. If we know that σ'_r and σ'_θ have different signs, or one of them is zero, then $\sigma'_z \equiv \sigma'_2$.

[1] The latter of these assumptions is used solely in the derivation of $q_{\min}$ and $\sigma_a^{\min}$ and not explicitly in the following discussion.

[2] Although note some 'physical materials', such as cork, exist such that the Poisson's ratio, $\nu < 0 \implies \Gamma < 0$

The six possible permutations of yield condition are

$$\mathcal{F}_{\theta,r} = \alpha\sigma'_\theta - \sigma'_r - y \leq 0 \tag{F.2a}$$

$$\mathcal{F}_{\theta,z} = \alpha\sigma'_\theta - \sigma'_z - y \leq 0 \tag{F.2b}$$

$$\mathcal{F}_{r,\theta} = \alpha\sigma'_r - \sigma'_\theta - y \leq 0 \tag{F.2c}$$

$$\mathcal{F}_{r,z} = \alpha\sigma'_r - \sigma'_z - y \leq 0 \tag{F.2d}$$

$$\mathcal{F}_{z,\theta} = \alpha\sigma'_z - \sigma'_\theta - y \leq 0 \tag{F.2e}$$

$$\mathcal{F}_{z,r} = \alpha\sigma'_z - \sigma'_r - y \leq 0. \tag{F.2f}$$

We then need to determine when each of these yield criteria is possible. Note that due to the assumptions that yield first occurs at the inner boundary and that once a material has yielded due to a specific yield function this is the only failure mechanism, we are only concerned with $\sigma'_i(a_{\text{min}})$ (*i.e.,* the effective stresses at the inner boundary at the point of first yield).

F.1 Fully permeable ($\zeta \equiv 1$)

For $\zeta \equiv 1$ we know that $\sigma'_r(a) = 0$ which implies that $\sigma'_z(a) = \frac{\Gamma}{1+\Gamma}\sigma'_\theta(a)$ and as such $\sigma'_z \equiv \sigma'_2$. Hence there are only two possible yield conditions, either $\mathcal{F}_{\theta,r}$ or $\mathcal{F}_{r,\theta}$. The former of which is the condition we have used throughout Chapter 5 and Appendix E ($\sigma'_\theta \geq \sigma'_z \geq 0 = \sigma'_r$). We now show the conditions under which the latter of these holds.

F.1.1 $\mathcal{F}_{r,\theta}$

Assuming the latter to be true, implies $0 = \sigma'_r \geq \sigma'_z \geq \sigma'_\theta$ with

$$\sigma'_\theta(a) = \frac{2B_2}{a^2} + \frac{q(1-\Gamma)}{2} \tag{F.3}$$

where B_2 is defined in Equation (E.3). We are only concerned with fluid injection (not extraction) problems and as such we only consider $q \geq 0$; additionally enforcing $\sigma'_\theta(a) < 0$ leads to a restriction of the allowable q. These constraints give $q \in \left[0, \frac{-4b^2\sigma'_b}{2b^2(1+\Gamma)\ln\left(\frac{b}{a}\right)+(b^2-a^2)(1-\Gamma)}\right]$ where $\sigma'_b < 0$ for a compressive far-field effective stress, as considered in Chapter 5 and Appendix E. We rearrange the yield criterion $\mathcal{F}_{r,\theta} \leq 0$ to give

$$q \geq q_\star := \frac{2[-(b^2-a^2)y - 2b^2\sigma'_b]}{2b^2(1+\Gamma)\ln\left(\frac{b}{a}\right) + (b^2-a^2)(1-\Gamma)}. \tag{F.4}$$

Note that now we have a restriction on q that it must be greater than a function of the parameters. This means that the material will only yield if the flow is too small or is sufficiently negative (suction), this corresponding to a cavity collapse when a cavity is insufficiently pressurised. In the following we refer to this as 'negative yield' and the converse as 'positive yield'. Thus, if we can ensure the parameters are such that $q_\star < 0$ we have no chance of such yield occurring for fluid injection. This simply requires the cylinder to be sufficiently 'strong' compared to the compressive far-field stress (σ'_b) to which it is subject, that is

$$(b^2-a^2)y > -2b^2\sigma'_b. \tag{F.5}$$

As demonstrated in §5.3 this is satisfied for the chosen poroelasto-plastic parameters. Hence for a sufficiently strong, fully permeable model we can conclusively say that $\mathcal{F}_{\theta,r}$ is the correct yield condition.

F.2 Varying permeability-load parameter ($\zeta \not\equiv 1$)

Now things get understandably more complicated for the case $\zeta \in [0, 1)$. For this case, for fluid injection, $\sigma'_r(a) = (1-\zeta)\sigma_a \in [-|\sigma_a|, 0)$. Hence, as $\sigma'_r(a) < 0$ for injection (cavity pressurisation), we are left with two cases to consider: either $\sigma'_\theta(a) > 0$ and $\sigma'_r(a) < 0$, in which case $\sigma'_z \equiv \sigma'_2$ and the only two possible yield criteria are Equation (F.2a) or Equa-

tion (F.2c); alternatively $\sigma'_\theta(a), \sigma'_r(a) < 0$, in which case Equations (F.2a), (F.2c), (F.2e) and (F.2f) are the possible yield criteria. Note that as discussed earlier, if $\sigma'_\theta(a), \sigma'_r(a) < 0$ then $\sigma'_z(a) \neq \sigma'_3$ by the definition of σ'_z, or if $\sigma'_\theta(a) > 0$ with $\sigma'_r(a) < 0$ then $\sigma'_z \equiv \sigma'_2$; hence Equations (F.2b) and (F.2d) are not possible. Thus, we have three possible alternative flow laws to consider.

F.2.1 $\mathcal{F}_{r,\theta}$

First, consider Equation (F.2c):

$$\mathcal{F}_{r,\theta}(a) = (\alpha - 1)(1 - \zeta)\sigma_a - \left[\frac{2\mathfrak{B}_2}{a^2} - \frac{\zeta\sigma_a(1-\Gamma)}{2\ln\left(\frac{b}{a}\right)}\right] - y \leq 0, \tag{F.6}$$

where $\mathfrak{B}_2$ is defined in Equation (5.38). Via comparison to Equation (5.40), we have

$$\sigma_a^{\min,r,\theta} = \frac{-2\ln\left(\frac{b}{a}\right)\left[y\left(\frac{b^2}{a^2} - 1\right) + 2\sigma'_b\left(\frac{b^2}{a^2}\right)\right]}{2\ln\left(\frac{b^2}{a^2}\right)\left\{\left(\frac{b^2}{a^2}\right)\left[\zeta(\alpha - \Gamma) - \alpha - 1\right] + (\alpha - 1)(1 - \zeta)\right\} - \zeta(1-\Gamma)\left(\frac{b^2}{a^2} - 1\right)}, \tag{F.7}$$

which gives the least compressive value of σ_a (*i.e.,* the minimum required $-\sigma_a$) to prevent negative yield. As such, if we can enforce $\sigma_a^{\min,r,\theta}$ to be positive via a choice of material parameters, then there would only be collapse when there is suction in the inner cavity. Since the denominator is negative, as for the $\zeta \equiv 1$ case, this simply requires Equation (F.5) to be satisfied. Thus for fluid injection, $\mathcal{F}_{r,\theta}$ is not possible.

F.2.2 $\mathcal{F}_{z,\theta}$

Next we consider Equation (F.2e), which requires $\sigma'_\theta(a), \sigma'_r(a) < 0$, for which there are two distinct possibilities; firstly if $\alpha\nu > 1$, as is the case for the chosen poroelasto-plastic

parameters (*cf.* §5.3), then the yield condition re-arranges to

$$\underbrace{\alpha\nu\sigma'_r}_{<0} + \underbrace{\sigma'_\theta(\alpha\nu - 1)}_{<0} \leq \underbrace{y}_{>0} \tag{F.8}$$

with equality signifying yield. Obviously the left hand side is negative and the right hand side positive so that equality will never be achieved; as such a material will never yield according to this yield criterion if $\alpha\nu > 1$. Hence we consider the case $\alpha\nu < 1$: this requires $0 > \sigma'_z(a) > \sigma'_r(a) > \sigma'_\theta(a)$. Thus, from Equation (5.36c)

$$0 > \sigma'_\theta(a) - \sigma'_r(a) = \left[\frac{2\mathfrak{B}_2}{a^2} - \zeta\frac{\sigma_a(1-\Gamma)}{2\ln\left(\frac{b}{a}\right)}\right], \tag{F.9}$$

with $\mathfrak{B}_2$ defined in Equation (5.38). Therefore, if

$$\underbrace{2b^2\ln\left(\frac{b}{a}\right)}_{>0}\left\{\underbrace{\sigma_a[\zeta(1-\Gamma)-2]}_{>0} + \underbrace{2\sigma'_b}_{<0}\right\} - \underbrace{(b^2-a^2)\zeta\sigma_a(1-\Gamma)}_{>0} > 0, \tag{F.10}$$

then the material cannot yield according to $\mathcal{F}_{z,\theta}$. This is true for sufficiently large $|\sigma_a|$; that is

$$|\sigma_a| > \frac{4b^2|\sigma'_b|\ln\left(\frac{b}{a}\right)}{\zeta(b^2-a^2)(1-\Gamma) + 2b^2\ln\left(\frac{b}{a}\right)[2-\zeta(1-\Gamma)]}. \tag{F.11}$$

The most extreme value of the right hand side of the above inequality occurs in the limit $a \to 0$, and is given by $\dfrac{|\sigma'_b|}{1-\frac{\zeta(1-\Gamma)}{2}}$; thus for all a_0 if $|\sigma_a| > \dfrac{|\sigma'_b|}{1-\frac{\zeta(1-\Gamma)}{2}}$ then there will be no negative yield. To simplify further, this inequality is safely satisfied for all ζ and all other physically reasonable parameters, for $|\sigma_a| > 2|\sigma'_b|$.

F.2.3 $\mathcal{F}_{z,r}$

Finally, consider the yield condition (F.2f); this holds only for $0 > \sigma'_z(a) > \sigma'_\theta(a) > \sigma'_r(a)$ and re-arranges to

$$\alpha\nu \underbrace{\sigma'_\theta(a)}_{<0} + \underbrace{\sigma'_r(a)}_{<0}(\alpha\nu - 1) \leq y. \tag{F.12}$$

Thus for $\alpha\nu > 1$, again we do not get equality as the left hand side is negative and y positive. Thus considering $\alpha\nu < 1$, we enforce $\sigma'_z(a) > \sigma'_\theta(a)$ which implies $\sigma'_\theta(a) < \Gamma\sigma'_r(a)$; this is equivalent to

$$|\sigma_a|(1-\Gamma)(1-\zeta) > \frac{2\mathfrak{B}_2}{a^2} + \frac{|\sigma_a|\zeta(1-\Gamma)}{2\ln\left(\frac{b}{a}\right)} \tag{F.13}$$

which rearranges to

$$|\sigma_a| < \frac{4b^2|\sigma'_b|\ln\left(\frac{b}{a}\right)}{2\ln\left(\frac{b}{a}\right)\left[b^2(1+\Gamma) + a^2(1-\Gamma)(1-\zeta)\right] + \zeta(b^2-a^2)(1-\Gamma)}. \tag{F.14}$$

Again the righthand side is maximised for $a \to 0$; thus for all

$$|\sigma_a| > \frac{2|\sigma'_b|}{1+\Gamma} \tag{F.15}$$

F.3 Summary

In summary, for q-driven flow into a fully permeable cylinder ($\zeta \equiv 1$) there are only two possible yield conditions: Equation (F.2a) or Equation (F.2c). Equation (F.2c) corresponds to a collapse or negative yield; there is a value of q above which this negative yield cannot occur. If q and the cylinder are 'sufficiently strong' compared to the compressive far-field stress, then collapse is prevented — that is Equation (F.5) is satisfied. Then the maximum value of q for which negative yield occurs is itself negative (*i.e.,* q must be a sink) to induce failure subject to Equation (F.2c). Hence for $q \geq q_{\min} > 0 > q_\star$, the cylinder yields

exclusively according to Equation (F.2a).

For $\zeta \in [0, 1)$ there are more possibilities; however, if $\alpha\nu > 1$ and Equation (F.5) is satisfied, then once again for all fluid injection ($\sigma_a \leq 0$) yield occurs exclusively according to Equation (F.2a). More specifically, Equation (F.2c) and Equation (F.2e) both model negative yield — that is cavity collapse. If Equation (F.5) is not satisfied then we could have collapse via Equation (F.2c). If $\alpha\nu < 1$ provided $|\sigma_a| > \dfrac{|\sigma_b'|}{1 - \frac{\zeta(1-\Gamma)}{2}}$, then there will be no collapse possible via Equation (F.2e); if the latter inequality does not hold then we could have a collapse via Equation (F.2e). Equation (F.2f) is the other positive yield criterion; for $\alpha\nu < 1$, if $|\sigma_a| > \dfrac{2|\sigma_b'|}{1+\Gamma}$ yield is not possible via this mechanism.

Appendix G

Geophysical Parameter Review

In Chapter 5 we focused on the model problem of radially outward fluid injection into a poroelasto-plastic material. This has many direct applications in the shallow subsurface including cavity expanison, borehole integrity, compensation grouting and fracking. These applications entail fluid injection into a variety of soils and rocks. Below we present poroelasto–perfectly-plastic parameter values, from a substantial literature review of shales, clays and sands.

We provide a table for each of these soils/rocks. In each table we give the parameter value or range of values as well as: brief contextual information such as the specific shale or type of test used in the determination of the parameter; whether the value is from *in situ* measurement or from a laboratory test on a core sample; the nature of the source (*i.e.,* primary *vs* secondary) and the source itself. Within each table we provide the elastic parameters, the plastic parameters and fluid-flow parameters. The elastic parameters are the elastic moduli; we find data in terms of $\breve{\mathcal{M}}$ and $\breve{\Lambda}$ and an additional four elastic moduli. We do not convert these into $\breve{\mathcal{M}}$ and $\breve{\Lambda}$ (as used throughout), because the pairings are non-unique (*i.e.,* some papers provide more than two elastic moduli and others just one — this is discussed in more detail below). Any two of these are sufficient to fully prescribe the

linear (or Hencky) elastic behaviour of a homogeneous isotropic elastic material:

$$\bullet \text{ Poisson ratio,} \qquad \nu \equiv \frac{\breve{\Lambda}}{\breve{\mathcal{M}} + \breve{\Lambda}}; \tag{G.1a}$$

$$\bullet \text{ Young modulus,} \qquad \breve{E} \equiv \frac{(\breve{\mathcal{M}} - \breve{\Lambda})(\breve{\mathcal{M}} + 2\breve{\Lambda})}{\breve{\mathcal{M}} + \breve{\Lambda};} \tag{G.1b}$$

$$\bullet \text{ The bulk modulus,} \qquad \breve{\mathcal{K}} \equiv \frac{\breve{\mathcal{M}} + 2\breve{\Lambda}}{3}; \tag{G.1c}$$

$$\bullet \text{ The shear modulus,} \qquad \breve{\mathcal{G}} \equiv \frac{\breve{\mathcal{M}} - \breve{\Lambda}}{2}. \tag{G.1d}$$

The plastic parameters are the friction angle φ, the dilation angle ψ and the cohesion $\breve{c}$. Finally, the fluid-flow parameters are the characteristic porosity $\phi_{f,0}$ given as a percentage and the characteristic permeability k_0.

G.1 Shales

Although soils, clays and sands are consistently modelled as (cohesive) granular materials that fail plastically, the ductility of shales is often neglected. However, many gas-bearing shales are known to have a high clay content and typically exist in a state of compression which suggests that they may in some cases fail plastically before fracturing.

For example, the Haynesville Shale Formation in East Texas and Northern Louisiana, has a relatively high clay content (around 40%) and the ductility of the formation has proved to be an issue for fracking [21, 113]. Pierre shale located in east-central Dakotas and in west-central Montana comprises from 40–50% clay mineral up to 65–70% in other areas [82]; Pierre II shale has been reported to have 44% clay content [113]. Due to this high clay content Pierre shale is soft and challenging to frack, and new techniques are being suggested to help combat the issue of ductility [41]. Utica shale underlies large areas of America [89] and may behave in a ductile manner [26, 89, 95, 97]. The compacted clay in shale has been said to possess a distinct nanogranular nature that underlies

the cohesive-frictional properties of shales [17]. As shown in Chapter 5, the ductile nature of some shales is important because the tensile stress in the plastic region will be much less than would be predicted by the theory of elasticity, which could delay or prevent the onset of fracture [21, 30, 40, 80, 95]. That said, ductile shale is not entirely bad, it does make a good frack barrier and reservoir seal.

Hydrocarbon-bearing shales are typically found at depths of 0.5–4km [35, 57]. Shales are intrinsically anisotropic; they are sedimentary rocks made from layers of deposits of organic materials and mineral particles. These layers are compressed over geologic timescales to form a laminated, fissile[1] rock, distinguishing shale from other sedimentary rocks such as a more isotropic sandstone; this makes the evaluation of anisotropic elastic parameters particularly challenging. Compared to other shales Pierre-1 shale is of a homogeneous nature and is thus an easier choice with less inherent anisotropy [50].

Physical range of parameters: Shales				
Parameter	Value	Notes/ Contextual data	Sample	Source
$\breve{E}$ [GPa]	> 24	Prospective shales		[21]
	$\in (3.5, 58)$	Data taken from Figure — we inferred the units of data to be MPsi	*In situ*[2]	[80]
	$\in (0.64, 1.56)$	Pierre-1 shale: drained[3]	Core	[51]
ν	$\in (0.16, 0.37)$	Data taken from figure	*In situ*[2]	[80]
.....	.....	.....	.....	.....
	$\in (0.095, 0.19)$	Pierre-1 shale: drained[3]	Core	[51]
.....	.....	.....	.....	.....
	0.25	Flaming Gorge shale; static values	Core	[38]
	0.29	Micaceous shale; static values		

[1] It readily breaks into thin layers along the laminated surfaces.
[2] Composite determination (see [65]).
[3] We give a range defined by the extremum values presented across all loading and measuring orientations; the range is due to the natural anisotropy and its magnitude can be seen as a measurement of the anisotropy.

Physical range of parameters: Shales cont'd				
Parameter	Value	Notes/ Contextual data	Sample	Source
ν	0.24	Data from triaxial testing of shale at depth 2000 m; North Sea well; Gullfisk field[4] sample at zero degrees inclination to loading	Core	[50]
	0.30	Data from triaxial testing of shale at depth 2800 m; North Sea well[4] sample at zero degrees inclination to loading		
$\breve{\Lambda}$ [GPa]	$\in (0.07, 0.4)$	Pierre-1 shale: drained[3]	Core	[51]
$\breve{\mathcal{K}}$ [GPa]	$\in (0.27, 0.84)$	Pierre-1 shale: drained[3]	Core	[51]
$\breve{\mathcal{G}}$ [GPa]	$\in (0.29, 0.71)$	Pierre-1 shale: drained[3]	Core	[51]
φ°	14.4	Muddy shale[5]		
	22.0	Stockton shale[5]	?	[38]
	7.5	Edmonton bentonitic shales[5]		
.....	.....	.....	.....	.....
	25	Data from triaxial testing of shale at depth 2000 m; North Sea well; Gullfisk field[4] sample at zero degrees inclination to loading	Core	[50]
	32	Data from triaxial testing of shale at depth 2800 m; North Sea well[4] sample at zero degrees inclination to loading		
.....	.....	.....	.....	.....
	$\in (3, 22)$	From shale nanoindentation; they use a Drucker–Prager model to estimate φ. They provide 12 sample means from which we give the range of means with data from both testing directions[5]	Core	[17]

[4]Secondary source.
[5]We converted from coefficient of friction ($= \tan(\varphi)$).

Physical range of parameters: Shales cont'd				
Parameter	Value	Notes/ Contextual data	Sample	Source
φ°	$\in (23.1, 38.3)$,	Shale crushed completely and re-constituted as a		
	$\in (21.8, 31.6)$,	paste for triaxial testing — multiple ranges given	Core	[59]
	$\in (29.4, 35)$	for each shale; we state the extremes: Barnett, Haynesville & Eagleford shales, respectively[5].		
.....	.....	.....	.....	.....
	35	General sandstone, shale etc	?	[62]
ψ°	$\psi + 20 < \varphi$	For concrete and rock[5]; used in [52] for shale[6]		
	$\in (12, 20)$	For rocks[5] (granulated and intact marble) and concrete[6]	Core/ stated	[98]
	$\in (6, 9)$	Granular rock/marble under high confining pressure[6] (200 MPa); data from [64]		
$\check{c}$ [MPa]	$\in (40, 170)$	From shale nanoindentation they use a Drucker–Prager model to estimate $\check{c}$. They provide 12 sample means from which we give the range of means	Core	[17]
.....	.....	.....	.....	.....
	$\in (10, 20)$	General sandstone, shale etc	?	[62]
.....	.....	.....	.....	.....
	126	Value estimated via minimising error between experimental data (from nanoindentation) and model	Core/ model	[16]
$\phi_{f,0}[\%]$	1.6	Pre-Cambrian; surface[4]		
	17	Pennsylvanian; 1000 ft[4]		
	7	Pennsylvanian; 3000 ft[4]	?	[38]
	4	Pennsylvanian; 5000 ft[4]		
	33.5	Cretaceous; 600 ft[4]		

[6] Vermeer and Borst [98] introduce an equation to calculate ψ from triaxial test data.

Physical range of parameters: Shales cont'd				
Parameter	Value	Notes/ Contextual data	Sample	Source
$\phi_{f,0}[\%]$	25.4	Cretaceous; 2500 ft[4]		
	21.1	Cretaceous; 3500 ft[4]		
	7.6	Cretaceous; 6100 ft[4]	?	[38]
	$\in (22, 32)$	Upper Tertiary Japanese Mudstone; near surface[5]		
	4.7	Muddy shale[5]		
	44.0	Edmonton bentonitic shale[5]		
.....	.....	.....	.....	.....
	$\in (5.7, 27.9)$	From mercury intrusion porosimetry and bulk density information. They provide 12 sample means from which we give the range of means	Core	[17]
.....	.....	.....	.....	.....
	$\in (6.5, 29.9)$	Determined by nanoindentation: Extremes values for each of 8 samples of shale are provided — we take the overall extremum values	Core	[16]
.....	.....	.....	.....	.....
	5–7	Marcellus[4]		
	4.5–6.5	Barnett[4]		
	3–8	Horn River[4]	Mixed[7]	[35]
	8–12	Haynesville[4]		
	2–10	Woodford[4]		
.....	.....	.....	.....	.....
	$\in (\sim 29, \sim 34)$	Data taken from Figure[4]: Pierre Shale (Central South Dakota) — claystone (mixed layer, montmorillonite, illite)	Core	[67]

[7] See source data.

Physical range of parameters: Shales cont'd				
Parameter	Value	Notes/ Contextual data	Sample	Source
$\phi_{f,0}[\%]$	$\in (\sim 35, \sim 65)$	Data taken from Figure[4]: (Barbados Accretionary Ridge complex) — clay, calcareous mudstone	Core	[67]
	$\in (\sim 12, \sim 37)$	Data taken from Figure[4]: Gulf of Mexico — clay, shale		
.....	.....	.....	.....	.....
	$\in (\sim 19, \sim 28)$	Data taken from Figure[4]: Estimated value from depth and thickness of sediments Colorado Group and Upper Manville Shales (Alberta) — claystone, shale	Estimation	[67]
	$\in (\sim 15, \sim 25)$	Data taken from Figure[4]: Estimated value from depth and thickness of sediments Pierre, Cafiile, Graneros Shales (Denver Basin) — claystone, shale		
.....	.....	.....	.....	.....
	$\in (\sim 50, \sim 63)$	Data taken from Figure: pure shale	Model?	[78]
	65	The un-compacted φ of pure shale in Eugene Island (at 1650 m)	Core	
$\breve{k}$ [ηD]	14 & 49	Measured via pulse-decay technique on sample under hydrostatic stress & constant confining pressure (15 MPa)– measured on different orientations as anisotropy common in shales	Core	[51]
.....	.....	.....	.....	.....
	20–1000	Marcellus[4]		
	20–1800	Barnett[4]		
	100–900	Horn River[4]	Mixed[7]	[35]
	100–500	Haynesville[4]		

Physical range of parameters: Shales cont'd				
Parameter	Value	Notes/ Contextual data	Sample	Source
$\breve{k}$ $[\eta \mathrm{D}]$	6–40	Eagle Ford[4]	Mixed	[35]
.....	.....	.....	.....	.....
	$\in (\sim 1, \sim 10)$	Data taken from Figure[4]: Pierre Shale (Central South Dakota) — claystone (mixed layer, montmorillonite, illite)		
	$\in (\sim 100, \sim 10^4)$	Data taken from Figure[4]: Barbados Accretionary Ridge complex — clay, calcareous mudstone		
	$\in (\sim 10, \sim 1000)$	Data taken from Figure[4]: Gulf of Mexico — clay, shale	Core	[67]
	$\in (\sim 0.1, \sim 100)$	Data taken from Figure[4]: Pierre, Cafiile, Graneros Shales (Denver Basin) — claystone, shale		
	$\in (\sim 1, \sim 100)$	Data taken from Figure[4]: Colorado Group and Upper Manville Shales (Alberta) — claystone, shale		
.....	.....	.....	.....	.....
	$\in (\sim 10^4, \sim 5\times 10^5)$	Data taken from Figure: pure shale	Model?	[78]

G.1.1 Elastic moduli analysis for shales

For comparison between different elastic parameters we must convert all the different elastic moduli to the same two elastic moduli. Clearly we use $\breve{\mathcal{M}}$ as the characteristic stress/pressure scale and our dimensionless elastic parameter is Γ; however, because Γ can be expressed in terms of only $\nu = \frac{\breve{\Lambda}}{\breve{\mathcal{M}}} = \frac{\Gamma}{1+\Gamma}$, for convenience we convert all the possible pairings of elastic parameters to ranges for $\breve{\mathcal{M}}$ and ν. Not all pairings of the elastic parameter compiled above lead to physically viable values for $\breve{\mathcal{M}}$ and ν. We hypothesise that this is because of a number of factors, the two most significant being whether the measure-

ment was taken *in situ* or from a core sample in a laboratory, and the intrinsic anisotropy of shale. Firstly, due to the depths common to shale formations, and the correspondingly high confining stresses, how the measurement is taken (*In situ vs* Core) is particularly noticeable. This can be seen most evidently in the significant difference in the values of $\breve{E}$ where lab results yield $\breve{E} \in (0.64, 1.56)$ GPa, while field data gives $\breve{E} \in (3.5, 58)$ GPa with $\sim \breve{E} \in (24, 58)$ GPa corresponding to a prospective shale. This is reflected in ν to a lesser extent where lab data gives $\nu \in (0.095, 0.30)$, while the field data for prospective shales gives $\sim \nu \in (0.16, 0.3)$ [21, 80].

Secondly, shale is layered and composed of different sediments; thus the orientation of measurement and loading will impact the apparent material properties. For example, this is the reason for the ranges in the data from Islam and Skalle [51]. In fact, shales that are prospective with $\sim \breve{E} \in (24, 58)$ typically exhibit little anisotropy but those with a lower $\breve{E}$ typically exhibit around four times more anisotropy [21].

Thus, to make sense of parameters from multiple sources we consider a sensible range for ν. For both lab and field data measured and loaded in any orientation $\nu \in (0.095, 0.37)$. This is entirely physically reasonable for any material and we enforce this to be true for any combination of two material parameters (either ν and one additional parameter, or two distinct parameters— see below). From this we provide a range of physically realistic $\breve{\mathcal{M}}$.

Elastic parameter summary: shales			
Params	$\breve{\mathcal{M}}$ [GPa]	ν	Context
$\breve{E}$ & ν	$\in (0.653, 103)$	$\in (0.095, 0.37)$	For full range of values above ($\breve{E}$ & ν from both lab and field data)
$\breve{E}$ & ν	$\in (24.5, 78.1)$	$\in (0.16, 0.30)$	Field – for a prospective shale
.....	.....	.....	.....
$\breve{\Lambda}$ & ν	$\in (0.119, 3.81)$	$\in (0.095, 0.37)$	For full range of values above ($\breve{\Lambda}$ from lab data & ν from both)
$\breve{\mathcal{K}}$ & ν	$\in (0.373, 2.08)$	$\in (0.095, 0.37)$	For full range of values above ($\breve{\mathcal{K}}$ from lab data & ν from both)

Elastic parameter summary: shales			
Params	$\breve{\mathcal{M}}$ [GPa]	ν	Context
$\breve{\mathcal{G}}$ & ν	$\in (0.648, 3.44)$	$\in (0.095, 0.37)$	For full range of values above ($\breve{\mathcal{G}}$ from lab data & ν from both)
$\breve{E}$ & $\breve{\Lambda}$	$\in (0.654, 7.17)$	$\in (0.095, 0.37)$	For full range of values above ($\breve{\Lambda}$ from lab data & $\breve{E}$ from both; ν spans both)
$\breve{\mathcal{K}}$ & $\breve{\Lambda}$	$\in (0.37, 2.08)$	$\in (0.095, 0.37)$	For full range of values above ($\breve{\Lambda}$ from lab data and $\breve{E}$ from both; ν spans both)
$\breve{\mathcal{G}}$ & $\breve{\Lambda}$	$\in (0.65, 1.82)$	$\in (0.095, 0.29)$	For full range of values above ($\breve{\Lambda}$ & $\breve{\mathcal{G}}$ from lab data; ν spans both)
$\breve{\mathcal{K}}$ & $\breve{E}$	$\in (0.656, 2.08)$	$\in (0.095, 0.37)$	For full range of values above ($\breve{\mathcal{K}}$ from lab data & $\breve{E}$ from both; ν spans both)
$\breve{\mathcal{K}}$ & $\breve{\mathcal{G}}$	$\in (0.657, 1.79)$	$\in (0.095, 0.345)$	For full range of values above ($\breve{\mathcal{K}}$ & $\breve{\mathcal{G}}$ from lab data; ν spans both)
$\breve{\mathcal{G}}$ & $\breve{E}$	$\in (0.660, 1.27)$	$\in (0.095, 0.37)$	For full range of values above ($\breve{\mathcal{K}}$ from lab data &$\breve{E}$ from both; ν spans both)
Overall ranges for all shales: lab tested, field data & field data (only prospective)			
Lab:	$\in (\sim 0.5, \sim 1.5)$	$\in (\sim 0.1, \sim 0.3)$	From core samples
Field	$\in (\sim 25, \sim 100)$	$\in (\sim 0.15, \sim 0.37)$	For all shales measured *in situ*
Prospective	$\in (\sim 25, \sim 80)$	$\in (\sim 0.15, \sim 0.3)$	For a prospective shale measured *in situ*

As discussed in §5.3, material parameters including elasticity moduli and friction angle are related to the clay content of shales. For example, the lower the p-wave modulus $\breve{\mathcal{M}}$ and the higher the Poisson's ratio ν, the more ductile the shale. Shale samples with clay and organic content above ∼30% by weight have $\varphi \sim 25°$ [59], although the friction angle for prospective shales can reach up to $\sim 50°$. The origin of all shales considered above is not known, but it seems that prospective shales tend to be on the lower end of that scale, such that $\phi_{f,0} \lesssim 35\%$.

G.2 Soils: clays and sands

Soil is a granular material with varying levels of cohesion between particles which deforms by irreversible movement of the grains; as such, soil is invariably modelled as a poroelasto-plastic material. There are many engineering problems for which we need poroelasto-plastic parameters of soil; for example compensation grouting[8], cavity expansion and bore-hole integrity problems. Due to the composition of soil in the shallow subsurface, we provide the poroelasto-plasic parameter values for clays and sands below.

Physical range of parameters: Clays				
Parameter	Value	Notes/ Contextual data	Sample	Source
$\breve{E}$ [GPa]	0.0017–0.0035	Soft clay	?	[27]
	0.0059–0.0138	Hard clay	?	
.....	.....	.....	.....	.....
	0.0020–0.0049	Low plasticity clay[4] (given in kilopond/cm^2)		
	0.0010–0.0029	Medium plasticity clay[4] (given in kilopond/cm^2)	?[7]	[69][9]
	0.0006–0.0020	High plasticity clay[4] (given in kilopond/cm^2)		
	0.0005–0.0020	Organic silt or clay[4] (given in kilopond/cm^2)		
.....	.....	.....	.....	.....
	$\in (0.156, 0.234)$	Woolwich & Reading bed clay modelled as Mohr-Coulomb; increasing with depth	Stated	[93]
.....	.....	.....	.....	.....
	0.238	London clay: mean values for Bender-element-aided triaxial tests — drained, in the horizontal direction	Core	[37]

[8]Compensation grouting is the process of injecting grout between the underground excavations and the surface helping ensure the stability of underground tunnels and the buildings that sit atop them [5].

[9]In Spanish.

Physical range of parameters: Clays cont'd				
Parameter	Value	Notes/ Contextual data	Sample	Source
$\breve{E}$	0.236	London clay: mean values for Static HCA tests: drained, in the horizontal direction		
	0.122	London clay: mean values for Bender-element-aided triaxial tests: drained, in the vertical direction	Core	[37]
	0.112	London clay: mean values for Static HCA tests: drained, in the vertical direction		
ν	0.15–0.25	Soft clay	?	[27]
	0.2–0.5	Medium clay		
.....	.....	.....	.....	.....
	$\in (0.156, 0.234)$	Woolwich & Reading bed clay modelled as Mohr-Coulomb	Stated	[93]
.....	.....	.....	.....	.....
	0.1	London clay: mean values for Bender-element-aided triaxial tests: drained, for vertical strains due to horizontal strain		
	0.25	London clay: mean values for Static HCA tests: drained, for vertical strains due to horizontal strain		
	-0.02	London clay: mean values for Bender-element-aided triaxial tests: drained, for horizontal strains due to horizontal strain	Core	[37]
	-0.19	London clay: mean values for Static HCA tests: drained, for horizontal strains due to horizontal strain		
	0.71	London clay: mean values for Bender-element-aided triaxial tests: drained, for vertical strains due to horizontal strain		

Physical range of parameters: Clays cont'd				
Parameter	Value	Notes/ Contextual data	Sample	Source
ν	0.49	London clay: mean values for Static HCA tests: drained, for vertical strains due to horizontal strain	Core	[37]
φ°	$\in (15, 30)$	Typical for clays; from triaxial tests[5]	Core/stated	[98]
.....	.....	.....	.....	.....
	24–32,	Low plasticity clay[4]		
	20–30	Medium plasticity clay[4]		
	17–27	High plasticity clay[4]		
	20–26,	Organic silt or clay	Stated[7]	[69][9]
	17.5	Soft, mouldable clay[4]		
	25	Semi-hard clay[4]		
	20	Hard, difficult to mould clay[4]		
.....	.....	.....	.....	.....
	27	Woolwich & Reading bed clay; modelled as Mohr-Coulomb	Stated	[93]
.....	.....	.....	.....	.....
	22–26	Very stiff and hard residual or pre-consolidated clay	Stated	[66]
	17–19	Medium stiff and stiff clay and silty clay		
.....	.....	.....	.....	.....
	28	Drained direct shear test on compacted silty clay[10] at high normal stresses	Core	[29]
.....	.....	.....	.....	.....
	20	Average result from drained triaxial and shear box test of London clay at Bradwell	Core	[85]
ψ°	0	Normally consolidated clays; from triaxial tests[6]	Core	[98]
	$\in (0, 20)$	For all soils, concrete or rocks; from triaxial tests[6]		

Physical range of parameters: Clays cont'd				
Parameter	Value	Notes/ Contextual data	Sample	Source
$\psi°$	13.5	Woolwich & Reading bed clay; modelled as Mohr-Coulomb	Stated	[93]
$\breve{c}$ [MPa]	0.015–0.0059	Low plasticity clay[4,12]		
	0.020–0.078	Medium plasticity clay[4,12]		
	0.029–0.098	High plasticity clay[4,12]		
	0.020–0.069	Organic silt or clay[4,12]	Stated	[69][9]
	0.025	Semi-hard clay[4]		
	0.020	Hard clay[4]		
	0.01	Soft clay[4]		
.....	.....	.....	.....	.....
	0.2	Woolwich & Reading bed clay; modelled as Mohr-Coulomb	Stated	[93]
.....	.....	.....	.....	.....
	0.013	Drained direct shear test on compacted silty clay[10] at high normal stresses	Core	
	0.0004–0.0022	From triaxial compression tests on cured[11] compacted silty clay[10]. Increasing with curing time (1–21 days)	Core & model	[29]
.....	.....	.....	.....	.....
	0.018	Average result from drained triaxial and shear box test of London clay at Bradwell	Core	[85]

[10]The clay minerals are mainly kaolinite but montmorillonite is also present.
[11]Curing is sealing the compressed clay in a moisture-resistant container and leaving for a period of time.
[12]Data given in $[t]/\text{m}^2$, we assume t means metric-ton force, with $[t]$ the associated units.

Physical range of parameters: Clays cont'd				
Parameter	Value	Notes/ Contextual data	Sample	Source
$\breve{c}$ [MPa]	$\in (0.059, 0.637)$	Kibushi clay, a porcelain clay taken from Tajimi city (converted from $\mathrm{kg/cm^2}$) varying moisture content (water content $\downarrow$, $\breve{c}$ $\uparrow$); we present the extreme values	Core	[110]
$\phi_{f,0}[\%]$	$\in (44.3, 59.1)$	Clay soil[4]. We take extreme values as a range	?	[22]
	$\in (28.4, 59.3)$	Clays[4]. From three samples– we take extreme values as a range	Core	
$\breve{k}$ [ηD]	$\in (.123, .972)$	Clay soil[4]. We take extreme values as a range[13]	?	[22]
	$\in (0.005, 0.24)$	Clays[4]. From three samples– we take extreme values as a range[13]	Core	[22]
.....	.....	.....	.....	.....
	1×10^8	Kaolinte, ($\phi_{f,0} = 50\%$) with data from [63] – a slurry is made, then consolidated		
	500	Illite ($\phi_{f,0} = 50\%$) with data from [63] – a slurry is made, then consolidated	Experiment	[78]
	1	Smectite ($\phi_{f,0} = 50\%$) with data from [63] – a slurry is made, then consolidated		
.....	.....	.....	.....	.....
	$7.1 \times 10^6 - 0.1 \times 10^6$	Kaolinte ($\phi_{f,0} = 50\%$) with data from [63] & [68]		
	510	Illite ($\phi_{f,0} = 50\%$) with data from [63] & [68]	Model & Core	[78]
	0.31	Smectite ($\phi_{f,0} = 50\%$) with data from [63] & [68]		

There is a significant variation in reported values of Young's Modulus and Poisson's ratio for clays. We hypothesise that this is due to the difference between ideal clays and

[13] Assumed units are Darcys.

geologically occurring clay formations such as London clay or Woolwich and Reading bed clay. These geological formations are less pure and have been cemented over many thousands of years. Similarly, natural clays are not homogeneous as can be seen from the results of Gasparre et al. [37]. For the data presented in Gasparre et al. [37] we average the values of $\breve{E}$ and ν across their different orientations to yield values that are representative for a homogeneous piece of London clay. Bender-element-aided triaxial tests lead to $\breve{E} \approx 0.18$ GPa and $\nu \approx 0.26$, while for Static HCA tests we obtain $\breve{E} \approx 0.17$ GPa and $\nu \approx 0.18$.

Physical range of parameters: Sand				
Parameter	Value	Notes/ Contextual data	Sample	Source
$\breve{E}$ [GPa]	0.0104–0.0276	Loose sand	?	[27]
	0.0345–0.069	Dense sand		
.....	.....	.....	.....	.....
	0.039–0.11	Sandy gravel[4] (given in kilopond/cm^2)		
	0.039–0.12	Sandy gravel with silt or clay (still granular structure)[4] (given in kilopond/cm^2)		
	0.015–0.039	Sand-gravel mix[4] (given in kilopond/cm^2)	Stated	[69][9]
	0.015–0.029	Fine sand[4] (given in kilopond/cm^2)		
	0.025–0.069	Course sand[4] (given in kilopond/cm^2)		
	0.020–0.059	Well graded sand[4] (given in kilopond/cm^2)		
	0.015–0.049	Silty sand[4] (given in kilopond/cm^2)		
	0.005–0.025	Plastic-silty sand [4] (given in kilopond/cm^2)		
.....	.....	.....	.....	.....
	0.17	Compacted quartz sand with grain size[4] ~ 90 μm	Core	[18]
.....	.....	.....	.....	.....
	~ 0.002–0.004	Values common for sand	?	[98]
ν	0.2–0.4	Loose sand	?	[27]

Physical range of parameters: Sand				
Parameter	Value	Notes/ Contextual data	Sample	Source
ν	0.25–0.4	Medium sand		
	0.3–0.45	Dense sand	?	[27]
	0.2–0.4	Silty sand		
.....	.....	.....	.....	.....
	0.25	Compacted quartz sand with grain size $\sim$ 90 μm; from triaxial test[4]	Core	[18]
$\breve{\mathcal{G}}$ [GPa]	$\in (\sim 0.013, \sim 0.039)$	Reloading cycles of a self-boring pressuremeter: wash sand at $\sim$ 3–7 m. Data taken from figure	*In situ*	[49]
	$\in (\sim 0.008, \sim 0.040)$	Reloading cycles of a self-boring pressuremeter: well-graded loose sand at Kernick $\sim$1–7.5 m. Data taken from figure		
φ°	43	Very dense sand; from triaxial tests[4]		
	≤ 45	Sand in general from triaxial tests [4]	Core	[98]
	$\in (25, 33)$	Quartz sands; from triaxial tests[4]		
.....	.....	.....	.....	.....
	< 29	Very loose sand[4]		
	29–30 & > 41	Loose sand[4]		
	30–36	Medium sand[4]		
	36–41	Dense sand[4]		
	> 41	Very dense sand[4]	?	[69][9]
	35–45	Sandy gravel[4]		
	35–43	Sandy gravel with silt or clay (still granular structure)[4]		
	28–35	Sand-gravel mix[4]		
	32–40	Fine sand[4]		

Physical range of parameters: Sand				
Parameter	Value	Notes/ Contextual data	Sample	Source
φ°	34–42	Course sand[4]		
	33–41	Well graded sand[4]		
	32–40	Silty sand[4]		
	25–32	Plastic-silty sand[4]	?	[69][9]
	30	Rounded loose sand[4]		
	32.5	Angular loose sand[4]		
	32.5	Semi-rounded loose sand[4]		
	35	Semi-angular loose sand[4]		
.....	.....	.....	.....	.....
	29–31	Clean gravel, gravel-sand mixtures, coarse sand		
	24–29	Clean fine to medium sand, silty medium to coarse sand, silty or clayey gravel	Stated	[66]
	19–24	Clean fine sand, silty or clayey fine to medium sand		
	17–19	Fine sandy silt, nonplastic silt		
.....	.....	.....	.....	.....
	$\sim\in(28, 40)$	Derived values from self-boring pressuremeter: wash sand at $\sim$ 3–7 m. Data taken from figure	*In situ* & model	
	$\sim\in(32, 42)$	Derived values from self-boring pressuremeter: well-graded loose sand at Kernick $\sim$2–8 m. Data taken from figure	*In situ* & model	[49]
	33	From triaxial tests[4]	Core	
.....	.....	.....	.....	.....
	42	Compacted quartz sand with grain size $\sim$ 90 μm; from triaxial test[4]	Core	[18]

Physical range of parameters: Sand cont'd				
Parameter	Value	Notes/ Contextual data	Sample	Source
$\psi°$	15, a few degrees	Very dense sand[6]; from triaxial tests[4]	Core	[98]
	$\in (0, 20)$	For all soils, concrete or rocks	Stated/ core	
	17	Compacted quartz sand with grain size $\sim$ 90 μm; from triaxial test[4]	Core	[18]
.....	.....	.....	.....	.....
	$\in (\sim -7, \sim 8)$	Derived values from self-boring pressuremeter: wash sand at $\sim$ 3–7 m. Data taken from figure; extremes provided as a range	*In situ* & model	[49]
	$\in (\sim -9, \sim 5)$	Derived values from self-boring pressuremeter: well-graded loose sand at Kernick $\sim$2–8 m. Data taken from figure; extremes provided as a range	*In situ* & model	[49]
$\breve{c}$ [MPa]	0	—	Stated/ core	[98]
.....	.....	.....	.....	.....
	0	Sandy gravel[4,12]		
	0–0.01	Sandy gravel with silt or clay (still granular structure)[4,12]		
	0.005–0.029	Sand-gravel mix[4,12]		
	0	Fine sand[4,12]	Stated	[69][9]
	0	Course sand[4,12]		
	0	Well graded sand[4,12]		
	0–0.01	Silty sand[4,12]		
	0.01–0.049	Plastic-silty sand[4,12]		

Physical range of parameters: Sand cont'd				
Parameter	Value	Notes/ Contextual data	Sample	Source
$\phi_{f,0}[\%]$	$\in (20, 33)$	Clayey sand; properties via digital image processing and analysis	Core/ model	[109]
.....	.....	.....	.....	.....
	$\in (33.8, 39.2)$	Packing of glass spheres; extremes for a range of average diameters[4]	Lab	[22]
.....	.....	.....	.....	.....
	$\in (\sim 42, \sim 56)$	Clean sand; data taken from figures	Model	[78]
	$\in (\sim 16, \sim 36)$	Clayey sand; data taken from figures	Core	
.....	.....	.....	.....	.....
	41	Compacted quartz sand with grain size ~ 90 μm; from triaxial test[4]	Core	[18]
$\breve{k}$ [ηD]	$\in (4.2 \times 10^3, 7.4 \times 10^4)$	Packing of glass spheres[4]; extreme values for the range of average diameters [13]	Lab	[22]
.....	.....	.....	.....	.....
	$\sim (10^9, 10^{10})$	Clean sand; data taken from figure	Model	[78]
	$\sim (10^5, 10^{10})$	Clayey sand; two samples from 1450 m and 1650 m; data taken from figures	Core	
.....	.....	.....	.....	.....
	2^{10}	Compacted quartz sand with grain size ~ 90 μm; from triaxial test[4]	Core	[18]

G.3 Pre-existing stress conditions

The pre-existing effective stress condition depends on many factors, including the depth of the site in question, the tectonic state at the site and the material above the site. In general, even at significant depths, the difference between the maximum and minimum principal

stresses is less than one order of magnitude, and in relatively flat areas we take one principal stress to be equal to the weight of the overburden [12, 48]. Thus, we need to just consider the application. As stated above, hydrocarbon-bearing or black shales are typically found at a depth of $\sim$ 0.5 – 4km; we assume that the composition of the material above the site to be sedimentary rocks and thus take the effective overburden (effective vertical stress) to increase by 15 MPa/km [62], which leads us to an effective overburden stress of 7.5–58.5 MPa. From the shale zone of North Sea well, Gullfisk field, at depth 2000 m, the measured vertical stress of 40 MPa and the maximum and minimum horizontal stresses of 37 MPa and 35 MPa, respectively, are consistent with the above. Additionally the shale zone of North Sea well at depth 2800 m has measured vertical stress of 52.5 MPa and the maximum and minimum horizontal stresses of 50.5 MPa and 46.5 MPa, respectively [50], which is also consistent. The effective stress for Pierre shale (central South Dakota) ranges from 0.1–50 MPa [67].

As discussed above in Appendix G.2, for most applications of clays and sands we tend to be considering a much shallower site: sand considered at 1–8 m depth and clays such as London clay at a depth in the order of tens of meters with Woolwich and Reading bed clays immediately below [85, 93]. In general, London clay is situated at 5–150 m [85]; in St James Park in London, London clay is present from 7.2–41.5 m and then at 41.5 m Woolwich and Reading bed clay starts [93]. An estimate for the effective overburden for sands found at around 1–8 m is given by 0.01 – 0.08 MPa, where the bulk weight of sand is taken to be $19\ \mathrm{kN/m^3}$ [49]. We take the bulk weight of clay to be similar and assume the same porosity. Thus, for clays commonly located at $\sim$5–50 m we get an estimate for the effective stress of 0.05 – 0.5 MPa.

Bibliography

[1] M. Abramowitz and I. A. Stegun. *Handbook of mathematical functions with formulas, graphs, and mathematical tables*, volume 55 of *Applied Mathematics Series*. United States National Bureau of Standards, 10th edition, 1972.

[2] L. Anand. On H. Hencky's approximate strain-energy function for moderate deformations. *Journal of Applied Mechanics*, 46(1):78–82, 1979.

[3] L. Anand. Moderate deformations in extension-torsion of incompressible isotropic elastic materials. *Journal of the Mechanics and Physics of Solids*, 34(3):293–304, 1986.

[4] M. Argoubi and A. Shirazi-Adl. Poroelastic creep response analysis of a lumbar motion segment in compression. *Journal of Biomechanics*, 29(10):1331–1339, 1996.

[5] S. K. A. Au, K. Soga, M. R. Jafari, M. D. Bolton, and K. Komiya. Factors affecting long-term efficiency of compensation grouting in clays. *Journal of Geotechnical and Geoenviromental Engineering*, 129:254–262, 2003.

[6] L. C. Auton and C. W. MacMinn. From arteries to boreholes: steady-state response of a poroelastic cylinder to fluid injection. *Proceedings of the Royal Society A*, 473: 20160753, 2017.

[7] L. C. Auton and C. W. MacMinn. From arteries to boreholes: transient response of a poroelastic cylinder to fluid injection. *Proceedings of the Royal Society A*, 474: 20180284, 2018.

[8] S. I. Barry and G. Aldis. Unsteady flow induced deformation of porous materials. *International Journal of Non-Linear Mechanics*, 26(5):687–699, 1991.

[9] S. I. Barry and G. Aldis. Radial flow through deformable porous shells. *The Journal of the Australian Mathematical Society. Series B. Applied Mathematics*, 34(03):333–354, 1993.

[10] S. I. Barry and G. N. Mercer. Effect of a moving boundary on the deformation of a poro-elastic cylinder. *ANZIAM Journal*, 39:627–666, 1998.

[11] Z. P. Bažant. Easy-to-compute tensors with symmetric inverse approximating Hencky finite strain and its rate. *Journal of Engineering Materials and Technology*, 120(2):131–136, 1998.

[12] Z. P. Bažant, M. Salviato, V. T. Chau, H. Viswanathan, and A. Zubelewicz. Why fracking works. *Journal of Applied Mechanics*, 81:101010, 2014.

[13] G. S. Beavers, K. Wittenberg, and E. M. Sparrow. Fluid flow through a class of highly-deformable porous media. Part II: Experiments with water. *Journal of Fluids Engineering*, 103(3):440–444, 1981.

[14] M. A. Biot. General theory of three-dimensional consolidation. *Journal of Applied Physics*, 12(2):155–164, 1941.

[15] T. I. Bjørnarå and S. A. Mathias. A pseudospectral approach to the McWhorter and Sunada Equation for two-phase flow in porous media with capillary pressure. *Computational Geosciences*, 17(6):889–897, 2013.

[16] C. P. Bobko and F.-J. Ulm. The nano-mechanical morphology of shale. *Mechanics of Materials*, 40:318–337, 2008.

[17] C. P. Bobko, B. Gathier, J. A. Ortega, F.-J. Ulm, L. Borges, and Y. N. Abousleiman. The nanogranular origin of friction and cohesion in shale—a strength homogenization approach to interpretation of nanoindentation results. *International Journal for Numerical and Analytical Methods in Geomechanics*, 35:1854–1876, 2011.

[18] B. Bohloli and C. J. De Pater. Experimental study on hydraulic fracturing of soft rocks: Influence of fluid rheology and confining stress. *Journal of Petroleum Science and Engineering*, 53:1–12, 2006.

[19] R. I. Borja and J. Choo. Cam-Clay plasticity, Part VIII: A constitutive framework for porous materials with evolving internal structure. *Computer Methods in Applied Mechanics and Engineering*, 309:653–679, 2016.

[20] R. I. Borja and S. R. Lee. Cam-clay plasticity, part 1: implicit integration of elasto-plastic constitutive relations. *Computer Methods in Applied Mechanics and Engineering*, 78:49–72, 1990.

[21] L. K. Britt and J. Schoeffler. The geomechanics of a shale play: What makes a shale prospective. In *Society of Petroleum Engineers Eastern Regional Meeting*, Charleston, West Virginia, USA, 23–25 September 2009.

[22] P. C. Carman. Permeability of saturated sands, soils and clays. *The Journal of Agricultural Science*, 29:262–273, 1939.

[23] J. P. Carter, J. R. Booker, and S. K. Yeung. Cavity expansion in cohesive frictional soils. *Géotechnique*, 36(3):349–358, 1986.

[24] S. Chou, R. Wang, and A. G. Fane. Robust and high performance hollow fiber membranes for energy harvesting from salinity gradients by pressure retarded osmosis. *Journal of Membrane Science*, 448:44–54, 2013.

[25] R. M. Corless, G. H. Gonnet, D. E. G. Hare, D. J. Jeffrey, and D. E. Knuth. On the Lambert W function. *Advances in Computational Mathematics*, 5(1):329–359, 1996.

[26] H. Daigle, A. Johnson, J. P. Gips, and M. Sharma. Porosity evaluation of shales using NMR secular relaxation. In *Proc. Unconventional Resources Technology Conference SPE*, page 1905272, Denver, Colorado, USA, 25–27 August 2014.

[27] B. M. Das. *Principles of Geotechnical Engineering*. PWS, Boston, 4th edition, 1998.

[28] R. O. Davis and A. P. S. Selvadurai. *Plasticity and Geomechanics*. Cambridge University Press, Cambridge, 2002.

[29] R. W. Day. Effective cohesion for compacted clay. *Journal of geotechnical engineering*, 118(4):611–619, 1992.

[30] D. Denney. Thirty years of gas-shale fracturing: What have we learned? *Journal of Petroleum Technology*, 62(11):88–90, 2010.

[31] E. Detournay. Propagation regimes of fluid-driven fractures in impermeable rocks. *International Journal of Geomechanics*, 4:35–45, 2004.

[32] E. Detournay and A. H. D. Cheng. Poroelastic response of a borehole in a non-hydrostatic stress field. *International Journal of Rock Mechanics and Mining Sciences & Geomechanics Abstracts*, 25(3):171–182, 1988.

[33] E. Detournay and C. Fairhurst. Two-dimensional elastoplastic analysis of a long, cylindrical cavity under non-hydrostatic loading. *International Journal of Rock Mechanics and Mining Sciences & Geomechanics Abstracts*, 24(4):197–211, 1987.

[34] M. J. Economides and K. G. Nolte, editors. *Reservoir Stimulation*. J. Wiley, 3rd edition, 2000.

[35] R. W. J. Edwards and M. A. Celia§. Shale gas well, hydraulic fracturing, and formation data to support modeling of gas and water flow in shale formations. *Water Resources Research*, 54:3196–3206, 2018.

[36] S. Federico and A. Grillo. Elasticity and permeability of porous fibre-reinforced materials under large deformations. *Mechanics of Materials*, 44:58–71, 2012.

[37] A. Gasparre, S. Nishimura, N. A. Minh, M. R. Coop, and R. J. Jardine. The stiffness of natural london clay. *Géotechnique*, 57(1):33–47, 2007.

[38] R. E. Goodman. *Introduction to Rock Mechanics*. Wiley, New York, 1980.

[39] B. Haimson and C. Fairhurst. Hydraulic fracturing in porous-permeable materials. *Journal of Petroleum Technology*, pages 811–817, July 1969.

[40] P. D. Hallett and T. A. Newson. Describing soil crack formation using elastic–plastic fracture mechanics. *European Journal of Soil Science*, 56:31–38, 2005.

[41] A. Hayatdavoudi, R. Nizamutdinov, J. Kravets, M. Fadden, M. J. Khattak, D. Hardy, et al. Increasing the pierre shale reservoir volume using heat-part I. In *49th US Rock Mechanics/Geomechanics Symposium*, San Francisco, California, 28 June-1 July 2015. American Rock Mechanics Association.

[42] H. Hencky. The law of elasticity for isotropic and quasi-isotropic substances by finite deformations. *Journal of Rheology*, 2(2):169–176, 1931.

[43] J. Herterich, I. Griffiths, and D. Vella. Reproducing the pressure–time signature of membrane filtration: The interplay between fouling, caking, and elasticity. *Journal of Membrane Science*, 2018. In press. Available at https://doi.org/10.1016/j.memsci.2018.12.073.

[44] J. G. Herterich, Q. Xu, R. W. Field, D. Vella, and I. M. Griffiths. Optimizing the operation of a direct-flow filtration device. *Journal of Engineering Mathematics*, 104:195–211, 2017.

[45] D. R. Hewitt, J. S. Nijjer, M. G. Worster, and J. A. Neufeld. Flow-induced compaction of a deformable porous medium. *Physical Review E*, 93(2):023116, 2016.

[46] R. Hill. *The Mathematical Theory of Plasticity*. Clarendon Press, Oxford, 1950.

[47] P. Howell, G. Kozyreff, and J. Ockendon. *Applied Solid Mechanics*. Cambridge University Press, Cambridge, UK, 2009.

[48] M. K. Hubbert and D. G. Willis. Mechanics of hydraulic fracturing. *AIME Petroleum Transactions*, 210:153–168, 1957.

[49] J. M. O. Hughes, C. P. Wroth, and D. Windle. Pressuremeter tests in sands. *Géotechnique*, 27(4):455–477, 1977.

[50] M. Islam, P. Skalle, A. Al-Ajmi, O. Søreide, et al. Stability analysis in shale through deviated boreholes using the mohr and mogi-coulomb failure criteria. In *44th US Rock Mechanics Symposium and 5th US-Canada Rock Mechanics Symposium*, Salt Lake City, UT, 2010. ARMA.

[51] M. A. Islam and P. Skalle. An experimental investigation of shale mechanical properties through drained and undrained test mechanisms. *Rock Mechanics and Rock Engineering*, 46:1391–1413, 2013.

[52] M. A. Islam, P. Skalle, and K. Konstantinos. *Critical assessment of shale resource plays*, chapter 7: Experimentally evaluating shale dilation behavior, pages 121–132. AAPG Memoir 103, 2013.

[53] R. N. Jana. Deformation in an infinite poroelastic medium with a long circular cylindrical hole. *The Quarterly Journal of Mechanics and Applied Mathematics*, 16 (2):137–148, 1963.

[54] G. Jayaraman. Water transport in the arterial wall—A theoretical study. *Journal of biomechanics*, 16(10):833–840, 1983.

[55] D. E. Kenyon. Transient filtration in a porous elastic cylinder. *Journal of Applied Mechanics*, 43(4):594–598, 1976.

[56] D. E. Kenyon. A mathematical model of water flux through aortic tissue. *Bulletin of Mathematical Biology*, 41(1):79–90, 1979.

[57] G. E. King. Hydraulic fracturing 101: What every representative, environmentalist, regulator, reporter, investor, university researcher, neighbor and engineer should know about estimating frac risk and improving frac performance in unconventional gas and oil wells. In *Society of Petroleum Engineers Hydraulic Fracturing Technology Conference*, The Woodlands, Texas, USA, 6-8th Feburary 2012.

[58] M. Klanchar and J. M. Tarbell. Modeling water flow through arterial tissue. *Bulletin of Mathematical Biology*, 49(6):651–669, 1987.

[59] A. H. Kohli and M. D. Zoback. Frictional properties of shale reservoir rocks. *Journal of Geophysical Research: Solid Earth*, 118(9):5109–5125, 2013.

[60] C. W. MacMinn, E. R. Dufresne, and J. S. Wettlaufer. Fluid-driven deformation of a soft granular material. *Physical Review X*, 5:011020, 2015.

[61] C. W. MacMinn, E. R. Dufresne, and J. S. Wettlaufer. Large deformations of a soft porous material. *Physical Review Applied*, 5(4):044020, 2016.

[62] G. Mandl. *Rock joints*. Springer, 2005.

[63] G. Mesri and R. E. Olson. Mechanisms controlling the permeability of clays. *Clays and Clay Minerals*, 19(151–158), 1971.

[64] P. N. Michelis. Work-softening and hardening behaviour of granular rocks. *Rock mechanics*, 14:187–200, 1981.

[65] M. J. Mullen, R. Roundtree, G. A. Turk, et al. A composite determination of mechanical rock properties for stimulation design (what to do when you don't have a sonic log). In *SPE Rocky Mountain Oil & Gas Technology Symposium*, Denver, Colorado, April 2007. Society of Petroleum Engineers.

[66] Naval Facilities Engineering Command. *Foundations & Earth Structures*. NARVAC manual, 7.02 edition, 1986.

[67] C. Neuzil. How permeable are clays and shales? *Water resources research*, 30(2): 145–150, February 1994.

[68] H. W. Olsen. Darcy's law in saturated kaolinite. *Water Resources Research*, 2(2): 287–295, Second Quarter 1966.

[69] J. M. Ortiz, J. S. Gesta, and C. O. Mazo. *Curso aplicado de cimentaciones*. Colegio Oficial de Arquitectos de Madrid (COAM)., Madrid, 4th edition, 1989.

[70] K. H. Parker, R. V. Mehta, and C. G. Caro. Steady flow in porous, elastically deformable materials. *Journal of Applied Mechanics*, 54:794–800, December 1987.

[71] R. Piché and J. Kanniainen. Solving financial differential equations using differentiation matrices. In *Proc. WCE 2007*, volume II, pages 1016–1022. World Congress on Engineering, London, UK, 2–4 July, Hong Kong: Newswood Ltd., 2-4 July 2007.

[72] R. Piché and J. Kanniainen. Matrix-based numerical modelling of financial differential equations. *International Journal of Mathematical Modelling and Numerical Optimisation*, 1(1-2):88–100, 2009.

[73] Y. Pinchover and J. Rubinstein. *An introduction to partial differential equations*. Cambridge University Press, Cambridge, UK, 2005.

[74] L. Preziosi, D. D. Joseph, and G. S. Beavers. Infiltration of initially dry, deformable porous media. *International Journal of Multiphase Flow*, 22(6):1205–1222, 1996.

[75] D. Pye. Hydraulic fracturing process, January 1973. US Patent 3,709,300.

[76] M. F. Randolph and C. P. Wroth. An analytical solution for the consolidation around a driven pile. *International Journal for Numerical and Analytical Methods in Geomechanics*, 3:217–229, 1979.

[77] J. Reichold, M. Stampanoni, A. L. Keller, A. Buck, P. Jenny, and B. Weber. Vascular graph model to simulate the cerebral blood flow in realistic vascular networks. *Journal of Cerebral Blood Flow & Metabolism*, 29(8):1429–1443, 2009.

[78] A. Revil and L. Cathles. Permeability of shaly sands. *Water Resources Research*, 35 (3):651–662, 1999.

[79] J. R. Rice and M. P. Cleary. Some basic stress diffusion solutions for fluid-saturated elastic porous media with compressible constituents. *Reviews of Geophysics and Space Physics*, 14(2):227–241, May 1976.

[80] R. Rickman, M. J. Mullen, J. E. Petre, W. V. Grieser, and D. Kundert. A practical use of shale petrophysics for stimulation design optimization: All shale plays are not clones of the Barnett Shale. In *Society of Petroleum Engineers Annual Technical Conference and Exhibition*, Denver, Colorado, USA, 21–24 September 2008.

[81] R. Risnes, R. K. Bratli, and P. Horsrud. Sand stresses around a wellbore. *Society of Petroleum Engineers of AIME*, 22(6):883–898, December 1982.

[82] L. G. Schultz, H. A. Tourtelot, J. R. Gill, and J. G. Boerngen. Composition and properties of the pierre shale and equivalent rocks, northern great plains region. U.S. Geological Survey Professional Paper 1064, U.S. Department of the Interior, 1980.

[83] G. Sciarra, F. dell'Isola, and K. Hutter. Dilatational and compacting behavior around a cylindrical cavern leached out in a solid-fluid elastic rock salt. *International Journal of Geomechanics*, 5(3):233–243, 2005.

[84] M. S. Seth and K. E. Gray. Transient stresses and displacement around a wellbore due to fluid flow in transversely isotropic, porous media: II. finite reservoirs. *Transactions SPE*, 243:79–86, 1968.

[85] A. W. Skempton. Horizontal stresses in an overconsolidated Eocene clay. In *Proc. 5th International Conference for Soil Mechanics and Foundation Engineering*, pages 351–357, Dunod, Paris, 1961.

[86] J. M. Skotheim and L. Mahadevan. Physical limits and design principles for plant and fungal movements. *Science*, 308:1308–1310, 2005.

[87] J. L. Sommer and A. Mortensen. Forced unidirectional infiltration of deformable porous media. *Journal of Fluid Mechanics*, 311:193–217, 1996.

[88] X. Song and R. I. Borja. Finite deformation and fluid flow in unsaturated soils with random heterogeneity. *Vadose Zone Journal*, 13(5), 2014.

[89] A. Swift, J. Sheets, D. Cole, L. Anovitz, S. Welch, X. Gu, D. Mildner, S. Chipera, E. Buchwalter, and A. Cook. Nano- to microscale pore characterization of the Utica Shale. In *Proc. Unconventional Resources Technology Conference SPE*, page 1923522, Denver, Colorado, USA, 25–27 August 2014.

[90] A. Tomic, A. Grillo, and S. Federico. Poroelastic materials reinforced by statistically oriented fibers—numerical implementation and applications to articular cartilage. *IMA Journal of Applied Mathematics*, 79(5):1027–1059, 2014.

[91] L. N. Trefethen. *Spectral Methods in MATLAB*. SIAM, 2000.

[92] L. N. Trefethen. *Approximation Theory and Approximation Practice*. SIAM, Philadelphia, 2013.

[93] A. Truty and R. Obrzud. Improved formulation of the hardening soil model in the context of modeling the undrained behavior of cohesive soils. *Studia Geotechnica et Mechanica*, 37(2):61–68, 2015.

[94] R. Uzuoka and R. I. Borja. Dynamics of unsaturated poroelastic solids at finite strain. *International Journal for Numerical and Analytical Methods in Geomechanics*, 36 (13):1535–1573, 2011.

[95] L. E. Vallejo. The brittle and ductile behavior of clay samples containing a crack under mixed mode loading. *Theoretical and Applied Fracture Mechanics*, 10:73–78, 1988.

[96] D. J. van Gerwen, J. Dankelman, and J. J. van den Dobbelsteen. Needle–tissue interaction forces—a survey of experimental data. *Medical Engineering & Physics*, 34(6):665–680, 2012.

[97] B. Vega, A. Dutta, and A. R. Kovscek. CT imaging of low-permeability, dual-porosity systems using high X-Ray contrast gas. *Transport in Porous Media*, 101: 81–97, October 2014.

[98] P. A. Vermeer and R. D. Borst. Non-associated plasticity for soils, concrete and rock. *HERON*, 29(3), 1984.

[99] A. S. Vesic. Expansion of cavities in infinite soil mass. *Journal of Soil Mechanics & Foundations (Division ASCE)*, 98(3):265–290, 1972.

[100] A.-T. Vuong, L. Yoshihara, and W. A. Wall. A general approach for modeling interacting flow through porous media under finite deformations. *Computer Methods in Applied Mechanics and Engineering*, 283:1240–1259, 2015.

[101] H. Wang. *Theory of linear poroelasticity with applications to geomechanics and hydrogeology*. Princeton University Press, 2000.

[102] Y. Wang. The effect of a nonlinear Mohr-Coulomb criterion on the stresses and plastic deformation near a circular opening in a poorly consolidated permeable medium. *Int. J. Rock Mech. Min. Sci. & Geomech. Abstr.*, 33(2):197–203, 1996.

[103] Y. Wang and M. B. Dusseault. Borehole yield and hydraulic fracture initiation in poorly consolidated rock strata—Part I. impermeable media. *Int. J. Rock Mech. Min. Sci. & Geomech. Abstr.*, 28(4):235–246, 1991.

[104] Y. Wang and M. B. Dusseault. Borehole yield and hydraulic fracture initiation in poorly consolidated rock strata—Part II. permeable media. *Int. J. Rock Mech. Min. Sci. & Geomech. Abstr.*, 28(4):247–260, 1991.

[105] Y. Wang and M. B. Dusseault. Stresses around a circular opening in an elastoplastic porous medium subjected to repeated hydraulic loading. *Int. J. Rock Mech. Min. Sci. & Geomech. Abstr.*, 31(6):597–616, 1994.

[106] Y. Wang, J. D. Scott, and M. B. Dusseault. Borehole rupture from plastic yield to hydraulic fracture—a nonlinear model including elastoplasticity. *Journal of Petroleum Science and Engineering*, 12:97–111, 1994.

[107] J. A. C. Weideman and S. C. Reddy. A MATLAB differentiation matrix suite. *ACM Transactions on Mathematical Software (TOMS)*, 26(4):465–519, 2000. The codes are available at `http://dip.sun.ac.za/~weideman/research/differ.html`.

[108] H. Xiao and L. S. Chen. Hencky's elasticity model and linear stress-strain relations in isotropic finite hyperelasticity. *Acta Mechanica*, 157(1-4):51–60, 2002.

[109] B. Yiediboe, H. Lin, Y. Jian, L. Cong, and W. Zhenliang. The relationship between the physical properties of soil and shape factors of its fragmented aggregates: A two-dimensional digital image processing and analysis approach. *International Journal of Engineering Research and Reviews*, 3(3):1–15, July–September 2015.

[110] H. Yokoi. Relationship between soil cohesion and shear strength. *Soil Science and Plant Nutrition*, 14(3):89–93, 1968.

[111] H.-S. Yu. *Cavity Expansion Methods in Geomechanics*. Kluwer Academic Publishers, Dordrecht, the Netherlands, 2000.

[112] H.-S. Yu and G. T. Houlsby. Finite cavity expansion in dilatant soils: Loading analysis. *Géotechnique*, 41(2):173–183, 1991.

[113] C. Zhang, R. P. Gamage, M. S. A. Perera, and J. Zhao. Characteristics of clay-abundant shale formations: use of CO2 for production enhancement. *Energies*, 10: 1887, 27p, 2017.

[114] J. Zhang and R. Salgado. Stress-dilatancy relation for mohr-coulomb soils following a non-associated flow rule. *Géotechnique*, 60(3):223–226, 2010.